OPTICAL SPECTROSCOPY STUDY OF CARRIERS RECOMBINATION IN QUANTUM WIRES

THÈSE N° 1877 (1998)

PRÉSENTÉE AU DÉPARTEMENT DE PHYSIQUE

ÉCOLE POLYTECHNIQUE FÉDÉRALE DE LAUSANNE

POUR L'OBTENTION DU GRADE DE DOCTEUR ÈS SCIENCES

PAR

Fabrice VOUILLOZ

Ingénieur physicien diplômé EPF
originaire de Martigny (VS) et de nationalité française

acceptée sur proposition du jury:

Prof. E. Kapon, directeur de thèse
Dr J.-Y. Marzin, rapporteur
Prof. A. Quattropani, rapporteur

Lausanne, EPFL
1998

à Marielle

Contents

Remerciements

En premier lieu, je tiens à remercier le professeur Eli Kapon de m'avoir accueilli dans son groupe de recherche et d'avoir dirigé ce travail de thèse avec une grande compétence scientifique.

Je tiens également à remercier Daniel Oberli pour son encadrement scientifique, ses conseils, ainsi que pour les nombreuses heures de discussions animées que nous avons eues.

J'exprime ma gratitude à François Lelarge pour son aide extrêmement précieuse dans l'analyse structurelle des fils, en particulier ses schémas inoubliables concernant la formation des images AFM...

Merci à Benjamin Dwir pour sa disponibilité et pour ses compétences aussi nombreuses que variées en informatique, électronique ou encore microscopie électronique.

Je souhaite remercier les personnes qui ont été impliquées dans la modélisation, la fabrication ou l'analyse des fils quantiques: Marc-André Dupertuis pour ses simulations numériques, Frank Reinhardt, Alok Rudra et Giorgio Biasiol pour la fabrication des structures ou les images AFM, ainsi que Anders Gustafsson et Klaus Leiffer pour les images TEM.

Merci aux Prof. Benoît Deveaud-Plédran, Prof. Antonio Quattropani, et Dr. Jean-Yves Marzin d'avoir accepté de constituer le jury de l'examen de thèse.

Je tiens à exprimer ma reconnaissance à ma famille et à ma belle-famille pour leur soutien au cours des années et pour l'intérêt constant qu'ils ont porté à mon travail.

Enfin, mais surtout, je tiens à remercier mon épouse pour son soutien de chaque instant, pour ses encouragements, pour sa patience, ainsi que pour sa curiosité scientifique hors pair qui m'a amené maintes fois à découvrir sa compréhension étonnante des phénomènes quantiques.

Abstract

We report the optical properties of high quality V-groove GaAs/$Al_{0.3}Ga_{0.7}As$ quantum wires (QWRs) with different thicknesses of the GaAs layer. The systematic investigation of photoluminescence (PL) and photoluminescence excitation (PLE) spectra as a function of the wire size combined with model calculations allows us to study in detail the effect of two-dimensional quantum confinement on valence band mixing and *polarization anisotropy*. We show that the polarization anisotropy of PL spectra critically depends on localization effects thus making any polarization analysis based on extended states insufficient at low temperature. The influence of exciton localization and surface corrugation on PLE spectra is also clarified; the observed large polarization anisotropy is unambiguously related to the one-dimensional (1D) character of our QWRs. Comparison of the experimental results obtained for all three QWR samples with theoretical predictions is clearly compatible with a strong *suppression of the 1D band-edge singularity* in PLE spectra.

The temperature dependence of PL and PLE spectra for QWRs of different thicknesses is investigated. We are able to measure photoluminescence up to room temperature due to high quantum efficiency. Additionally, large subband spacings and small inhomogeneous broadenings allow us to perform PLE measurements up to high temperature (100 − 200 K, depending on the wire size). A thermally-enhanced transfer of carriers from the side-QWs into the QWRs is evidenced and attributed to increasing 2D exciton mobilities with increasing temperature and to the combination of classical activation and tunneling through the potential barrier due to the "necking" in the side quantum wells (QWs) next to the QWRs. A strong impact of disorder on the PL (PLE) peak position and on the line shape is clearly shown. The evolution of the PL and PLE peak positions with increasing temperature together with a lineshape analysis of PL spectra indicates the *dominance of excitonic effects* over the whole temperature range. The enhancement of the lowest-energy PLE peak with respect to higher-energy transitions with increasing temperature is explained in terms of an effective mobility edge. The variation of the full width at half maximum of PL and PLE spectra with increasing temperature is attributed to the combined effects of structural disorder and exciton-phonon scattering.

We measure PL spectra of our high-quality QWRs through holes which vary from 2.0 μm down to 0.2 μm in width (micro-PL experiments). For sufficiently thin QWRs it is possible to observe directly the *localization of 1D excitons* in local potential minima. PL spectra detected through the smallest apertures (0.2 μm) are attributed to recombination of excitons in isolated quantum dot (QD)-like potentials wells. Homogeneously broadened lines can be resolved. The correlation between structural disorder and micro-PL features is studied. We determine the most realistic wire morphology as inferred from studies on planar and non-planar AlGaAs and GaAs layers by transmission electron and atomic force microscopy. A localization potential due to fluctuations of the wire cross-section along the wire axis is estimated and used to evaluate the impact of disorder on the optical properties. The effect of *exciton-exciton interactions* on the PL properties of localized excitons is evidenced. A shift to high energy of the exciton resonance at exciton densities much below the Mott density is attributed to the predominantly repulsive interaction between excitons due to the Pauli exclusion principle. The formation of *multi-excitonic states* in the dot-like structure is also evidenced by the evolution of the finely structured PL spectrum with increasing excitation density.

We also investigate the diffusion of 1D excitons as a function of temperature (5 < T < 80 K) and wire size. The longitudinal motion of the excitons can be well described by isothermal diffusion. A strong dependence of the diffusivity on temperature and wire size is observed. The increase of the exciton diffusivity with increasing temperature is attributed to the preponderant role of scattering by the interface roughness. The impact of the 1D nature of the excitons on the diffusion process is shown to appear at temperatures corresponding to a clear delocalization of the carriers (T > 60 K): In this temperature range, *larger diffusivities are found for thinner wires*. This result, in striking constrast with similar investigations in 2D systems, is explained by the *strong suppression of elastic scattering in 1D structures* due to the reduced phase space and by the wire-size dependent contribution of intersubband scattering. Finally, a decrease of the diffusivity with increasing excitation power density is explained in terms of exciton-exciton interactions.

Version abrégée

Ce travail de doctorat concerne l'étude des propriétés optiques de fils quantiques de GaAs/Al$_{0.3}$Ga$_{0.7}$As formés sur des substrats gravés en forme de V. L'investigation systématique des spectres de photoluminescence (PL) et de photoluminescence en excitation (PLE) en fonction de la taille des fils nous a permis une étude détaillée de l'effet du confinement bidimensionnel sur le mélange dans la bande de valence ainsi que son influence sur *l'anisotropie de polarisation*. Nous montrons que l'anisotropie de polarisation mesurée sur des spectres de PL dépend de manière critique des effets de localisation des excitons, rendant insuffisante toute analyse basée sur des états électroniques étendus. L'influence de la localisation des excitons et de l'ondulation de surface sur les spectres de PLE est également clarifiée. Ceci permet d'établir alors sans ambiguïté le lien entre le caractère unidimensionnel (1D) de nos fils et l'anisotropie de polarisation mesurée pour la transition optique fondamentale ainsi que pour les transitions entre états excités. La comparaison des résultats obtenus pour les différentes tailles de fils avec les calculs théoriques est clairement compatible avec une *forte suppression des divergences de Van Hove* sur les spectres de PLE.

Nous étudions également la dépendance en température des spectres de PL et PLE pour différentes tailles de fils. Grâce à la haute efficacité quantique de nos fils, des mesures de luminescence jusqu'à température ambiante peuvent être réalisées. De plus, la grande séparation énergétique entre les transitions excitoniques et le faible élargissement inhomogène de ces mêmes transitions nous permettent des expériences de PLE jusqu'à haute température (entre 100 K et 200 K suivant la taille du fil). Un accroissement thermique du transfert de porteurs des puits latéraux vers les fils est mis en évidence. Cet accroissement est attribué à la combinaison de l'activation thermique et de l'effet tunnel à travers la barrière de potentiel due à l'étranglement des puits latéraux au niveau de leur jonction avec les fils. Un effet marqué du désordre sur la position spectrale des pics de PL et PLE ainsi que sur la forme de ces pics est clairement démontré. L'analyse combinée de la dépendance en température de la position des pics de PL et PLE et de la forme spectrale des lignes de PL indique le *rôle dominant des corrélations excitoniques sur toute la gamme de température*. Le renforcement du pic de PLE de plus basse énergie vis-à-vis des autres transitions lorsque l'on augmente

la température est expliqué par l'existence d'une frontière effective de mobilité. La variation de la largeur de ligne des spectres de PL et PLE lors d'un accroissement de température est attribuée aux effets du désordre structurel ainsi qu'à la diffusion des excitons par les phonons.

Des spectres de luminescence ont aussi été mesurés à travers de microscopiques ouvertures (entre 0.2 μm et 2 μm) réalisées dans des masques métalliques couvrant la surface de l'échantillon. Ces expériences de micro-PL ont permis une observation directe d'*excitons 1D localisés* dans des minima de potentiel le long de fils très minces. Les spectres de PL mesurés à travers les plus petites ouvertures (0.2 μm) sont attribués à la recombinaison d'excitons dans des quasi-boîtes quantiques. Des lignes élargies de manière homogène ont ainsi pu être observées. La corrélation entre le désordre structurel et les caractéristiques de la micro-PL est étudiée. Nous déterminons la morphologie la plus réaliste possible pour nos fils, en nous basant sur des études de surfaces non-planaires et planaires de GaAs et AlGaAs, effectuées par microscopie à force atomique et microscopie électronique à transmission. Un potentiel de localisation, dû aux fluctuations de la section du fil le long de son axe, est estimé et utilisé pour évaluer l'impact du désordre sur les propriétés optiques. L'effet des *interactions exciton-exciton* sur la luminescence d'excitons localisés est mis en évidence. Un déplacement à haute énergie de la résonance excitonique, pour une densité d'excitons bien au-dessous de la densité de Mott, est attribuée à la prépondérance de la répulsion entre excitons due au principe d'exclusion de Pauli. La formation d'*états multi-excitoniques* dans la quasi-boîte quantique est également mise en évidence par l'évolution du spectre de micro-PL avec une augmentation de la densité d'excitation.

Nous investiguons aussi la diffusion d'excitons 1D en fonction de la température et de la taille des fils. Le mouvement longitudinal des excitons est très bien modélisé par une diffusion isotherme, excepté dans l'un des fils au-dessous de 10 K. Une forte dépendance de la diffusivité sur la température et la taille du fil est observée. L'accroissement de la diffusivité excitonique lors d'une augmentation de température est expliqué par le rôle dominant de la diffusion par la rugosité d'interface. La nature 1D des excitons est révélée à des températures supérieures à 60 K: dans cette gamme de temperature, nous trouvons une *diffusivité d'autant plus grande que le fil est étroit*. Ce résultat, en contraste frappant avec des études similaires dans des systèmes 2D, est attribué à la combinaison de deux effets: la *forte suppression de la diffusion élastique dans les fils* résultant de la reduction de l'espace de phase d'une part et la diffusion inter-sous-bandes d'autre part. Finalement, une décroissance de la diffusivité avec une augmentation de la densité d'excitation est expliquée par des interactions exciton-exciton.

Chapter 1

Introduction

1.1   Low-dimensional semiconductor structures

Modern material preparation technologies make it possible to fabricate artificial semi-conductor structures with well controlled features virtually down to the atomic level. The range of sizes accessible by various fabrication techniques as well as characterization methods is shown in Fig. 1.1 (a). The semiconductor nanostructures investigated in this thesis, with typical dimensions of the order of 10 nm, approach in size large molecules, and are quite smaller than structures which are commercially available in electronic circuits, such as short gate field-effect transistors. Thus, two classes of approaches for making semiconductor nanostructures have emerged, one based on fashioning them from larger pieces of material using lithography techniques, the other making use of self-assembly of nanostructures from atomic or molecular pieces. At the same time, methods for observing these nanostructures with virtually atomic resolution have also been developed, most notably transmission electron and scanning tunneling microscopies.

Research on low dimensional semiconductor was initiated in 1969 by Esaki and Tsu [Esaki and Tsu, 1969, Esaki and Tsu, 1970] who proposed an "engineered" semi-conductor superlattice. The advent of two new methods in film growth techniques, the molecular beam epitaxy (MBE) since 1970 and organometallic chemical vapor deposition (OMCVD) since 1968-9 have made it possible to grow atomic semiconductor layer upon layer, such as the artificial superlattice and two-dimensional (2D) quantum well (QW) structures. The advent of high-resolution lithography and dry etching techniques in the 1980s has lead to the realization of 1D and 0D semiconductor structures, the quantum wire (QWR) and quantum dot (QD, or quantum box, QB) structures, respectively. When the electrons are confined in space with a size comparable to the de Broglie wavelength in these low-dimensional structures, quantum size effect becomes important which drastically modifies the physical properties of the structures. Because
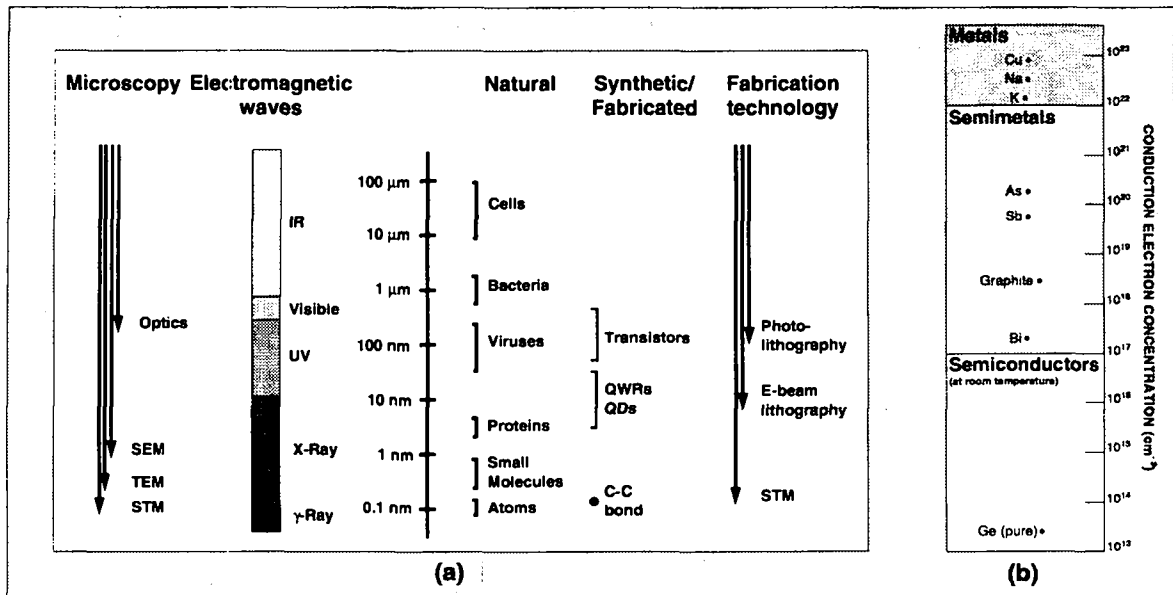
Figure 1.1: (a) Sizes: a perspective of the nanometer range; SEM $\equiv$ scanning electron microscopy, TEM $\equiv$ transmission electron microscopy, and STM $\equiv$ scanning tunneling microscopy. (b) Conduction electron concentration for semiconductors, semimetals, and metals.

of their new physical properties and their potential in device applications, the investigation of low-dimensional semiconductor structures has become one the most active areas in semiconductor and device physics.

To appreciate the dimensions required for obtaining such size quantization effects, we compare the de Broglie wavelength of conduction electrons in metals and semiconductors. At a temperature of 0 K, the electrons occupy the available energy states up to a maximum Fermi energy E_F, corresponding, in the free electron picture, to a Fermi wavelength λ_F (de Broglie wavelength of electrons having the maximum individual energy in the ground state of the system). The Fermi wavelength only depends on the number of electrons n per unit volume and can be written as [Ashcroft and Mermin, 1976]:

$$\lambda_F = 2\pi / \left(3\pi^2 n\right)^{1/3}.$$ (1.1)

For metals, the carrier density is relatively high since one or more electrons per atom contribute to the free electron gas, which results in small Fermi wavelengths. As an illustration, $\lambda_F \cong 0.46$ nm for copper and $\lambda_F \cong 0.52$ nm for silver. In pure semiconductors, the number of free carriers is lower than that in metals by orders of magnitude due to the gap between the filled and empty bands (see Fig. 1.1 (b)). In doped semiconductors, the carrier density is determined by the concentration of donors and acceptors. For example, for $n = 10^{18}$ cm^{-3} we have $\lambda_F = 29.3$ nm. This means that *structures with dimensions in the 10 nm range are sufficient for giving rise to quantum size effects*

in semiconductors.

1.1.1 Density of states in low-dimensional semiconductor structures

Confinement of charge carriers in semiconductors within potential wells of sufficiently small dimensions can lead to significant modification of the energy band structure and of the density of states (DOS) in these materials. This is at the origin of peculiar transport and optical properties of low-dimensional quantum confined structures (see, e.g., [Weisbuch and Vinter, 1991]). This quantum confinement gives rise to a set of bound states whose energy spectrum depends on the size of the potential well and on the number of dimensions in which the carrier motion is restricted. In the effective mass approximation, the energy spectrum E is obtained by solving the Schrödinger equation:

$$\left[-\frac{\hbar^2}{2m^*}\nabla^2 + V(x,y,z) \right] \psi(x,y,z) = E\psi(x,y,z), \tag{1.2}$$

where $\psi(x,y,z)$ is the carrier envelope wave function, m^* is the carrier effective mass, and $V(x,y,z)$ is the potential distribution [1]. For potential wells of rectangular shape (see insets in Fig. 1.2) 1D, 2D, and 3D quantum confinement can be achieved in film-, wire-, and box-like geometries by successively reducing the well dimensions t_z, t_y, and t_x. In the simple case of infinitely deep potential wells, the energy of the confined carriers (with respect to the band edge) is given by:

$$E_l = \frac{\hbar^2\pi^2 l^2}{2m^* t_z^2} + \frac{\hbar^2(k_y^2 + k_x^2)}{2m^*}; \qquad \text{1Dconfinement} \tag{1.3}$$

$$E_{l,m} = \frac{\hbar^2\pi^2}{2m^*}\left(\frac{l^2}{t_z^2} + \frac{m^2}{t_y^2} \right) + \frac{\hbar^2 k_x^2}{2m^*}; \quad \text{2Dconfinement} \tag{1.4}$$

$$E_{l,m,n} = \frac{\hbar^2\pi^2}{2m^*}\left(\frac{l^2}{t_z^2} + \frac{m^2}{t_y^2} + \frac{n^2}{t_x^2} \right); \qquad \text{3Dconfinement}, \tag{1.5}$$

where $l, m, n = 1, 2 \ldots$ are the level quantum numbers and $k_{y,x}$ are the wave vector components along the non-confined directions. Quantum confinement in such QW, QWR, or QD structures thus results in charge carriers of quasi-2D, 1D, or 0D nature.

The discrete energy levels arising from quantum confinement lead to modification of the DOS functions, which are given by [Kapon, 1992]:

---

[1] We note that the single band model for quantum confinement discussed here, while adequate for the conduction band, does not account for band mixing effects in the valence band. A multiband model should be used for the hole states (see Sec. 2.4.1).
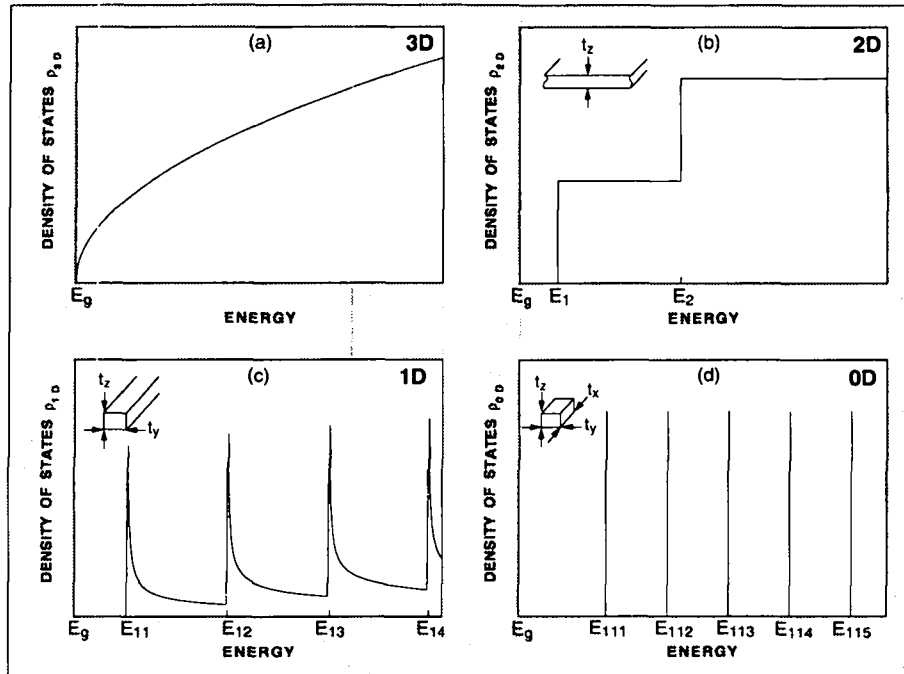
Figure 1.2: Schematic description of the density of states versus dimensionality. The insets illustrate rectangular potential well configurations of the corresponding quantum-confined structure. (a) bulk (3D), (b) quantum well (2D), (c) quantum wire (1D), and (d) quantum dot (0D).

$$\rho_{3D} = \frac{(2m^*/\hbar^2)^{3/2}}{2\pi^2}\sqrt{E} \qquad (1.6)$$

$$\rho_{2D} = \frac{m^*}{\pi\hbar^2 t_z}\sum_l \theta(E - E_l) \qquad (1.7)$$

$$\rho_{1D} = \frac{(2m^*)^{1/2}}{\pi\hbar t_z t_y}\sum_{l,m}(E - E_{l,m})^{-1/2} \qquad (1.8)$$

$$\rho_{0D} = \frac{2}{t_z t_y t_x}\sum_{l,m,n}\delta(E - E_{l,m,n}); \qquad (1.9)$$

for 3D, 2D, 1D, and 0D carriers (per unit volume, including spin degeneracy), respectively, with $\theta(x)$ representing the Heaviside function. The DOS distributions acquire sharper features as the carrier dimensionality is reduced, particularly in the case of 1D and 0D structures (see Fig. 1.2). As a result of the reduced carrier energy distribution, higher optical and differential gains should be achievable in quantum confined laser structures. This higher optical gain and the reduced volume of the active regions should in turn reduce the threshold currents of QWR and QD lasers [Yariv, 1988].
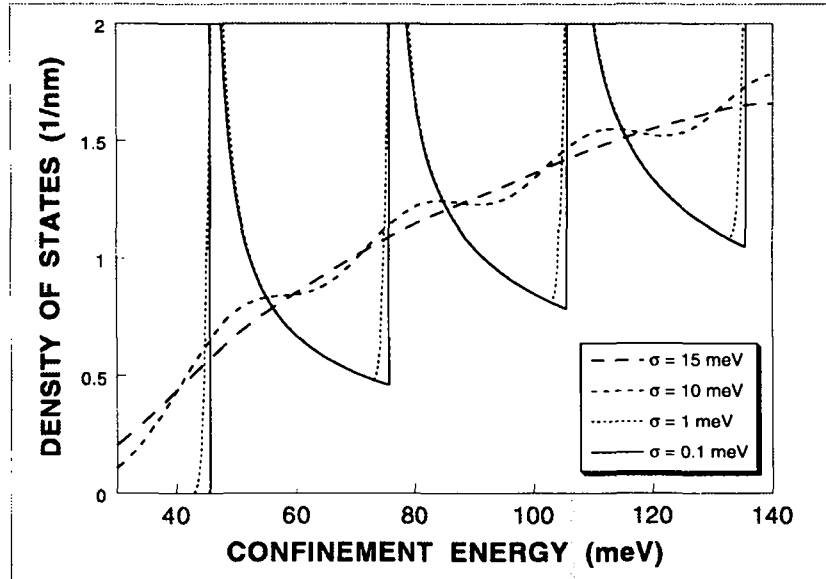
Figure 1.3: Electron DOS in a crescent-shaped GaAs/AlGaAs QWR (thickness at crescent center: 8.8 nm) for different standard deviation σ of the Gaussian broadening distribution.

1.1.2 Requirements for the observation of quantum confinement effects

Well resolved subbands

The above picture of quantized energy levels and DOS profiles is an idealized one. In particular, it ignores nonuniformities in the quantum well dimensions. Such nonuniformities result in inhomogeneous broadening of the energy spectra. For a 1D infinite square well (Eq. 1.3), fluctuations δt_z in the well width are related to the variations in confinement energy δE_l by $|\delta E_l|/E_l = 2\delta t_z/t_z$. Random variations in t_z and in the subband energies can be represented by a Gaussian distribution:

$$\Delta(E_l) = \frac{1}{\sqrt{2\pi}\sigma} e^{-(E_l-\langle E_l\rangle)^2/2\sigma^2}, \tag{1.10}$$

with a mean $\langle E_l\rangle$ and a standard deviation σ. In case of a QWR structure, one then obtains the following expression for the broadened DOS:

$$\rho_{1D}^{broad}(E) = \sqrt{\frac{m^*}{\pi}}\frac{1}{\pi\hbar\sigma} \int_0^E dE_l(E - E_l)^{-1/2} e^{-(E_l-\langle E_l\rangle)^2/2\sigma^2}. \tag{1.11}$$

When the width of the distribution Δ is comparable with the subband spacing, the unique features of the low-dimensional DOD are washed out, as illustrated in Fig. 1.3.

Population of ground state only

In addition to constraints on the uniformity of the QWRs, the size of the wire and the carrier density in the wire have to satisfy some criteria in order to preserve the reduced dimensionality. If at a temperature T several subbands are populated, a motion normal to the wire axis results. Therefore, to retain the reduced dimensionality associated with the confinement, the carriers should reside at the ground state. This requires:

(i) a subband separation $\Delta E_{1,2}$ greater than $k_B T$ to avoid thermal population; for infinite square QWs, for example, Eq. 1.3 implies that

$$t_z < \sqrt{\frac{3\hbar^2 \pi^2}{2m^* k_B T}}.$$

For GaAs at 300 K, it corresponds to $t_z < 20$ nm. Equivalent sizes can be deduced for the additional confinement directions in QWRs and QDs.

(ii) low enough carrier density (N) to avoid filling of higher subbands; in terms of the Fermi level E_F, this means $E_F < \Delta E_{1,2}$. At $T = 0$ and infinite square wells, we get $N < 1/L^2$ (per unit area) for QWs, and $N < 1/L$ (per unit length) for QWRs. For example, for a 10 nm wide QWR, the carrier density should be less than about 10^6 1/cm, or less than about one carrier per 10 nm.

1.2   Peculiarities of quantum wires

Semiconductor QWRs are expected to exhibit unique optical features due to the quantum confinement of their charge carriers in two directions. These features include very large exciton binding energy [Kodama et al., 1985], modified electroabsorption and electrorefraction spectra [Miller et al., 1988], and enhanced optical nonlinearities [Schmitt-Rink et al., 1989] and optical gain [Arakawa and Yariv, 1986]. Such properties, in turn, would make QWR heterostructures attractive for applications in novel optoelectronic devices offering new functionalities and improved performance. The higher optical gain and narrower spectral gain profiles should be particularly useful in QWR lasers showing extremely low threshold currents, reduced temperature sensitivity, higher modulation speed and narrower spectral linewidths [Arakawa and Sakaki, 1982, Asada et al., 1985, Arakawa and Yariv, 1986, Yariv, 1988, Kapon, 1992]. Such improved lasers would be interesting for optoelectronic applications involving integration of lasers with low power electronics or highly dense laser arrays, e.g., optical computer interconnects, image processing and optical computing. Sharper absorption and refraction spectra can be employed in lower voltage optical modulators and switches [Matsubara et al., 1989] as well as in high speed photodetectors [Crawford et al., 1991].

However, QWR heterostructures suitable for such optoelectronic applications need to meet a number of structural qualities. Beside the restrictions presented in the preceding section and that hold for any attempt to realize reduced-dimensionality structures, there are additional constraints imposed on QWRs acceptable for optoelectronic applications. First, the QWR interfaces should be free of defects in order to minimize nonradiative interface recombination effects which reduce quantum efficiency and carrier lifetime. The *in situ* formation of QWR structures during epitaxial growth is one of the most attractive solutions to achieve this objective (see section 1.3.2). Second, in order to ensure adequate interaction between the confined carriers and the optical beams, high density and uniform arrays of wires are desirable. And third, an efficient mechanism of carrier capture from the surrounding barriers into the QWRs is essential to efficiently utilize the excess carriers.

1.3   Fabrication technologies

The quantum size effect in semiconductors depends on the physical size of the structure and on the shape of the confining potential. Quantum wires of different shapes can be realized, depending on the fabrication technique. Therefore, the fabrication technology plays a crucial role in tailoring the desired electronic and optical properties. So far, several different approaches have been adopted to fabricate QWR structures. A representative group of demonstrated approaches for lateral patterning of semiconductor heterostructures is shown in Fig. 1.4 [Kapon, 1994]. The lightly shaded areas in this figure represent low band-gap materials (e.g., GaAs) whereas the unshaded ones correspond to higher band-gap regions (e.g., AlGaAs). These different approaches can be regrouped in two classes, the key features of which we discuss in the next two sections:

a) the patterning and etching technology, eventually followed by the regrowth of additional (passivating) semiconductor layers on the patterned structures (Fig. 1.4 (a)-(d));

b) the direct growth by special epitaxial methods (Fig. 1.4 (e)-(h)).

1.3.1   The patterning and etching technology

This technology is based on the chemical beam etching of semiconductor surfaces patterned by resist masks which define nanometer crystalline regions of different shapes. The patterning can be performed, e.g., by holographic lithography or electron-beam lithography on resists. The most direct patterning approach (Fig. 1.4 (a)) consists of selective removal of parts of the grown heterostructure using lithography and etching
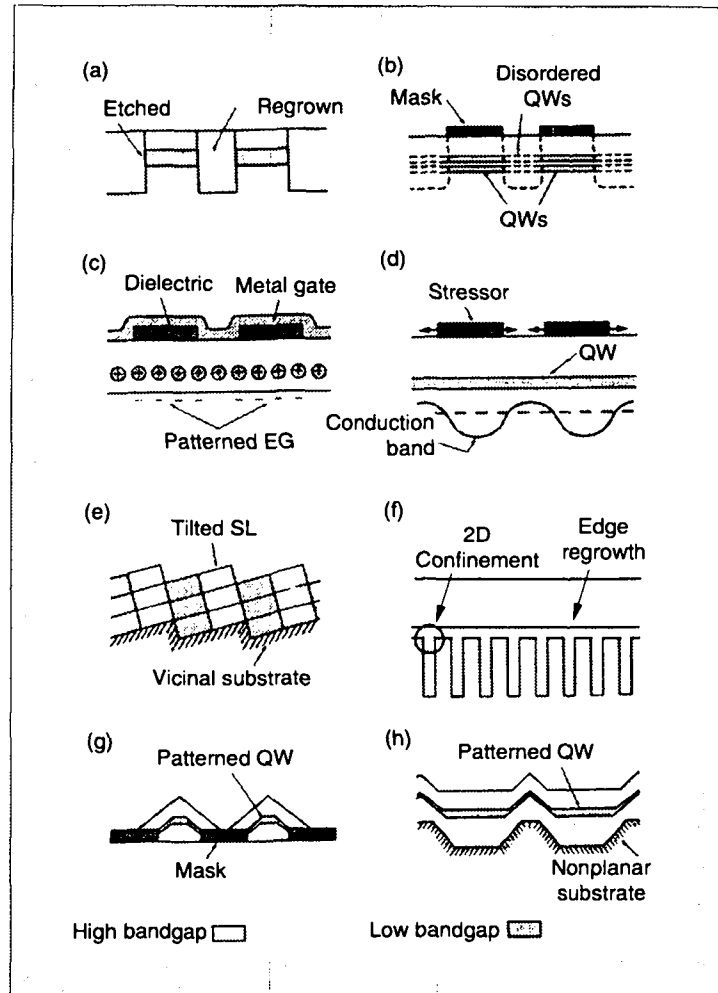
Figure 1.4: Approaches for lateral patterning of semiconductor heterostructures: (a) etching and regrowth, (b) selective QW disordering, (c) electrostatic gating, (d) strain-induced band-gap modulation, (e) growth on vicinal substrates, (f) regrowth on cleaved-edge of a QW structure (T-shaped QWRs), (g) growth on masked substrates and (h) growth on nonplanar substrates [Kapon, 1994].

techniques, followed by epitaxial regrowth for surface passivation [Kash et al., 1986, Marzin et al., 1992]. Selective disordering of QW layers (Fig. 1.4 (b)) induced by implanted or diffused impurities, introduced through a mask or using focused ion beams, has also been used to pattern the bandgap and refractive index of QW and super-lattice heterostructures [Laidig et al., 1981, Cibert et al., 1986, Kapon et al., 1988]. A number of methods have been specifically aimed at lateral patterning of 2D electron gas structures. As an example, electrostatic gating (Fig. 1.4 (c)) has been employed to deplete electrons from the reversed-biased gate regions, leaving islands of electron gas underneath the patterned dielectric mask [Ford et al., 1988]. Another method consists in depositing patterned "stressors" adjacent to the QW (Fig. 1.4 (d)), to produce lateral bandgap modulation via strain effects [Kash et al., 1989]. These approaches

provide flexibility in designing the patterned heterostructures. However, they are limited, in terms of lateral dimensions of the patterned features, by the resolution of the lithography technique employed. This limitation implies that imperfections in the lithographically defined features may directly affect the structural quality of the patterned semiconductor, and, consequently, lead to inhomogeneous broadening effects in the energy spectrum. Finally, while stressor deposition can yield smooth and defect-free lateral interfaces, etching and regrowth produces incorporation of defects into these interfaces, and impurities implantation can result in material contamination. Other approaches have attempted to overcome this limitation of by relying, to a varying degree, on the growth itself to generate the lateral patterning.

1.3.2 The direct growth by special epitaxial methods

The cleaved edge overgrowth method (Fig. 1.4 (f)) consists in the regrowth of a QW or of a modulation-doped heterostructure on the cleaved (011) edge of a (multiple) QW structure. Near the T intersection confinement is somewhat relaxed leading to a smaller kinetic contribution to the total energy. A carrier in such a bound state is free to move along the line defined by the intersecting planes of the two QWs [Pfeiffer et al., 1990]. Similarly, a twofold cleaved edge overgrowth yields the formation of QDs [Wegscheider et al., 1997]. This technique allows control of the QWR and QD sizes to the monolayer scale, but suffers from weak lateral confinement (generally less than 30 meV) and reduced flexibility for design.

Lateral heterostructure patterning can also be achieved by epitaxial growth on substrates patterned with dielectric masks (Fig. 1.4 (g)) [Cho and Ballamy, 1975]. In this approach, the substrate is coated with a dielectric film which is patterned lithographically. Restriction of the epitaxial growth to the unmasked region can then yield the desired lateral patterning of the heterostructure.

Self-ordering techniques utilize the spontaneous modification of the growth front under certain growth conditions to yield 1D or 0D structures. One example is MBE or MOCVD growth on vicinal substrates (Fig. 1.4 (e)). Growth of alternate layers of GaAs and AlAs on a surface tilted by an angle θ relative to the (100) plane results in the formation of tilted superlattices [Petroff et al., 1984]. The main problem with this approach is the apparent nonuniformity of the lateral superlattice. Maintaining the structure regularity across the sample and during growth requires extremely good control of growth rate and other growth parameters. The major two disadvantages of methods relying on spontaneous self-ordering are the following. First, the position of the self-ordered structures is not controlled. Second, effects which tend to disorder the structure, e.g., defects, perturb the force that drives the structure towards a self-
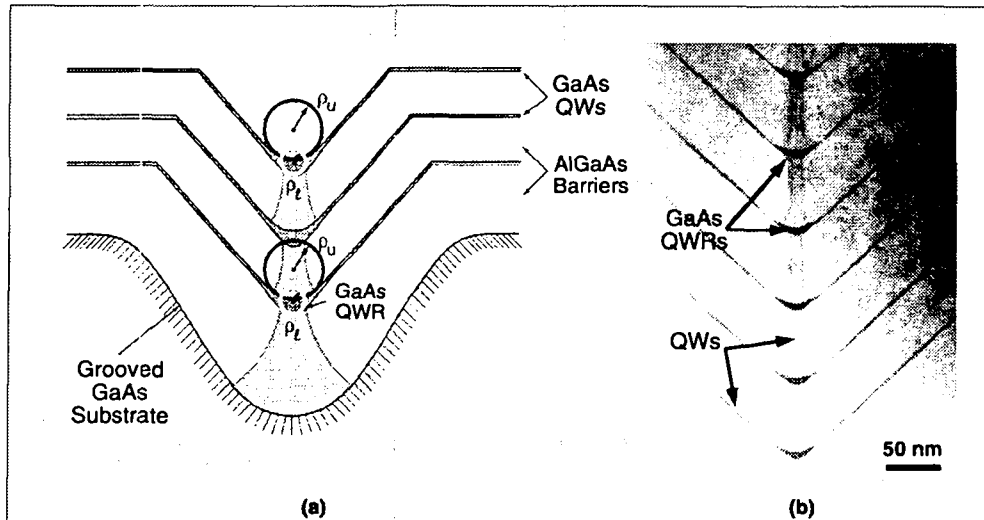
Figure 1.5: a) Schematic of the formation of crescent shaped GaAs/AlGaAs QWRs by OMCVD on grooved substrates; ρ indicates the radius of curvature at the bottom of the groove; b)TEM cross sectional image of a vertically-stacked GaAs/AlGaAs QWR array structure [Kapon et al., 1992b].

ordered phase. The nonuniformities resulting from these two problems lead to large inhomogeneous broadening of the energy spectra, which, in turn, prevents a detailed study of quantum confined effects.

To circumvent the intrinsic limitations of spontaneous self ordering a new approach, termed *seeded self ordering*, has been developed. In this method, the site of the self-ordered structure is defined by lithography ((Fig. 1.4 (h)), and the nanostructure is then formed during the epitaxial growth process [Tsang and Cho, 1977, Miller and Kleinman, 1985, Kapon et al., 1987, Meier et al., 1989]. GaAs/AlGaAs QWR structures grown by OMCVD on nonplanar substrates are a good example of this approach. In this case, a characteristic set of crystal planes evolves and redefines the surface profile in a self limiting manner. The formation of GaAs QWRs on self-limiting AlGaAs grown on V-shaped grooves occurs via a transient increase of the growth rates in a set of different nanofacets [Biasiol et al., 1997]. The self-limiting AlGaAs profiles are stable over (at least) μm long vertical distances, allowing the growth of uniform vertical arrays of wires [Gustafsson et al., 1995, Kapon et al., 1996, Biasiol et al., 1996]. This approach is illustrated in Fig. 1.5a), which shows the evolution of GaAs/AlGaAs multiple QWR structures during OMCVD growth on grooved (100)-GaAs substrates [Kapon et al., 1992b]; the wires are oriented in the [01$\bar{1}$] direction. A cross section picture taken with a transmission electron microscope (TEM) of such a structure is shown in Fig. 1.5b). The main advantage of this fabrication approach is the *in situ* formation of all interfaces during epitaxial growth, which leads to defect-free wire interfaces. Furthermore, the size and the shape of the wires depend mainly on the growth conditions
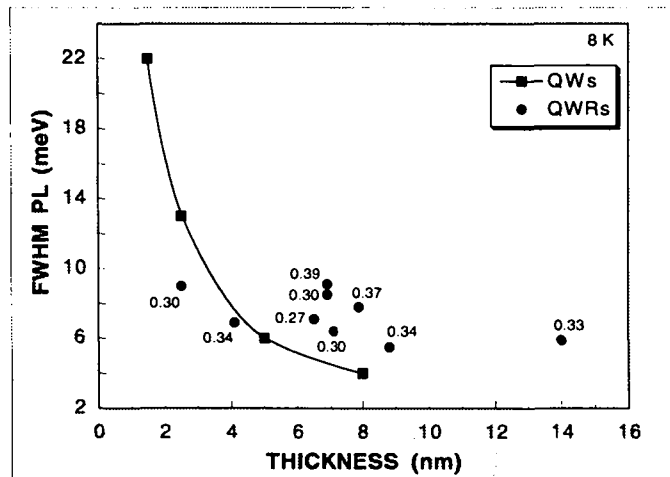
Figure 1.6: FWHM of photoluminescence spectra for GaAs/AlGaAs QW and QWR structures with different thicknesses of the GaAs layer. For QWR structures, the thickness is measured at the crescent center. The Al mole fraction is 0.35 for QWs; for QWRs, the Al mole fraction is indicated near the corresponding symbols. The exciting photon energy is 2.41 eV and the power density ~ 5 W/cm^2.

and material composition, which reduces the impact of imperfect lithography on the uniformity of the quantum structures. Effective wire widths of less than 10 nm are achievable with this technique. In Fig. 1.6 we compare the full width at half maximum (FWHM) of photoluminescence spectra for GaAs QWs and QWRs of different thickness. For QWRs, the thickness is measured at the center of the crescent. Although informations on the structural quality of heterostructures should be deduced with care from luminescence data [Miller and Bhat, 1988], this figure indicates that the interface disorder (thickness or alloy fluctuations) of QWR structures is not drastically modified by the growth on nonplanar substrates.

1.4 Goals of this work

The present work, funded partially by the Fonds National Suisse de la Recherche Scientifique, formed part of a wider project focused on the formation mechanisms and optical properties of quantum wires grown on nonplanar substrates. This thesis is concerned with the optical properties of GaAs/AlGaAs QWRs. Photoluminescence (PL) and photoluminescence excitation (PLE) experiments will be carried out to investigate the effect of the lateral confinement on valence-band mixing and polarization anisotropy. The impact of excitonic effects on the luminescence and absorption properties will be discussed. Linear and circular polarization analysis of the excitonic transitions will be combined with a calculation of the electronic band structure to identify the nature of the transitions and to *demonstrate unambiguously the 1D character of our QWRs.*

Spatially resolved PL (micro-PL) and temperature dependent optical spectroscopy will be employed to *address the effect of disorder in a 1D structure*. Cross-sectional and topographical informations obtained by TEM and atomic force microscopy (AFM), respectively, will be used to establish the relationship between the wires morphology and micro-PL features. Finally, time-of-flight (TOF) experiments will be conducted to *study the motion of excitons in the wires*. These TOF experiments are based on the detection of carrier motion as a function of spatial position and time. High spatial resolution needed for micro-PL and TOF measurements will be achieved by the realization of microstructured masks directly placed on the surface of the samples.

1.5   Thesis plan

In Chap. 2 we recall some of the electronic properties of the GaAs and AlGaAs materials used to fabricate our QWR structures and we perform calculations of the QWR eigenstates. The concept of excitons is then introduced and the impact of excitonic effects on the optical spectra of our QWRs is addressed.

A description of the samples structure and of the experimental setups is given in Chap. 3. We also determine the most realistic wire morphology as inferred from TEM and AFM studies. This allows us to estimate a localization potential due to fluctuations of the wire cross-section along the wire axis. The optical measurements methods are presented; in particular, we discuss the mask and the TOF techniques.

The polarization properties of PL and PLE spectra are investigated in Chap. 4. Linear and circular polarization analysis are used to study the nature of the optical transitions and the impact of localization effects on the optical properties. The influence of surface corrugations is also discussed.

In Chap. 5 we present the temperature dependence of PL and PLE spectra. The effect of disorder and that of excitonic correlations on the temperature dependence of optical properties are studied.

A direct observation of localization of 1D excitons in local potential minima is reported in Chap. 6. The correlation between structural disorder and micro-PL features is investigated. The effect of exciton-exciton interactions on the PL properties is discussed.

An optical investigation of the diffusion of 1D excitons is presented in Chap. 7. The dependence of the diffusion process on the wire size and on the temperature is addressed.

Finally, we draw some conclusions and give an outlook on open issues in Chap. 8.

Chapter 2

Theory

2.1 Introduction

In this chapter we recall some of the electronic properties of the bulk materials involved in the III-V heterostructures and we deal with the determination of the eigenstates of our QWRs. We present two models solving the 2D Schrödinger equations for electrons and holes: The first one includes valence band mixing and is used to determine, in particular, the polarization dependence of the interband transitions. The calculated eigenenergies and band-to-band matrix elements will allow us to analyze PL and PLE results in Chap. 4. The second one is simpler (no band mixing) and is used to estimate the confinement energy fluctuations along the wire axis. It will be involved in the determination of the longitudinal localization potential presented in Sec. 3.2.3 and used in Chap. 6. The concept of exciton is then introduced and the influence of excitonic effects on the optical properties of QWR structures is addressed.

2.2 Bulk III-V compounds

2.2.1 Crystalline properties

The III-V compounds crystallize in the zinc-blende structure. This lattice consists of two interpenetrating, face-centered cubic (f.c.c.) lattices, displaced from one another by a fourth of one of the cube main diagonals (see Fig. 2.1 (a)). The zinc blende lattice is not a Bravais lattice because the elementary cell contains two atoms. The lattice parameter a is 5.65 Å for GaAs and 5.62 Å for AlAs [Ashcroft and Mermin, 1976]. The very close values of a for the two binary compounds allows us to describe GaAs/AlGaAs heterostructures as nonstrained crystalline structures. The reciprocal lattice of the Bravais lattice underlying the zinc blende lattice is a body centered cubic lattice (see Fig. 2.1 (b)). Several high symmetry points or lines of the first Brillouin zone have received specific notations, e.g. the Γ, X, or L points.
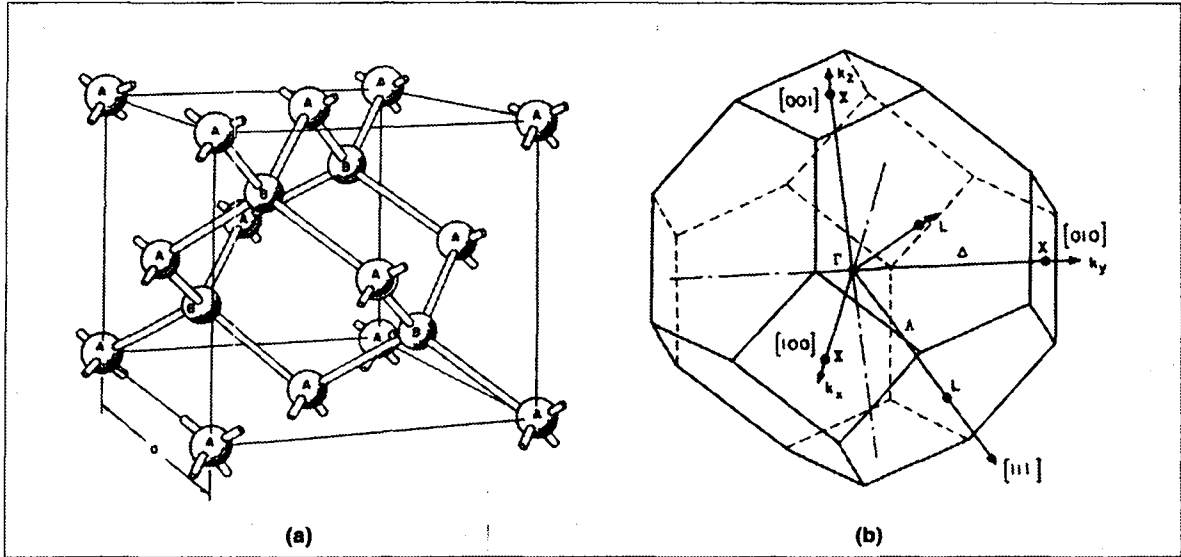
Figure 2.1: (a) Spatial arrangement of atoms in a zinc-blende lattice. (b) First Brillouin zone of a face-centered cubic lattice [Bastard, 1992].

2.2.2 Electronic properties

In III-V binary compounds like GaAs, there are 8 outer electrons per unit cell which contribute to the chemical bonds. These 8 electrons (3 from Ga and 5 from As) hybridize to form tetrahedral bonds between one kind of atom and its four nearest neighbours. The hybridization of the orbitals of every atom (s-like or p-like) with an orbital of the neighbouring atom produce two levels: one bonding and one antibonding. The 8 electrons fill the 2 s-bonding states and the 6 p-bonding states. The s-antibonding states are empty. As a consequence of the large number of unit cells, bonding and antibonding levels broaden into bands. The p-bonding states form the upper part of the valence band whereas the lowest lying band originating from the s-antibonding orbitals form the conduction band.

In all III-V materials the top of the valence band occurs at the center of the Brillouin zone (Γ point, see Fig. 2.2). In the absence of spin-orbit coupling, the three valence bands are degenerate at Γ. The spin-orbit coupling lifts this sixfold degeneracy and gives rise to a quadruplet (symmetry Γ_8) which corresponds to $J = \frac{3}{2}$, and to a doublet (symmetry Γ_7) which corresponds to $J = \frac{1}{2}$, where $\mathbf{J}$ is the total angular momentum. The conduction band edge is separated from the topmost valence band by an energy gap E_g. For GaAs and $Al_x Ga_{1-x} As$ with $x < 0.45$ the conduction band edge is found at the Γ point (direct gap materials, see Fig. 2.2).
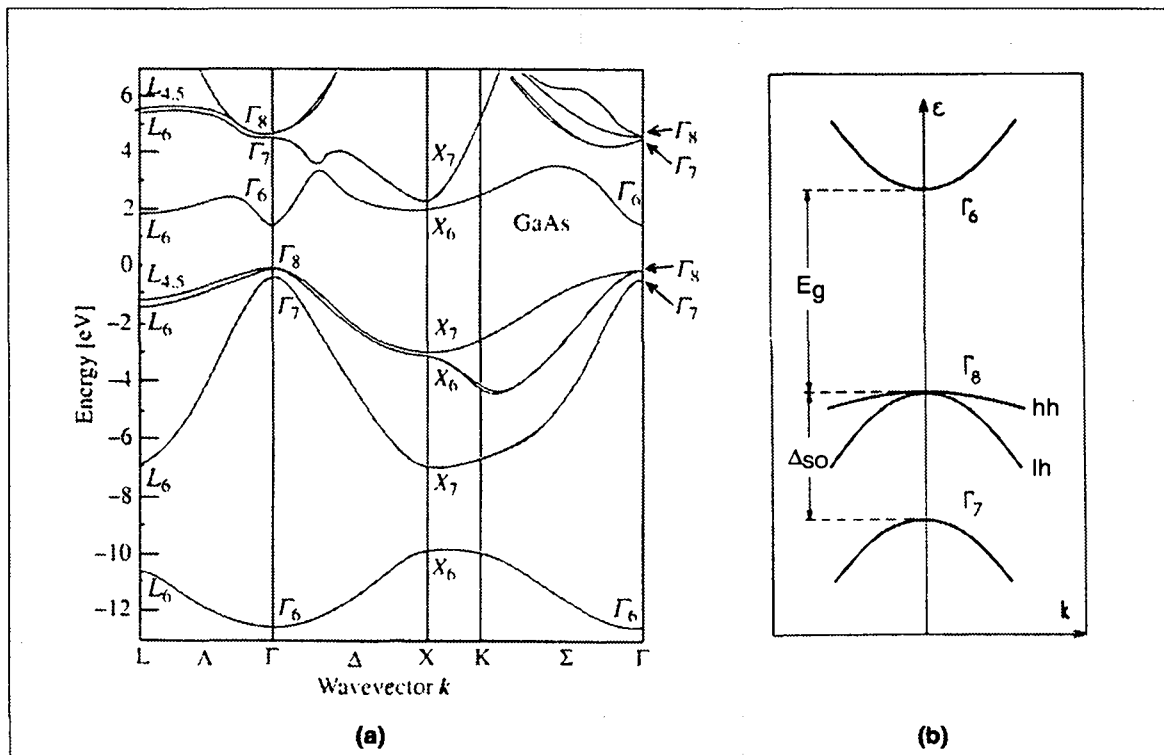
Figure 2.2: (a) Band structure of GaAs, showing the four valence bands and the first several conduction bands [Cardona and Yu, 1996]. (b) Band structure of a direct gap III-V compound in the vicinity of the zone center. If we choose the quantization axis z of the total angular momentum $\mathbf{J}$ along the $\mathbf{k}$ vector, the heavy hole (hh) and light hole (lh) bands correspond to a given value of J_z: $J_z = \pm\frac{3}{2}$ for hh and $J_z = \pm\frac{1}{2}$ for lh [Bastard, 1992].

k.p method

Near the band edges the dispersion relations can be approximated using perturbation theory. We start from the Schrödinger equation:

$$\left[\frac{\mathbf{p}^2}{2m_0} + V(\mathbf{r})\right]\Psi(\mathbf{r}) = E\Psi(\mathbf{r}),\tag{2.1}$$

where $\mathbf{p}$ is the momentum operator, m_0 is the free electron mass, and $V(\mathbf{r})$ is the periodic potential representing the interaction of electrons with the atomic cores. The solutions are of the Bloch form:

$$\Psi_{n,\mathbf{k}}(\mathbf{r}) = \frac{1}{\sqrt{\Omega}}u_{n,\mathbf{k}}(\mathbf{r})e^{i\mathbf{k}\cdot\mathbf{r}},\tag{2.2}$$

with $u_{n,\mathbf{k}}$ the periodic Bloch factors and $e^{i\mathbf{k}\cdot\mathbf{r}}$ a plane wave. We can rewrite the Schrödinger equation for the Bloch factors in the following way:

$$[H(\mathbf{k} = 0) + W(\mathbf{k})]u_{n,\mathbf{k}} = E_{n,\mathbf{k}}u_{n,\mathbf{k}},\tag{2.3}$$

where

$$H(\mathbf{k} = 0) = \frac{\mathbf{p}^2}{2m_0} + V(\mathbf{r}), \quad \text{and} \tag{2.4}$$

$$W(\mathbf{k}) = \frac{\hbar^2 k^2}{2m_0} + \frac{\hbar \mathbf{k} \cdot \mathbf{p}}{m_0} \quad \text{(perturbation term)}. \tag{2.5}$$

Once $E_{n,0}$ and $u_{n,0}$ are known, we can treat the terms $\hbar^2 k^2 / 2m_0$ and $\hbar \mathbf{k} \cdot \mathbf{p} / m_0$ as perturbations using either degenerate or nondegenerate perturbation theory (see, e.g., [Yu and Cardona, 1996]). This method for calculating the band dispersion is known as the **k.p** method. As an example of application of this method we will derive the band dispersion and effective mass for a nondegenerate band, which is applicable to the conduction band minimum in direct-bandgap semiconductors with the zinc-blende and wurtzite structures. We note that the top valence bands in many semiconductors with the diamond, zinc-blende or wurtzite structures have to be treated with the degenerate band model.

Let us assume that the band structure has an extremum at the energy $E_{n,0}$ and the band is nondegenerate at this energy. Using standard nondegenerate perturbation theory, the eigenfunctions $u_{n,\mathbf{k}}$ and eigenvalues $E_{n,\mathbf{k}}$ at a neighboring point $\mathbf{k}$ can be expanded to second order in k in terms of the unperturbed wave functions $u_{n,0}$ and energies $E_{n,0}$ by treating the terms involving $\mathbf{k}$ in Eq. 2.3 as perturbations.

$$u_{n,\mathbf{k}} \cong u_{n,0} + \frac{\hbar}{m_0} \sum_{m \neq n} \frac{\langle u_{n,0} | \mathbf{k}.\mathbf{p} | u_{m,0} \rangle}{E_{n,0} - E_{m,0}} u_{n,0}, \tag{2.6}$$

and

$$E_{n,\mathbf{k}} \cong E_{n,0} + \frac{\hbar^2 k^2}{2m_0} + \frac{\hbar^2}{m_0^2} \sum_{m \neq n} \frac{|\langle u_{n,0} | \mathbf{k}.\mathbf{p} | u_{m,0} \rangle|^2}{E_{n,0} - E_{m,0}}, \tag{2.7}$$

The linear terms in k vanish because $E_{n,0}$ has been assumed to be an extremum. It is conventional to express the energy $E_{n,k}$, for small values of k, as

$$E_{n,k} \cong E_{n,0} + \frac{\hbar^2 k^2}{2m^*}, \tag{2.8}$$

where m^* is defined as the effective mass of the band. Comparing Eq. 2.8 and 2.7 leads to the following expression of the effective mass:

$$\frac{1}{m^*} \equiv \frac{1}{m_0} + \frac{2}{m_0^2 k^2} \sum_{m \neq n} \frac{|\langle u_{n,0} | \mathbf{k}.\mathbf{p} | u_{m,0} \rangle|^2}{E_{n,0} - E_{m,0}}. \tag{2.9}$$

Kane model

Kane took a different approach (see, e.g., [Bastard, 1992]) from that of the perturbative expansion of $E_{n,\mathbf{k}}$ in ascending powers of k. He diagonalized exactly $W(\mathbf{k})$ within

a limited set of band edges $\{\Gamma_6, \Gamma_\nu\}$ (Γ_ν being a set of valence states) and afterwards introduced the $W(\mathbf{k})$ coupling between $\{\Gamma_6, \Gamma_\nu\}$ and the other Γ edges within the framework of a second order perturbative treatment. Figure 2.2 (b) illustrates the dispersion relations obtained by restricting the calculation to the $\Gamma_6, \Gamma_7, \Gamma_8$ band edges. We note that if we choose the quantization axis z of the total angular momentum $\mathbf{J}$ along the $\mathbf{k}$ vector, the heavy hole (hh) and light hole (lh) bands correspond to a given value of J_z: $J_z = \pm\frac{3}{2}$ for hh and $J_z = \pm\frac{1}{2}$ for lh.

2.2.3 Band structure parameters

Some important material parameters of $Al_xGa_{1-x}As$ used in the calculations are listed in Table 2.1 [Molenkamp et al., 1988]. We note that the hh and lh valence bands in

Table 2.1: Material parameters of $Al_xGa_{1-x}As$ used in the calculations.

Symbol	Parameter	Unit	$Al_xGa_{1-x}As$
E_g	energy gap	eV	$1.519 + 1.247x$
$\Delta E_c/\Delta E_v$	band offsets		$68/32$
m_e	electron mass	m_0	$0.0665 + 0.0835x$
γ_1	Luttinger parameter		$6.790 - 3.000x$
γ_2	"		$1.924 - 0.694x$
γ_3	"		$2.681 - 1.286x$

III-V semiconductors are anisotropic at the Γ-valence band maximum [Adachi, 1993]. This effect is most pronounced for the hh band which has a strongly directional dependent effective mass, with a larger mass along the [111] direction than along the [100] direction. The bulk hh and lh effective masses can be defined in terms of the Luttinger γ parameters, γ_1, γ_2 and γ_3 with:

$$
\begin{aligned}
m_{hh}^{[100]} &= m_0/(\gamma_1 - 2\gamma_2), \\
m_{lh}^{[100]} &= m_0/(\gamma_1 + 2\gamma_2), \\
m_{hh}^{[111]} &= m_0/(\gamma_1 - 2\gamma_3), \\
m_{lh}^{[111]} &= m_0/(\gamma_1 + 2\gamma_3).
\end{aligned}
\tag{2.10}
$$

In (100)-QW structures, the hole effective masses may be expressed as [Bastard, 1992]:

$$
\begin{aligned}
m_{hh}^z &= m_0/(\gamma_1 - 2\gamma_2), \\
m_{lh}^z &= m_0/(\gamma_1 + 2\gamma_2), \\
m_{hh}^\perp &= m_0/(\gamma_1 + \gamma_2), \\
m_{lh}^\perp &= m_0/(\gamma_1 - \gamma_2),
\end{aligned}
\tag{2.11}
$$

where z is the confinement direction ($\equiv$ quantization axis) and $\perp$ indicates the well plane.

Finally, the temperature and Al mole fraction dependence fo the energy band gap is given by [Logothetidis et al., 1991]:

$$E_g(x, T) = 1.5194 + 1.247x - \frac{(5.5 + 3.35x)10^{-4}}{(225 + 88x) + T}T^2. \qquad (2.12)$$

2.3 QWRs: Approximations and formalism

The understanding of the optical spectra obtained through experiments necessitates theoretical calculations of confinement energies and optical matrix elements of our QWR structures. In the following, x is assumed to be along the wire axis, y is the lateral-confinement direction, and z is the growth direction (see Fig. 2.3). The 2D-Schrödinger
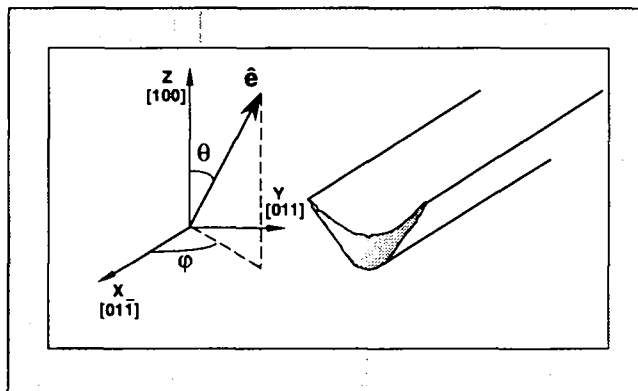
Figure 2.3: Axis orientation and schema of the relative orientation of the polarization vector of light with respect to the QWR.

equation is solved in the single-particle approximation using effective-mass Hamiltonians for conduction and valence band states and a potential profile $V_{e/h}(y, z)$ extracted from the TEM micrograph of the samples. The depth of $V_{e/h}(y, z)$ is given by the band offsets in $Al_xGa_{1-x}As$. The VQW is described by a square potential profile of fixed lateral width and constant depth (Sec. 2.4.1) or by a double Gaussian profile (Sec. 2.4.3, see Fig. 2.5).

Negligible coupling between Γ_6, Γ_7 and Γ_8 bands is assumed. The conduction and valence band states are built from these bulk bands in the envelope-function approximation [Bastard, 1992].

2.4 QWRs: Models

2.4.1 Two-dimensional model including valence band mixing

In this section we present calculations of confinement energies and squared optical matrix elements for a 2D finite potential-well model. The conduction-band wave functions are written as

$$\Psi^c_{s_z}(\mathbf{r}) = f^c(\mathbf{r})u^c_{s_z}(\mathbf{r}), \tag{2.13}$$

where the $u^c_{s_z}(\mathbf{r})$ are the two spin-degenerate ($s = \frac{1}{2}$, $s_z = \pm\frac{1}{2}$) Bloch functions at the bottom of the Γ_6 bulk band. The valence band states are written as

$$\Psi^v(\mathbf{r}) = \sum_{J_z} f^v_{J_z}(\mathbf{r})u^v_{J_z}(\mathbf{r}), \tag{2.14}$$

where the $u^v_{J_z}(\mathbf{r})$ are the degenerate Bloch functions at the top of the Γ_8 bulk bands. The sum extends over the J_z quantum number ($J_z = \pm\frac{3}{2}$ for the hh, $J_z = \pm\frac{1}{2}$ for the lh) of the $J = \frac{3}{2}$ quadruplet.

In the conduction band, the envelope functions

$$f^c(\mathbf{r}) = \frac{1}{\sqrt{L_x}} \exp(ik_x x)\phi(y, z) \tag{2.15}$$

are the solutions of the following equation:

$$\left[\frac{\hbar^2}{2}\left(\frac{k_x^2}{m^*(y, z)} - \frac{\partial}{\partial y}\frac{1}{m^*(y, z)}\frac{\partial}{\partial y} - \frac{\partial}{\partial z}\frac{1}{m^*(y, z)}\frac{\partial}{\partial z}\right)\right.$$
$$\left. +V_e(y, z)\right] f^c(\mathbf{r}) = E_e f^c(\mathbf{r}), \tag{2.16}$$

where L_x is the length of the wire, k_x the carrier wave vector along the wire, and $m^*(y, z)$ the bulk conduction electron effective mass at the bottom of the Γ_6 band.

Because of the fourfold degeneracy of the bulk hh and lh bands, the hole subbands are determined from the effective Hamiltonian made up of the 4×4 **k·p** Luttinger Hamiltonian [Luttinger and Kohn, 1955] with the potential $V_h(y, z)$ included along the diagonal. Given the orientation of the wires in the heterostructure, the Hamiltonian is rotated so that the new coordinate system is specified by the wire axis $x \equiv [01\bar{1}]$, $y \equiv [011]$, and $z \equiv [100]$. The total angular momentum **J** is quantized along the growth direction z. The Luttinger hamiltonian expressed in the basis of the eigenstates of **J** ($J = \frac{3}{2}$) and J_z,

$$\left|\frac{3}{2}, +\frac{3}{2}\right\rangle, \left|\frac{3}{2}, +\frac{1}{2}\right\rangle, \left|\frac{3}{2}, -\frac{1}{2}\right\rangle, \left|\frac{3}{2}, -\frac{3}{2}\right\rangle,$$

is written as

$$H_{\Gamma_8} = \frac{\hbar^2}{2m_0}\begin{pmatrix} P+Q & -S & R & 0 \\ -S^\dagger & P-Q & 0 & R \\ R^\dagger & 0 & P-Q & S \\ 0 & R^\dagger & S^\dagger & P+Q \end{pmatrix}, \tag{2.17}$$

with

$$P = \gamma_1 k_x^2 - \frac{\partial}{\partial y}\gamma_1\frac{\partial}{\partial y} - \frac{\partial}{\partial z}\gamma_1\frac{\partial}{\partial z} + \frac{2m_0}{\hbar^2}V_h(y,z),$$

$$Q = \gamma_2 k_x^2 - \frac{\partial}{\partial y}\gamma_2\frac{\partial}{\partial y} + 2\frac{\partial}{\partial z}\gamma_2\frac{\partial}{\partial z},$$

$$R = \sqrt{3}[\gamma_3 k_x^2 + \frac{\partial}{\partial y}\gamma_3\frac{\partial}{\partial y} + k_x(\gamma_2\frac{\partial}{\partial y} + \frac{\partial}{\partial y}\gamma_2)],$$

$$S = \sqrt{3}[k_x(\gamma_3\frac{\partial}{\partial z} + \frac{\partial}{\partial z}\gamma_3) + \frac{\partial}{\partial z}\gamma_3\frac{\partial}{\partial y} + \frac{\partial}{\partial y}\gamma_3\frac{\partial}{\partial z}], \qquad (2.18)$$

where $\gamma_1, \gamma_2, \gamma_3$ are the Luttinger parameters [Luttinger, 1956]. The wave vector components k_y and k_z have been replaced by $-i\frac{\partial}{\partial y}$ and $-i\frac{\partial}{\partial z}$, respectively, and the noncommuting products have been symmetrized. Three pecularities should be noted. First, the choice of the $45°$-rotated axes in the $x - y$ plane reverses the roles of γ_2 and γ_3 in the element R, compared to the standard principal axis orientation. Second, our choice of axes also keeps the Luttinger hamiltonian real. Third, the substitution of the wave vector components by differentials of the envelope functions must be made separately in the upper and lower triangles of H_{Γ_8}, giving rise to non-identical but adjoint real operators on both sides of the diagonal. The Schrödinger equations for electrons and holes are solved by a first order finite elements technique on an irregular mesh made up of quadrilaterals adapted to the actual boundaries of the QWRs. The program solving this problem has been written by Dr. M.-A. Dupertuis [1].

Fig. 2.4a (2.4b) shows the calculated valence subband dispersion curves for the 8.8 nm QWR without (with) hh-lh mixing (the QWR structures are parametrized by the thickness at the center of the GaAs crescent; for a detailed description of the samples, see Sec. 3.2). These results demonstrate that band mixing gives rise to non-parabolic dispersion curves and anticrossings of the subbands, a familiar occurence in the dispersion of QWs valence bands. The subband splitting at $k \neq 0$ is due to the lack of inversion symmetry of the structure. Unlike for QWs, *the zone-center states for the QWR already contain an admixture of both hh and lh*. The percentage lh character of the pair of states at the Γ point is given in Table 2.2 for the 4.1 nm, 8.8 nm, and 14.1 nm QWR samples. The uppermost valence subband is above 90% hh in all three cases whereas the h_6 state of the 14.1 nm and 8.8 nm QWRs and the h_7 state of the 4.1 nm QWR are above 70% lh at the Γ point (lh-like state). We also note a strong reduction in subband separation when introducing hh-lh mixing. Figure 2.4 (a) shows a mass reversal effect similar to that occuring in QW structure: The hh effective mass is heavy along z ($m_{hh}^z = m_0/(\gamma_1 - 2\gamma_2)$) but light in a plane perpendicular to z
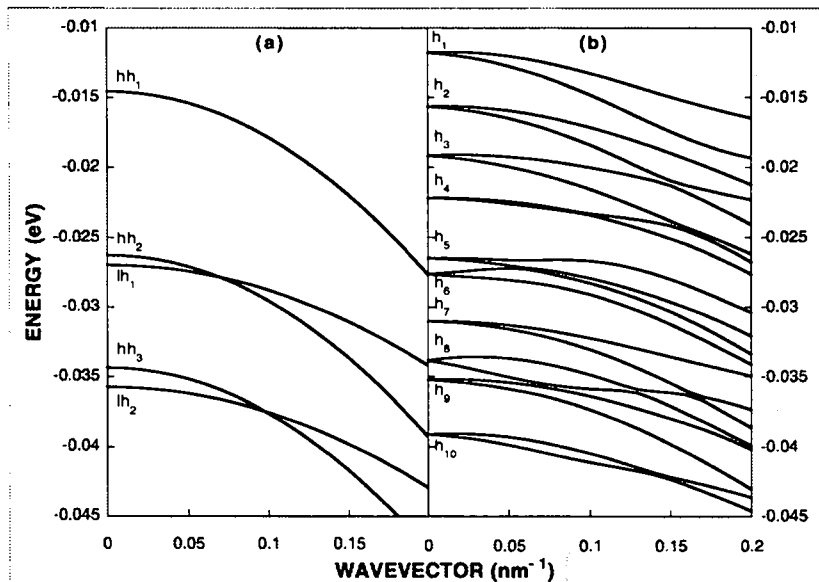
Figure 2.4: Valence band dispersions a) without and b) with hh-lh mixing in the 8.8 nm QWR. Subbands in (a) are labeled according to the light or heavy nature of the states. Band mixing gives rise to nonparabolic dispersion curves and anticrossing of the subbands; a strong reduction in subband separation is to be noted. Subband splitting away from zone center in (b) is due to the lack of inversion symmetry of the structure.

$(m_{hh}^{\perp} = m_0/(\gamma_1+\gamma_2))$ whereas the lh effective mass is light along z $(m_{lh}^z = m_0/(\gamma_1+2\gamma_2))$ but heavy in a plane perpendicular to z $(m_{lh}^{\perp} = m_0/(\gamma_1-\gamma_2))$ (see, e.g., [Bastard, 1992]). This explains the smaller separation between the lh_1 and lh_2 subbands as compared to the separation between the hh_1 and hh_2 subbands in the case of decoupled bands ((see Fig. 2.4 (a), heavier mass for lh subbands in the direction of the lateral confinement). However, coupling between hh and lh states increases the hh band mass and decreases the lh band mass, resulting in smaller subbands separation (see Fig. 2.4 (b)).

2.4.2 Optical absorption and polarization dependence of the interband matrix element

In the dipole approximation, the absorption coefficient α for a plane electromagnetic wave in a medium of refractive index n is given by

$$\alpha(\omega) = \frac{\pi e^2}{nc\varepsilon_0 m_0^2 \omega V} \sum_{i,f} |\langle f|\hat{e}.\mathbf{p}|i\rangle|^2 \, \delta(E_f - E_i - \hbar\omega). \tag{2.19}$$

ε_0, V, and $\hbar\omega$ represent the permittivity of vacuum, the sample volume, and the photon energy, respectively, and $\hat{e}$ is the polarization vector of the light and $\mathbf{p}$ is the momentum operator. For our heterostructure, the initial and final states, $|i\rangle$ and $|f\rangle$, correspond to $\Psi^v(\mathbf{r})$ and $\Psi^c_{s_z}(\mathbf{r})$, which are defined by Eqs. (2.14) and (2.13), respectively. Taking

Table 2.2: Percentage of lh character for valence subbands at the zone center for the a) 14.1 nm QWR, b) 8.8 nm QWR, and c) 4.1 nm QWR.

a) Subband	h_1	h_2	h_3	h_4	h_5	h_6	h_7	h_8	h_9	h_{10}
% lh	10	29	43	49	44	70	47	25	49	42

b) Subband	h_1	h_2	h_3	h_4	h_5	h_6	h_7	h_8	h_9	h_{10}
% lh	10	33	45	53	49	70	46	30	49	45

c) Subband	h_1	h_2	h_3	h_4	h_5	h_6	h_7	h_8	h_9	h_{10}
% lh	8	22	36	44	46	62	71	52	60	51

into account the statistical filling of $|i\rangle$ and $|f\rangle$, we get

$$\alpha(\omega) = \frac{4\pi^2 e^2}{nc\varepsilon_0 m_0^2 \omega V} \sum_{\substack{c,v \\ s_z}} \int_{B.Z.} \frac{dk_x}{2\pi} \left[\left| \langle \Psi^c_{s_z} | \hat{e}.p | \Psi^v \rangle \right|^2 \delta(E_c(k_x) - E_v(k_x) - \hbar\omega) \right.$$

$$\left. \times (f_v(E_v(k_x)) - f_c(E_c(k_x))) \right] \quad (2.20)$$

where $f_\nu(\varepsilon)$ is the Fermi distribution of carriers in subband ν with a quasi-Fermi level at ε_ν. Since the periodic part u^c (u^v) varies rapidly over the characteristic length of variation of the envelope function f^c (f^v), the dipole matrix element of a transition between a Γ_6 (Eq. 2.13) and a Γ_8 (Eq. 2.14) state can be written as

$$\langle \Psi^c_{s_z} | \hat{e}.p | \Psi^v \rangle = \sum_{J_z} I_{J_z} \langle u^c_{s_z} | \hat{e}.p | u^v_{J_z} \rangle, \quad (2.21)$$

$$I_{J_z} = \langle f^c(\mathbf{r}) | f^v_{J_z}(\mathbf{r}) \rangle. \quad (2.22)$$

The atomic-like dipole matrix elements give rise to the dependence on the polarization vector $\hat{e}$ of the light. They are weighed by the quantum numbers of the initial and final states via the overlap integrals I_{J_z}. The Bloch states u^c and u^v are written [Bastard, 1992]

$$u^c_{\frac{1}{2}} = i|S \uparrow\rangle,$$

$$u^c_{-\frac{1}{2}} = i|S \downarrow\rangle,$$

$$u^v_{\frac{3}{2}} = \frac{1}{\sqrt{2}} |(X + iY) \uparrow\rangle,$$

$$u^v_{-\frac{3}{2}} = \frac{1}{\sqrt{2}} |(X - iY) \downarrow\rangle,$$

$$u^v_{\frac{1}{2}} = \frac{1}{\sqrt{6}} |(X + iY) \downarrow\rangle - \sqrt{\frac{2}{3}} |Z \uparrow\rangle,$$

$$u^v_{-\frac{1}{2}} = -\frac{1}{\sqrt{6}}|(X - iY)\uparrow\rangle - \sqrt{\frac{2}{3}}|Z\downarrow\rangle, \tag{2.23}$$

The symmetry of the host functions $|S\rangle$, $|X\rangle$, $|Y\rangle$ and $|Z\rangle$ that define u^c and u^v gives rise to the selection rule

$$\langle S|\mathrm{p}_\nu|\nu'\rangle = \delta_{\nu,\nu'}i\frac{m_0 P}{\hbar}, \quad \nu, \nu' \in \{X, Y, Z\}, \tag{2.24}$$

where the Kane matrix element P in GaAs is defined by $2m_0 P^2 = 22.71$ eV. We express the polarization vector in spherical coordinates $\hat{e} = (\cos\varphi\sin\theta, \sin\varphi\sin\theta, \cos\theta)$ (see Fig. 2.3) and evaluate 2.22 using Eq. (2.23) and Eq. (2.24). We obtain

$$\sum_{s_z}\left|\langle\Psi^c_{s_z}|\hat{e}.\mathrm{p}|\Psi^v\rangle\right|^2 = \left[\frac{m_0 P}{\hbar}\right]^2 \left([\frac{1}{2}(I^2_{\frac{3}{2}} + I^2_{-\frac{3}{2}}) + \frac{1}{6}(I^2_{\frac{1}{2}} + I^2_{-\frac{1}{2}}) - \right.$$
$$\left.\frac{1}{\sqrt{3}}(I_{\frac{3}{2}}I_{-\frac{1}{2}} + I_{\frac{1}{2}}I_{-\frac{3}{2}})\cos(2\varphi)]\sin^2(\theta) + \frac{2}{3}(I^2_{\frac{1}{2}} + I^2_{-\frac{1}{2}})\cos^2(\theta)\right) \tag{2.25}$$

In a cubic 3D lattice the absorption is independent of the polarization direction, if the anisotropy of the lattice unit cell is neglected. In QWs the summation over the in-plane wave vector eliminates the term proportional to $\cos(2\varphi)$. The absorption depends, thus, only on the angle θ. In QWRs the integration over the in-wire momentum does not eliminate the dependence on the angle φ. We define the degree of linear polarization P as:

$$P = (\alpha_{||} - \alpha_\perp)/(\alpha_{||} + \alpha_\perp) \equiv (\alpha_x - \alpha_y)/(\alpha_x + \alpha_y). \tag{2.26}$$

Using Eq. 2.25, we get:

$$P = -\frac{\frac{2}{\sqrt{3}}\left(I_{\frac{3}{2}}I_{-\frac{1}{2}} + I_{\frac{1}{2}}I_{-\frac{3}{2}}\right)}{\left(I^2_{\frac{3}{2}} + I^2_{-\frac{3}{2}}\right) + \frac{1}{3}\left(I^2_{\frac{1}{2}} + I^2_{-\frac{1}{2}}\right)}. \tag{2.27}$$

Accordingly, the magnitude of the polarization anisotropy in the $x - y$ plane increases in proportion to $(I_{\frac{3}{2}}I_{-\frac{1}{2}} + I_{\frac{1}{2}}I_{-\frac{3}{2}})$ with increasing hh-lh mixing in the valence band [Bockelmann and Bastard, 1991].

2.4.3 Two-dimensional model used for disorder related effects

Variations of the wire cross-section along the wire axis x leads to fluctuations of the confinement-energy of electrons and holes which results in localization of carriers (see Sec. 3.2.3 and Chap. 6). For the sake of simplicity we use an adiabatic decoupling scheme [Kapon et al., 1989]. Thus, the potential $V_{e,h}(x, y, z)$ that confines the carriers

in the $y - z$ plane and localizes them along the x direction can be written as [2]:

$$V_{e,h}(x, y, z) = U_{e,h}(x) + U^x_{e,h}(y, z), \qquad (2.28)$$

and the envelope wave functions read:

$$f(\mathbf{r}) = \chi(x)\phi^x(y, z). \qquad (2.29)$$

Therefore, calculations of the energy levels of localized 1D carriers are performed in the following way: First a x coordinate is chosen, corresponding to a longitudinal position along the wire axis. The cross-sectional shape of the wire at this position is estimated on the basis of TEM pictures of the sample and AFM studies of GaAs and AlGaAs surfaces (see Sec. 3.2.3). Then, the 2D Schrödinger equation corresponding to that particular QWR cross-section is solved, yielding, in particular, the carrier-groundstate energy E_{conf}. The procedure is repeated for a set of x values, providing us with $E_{conf}(x)$, the longitudinal confining potential. The localization obtained with this procedure yields an estimation of the actual longitudinal potential, which is an average of the underlying energy fluctuations weighed with the square of the carriers wave function [Zimmermann, 1992, Runge et al., 1995]. Furthermore, we assume decoupling of hh and lh states in this model. Therefore, both electron and hole wave functions are written in the form of Eq. 2.13, with the envelope functions given by Eq. 2.29, which are solutions of a Schrödinger equation in the form of Eq. 2.16. The 2D Schrödinger equations for electrons and hh are solved by a finite differences technique on a rectangular mesh ($m_e = 0.0665\,m_0, m^z_{hh} = 0.33\,m_0$ are assumed). Finally, the energy levels and wave functions of the localization potential $E_{conf}(x)$ are calculated by a standard transfer matrix method ($m_e = 0.0665\,m_0, m^\perp_{hh} = 0.11\,m_0$ are assumed).

In Fig. 2.5 the potential well for the electrons in the 8.8 nm QWR structure is displayed. The variation of the Al mole fraction across the VQW is represented by a double Gaussian distribution.

The corresponding envelope wave functions of the first four electron states at the zone center are shown in Fig. 2.6. As the subband increases, the electrons are clearly delocalized further and further away from the symmetry plane. All the levels are of adiabatic aspect: the transverse state is always similar to the 1D well ground state. Finally, we note that our simulations are typically performed on a 22500-point grid.

---

[2]Obviously, the potential *confines* the carriers in all three directions of space; *localization* is introduced to differentiate the confinement due to the material-dependent band gap and the confinement resulting from cross-sectional fluctuations.
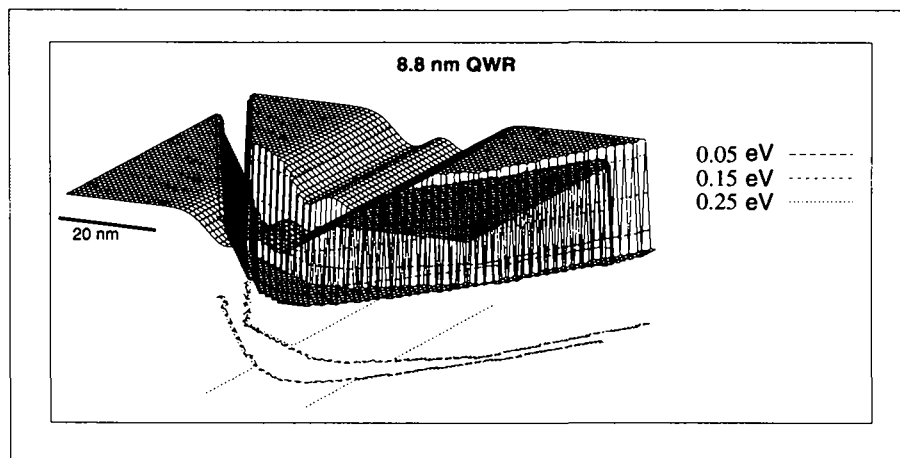
Figure 2.5: Potential well for electrons in the 8.8 nm QWR structure. The variation of the Al mole fraction across the VQW is represented by a double Gaussian distribution.

2.5 Excitons and excitonic effects

2.5.1 The concept of excitons

The concept of excitons was conceived in the 1930s [Frankel, 1931] and has undergone a certain amount of development [Peierls, 1932, Wannier, 1937, Mott, 1938]. A review of the development that has taken place can be found in [Knox, 1963] and [Bassani, 1975]. For more recent research, the reader is referred to [Cho, 1979] and [Rashba and Sturge, 1982].

In the one-electron approximation, the physical picture of an optical absorption process is the following: an incident radiation field excites an electron from the valence to the conduction band, which results in the formation of a hole in the valence band; the electron and the hole are assumed to have no interaction. Such a theory is, however, unable to explain many details observed in optical experiments. Excitonic effects clearly manisfest themselves, for example, with the appearance of sharp peaks in the interband absorption spectra of 3D and 2D structures. In particular, narrow and intense absorption lines appear below the bandgap energy E_g. These sharp structures are not predicted by non-interacting electron models. Excited states of the crystal with an energy lower than E_g are due to the interaction between the excited electron in the conduction band and those left behind in the now almost filled valence band. This interaction may be replaced by an electron-hole interaction. Attraction between the electron and the hole causes their motion to be correlated and the resultant electron-hole pair is known as an *exciton*.

Two limiting cases of excitons have been particularly studied. *Frenkel excitons* correspond to strong electron-hole attraction, as in ionic crystals; the electron and the
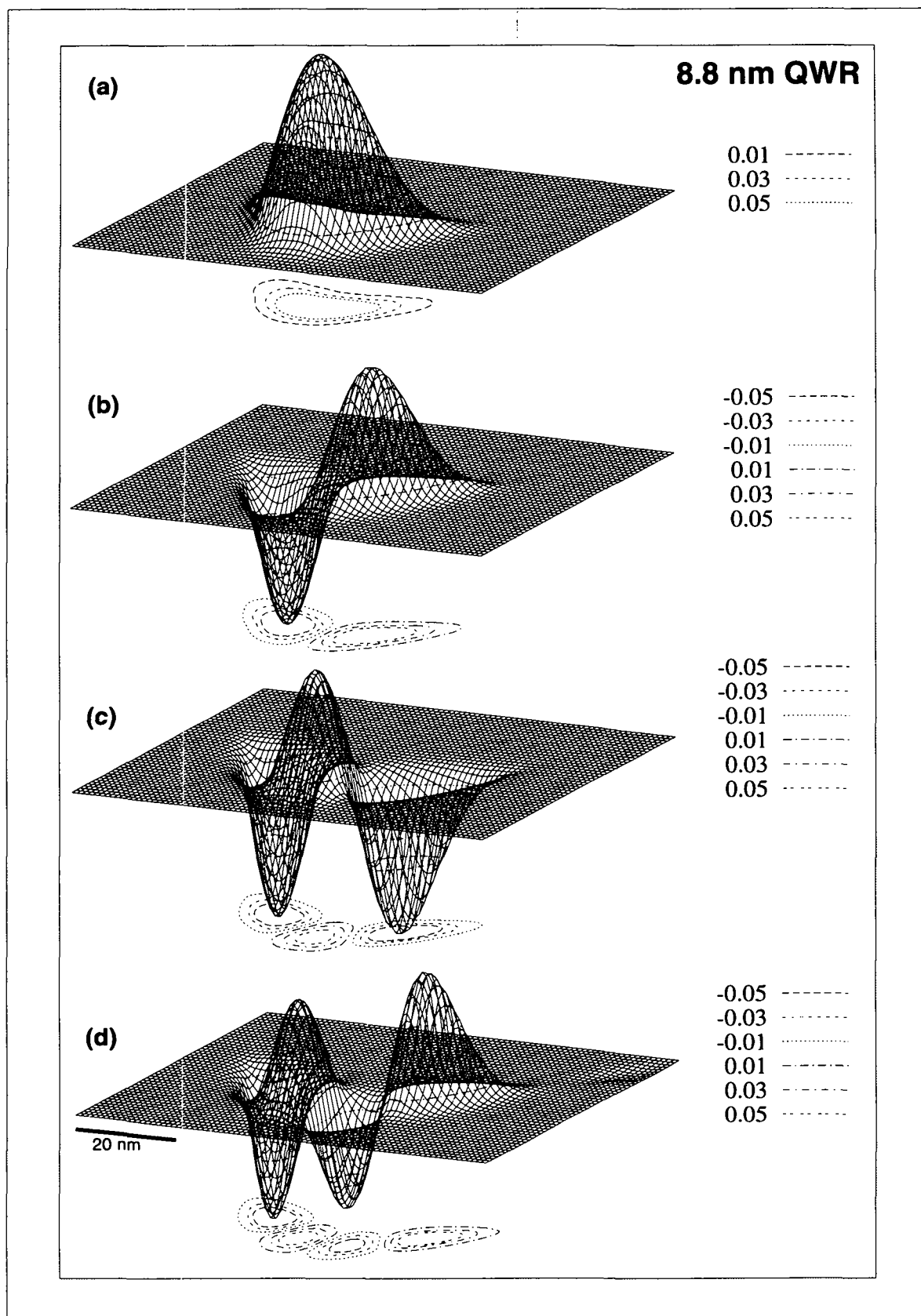
Figure 2.6: The probability amplitude for the first four electron states in the 8.8 nm QWR, depicted in (a), (b), (c), and (d) with increasing subband index. Values of the contour lines are indicated on the right.

hole are tightly bound to each other within the same or nearest-neighbor unit cells. *Wannier-Mott excitons*, or simply Wannier excitons, correspond to weak electron-hole attraction, as in most semiconductors; they result from the strong screening of the Coulomb interaction by the valence electrons via the dielectric constant.

The exciton picture emerges after lengthy many-body calculations (see e.g. [Knox, 1963]). A crystalline excited state with an energy lower than E_g is constructed by taking linear combinations of conduction and valence states which are such that they represent two clouds of particles of opposite signs orbiting around each other in a bound state. The spatial localization of the electron-hole pair carries an increase in kinetic energy over E_g. However, this extra energy is over-balanced due to the gain in electrostatic energy between the two clouds. The net result is a bound electron-hole pair which has finite binding energy. This pair travels freely over the whole crystal.

2.5.2 Excitons in idealized bulk systems

We consider the effect of Coulomb attraction on the motion of electrons and holes in the vicinity of an M_0 critical point of a direct bandgap semiconductor in three dimensions. The properties of Wannier excitons can be calculated with the effective mass approximation. Within this approximation, the electrons and the holes are considered as two particles moving with effective masses of the conduction and valence bands, respectively. The effective mass Hamiltonian for this system, assuming spherical bands at $\mathbf{k} = 0$, is

$$\mathcal{H} = \frac{\mathbf{p}_e^2}{2m_e} + \frac{\mathbf{p}_h^2}{2m_h} - \frac{e^2}{4\pi\varepsilon|\mathbf{r}_e - \mathbf{r}_h|}. \tag{2.30}$$

The wave equation for the envelope wavefunction of the exciton $\Phi(\mathbf{r}_e, \mathbf{r}_h)$, $\mathcal{H}\Phi = (E - E_g)\Phi$ can be solved in the same way as in the case of the hydrogen atom. One expresses $\mathbf{r}_e$ and $\mathbf{r}_h$ in terms of a center-of-mass coordinate $\mathbf{R}$ and a relative coordinate $\mathbf{r}$. The envelope wavefunction can now be written as

$$\Phi(\mathbf{r}, \mathbf{R}) = \frac{e^{i\mathbf{K}\cdot\mathbf{R}}}{\sqrt{N\Omega}} F(\mathbf{r}). \tag{2.31}$$

with $F(\mathbf{r})$ obeying

$$\left(-\frac{\hbar^2\nabla_r^2}{2\mu_{red}} - \frac{e^2}{4\pi\varepsilon r}\right) F(\mathbf{r}) = \left(E - E_g - \frac{\hbar^2 K^2}{2(m_e + m_h)}\right) F(\mathbf{r}), \tag{2.32}$$

where μ_{red} is the reduced mass of the exciton and ε is the dielectric permittivity of the semiconductor. The eigenvalues are then

$$E = E_n(\mathbf{K}) = E_g + \frac{\hbar^2 K^2}{2(m_e + m_h)} - \frac{R^*}{n^2}, \tag{2.33}$$
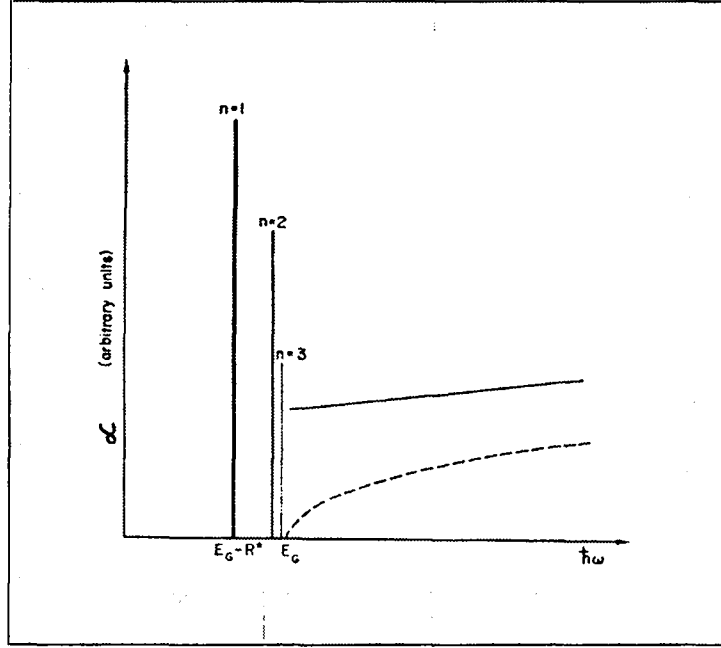
Figure 2.7: Schematic representation of the absorption spectra of the allowed direct transition with (solid line) and without (dashed line) the electron-hole interaction in a 3D system[Bassani, 1975]

where n is the principal quantum number and R^* the Rydberg constant of the exciton defined as

$$R^* = \frac{\mu_{red} e^4}{2\hbar^2 (4\pi\varepsilon)^2} = \left(\frac{\mu_{red}}{m_0 (4\pi\varepsilon)^2}\right) \times \underbrace{13.6 \text{ eV}}_{Rydberg\ constant\ of\ the\ hydrogen\ atom} \tag{2.34}$$

For the case of GaAs semiconductors, $R^* = 4.4$ meV [Baldereschi and Lipari, 1971]. The bound state wavefunction corresponding to $n = 1$ is given by Eq. (2.31) with

$$F(\mathbf{r}) = \frac{1}{\sqrt{\pi}} a_B^{-\frac{3}{2}} e^{-\frac{r}{a}}, \tag{2.35}$$

where $a_B = a_0 \varepsilon m_0 / \mu_{red}$ and a_0 is the Bohr radius. Using the parameters of GaAs, we can estimate $a_B \approx 110$ Å[Yu and Cardona, 1996]. Hence, as compared with the lattice constant (5.65 Å), this is a weakly bound wave function with a large spatial extension. By a Fourier transform of $\Phi(\mathbf{r}_e, \mathbf{r}_h)$ we find that $\mathbf{k}_e$ and $\mathbf{k}_h$ are localized in two separate small regions of the Brillouin zone. When $\mathbf{K} = 0$, $\mathbf{k}_e$ and $\mathbf{k}_h$ are separately localized near the Γ point of the conduction band minimum and valence band maximum, respectively.

Besides the above discussion of bound states of Eq. (2.30), there are still possible ionization states corresponding to ionized electron and hole having uncorrelated motion. But in reality, there is still some interaction existing between the electron and the hole due to the long-range nature of the Coulombic interaction, even when they do not form a bound state [Bastard, 1992]. It is interesting to note that this e-h correlation causes

an enhancement of the absorption coefficient in the continuum above the band edge as illustrated by Fig. 2.7 [Bassani, 1975]. This means that the Sommerfeld factor [3] is larger than unity in a 3D system [Elliot, 1957].

2.5.3 Excitons in idealized and actual 1D systems

Excitonic effects in a 1D system are expected to be even more significant than they are in 2D and 3D systems [Chang et al., 1985, Ogawa and Takagahara, 1991a, Glutsch and Bechstedt, 1993, Rossi and Molinari, 1996a]. This results essentially from the increasing overlap of the electron and hole wave functions with increasing localization in the nanostructure. The enhancement of excitonic correlations was demonstrated, e.g., by the observation of stimulated optical emission using exciton recombination in T-shaped QWRs [Wegscheider et al., 1993] and by the persistance of excitonic recombination in highly photo-excited V-groove QWRs [Ambigapathy et al., 1997]. Enhanced oscillator strengths of 1D excitons have been predicted theoretically [Chang et al., 1985] and have been observed experimentaly [Akiyama et al., 1996]. Moreover, the oscillator strength is expected to be concentrated on the lowest exciton state [Ogawa and Takagahara, 1991b, Ogawa and Takagahara, 1991a, Rossi and Molinari, 1996a].

The reduction of the dimensionality also causes an enhancement of the exciton binding energy E_b. For ideal 2D systems, the binding energy of the ground-state exciton is 4 times the 3D effective Rydberg (see Eq. 2.34). Theoretical calculations for QWs have shown that E_b approaches this limit as the well thickness is progressively reduced, provided the potential well is deep enough [Greene et al., 1984]. In the ideal 1D limit E_b diverges [Loudon, 1959], suggesting that exciton binding energies of quasi-1D systems can be in principle increased by an appropriate quantum confinement much beyond the 2D limit [Ogawa and Takagahara, 1991b, Ogawa and Takagahara, 1991a]. Larger exciton binding energies have indeed been observed in QWR structures fabricated by different techniques [Nagamune et al., 1992, Wegscheider et al., 1993, Rinaldi et al., 1994, Someya et al., 1995, Someya et al., 1996, Weman et al., 1996]. The scaling of E_b in semiconductor QWRs has also been investigated theoretically for a wide set of realistic 1D structures by Rossi et al. [Rossi et al., 1997]. They have found a universal (shape and barrier) variation of E_b vs the corresponding effective exciton Bohr radius a, $E_b \sim \frac{1}{a}$, as illustrated in Fig. 2.8. This universal behavior is explained as a consequence of the proportionality between the average Coulomb and kinetic energies in strongly confined QWRs; their constant ratio is very close to 4, i.e. twice the conventional "virial" value

---

[3] The Sommerfeld factor is defined as the absorption coefficient ratio of the unbound exciton to that of the free electron-hole pair above the band edge.

— which holds in bulk and QW structures — thus allowing enhanced binding energies.
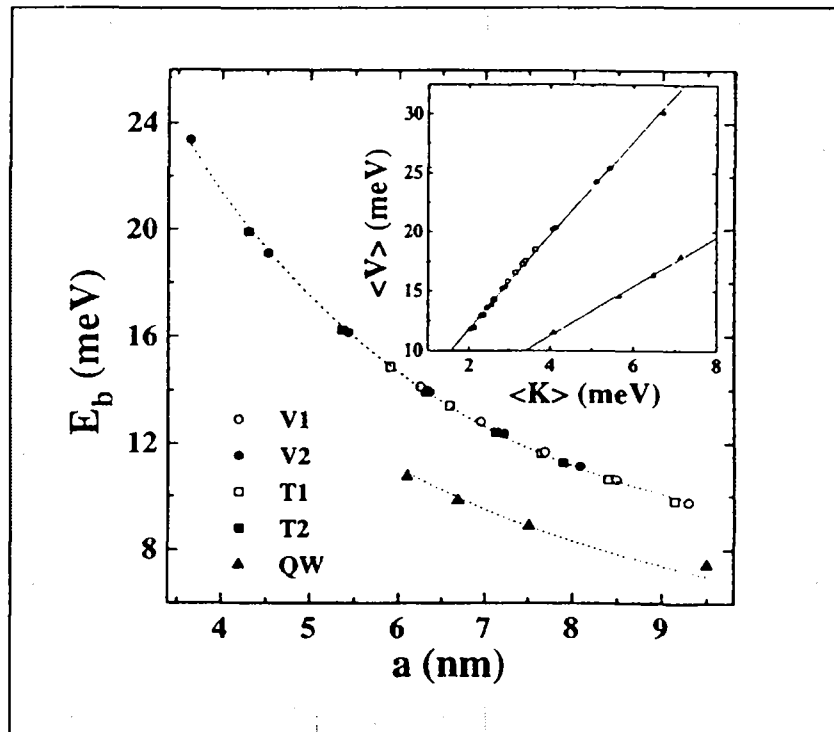
Figure 2.8: Exciton binding energy E_b vs effective exciton Bohr radius a, for different V-shaped and T-shaped QWRs, and for QWs. Dashed curves are a fitting to $1/a$ form. The inset reports the average potential vs kinetic energy, falling on a straight line with slope $\alpha \simeq 4$ for all wire samples. Results for QW structures are also shown for comparison; in this case $\alpha \simeq 2$. Solid lines are a linear fit to the calculated points [Rossi et al., 1997].

As already mentioned in section 2.5.2, the Sommerfeld factor in bulk systems is always larger than unity, indicating an enhancement of optical absorption by Coulomb attraction between an electron and a hole. This also holds for 2D systems [Shinada and Sugano, 1966]. In model 1D systems [Ogawa and Takagahara, 1991a, Glutsch and Bechstedt, 1993], as well as in realistic QWRs [Rossi and Molinari, 1996a], the Sommerfeld factor is found to be much less than unity for direct allowed transitions, in striking contrast to the 3D and 2D cases . These studies show that electron-hole Coulomb correlation removes the Van Hove singularities from the absorption spectra, whose shape is heavily modified with respect to the ideal free-carrier single subband case. The result of such a calculation performed by Rossi et al. for V-shaped QWRs is reproduced in Figure 2.9 [Rossi and Molinari, 1996a].
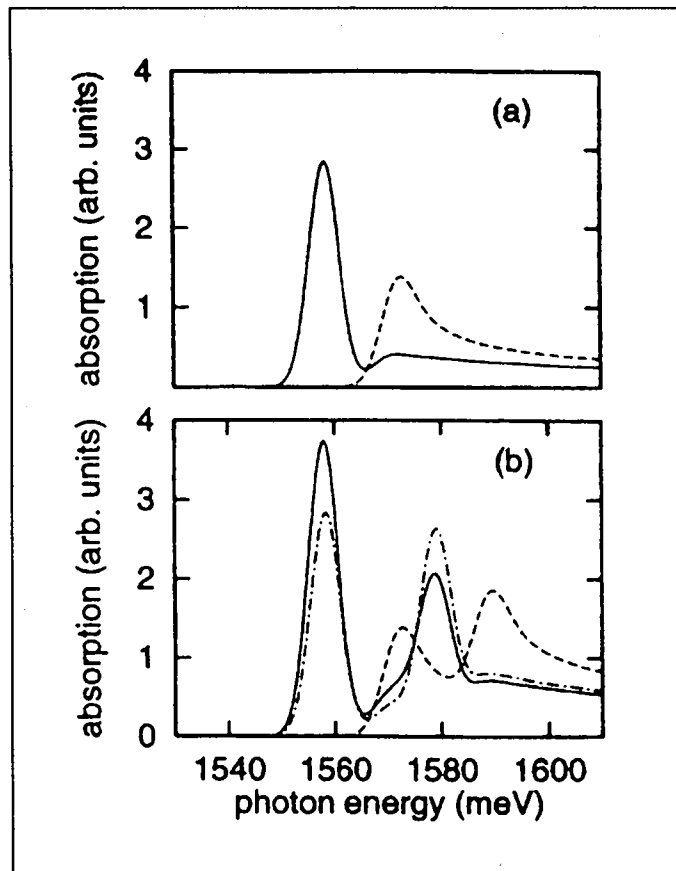
Figure 2.9: Comparison between the absorption spectra of the V-shaped wire obtained by including electron-hole Coulomb correlation (CC model, solid line) or by assuming free carriers (FC model, dashed line). In (a) only the first subband is considered, while in (b) the two lowest subbands are taken into account. The dash-dotted line in (b) illustrates the effect of neglecting intersubband coupling in the CC spectrum. All curves were computed assuming a Gaussian energy broadening of 2 meV [Rossi and Molinari, 1996a].

2.5.4 Interaction between excitons: some aspects of many-body phenomena

2.5.4.1 Exchange and correlation

The term exchange is commonly used to refer to those properties of many-fermion systems that are a direct consequence of the antisymmetry of the state function under interchange of particles. The antisymmetry of the state function under permutation of identical fermions leads to a correlation between the positions of two such particles, even if there is no interaction between the particles. On another hand, an interaction among the particles causes their positions to be correlated, even if there were no symmetrization postulate. The combination of these two effects is referred to by the jargon words "exchange and correlation", "exchange" referring to the effect of antisymmetry

and "correlation" referring to the effect of the interaction. But since both effects lead to a kind of correlation, the interaction effect is sometimes distinguished as "dynamic correlations". The two effects are not additive, and so a separation of them into exchange and correlation is only conventional. The usual separation is to describe as "exchange" those effects that are included in the Hartree-Fock approximation, and as "dynamic correlations" those effects that cannot be represented in a state function of the form

$$|\Psi\rangle = C_1^\dagger C_2^\dagger \dots C_N^\dagger |0\rangle,$$

$C_\alpha^\dagger$ being creation operators. This separation is natural inasmuch as the Hartree-Fock approximation is the simplest many-body theory that respects the symmetrization postulate.

2.5.4.2 Interaction between excitons

Dealing with exciton-exciton interaction is a complicated task. Fernández-Rossier et al. have calculated recently the energy levels for an interacting polarized exciton gas in 3D and 2D systems [Fernández-Rossier et al., 1996], using the formalism developed by Haug and Schmitt-Rink (1984). Their theoretical approach is based on a Hartree-Fock approximation of the many-exciton Hamiltonian. Consider the exciton creation operator:

$$a_i^\dagger = \int dedh\phi_i(e, h)a_h^\dagger a_e^\dagger, \qquad (2.36)$$

where the index i is the set of exciton quantum numbers $\{K, J, M, \nu\}$, K being the center of mass momentum, J the total angular momentum, M its third component, and ν labeling the internal state of the exciton. $a_e^\dagger$ creates a conduction band electron in e, where $e = \{r_e, s_e\}$, and analagously $a_h^\dagger$ for a hole for which valence band mixing effects are neglected. $\phi_i(e, h)$ is the exciton wave function. Physically speaking, $a_i^\dagger$ is an operator that creates an electron-hole cloud following the excitonic probability amplitude. One can show the following commutation relation:

$$[a_i, a_{i'}^\dagger] = \delta_{i,i'} - \int dedh\phi_i^*(e, h) \left\{ \int dh'\phi_{i'}(e, h')a_{h'}^\dagger a_h + \int de'\phi_{i'}(e', h)a_{e'}^\dagger a_e \right\}. \qquad (2.37)$$

The second term on the right hand side of Eq. 2.37 is an operator whose expectation value is of the order na_B^d, where n is the exciton density, a_B is the exciton Bohr radius, and d is the dimension of the space. This result shows that a composite particle made up by two fermions is not necessarily a boson.

The exciton wave function can be written as a product of factors, namely, the center of mass term, the orbital part, and the radial wave function. This factorization is possible if we assume that $\{K, J, M, \nu\}$ are good quantum numbers for the noninteracting

exciton. Up to order $(na_B^d)^2$ the Hamiltonian including the exciton-exciton interactions can be written as:

$$H = H_0 + H_{int},$$ (2.38)

where

$$H_0 = \sum_{i,i'} \langle i|T_e + T_h - V_{eh}|i'\rangle a_i^\dagger a_{i'},$$ (2.39)

and

$$H_{int} = \frac{1}{2} \sum_{i,i',i'',i'''} a_i^\dagger a_{i'}^\dagger a_{i''} a_{i'''} (\langle i,i'|I_d|i'',i'''\rangle + \langle i,i'|I_x|i'',i'''\rangle),$$ (2.40)

with

$$\langle i|T_e + T_h - V_{e,h}|i'\rangle = \int dedh \phi_i^*(e,h)(T_e + T_h - V_{e,h})\phi_{i'}(e,h),$$

$$\langle i,i'|I_d|i'',i'''\rangle = \int dedhde'dh' \phi_i^*(e,h)\phi_{i'}(e',h')(V_{ee'} + V_{hh'} -$$

$$V_{eh'} - V_{he'})\phi_{i''}(e,h)\phi_{i'''}(e',h'),$$

$$\langle i,i'|I_x|i'',i'''\rangle = -\int dedhde'dh' \phi_i^*(e,h)\phi_{i'}(e',h')(V_{ee'} + V_{hh'} -$$

$$V_{eh'} - V_{he'})\phi_{i''}(e',h)\phi_{i'''}(e,h').$$ (2.41)

In the above expressions we have:

$$T_e = -\frac{\nabla^2}{2m_e} + E_g, \quad T_h = -\frac{\nabla^2}{2m_h}, \quad \text{and} \quad V_{\nu\nu'} = \frac{q^2}{4\pi\varepsilon_0|\mathbf{r}_\nu - \mathbf{r}_{\nu'}|}.$$ (2.42)

The physical origin of I_d is the direct unscreened Coulomb interaction between fermions belonging to different excitons while I_x describes the interexcitonic exchange, or the unscreened exchange interaction between fermions of the same type. The interexcitonic exchange is a many exciton intraband (conduction-conduction or valence-valence) exchange and the intraexcitonic exchange is a single exciton or interband (conduction-valence) effect. The intraexcitonic exchange does not break the symmetry between spin +1 and spin −1 excitons and has a very weak influence on the exciton energy levels; nevertheless, it plays an important role in the spin flip mechanism [Maialle et al., 1993]. Using the above expression of the many-exciton Hamiltonian within a Hartree-Fock approximation, Fernández-Rossier et al. (1996) have calculated the renormalized exciton energy for QW systems; they retrieved the result of Schmitt-Rink et al. (1985,1989) who reported on a blue shift of the 2D excitonic resonance with increasing exciton density (see also our discussion in Sec. 6.4). However, the presence of a considerable amount of excited mobile carriers (electrons and holes) may screen the interaction between these carriers and the rest of the lattice, yielding a renormalization of the exciton

binding energy. Screening corrections have been estimated by Fernández-Rossier et al. (1996) in the random phase approximation and were found to result in a redshift that varies linearly with the exciton density. Finally, we note that the commonly accepted view that the bulk excitonic resonance stays nearly constant in a large density region has been recently questioned on the basis of experimental and theoretical investigations in bulk ZnSe [Manzke et al., 1998]. These new results have been explained by the interplay between Coulomb-Hartree-Fock renormalizations and carrier-carrier and carrier-polarization scattering including the dynamical screening.

2.6   Summary

We have recalled some of the crystalline and electronic properties of the bulk materials involved in the III-V heterostructures. Modelling of the QWR eigenstates and of the interband matrix elements has been presented. The polarization dependence of the band-to-band transitions has been shown to arise from mixing of hh and lh states at the center of the Brillouin zone. The results of this modelling will be used to analyze PL and PLE measurements. We have also presented a 2D model that will allow us to estimate the longitudinal potential which result in localization of carriers along the wire axis. Finally, the strong influence of excitonic effects on the optical properties of 1D systems has been pointed out.

Chapter 3

Materials and methods

3.1 Introduction

In this chapter, we give structural informations on the samples used in the experiments and we describe the experimental methods. In particular, we determine the most realistic wire morphology as inferred from studies on planar and non-planar AlGaAs and GaAs layers by transmission electron and atomic force microscopies. A localization potential due to fluctuations of the wire cross-section along the wire axis is estimated. We give a detailed description of the experimental setups and we highlight specificities of micro-PL and time-resolved measurements. Modelling of the time evolution of the PL measured from masked samples is also presented.

3.2 Samples

3.2.1 Fabrication

GaAs-QWRs embedded in (nominally) $Al_{0.3}Ga_{0.7}As$ were grown by low pressure OM-CVD on grooved (100)-GaAs substrates ($\pm 0.1°$), with the wires oriented in the [01$\bar{1}$] direction [Gustafsson et al., 1995]. The periodic corrugations were made by holographic photolithography and wet chemical etching. The growth of the structures was carried out in a horizontal reactor with a rotating susceptor plate. The partial pressures of the growth species were 0.159 μbar for trimethylaluminium, 1.52 μbar for trimethylgalium and 0.33 μbar for arsine. H_2 was used as the carrier gas at a total pressure of 20 mbar and a flux of 6 l/min, resulting in a nominal ((100) planar) growth rate of 0.38 and 0.25 nm/s for AlGaAs and GaAs, respectively. Depending on the sample, the substrate temperature was 650°C, 660°C, or 680°C.

We have studied five samples, each consisting of a 0.5 μm pitch lateral array of single QWRs of different sizes. The thicknesses of the GaAs layer at the crescent center were 2.5 nm, 4.1 nm, 6.9 nm, 8.8 nm, and 14.1 nm, respectively. A sufficiently

thick AlGaAs cladding layer was grown on top of the QWR array in order to elim-
inate the surface corrugation and reduce drastically electromagnetic effects (grating
coupler [Kohl et al., 1989], local field [Bockelmann and Bastard, 1991]) that might con-
tribute to the optical anisotropy of the samples [Kohl et al., 1989, Lage et al., 1991,
Ils et al., 1995, Ribeiro et al., 1995].

3.2.2   Cross-sectional images

A typical cross-sectional view of the QWR heterostructure is shown in the TEM pic-
ture of Fig. 3.1 (a). At the bottom of the grooves, crescent-shaped QWRs are pro-
duced due to the combined effects of groove sharpening during AlGaAs growth and
the higher growth rate of GaAs [Kapon et al., 1989]. The QWR regions are connected
to side-QW structures via a constriction. Note also the vertical dark stripe running
through the QWRs; this Ga-rich region constitutes a vertical AlGaAs QW (VQW) re-
gion which plays an important role in carrier capture into the wires [Walther et al., 1992,
Christen et al., 1992, Samuelson et al., 1995, Kiener et al., 1996, Biasiol et al., 1996].
Cross-sectional views of the QWR region for all investigated samples [1] are displayed in
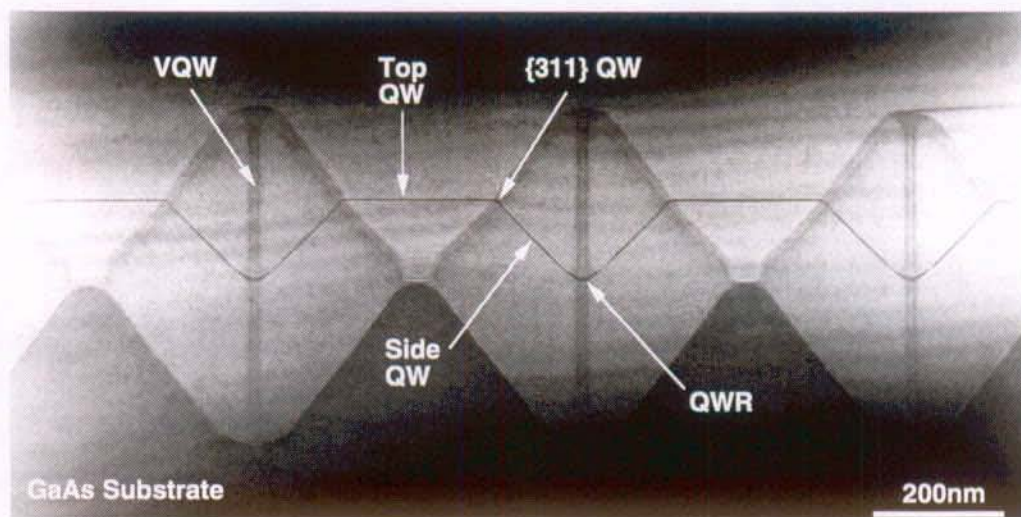
Figure 3.1: TEM micrograph showing a cross-sectional view of a part of a QWR array
on a 0.5 μm pitch grating.

the TEM micrographs of Fig. 3.2.

---

[1] All TEM pictures are due to Dr. A. Gustafsson, currently at Division of Solid State Physics, Lund
University, S-22100 Lund, and to Dr. K. Leifer, Institute of Micro- and Opto-electronics, Department
of Physics, EPFL, CH-1015 Lausanne.
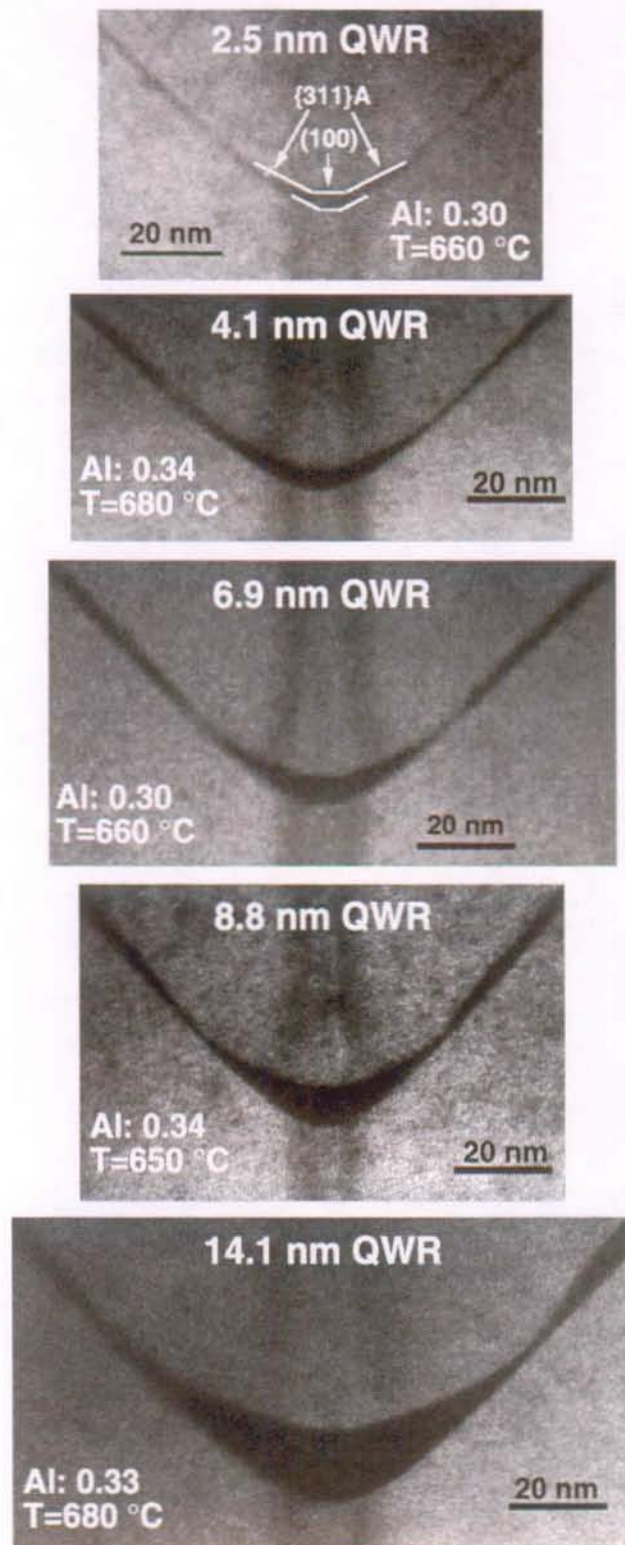
Figure 3.2: TEM cross-sectional images of GaAs/AlGaAs QWRs of different thickness. The aluminium concentration and the growth temperature are indicated at the corner of each image. The samples are referenced to by the thickness of the GaAs layer at the crescent center.

3.2.3 Longitudinal structure

Luminescence features in quantum structures are determined by exciton localization due to confinement potential fluctuations on different length scales (see Secs. 3.3.1 and 3.3.3). The investigation of the wire morphology in actual structures is, however, limited by several difficulties inherent to the heterostructure formation:

(i) The QWR is buried inside the sample which prevents the access to the wire layer by conventional scanning probe microscopy techniques such as AFM. In this case, information about the wire *cross-sectional* shape is obtained by TEM.

(ii) The wire morphology is defined by the topography of its lower and upper interfaces. Studying these interfaces requires a growth interruption immediately before or after deposition of the GaAs layer that forms the QWR. The impact of growth interruption of the surface topography is not well known.

(iii) For actual QWR structures grown at $650-680$ °C and with ~ 0.3 Al mole fraction (*i.e.* QWRs used in optical experiments), AFM observations of these surfaces along the groove are not possible due to the extremely narrow width (< 10 nm) of the profiles.

Keeping these limitations in mind, we will determine in the following the most realistic wire morphology as inferred from AFM studies of planar and non-planar $Al_{0.3}Ga_{0.7}As$ and GaAs layers. Although the results are quite general, we will examine more specifically the morphology of a very thin QWR (2.5 nm QWR) to correlate structural disorder with micro-PL features (see Chap. 6).

Figure 3.3 (a) shows a flattened, top view AFM image of the surface of a 15 nm-thick GaAs layer, grown at 750°C on a 200 nm-thick $Al_{0.45}Ga_{0.55}As$ buffer deposited on a 0.5 μm-pitch V-groove array [2]. The wire profile consists of several distinct nanofacets, consistent with TEM cross sectional images of these structures [Gustafsson et al., 1995]. Interface fluctuations along the wire axis clearly depend on facet orientation, as illustrated by the scan lines depicted in Fig.3.3 (b). The (100) facets on the ridges present atomically-smooth terraces separated by monolayer (ML) steps. The {311}A at the top show corrugations due to step bunching. The quasi-{111}A side walls of the grooves exhibit ~ 5 nm high undulations due to lithography imperfections. However, the self ordered growth yields much smoother bottom (100) facets. The (100) facets at the bottom of the V-groove coalesce into ~ 1 μm long domains exhibiting fluctuations at most one ML high, separated by moderate ($\sim 1°$ inclination) undulations correlated

---

[2] All AFM results are due to Dr. F. Reinhardt, currently at Lucent Technologies, Microelectronics, Reading, PA 19612, USA, and to Mr. G. Biasiol and Dr. F. Lelarge, Institute of Micro- and Opto-electronics, Department of Physics, EPFL, CH-1015 Lausanne.
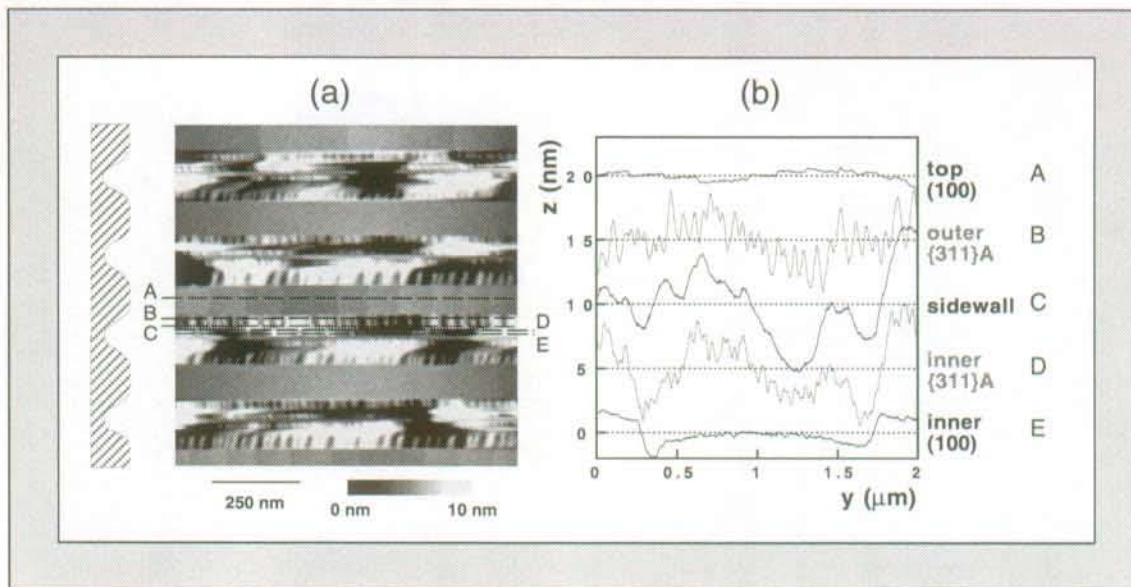
Figure 3.3: (a) $1 \times 1 \ \mu m^2$ AFM scan of a thick (37 nm at crescent center) surface GaAs QWR, grown on a 0.5 μm-pitch grating; (b) scan lines on the different facets forming the surface.

with sidewalls corrugation resulting in step bunching. The {311}A wire facets show in this case larger height variations due to quasi-periodic step bunching, superimposed on the long-range fluctuations found on the sidewalls. Finally, we note that similar investigations on other surface GaAs layers give evidence for ML steps fluctuations of the bottom (100) facets, as illustrated in Fig. 3.4. This figure shows line scans along the groove of the bottom (100) facet and of the two sidewall planes of a GaAs surface grown at 700°C. A hill-and-valley structure related to lithography imperfections with a height difference of about 10 nm and a period of about 1.5 μm is visible on both sidewall planes. These long-range fluctuations are also found on the (100) facet with reduced amplitude. Monolayer steps can be inferred from the (100) line scan in the central region. Height fluctuations of the underlying AlGaAs buffer are also expected to appear at the position of the step bunching found along the bottom (100) facets as it is fully correlated with lithography imperfections. The small bending of the GaAs wire due to these long-range undulations is, however, unable to explain the micro-PL features (the confinement energy variation due to the bending is very weak). We note also that large variations of the GaAs thickness would yield width fluctuations of the central (100) facet, which is almost never observed in AFM investigations of these surfaces [3].

This interface disorder translates into variations in the confinement energy of the 1D carriers along the wire axis, which can localize them. Electron and hole wave functions

---

[3]This observation is consistent with TEM pictures which show sharp delimitations between inner (100) and {311}A facets [Gustafsson et al., 1995].
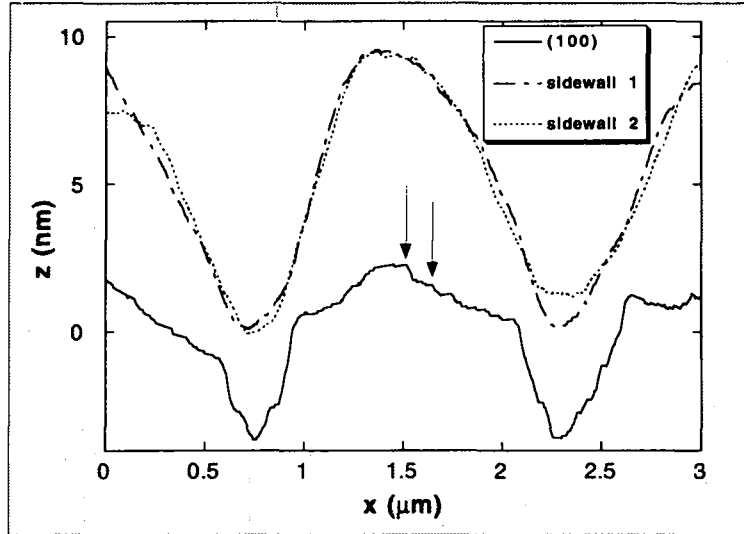
Figure 3.4: Line scans along the groove of the bottom (100) facet and of the two sidewall planes for a surface GaAs layer grown at 700°C. Arrows indicate monolayer steps inferred from the (100) line scan in the central region [Biasiol, 1998].

will be mainly influenced by height fluctuations of the bottom (100) and {311}A facets, as can be seen in Fig. 3.5 which displays the probability amplitude associated with the envelope wave function of the electron ground state in the 2.5 nm QWR.

Morphology of the bottom {311}A facets

The topography of {311}A facets has been studied systematically by AFM observations of the top surface of samples consisting of self-limiting AlGaAs layers on which GaAs films of increasing nominal thickness (0 to 100 nm) were deposited [Biasiol et al., 1997]. A growth temperature of 750°C and a nominal Al mole fraction of 0.2 have been selected, since, under these conditions (high T and low x) the AlGaAs profiles become wider than the lateral resolution of the AFM. The period d and the height h of the {311}A step bunching have been found to *increase* and then to saturate (d_{sat} and h_{sat}) *with increasing thickness*; the saturation curves are well fitted by exponential functions [Biasiol, 1998]. As the saturation values d_{sat} and h_{sat} were known for self-limiting GaAs at different growth temperatures (650 − 750°C), we could estimate d and h for a 2.5 nm QWR grown at 660°C. We found $d \approx 15$ nm and $h \approx 1$ ML. These height fluctuations (scaled for the 2.5 nm QWR) are displayed in Fig. 3.6. Using such a scaling procedure yields height fluctuations corresponding to fractions of a ML. Obviously, this result has no physical significance for a *single* scan line on a {311}A facet. However, such a result is consistent with height fluctuations *averaged* across a given {311}A facet. As the carrier wave function extends over a large part, if not over all, the width of theses facets (see Fig. 3.5), we keep these fractional MLs for our estimation of the localization potential.
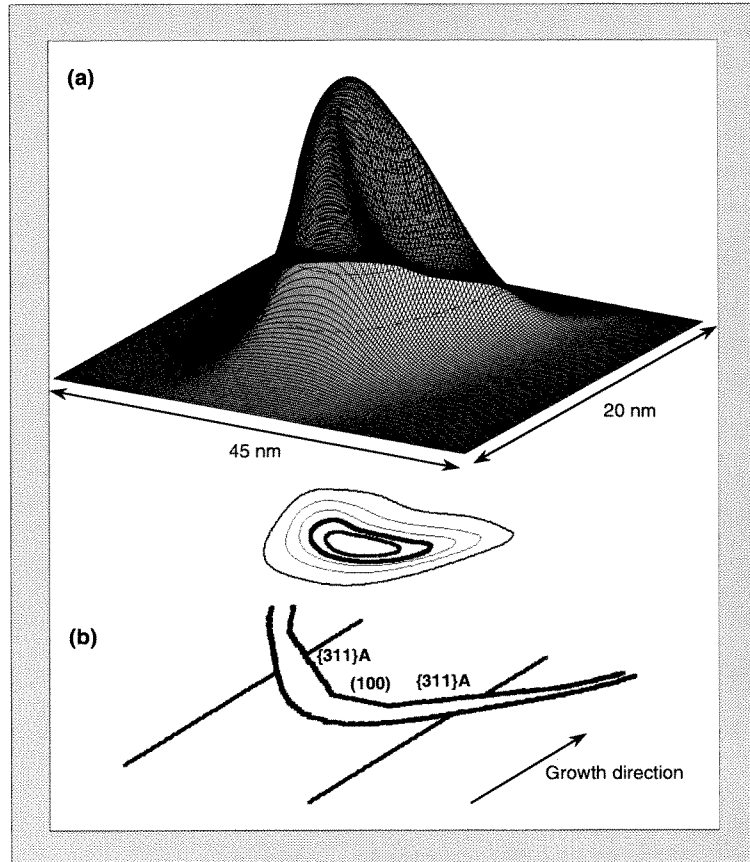
Figure 3.5: (a) Probability amplitude associated to the envelope wave function of the electron ground state in the 2.5 nm QWR; contour lines are displayed below the wave function. (b) Wire cross section derived from a TEM micrograph and used in the calculation; projections of contour lines of the VQW are also shown.

Morphology of the bottom (100) facets

The morphology of the (100) facet at the bottom of the groove is difficult to study, due to the small size of its width, compared to the AFM tip (silicon tip with a radius of curvature ~ 10 nm). Due to the self-limiting profile of the wire in the lateral-confinement direction, width fluctuations of the bottom (100) facets are found to be negligeable and confinement potential fluctuations mainly arise from thickness variations of the GaAs layer [4]. Obviously, the thickness of the GaAs layer below the (100) facets is determined by the height difference of the lower (AlGaAs) and upper (GaAs) interfaces. As we could not investigate bottom (100) facets of $Al_{0.3}Ga_{0.7}As$ and GaAs layers deposited at 660°C (due to the narrow groove), we studied similar layers grown under the same conditions on (100) GaAs substrates. Figure 3.7 shows AFM images of the surface of $Al_{0.3}Ga_{0.7}As$ and GaAs (1 nm thick) layers grown at 660°C on planar (100) GaAs

---

[4]Measurable width fluctuations of the central (100) facet result from large thickness fluctuations, which unlikely occur due to the self-limited growth.
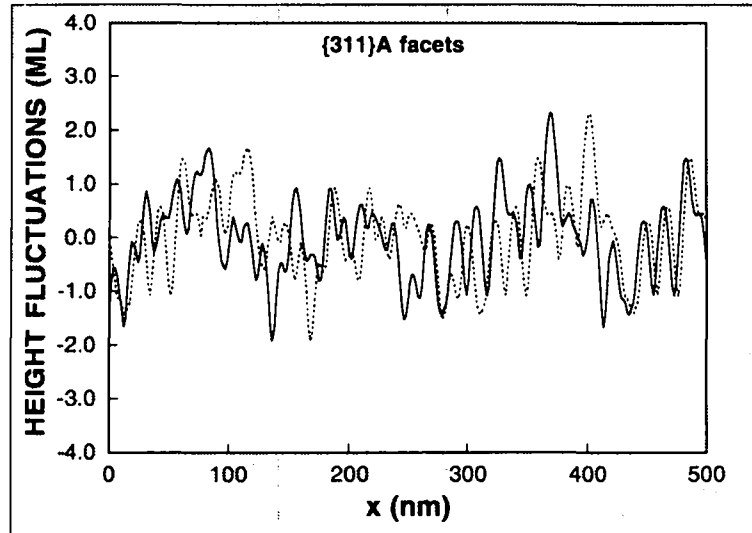
Figure 3.6: Scan lines along the {311}A facets of a 2.5 nm QWR, as inferred from results obtained for thicker wires (surface GaAs depicted in Fig. 3.3). Solid and dashed lines indicate scan lines measured on the two {311}A facets adjacent to the central (100) facet.

substrates (misorientation $< 0.1°$). The surface of the $Al_{0.3}Ga_{0.7}As$ exhibits 2D islands on the terraces between the ML steps (Figure 3.7 (a)). The deposition of a 1 nm thick GaAs layer (Figure 3.7 (b)) is sufficient to smooth out the islands and growth can be attributed to step flow because the surface diffusion length is then larger than the distance between steps. Increasing further the thickness of the GaAs layer gives similar results (not shown in the figure). This qualitative difference between the $Al_{0.3}Ga_{0.7}As$ and GaAs surfaces at the bottom of the groove is expected to be identical to that found for planar growth, if the misorientation remains small. The 2D growth mode found on planar surfaces is disturbed in the groove and results in step bunching, which can be observed on the (100) line scans in Figs. 3.3 and 3.4. At these positions, large misorientation results in similar growth mode for the upper *and* lower interfaces and we do not expect any thickness fluctuations of the QWR. On the contrary, between these long-range perturbations misorientation is small enough and thickness fluctuations of the GaAs layer at the (100) facet can be estimated by the difference of two height profiles measured on the planar $Al_{0.3}Ga_{0.7}As$ and GaAs surfaces. The position at which these height profiles were measured is indicated in Fig. 3.7 by a dashed line. The resulting height fluctuations are represented in Fig. 3.8.

The estimated thickness fluctuations at the {311}A facets and at the central (100) facet allows us to calculate the energy of the electron and heavy hole ground sates along the wire axis with the model presented in Sec. 2.4.3. Figure 3.9 shows the dependence of the energy of the electron ground state in the 2.5 nm QWR on the position along QWR
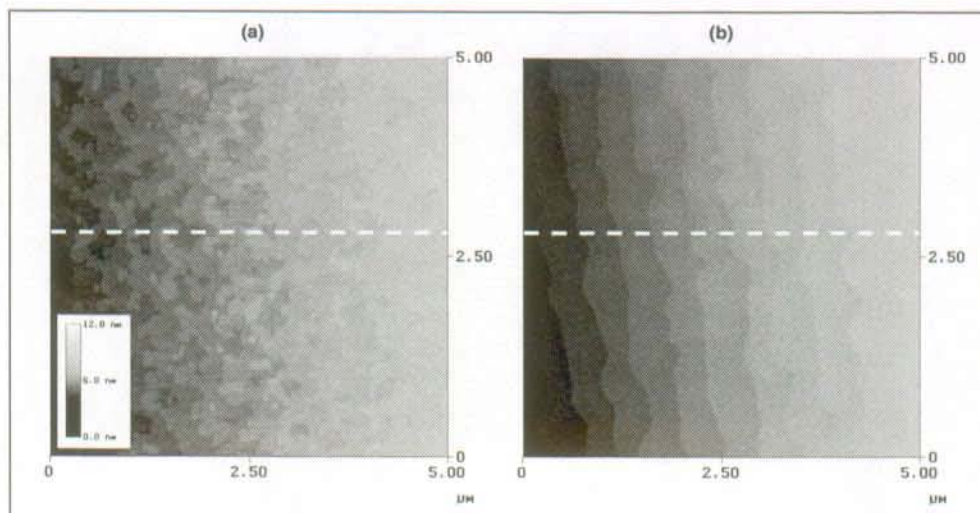
Figure 3.7: $5 \times 5 \ \mu m^2$ AFM images of the surface of (a) $Al_{0.3}Ga_{0.7}As$ and (b) 1 nm GaAs layers grown at 660°C on $Al_{0.3}Ga_{0.7}As$, deposited on planar (100) GaAs substrates.
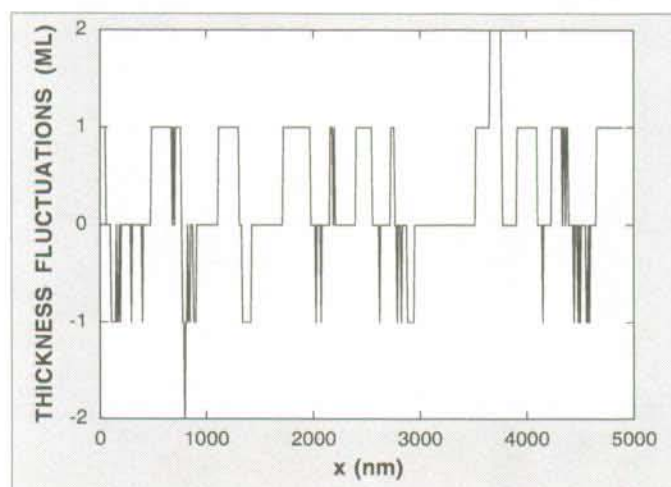
Figure 3.8: Estimated thickness fluctuations of the GaAs layer below the central (100) facet.

axis. Fluctuations at the central (100) facet translate into the formation of regions of the wire with a lower energy (mean depth of well ~ 7 meV) and an extension L_x which lies in the range $\sim 30 - 250$ nm (see Fig. 3.8). Perturbations of smaller amplitude (~ 2 meV) are superimposed over these fluctuations as a result of the short-range variations of the {311}A facets. We will see in Chap. 6 that both types of fluctuations determine the localization of carriers and, *a fortiori*, luminescence features.

In summary, confinement energy fluctuations along the wire axis may arise from three structural effects:

(i) long-range (period $\sim 1 \ \mu m$) undulations correlated to lithographic imperfections; this effect has been shown to yield negligeable contribution to the longitudinal
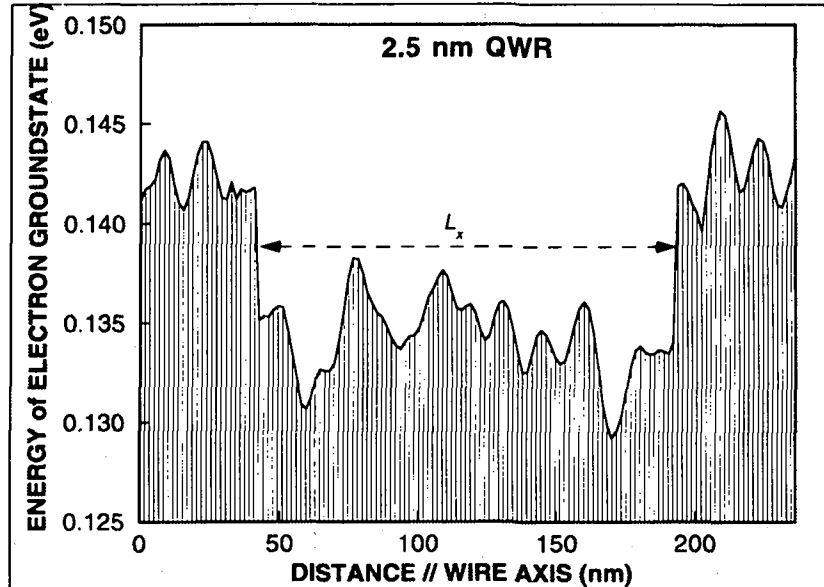
Figure 3.9: Localization potential for electrons in the 2.5 nm QWR, resulting from fluctuations at the (100) and {311}A facets which define the wire shape.

potential.

(ii) ML thickness fluctuations at the central (100) facet; this effect is expected to produce domains $\sim 30 - 300$ nm long corresponding to QD-like regions;

(iii) thickness fluctuations at the {311}A facets; we estimate this effect to give rise to energy fluctuations on a smaller scale (period ~ 15 nm) and with a reduced amplitude as compared to contribution (ii).

Although numerous hypotheses had to be made to estimate this longitudinal potential, we believe our model gives a reasonable description of it. The most drastic assumption concerns the scale down procedure used to estimate thickness fluctuations at the {311}A facets. However, we will see in Sec. 6.3.2 that the energy separation between the electron ground state and the first excited states in such a QD-like region is mainly determined by the extension L_x of the dot. Therefore, we believe that the analysis of experimental micro-PL results with the model presented above can yield valuable information on the structural disorder.

3.3   Optical measurement techniques

3.3.1   Photoluminescence

Photoluminescence spectroscopy is widely recognized as a very useful non-destructive technique for characterizing the quality of semiconductors and for fundamental research

in the physics of semiconducors (for a recent review, see, e.g., [Gilliland, 1997]. It consists in studying the radiation emitted spontaneously after excitation of the material by light. As we have seen in Sec. 2.5, the lowest energy excited state of the crystal corresponds to the formation of excitons. Therefore, photoluminescence in a semiconductor heterostructure requires that the exciting photons have an energy E_L such that:

$$E_L > E_g + e_1 + h_1 - E_b,$$

where E_g is the energy gap of the bulk material, e_1 and h_1 are the lowest confinement energies of electrons and holes, respectively, and E_b is the binding energy of the corresponding exciton. After excitation, the system returns to its equilibrium state via non-radiative and radiative processes. In a first step, photoexcited carriers relax to the center of the Brillouin zone by interaction with optical and acoustic phonons; this thermalization process takes place within about one to a few tens of picoseconds. After relaxation to the band edge, carriers recombine either radiatively (luminescence) or non-radiatively; typical radiative lifetimes at low temperature are of the order of a few hundred of picoseconds. Photoluminescence spectra correspond to the intensity of the emitted light as a function of the wavelength. Dynamical properties of semiconductors (carrier relaxation, diffusion, lifetimes, ...) can be investigated in time resolved photoluminescence experiments (for a recent review, see, e.g., [Othonos, 1998]).

Excitons in ideal QWR heterostructures are confined in two directions of space and are free to propagate along the wire axis. In case of such a perfect QWR, luminescence would be due to recombination of these "free excitons" which are delocalized in the wire direction. However, actual structures are influenced by disorder related to interface roughness and possibly alloy fluctuations. Modifications of the wire shape or of the potential barrier result in a fluctuating confinement potential along the wire axis, as discussed in Sec. 3.2.3. Regions of the wire having a lower confinement energy will trapp the excitons which correspond then to localized states [Bastard et al., 1984]. Thus, the excitons are confined in two directions by the QWR potential and by a weaker potential due to disorder along the wire axis . Consequently, 1D localized excitons may be considered as 0D excitons.

In a standard PL experiment, the excited area of the sample is $\sim 10^3 \mu\mathrm{m}^2$. In this case, the PL line is inhomogeneously broadened and results from the superposition of many individual lines associated with 1D localized or delocalized excitons in the excited part of the structure. In particular, a very high number of localized states will contribute to the luminescence and they are indistinguishable from each other. Therefore, the investigation of the impact of disorder on the optical properties necessitates the probing of the structure on a much smaller scale than that associated with standard PL (see micro-PL experiments, Sec. 3.3.3).

3.3.2 Photoluminescence excitation

Photoluminescence experiments yield information on the lowest energy states of the structure. Photoluminescence excitation gives access to the investigation of excited states by combining absorption and luminescence properties of the sample. In this technique, the spectrometer is set to detect emission at a particular photon energy. The intensity of this emission is then recorded as a function of the excitation photon energy, highlighting in this way the absorption resonances of the heterostructure. Once populated, the excited states relax either radiatively or non-radiatively towards lower energies. It is generally assumed that the PLE spectrum is equivalent to the absorption spectrum of the sample. This correspondence holds if the relaxation rate from the excited state towards the emitting state dominates over non-radiative recombinatinon rates (for more details, see, e.g., Chap. VII in [Bastard, 1992]). The advantages of PLE measurements over absorption spectroscopy are (i) the absence of sample preparation (e.g., no need for substrate removal), and (ii) the high sensitivity of the technique; PLE does not require thick samples (a single QWR is sufficient), whereas absorption experiments usually require a stack of quantum wells [5].

As discussed in Sec. 2.5.3, excitonic effects are expected to dominate the absorption spectra of semiconductor QWRs, yielding, in particular, a strong suppression of the band-edge singularity (Sommerfeld factor much less than unity). This means that a PLE spectrum will not reflect in a simple way the joint density of states (JDOS) of electrons and holes. The saw-toothed shape of experimental PLE spectra (see Chap. 4) results then from the dominant contribution of excitonic peaks and not from singularities in the JDOS. Band-structure effects influence, however, the oscillator strength of excitons, which is closely related to the magnitude of the exciton peaks [Winkler, 1995]. Moreover, it should be kept in mind that the relative intensities of excitonic transitions can be strongly influenced by mixing of different subband pairs caused by the Coulomb interaction [Winkler, 1995, Rossi and Molinari, 1996b].

3.3.3 Micro-photoluminescence and the mask technique

Several techniques have been used in the last four years to resolve the different spectral lines that contribute to the inhomogeneous broadening of the PL line in semiconductor heterostructures (For a global review, see, e.g., [Gustafsson et al., 1998]). In particular, several groups have shown that it is possible to study single QDs with photoluminescence either by reducing the number of emitting dots [Marzin et al., 1994], or by reducing the size of the laser spot on two-dimensional structures through microscopic (micro-PL) [Zrenner et al., 1994, Brunner et al., 1994a] or optical near-field techniques [Hess et al., 1994]. In this thesis work, we perform micro-PL experiments in combina-

---

[5]We note that a solution to circumvent this limitation can be realized by placing the structure in a waveguide configuration.

tion with apertured masks, a technique previously reported by Gammon et al. for the investigation of QDs formed by interface fluctuations in narrow GaAs/AlGaAs QWs [Gammon et al., 1995b, Gammon et al., 1996]. Optical spectra are measured through small holes made in a metallic mask deposited on the surface of the sample. This technique allows for simple submicron spatial-resolution optical measurements without the necessity of the usual near-field optical techniques.

We have used Al layers (thickness 80 nm) to define the masks. By electron-beam lithography and wet chemical etching, square holes of different width (0.2, 0.5, 1.0, and 2.0 nm) are etched into the Al to define areas in the mask which are transparent for both the excitation light from the laser and the luminescence from the sample.

Figure 3.10: Square hole, 0.5 μm in width, as visualized by atomic force microscopy.

In a first step, the samples are cleaned in successive baths of trichlorethylene, acetone, isopropanol, and deionized water. In a photolithographic step followed by resistive evaporation of aluminium in high vacuum, an array of 33 by 33 Al squares (100 μm in width) is deposited on the sample. The spacing between the edges of the squares is 50 μm so that the total area covered amounts to $\sim 4 \times 4$ mm^2. Polymethyle-methacrylate (PMMA) is deposited on the sample after lift-off [6]. A long spinning time (60 seconds at 6000 r.p.m.) is necessary to reach a thin enough layer of PMMA. For a thicker PMMA layer, the squares underneath it can not be distinguished by the scanning electron microscope (SEM). The positionning of the SEM is crucial as the electrom-beam has to be centered on each Al square before writing the corresponding hole. The holes and numbers for their identification are drawn by electron-beam lithography and the Al under these structures is etched by KOH (0.1N). Etching times for an 80 nm thick Al layer are 35 seconds for square holes with a width of 0.2 or 0.5 μm and 27 seconds for square holes with a width of 1.0 or 2.0 μm. To illustrate the fabrication of these micro-structured masks, we show in Fig. 3.10 a square hole, 0.5 μm in width, etched in an 80 nm thick Al layer deposited on the surface of the 2.5 nm QWR sample.

3.3.4 Time-resolved photoluminescence and the time-of-flight technique

Time-of-flight experiments are based on the detection of carrier motion as a function of spatial position and time. In ambipolar transport experiments, the radiative recombi-

---

[6]We note that it is important to thoroughly clean the samples of acetone after each processing step (especially after the liftoff) by successive baths of isopropanol and deionized water followed by at least half an hour on a hot plate at 160°C. Otherwise, degassing produces bubbles under the PMMA and deteriorates the aluminium layer.
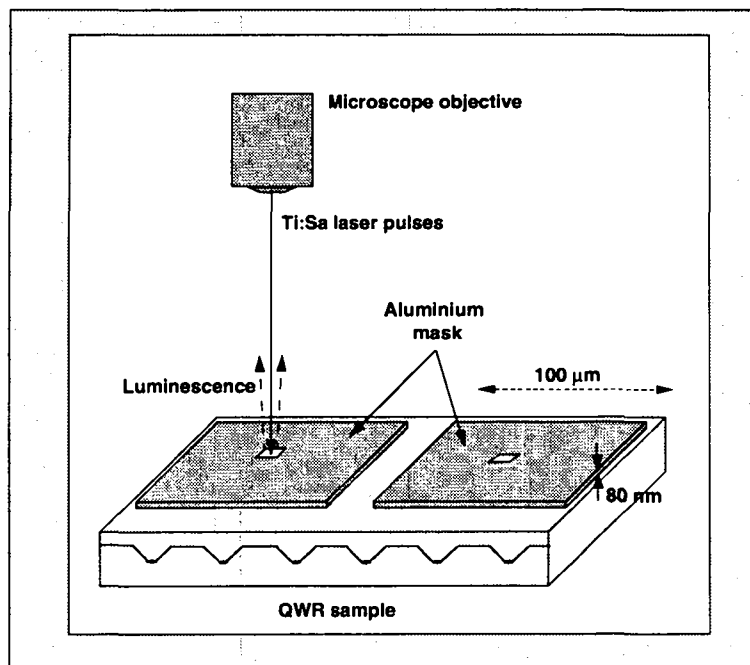
Figure 3.11: Schematic design of the sample-mask combination used to obtain a high lateral resolution. By short laser pulses (solid vertical arrow) electron-hole pairs are generated inside the QWRs seen through the aperture. The radiative recombination (dashed arrows) is detected time-resolved and used to probe the exciton concentration remaining under the hole area.

nation, which is proportional to the carrier concentration if the latter is not too high, represents an excellent access to probe the carrier motion. To study the longitudinal motion of excitons by optical spectroscopy, we use the sample mask combination schematically displayed in Fig. 3.11. The transport distances are defined by microstructured masks which are deposited directly on the semiconductor surface (see preceding section). Photocarriers are initially generated only inside the hole area by a short laser pulse, then the excitons move out of the hole area. We detect the PL from the excitons that remain inside the hole. The time evolution of the PL is determined both by the recombination (radiative or nonradiative) and the escape of excitons from the hole area. Information on the longitudinal motion of excitons in QWRs can, thus, be obtained by comparing the PL time evolutions with and without mask.

The 1D diffusion equation for a three-level system

If the scattering processes are independent of the exciton density, the exciton transport is diffusive, characterized by a single diffusion constant D. We assume that the energy relaxation of an exciton is decribed by a simple three-level model (see Fig. 3.12). Initial carriers are generated at level 1, relax to the bottom of the $e_1 - h_1$ exciton subband with a time constant τ_R, and then decay to the (crystal) ground state with a decay
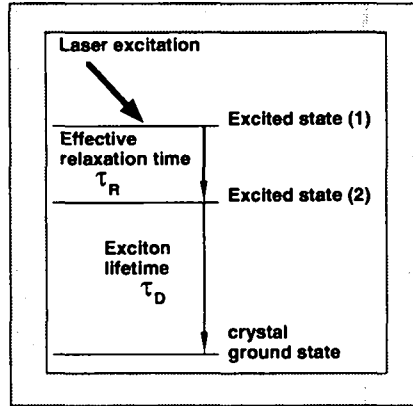
Figure 3.12: Three-level system modelling the energy relaxation of an exciton; τ_R is an effective relaxation time corresponding to carrier cooling and exciton-formation time, whereas τ_D is the exciton lifetime.

time τ_D. The exciton density at each level after laser excitation, $n_1(x, t)$ and $n_2(x, t)$, is described by the following rate equations:

$$\frac{\partial n_1}{\partial t} = D \frac{\partial^2 n_1}{\partial x^2} - \frac{n_1}{\tau_R}, \text{ and}$$

$$\frac{\partial n_2}{\partial t} = D \frac{\partial^2 n_2}{\partial x^2} - \frac{n_2}{\tau_D} + \frac{n_1}{\tau_R},$$

where x corresponds to the wire direction, and an identical diffusion constant D is assumed for excitons at levels 1 and 2. The time dependent intensity of the luminescence measured through a square hole, 2 μm in width, is then written as (y is the lateral-confinement direction):

$$I_{hole}^{PL}(t) \propto \iint_{hole} n_2(x, y, t) dx dy \propto \int_{-1}^{1} n_2(x, t) dx. \tag{3.1}$$

In the above expression of the PL intensity we assumed that the diffusivity is similar in adjacent QWRs and that the diffusion in the lateral-confinement direction is negligeable. The latter point was verified at 60 K by looking at the 2D image of the luminescence on the charge coupled device (CCD) detector. For a Gaussian distribution of the laser beam intensity, the density of excitons at level 2 is given by:

$$n_2(x, t) = \frac{\sigma_0 n_1(0, 0)}{\sqrt{4Dt + \sigma_0^2}} \frac{\tau_D}{(\tau_R - \tau_D)} e^{-\frac{x^2}{4Dt + \sigma_0^2}} \left\{ -e^{-t/\tau_D} + e^{-t/\tau_R} \right\}. \tag{3.2}$$

where $\sigma_0 = 1.5$ μm is the full width at $1/e^2$ of the maximum of the laser intensity and $n_1(0, 0)$ is the initial exciton density. The intensity distribution of the laser beam across a 2 μm hole and the corresponding profiles of exciton density in the wires under the hole are depicted in Fig. 3.13.
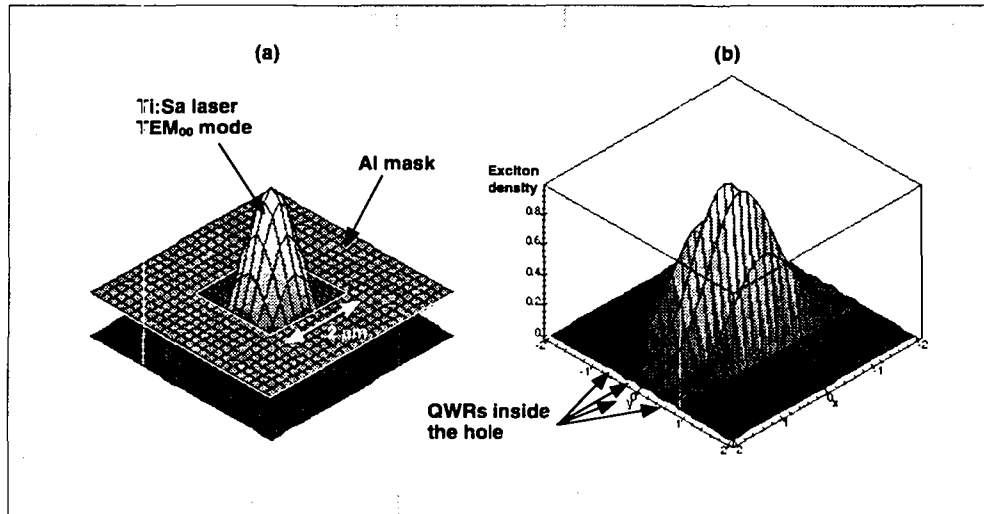
Figure 3.13: (a) Representation of the distribution of the laser beam intensity over a 2 μm hole; (b) profiles of the 1D exciton density in the wires excited through the hole .

Sensitivity of the method

Figure 3.14 (a) shows the influence of the mask on time-resolved luminescence profiles of the 6.9 nm QWR at 80 K. The PL measured through the hole decays faster as excitons move to the opaque area during their lifetime and become undetectable. The information on the exciton diffusion is obtained by fitting the luminescence profile with the above expression of $I_{hole}^{PL}(t)$ (Eqs. 3.1 and 3.2). The PL decay time τ_D is deduced from the profile measured without the mask; the effective relaxation time τ_R only influences the rise time of the profiles, due to the time scales involved here (τ_R is typically in the range 30 − 60 ps). Therefore, the diffusivity D is the only free parameter for the fitting procedure. To demonstrate the sensitivity of the method, we show in Fig. 3.14 (b) the time-resolved PL profile of the 6.9 nm QWR measured at 60 K through a 2 μm hole together with theoretical profiles for different values of D. We also notice on this figure a small shift of the maximum of the profiles measured without mask and through a 2 μm hole. Indeed, if we have long relaxation and exciton-formation times, some excitons can diffuse to masked parts before they reach the (radiative) level 2. Hence, the shift is observed when the effective relaxation time and a characteristic transport time, given by the diffusion, reach the same order of magnitude.

3.4   Experimental setups

Schematic representations of the experimental setups are shown in Fig. 3.15 and 3.16. The setups can be separated into four main components, an excitation source (a laser), a cryostat, a spectrometer or a spectrograph, and a detector.
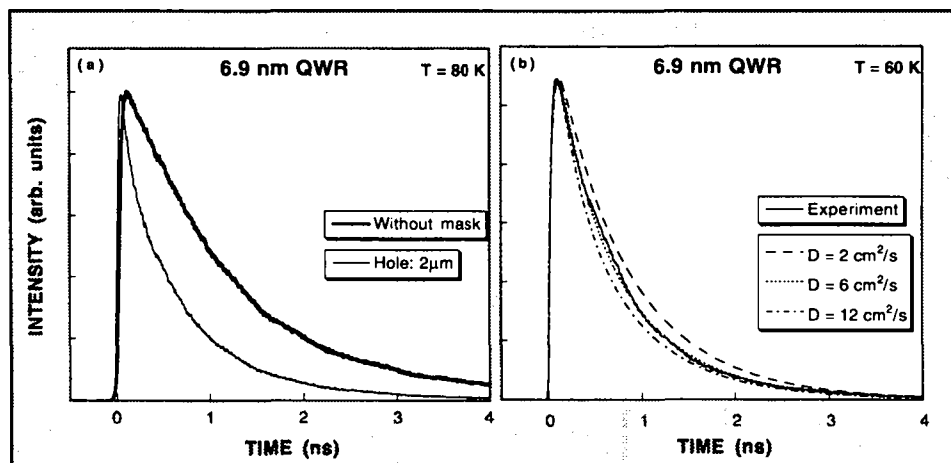
Figure 3.14: (a) Time-resolved luminescence profiles measured without mask and through a 2 μm hole. (b) Evaluation of an experimental profile by line-shape fits. Three theoretical profiles for different diffusivities are displayed by different line types. The best fit yields $D = 6$ cm^2/s.

3.4.1 Laser sources

Two different types of laser sources have been used: An argon-ion laser (Coherent, Innova 400) and a tunable titanium:sapphire (Ti:Sa) laser (Coherent, Mira 900-P) pumped by the Ar$^+$ laser in multiline mode. The 514.5 nm line of the Ar$^+$ laser (photon energy: 2.41 eV) allowed excitation of the structures in the AlGaAs barrier material. The spectral range covered by the Ti:Sa laser (680–830 nm; photon energy: 1.49–1.82 eV) allows selective or resonant excitation and photoluminescence excitation spectroscopy. A computer driven Lyot filter placed inside the Ti:Sa cavity selects the desired wavelength of the light. Both laser beams can be used for standard or micro-PL measurements. The cavity of the Ti:Sa laser can also be modified to generate ~ 3 ps pulses at 76 MHz. The Ti:Sa laser is operated in this mode-blocked regime for time-resolved experiments.

3.4.2 Cryostat systems

Two different cryostats have been used: One for standard PL and PLE measurements (C_1 in Fig. 3.15) and the other one for micro-PL and time-resolved experiments (C_2 Fig. 3.16). C_1 is a helium-flow cryostat (Janis Supertran-VP system) which can be operated in the range 4.2 − 300 K. The quartz windows of the cryostat (Suprasil II) have been checked to rotate the polarization direction of the laser beam by less than 8° for extreme positions of the laser beam on the windows and over the whole temperature range. C_2 is a helium-flow cryostat (Cryovac Konti-cryostat) specially conceived for minimum laser spot size and minimum temperature drift. As for C_1,it can be operated in the range 4.2 − 300 K. The quartz optical window (Suprasil 1) is 8 mm in diameter

and 200 μm thick.

3.4.3 Spectrometer and detection systems

Luminescence in standard PL and PLE experiments is dispersed by a Spex 1404 double grating spectrometer and detected by a GaAs photomultiplier tube (Products For Research Inc., PR 302) coupled to a photon counting unit (Stanford Research Systems SR 400). The gratings position is controlled by a computer. For micro-PL measurements, we use a Jobin Yvon spectrograph (HR460, 1200 l/mm grating) equipped with a nitrogen-cooled charge coupled device (CCD) detector (Jobin Yvon-Spex Spectrum One, 2000 × 800 pixels). For time-resolved experiments, we use the same spectrograph but after dispersion the luminescence is deflected towards a micro-channel plate (Hamamatsu, C2773 MCP-photomultiplier); a 300 l/mm grating is mounted in this case. The MCP is coupled to a time-correlated photon counting unit. The temporal resolution of the detection system is ~60 ps.

3.4.4 Setup for CW experiments

The laser beam is directed to the sample by means of a set of mirrors ($M_{1,2}$). A small prism (Pr) performs the last deviation of the laser before focussing it on the sample, thus allowing measurements in a backscattering geometry. A metallic variable attenuator (A) is used to select the appropriate exciting laser power. The laser is focussed on the sample by a lens (L_1) with a focal length of 80 mm. The same lens is used to collect the luminescence of the sample. We note that a small angle (8°) between the normal of the sample and the laser beam avoids collecting the reflection of the laser light. The polarization state of the laser beam and that of the luminescence are selected by a polarization rotator (R) and a linear polarizer (P), or by quarter-wave plates for circular polarization measurements. For the polarization analysis of the PL we combine a linear polarizer with a half-wave plate ($\lambda/2$) in front of the spectrometer to prevent any influence of the gratings on the detected intensity. The luminescence is focussed by a second lens (L_2) on the entrance slit of the spectrometer.

3.4.5 Setup for micro-photoluminescence or time-resolved experiments

The micro-PL setup combines standard photoluminescence equipment with a microscope. The laser beam is deflected by a set of mirrors (M_{1-5}) and by beamsplitter plates ($B_{1,2}$), and focussed on the sample by a microscope objective (Zeiss Epiplan LD
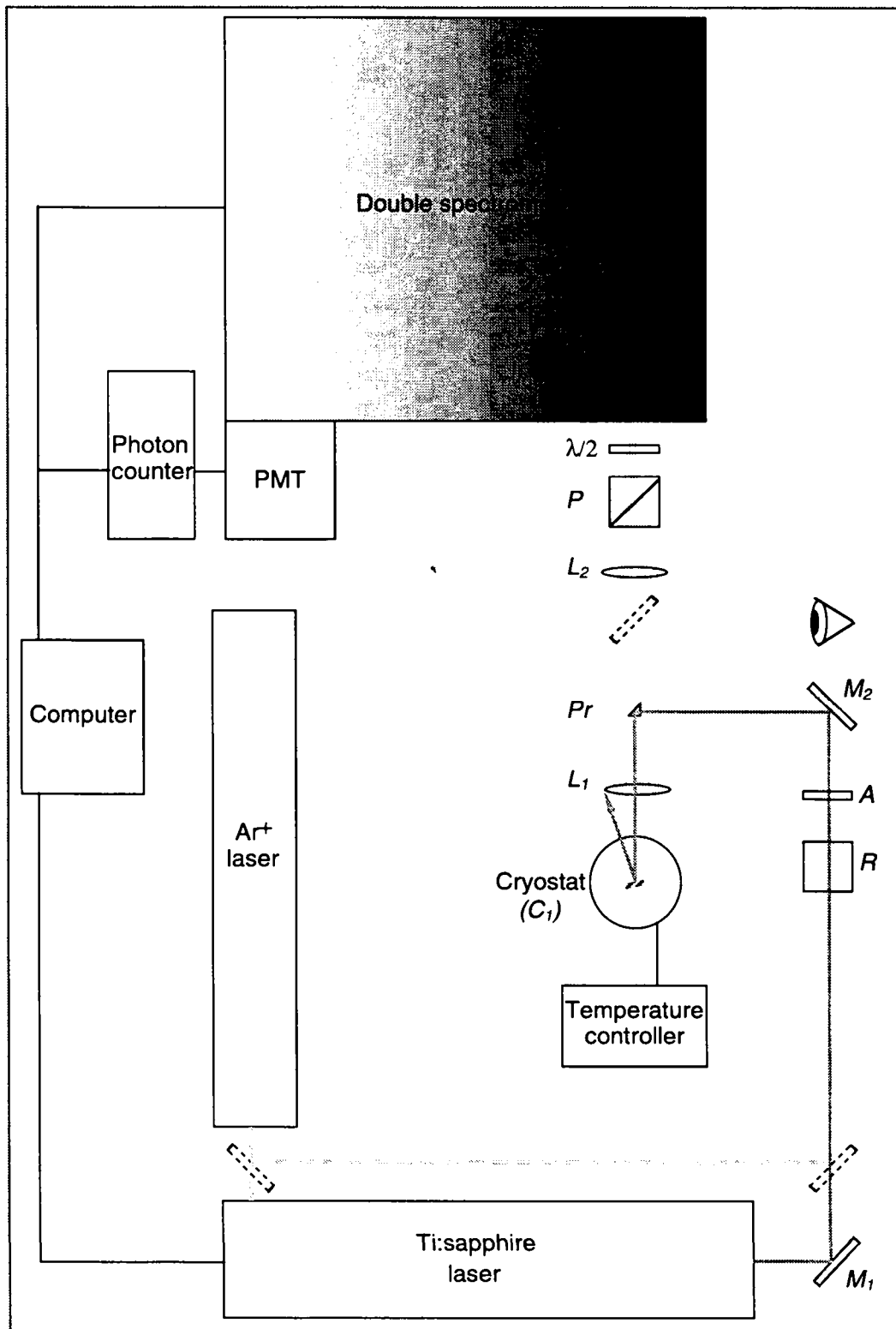
Figure 3.15: Schematic of the experimental setup used for CW measurements.

$50\times$, NA $= 0.5$) [7]. For time-resolved measurements, part of the exciting laser beam is taken by a beamsplitter (B_3) and sent towards the trigger diode which is coupled to the time-correlated photon counting unit. In case of excitation by the Ti:Sa laser, spectral filtering is realized by impinging the laser beam on a small diffraction grating and spatial cleaning is achieved by the system $L_1 - Pi - L_2$, where $L_{1,2}$ are two lenses and Pi is a pinhole (50 μm diameter). This allows us to eliminate the modes introduced by the Lyot filter of the Ti:Sa cavity and to obtain an almost perfectly Gaussian shape of the beam. The size of the excitation spot (full width at $1/e^2$ of the maximum) is $\sim 1 \mu$m for the Ar$^+$ laser and $\sim 1.5 \mu$m for the Ti:Sa laser. A system of two beamsplitter plates $B_{1,2}$ is used for directing the laser towards the sample, sending the PL towards the spectrograph, and visualizing the PL and the image of the sample either in the microscope eyepieces or by a CCD camera placed on top of the microscope. The PL is deflected by the beamsplitter B_2 and directed by mirrors $M_{6,7}$ to the spectrograph. Focussing of the luminescence on the entrance slit of the spectrograph is finally achieved by the lens L_3. For excitation by the Ti:Sa laser, a polarizer (P, crossed with the polarization of the laser) and a bandpass filter (BF) are used to attenuate the laser light reflected by the sample. The luminescence is then dispersed by the spectrograph.

---

[7]The focal length is 0.44 mm and the working distance is 6.9 mm.
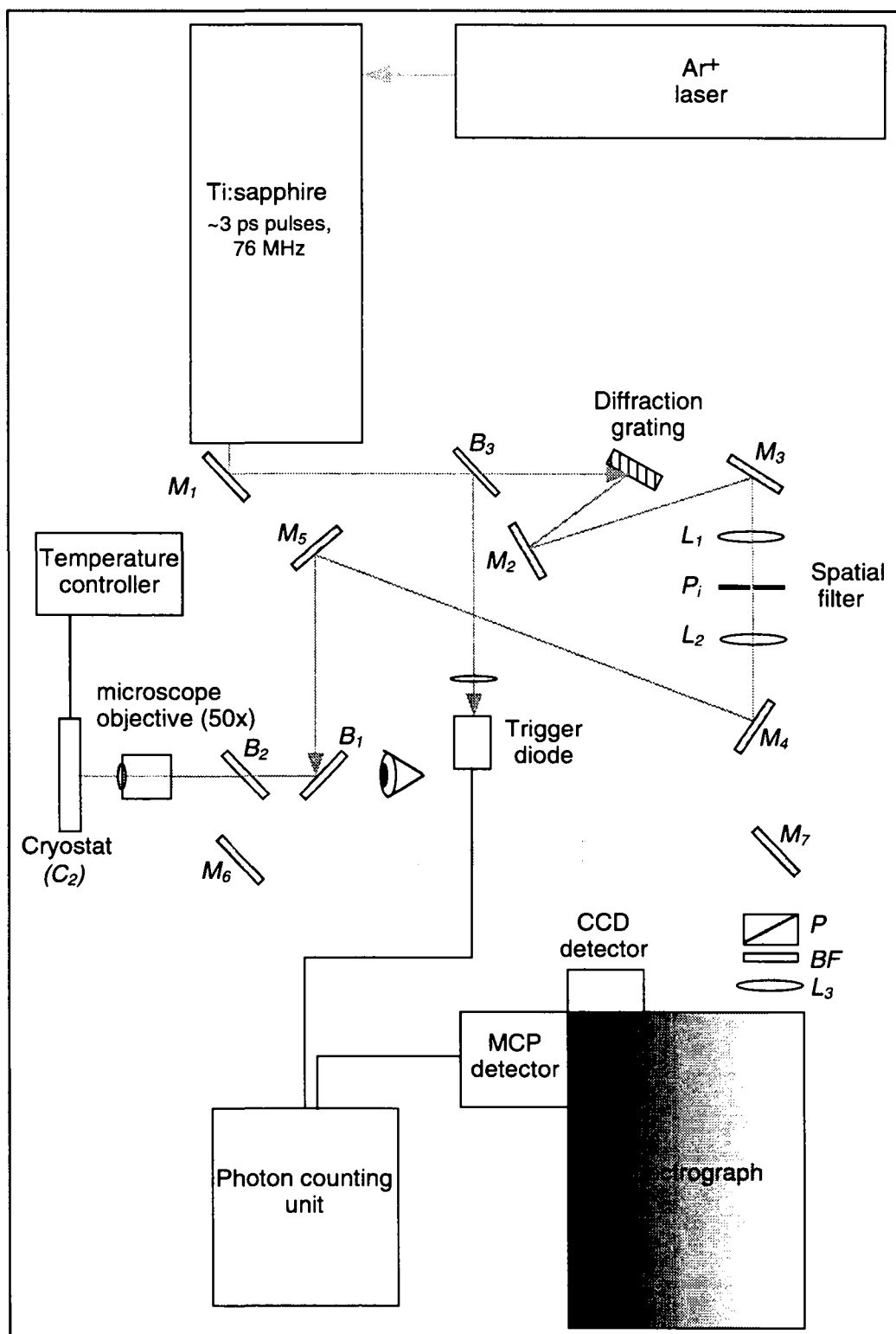
Figure 3.16: Schematic of the experimental setup used for micro-PL and time-resolved measurements.

3.5 Summary

In this chapter, we have determined the most realistic wire morphology as inferred from studies on planar and non-planar AlGaAs and GaAs layers by transmission electron and atomic force microscopies. A localization potential due to fluctuations of the wire cross-section along the wire axis has been estimated. The major components of the experimental setups have been described. We have presented the mask method used for micro-PL measurements and a time-of-flight technique that allows us to investigate the diffusion of 1D excitons. Modelling of the time evolution of the PL measured from masked samples and based on the 1D diffusion equation has also been expounded.

RESULTS AND DISCUSSION

Chapter 4

Polarization properties of optical spectra

4.1   Introduction

The electronic band structure and the optical properties of low dimensional systems, particularly semiconductor QWRs and QDs, have been attracting considerable interest recently (for a review, see, e.g., [Jaskólski, 1996]). The lateral quantum confinement and reduced dimensionality in these artificial structures can be employed to tailor their electronic and optical properties so as to allow the realization of band structures not achievable in bulk materials. The resulting structured materials may find important applications in novel electronic and optical devices, especially since the quantum confinement and low dimensionality lead to enhancement of the density of states at specific energies. Furthermore, modification in the electron-hole Coulomb interaction in these structures increases the importance of excitonic effects [Ogawa and Takagahara, 1991a, Rossi and Molinari, 1996a, Rossi and Molinari, 1996b]. These features could allow the utilization of the more confined character of the electronic states in low dimensional systems, particularly useful in optical applications, together with the delocalized nature of the states in bulk semiconductors, widely employed in devices relying on carrier transport.

The band structure of one dimensional (1D) semiconductor QWRs has been extensively investigated theoretically using model systems [Bockelmann and Bastard, 1991, Citrin and Chang, 1991]. Whereas theoretical models of the 1D conduction band predict effects largely similar to that in 2D quantum wells, i.e., quantization of subbands due to quantum confinement, studies of the nature of the valence band states have revealed features unique to 1D systems. Unlike the case of QWs, the quantum confinement in two spatial directions gives rise to valence band mixing at the *center* of the Brillouin zone. The mixing of the hh and lh states, which can be tuned by the lateral

confinement potential, leads to modified energies of the optical interband transitions and to a redistribution of the oscillator strength. Moreover, we will demonstrate that the modified valence band structure results in intrinsic polarization anisotropy of the interband absorption spectra, whose nature is intimately related to the details of the band mixing in the 1D system.

The purpose of this chapter is to present a systematic investigation of the effect of lateral confinement on PL and PLE spectra of GaAs/AlGaAs QWRs. Owing to the nonmonotonous evolution of the optical properties with changing wire thickness this requires the simultaneous experimental study of QWRs of various sizes and theoretical calculations of the corresponding band structures and optical transitions. Moreover, we will show that *localization effects strongly influence the polarization anisotropy of PL spectra thus making polarization analysis based on extended states insufficient at low temperature.*

Up to now the experimental study of the band structure of 1D systems has been hampered by the technological challenge in producing QWRs with sufficiently small inhomogeneous broadening. The effect of lateral quantum confinement on the conduction band has been evidenced by the emergence of 1D subbands in the optical luminescence characteristics of QWR structures prepared by different approaches [Kapon et al., 1989, Gershoni et al., 1990, Cingolani et al., 1992, Rinaldi et al., 1994]. However, the observation of the details of the valence band structure requires the resolution and identification of several 1D valence band states. Furthermore, the use of optical anisotropy as a probe of the valence band mixing pre-requires the identification and separation of other physical effects [Bauer and Sakaki, 1992], particularly strain [Kash et al., 1990, Chen et al., 1993, Notomi et al., 1998], electromagnetic effects due to surface corrugations [Bockelmann, 1991], and intrinsic bulk valence band anisotropy [Kajikawa, 1993], which can screen the intrinsic 1D effects. Specific morphologies of a quantum well interface which contains partially ordered and elongated monolayer islands are also known to be a source of optical anisotropies unrelated to any lateral confinement [Bauer and Sakaki, 1991]. Indeed, attempts to observe the intrinsic polarization anisotropy in several types of QWR structures could not unveil the intrinsic 1D valence band structure because of these spurious effects [Kash et al., 1990, Kohl et al., 1989, Lage et al., 1991, Birotheau et al., 1992]. Among the experimental studies, Bloch et al. [Bloch et al., 1994] and more recently Goldoni et al. [Goldoni et al., 1996] obtained information about the valence subbands of their QWR structures from anisotropy spectra but could not directly relate them to the observation of 1D excitonic transitions. Akiyama et al. [Akiyama et al., 1996] have observed optical anisotropy induced by lateral confinement in T-shaped QWRs but the

overlap of photoluminescence excitation peaks with other spectral features hindered observation of excited 1D states.

On the contrary, the high quality of our QWRs results in clear observation of excitonic transitions between 1D quantum-confined energy levels. This enables us to study in detail the impact of two-dimensional quantum confinement on valence band mixing and polarization anisotropy of PL and PLE spectra. Our systematic studies provide further insight into the relationship between the optical polarization anisotropy and the valence band structure of 1D semiconductors. In this chapter, we present PL spectra for different wire thicknesses and we show the influence of localization effects on their polarization properties. Linearly and circularly polarized PLE spectra are also studied and we discuss polarization effects related to exciton localization and surface corrugation. Finally, we use the results of the model presented in Sec. 2.4.1, namely, subband spacings and optical matrix elements, to analyse and discuss the experimental linearly and circularly polarized PLE spectra. Parts of these results have been published in Physical Review Letters [Vouilloz et al., 1997a] and Physical Review B [Vouilloz et al., 1998a].

4.2 Experimental

The experiments were performed on the 4.1 nm, 8.8 nm, and 14.1 nm QWRs. The optical spectra were obtained in a pseudo-bascattering geometry from the (100) plane using polarized light from an Ar^+ laser (514.5 nm) for the PL measurements and from a tunable Ti:Sa laser for PLE experiments. The excitation light was focussed into a spot approximately 35 μm in diameter; typical power densities of 25 W/cm^2 were used. For linear polarization measurements, perpendicular (parallel) refers to the [011] ([01$\bar{1}$]) direction. For circular polarization measurements the helicity of the exciting light (σ^+) was fixed. The helicity of the luminescence was analyzed by combining a quarter-wave plate and a linear polarizer in order to transmit the σ^+ or the σ^- component. The spectral resolution was fixed at 4 Å. The samples and the experimental techniques are described in detail in Chap. 3.

4.3 Photoluminescence and its polarization properties

4.3.1 Dependence of photoluminescence on wire thickness

PL spectra for the three QWR samples are displayed in Fig. 4.1. The different parts of the heterostructure have their distinct luminescence signature. The lowest energy peak of each spectrum is assigned to the luminescence of the QWR. At higher energy,

the luminescence from the side and top QWs appears either as a broad peak (Fig. 4.1 (a)) or as closely spaced peaks (Fig. 4.1 (b) and (c)). The luminescence from the VQW is observed either as a separated PL line (Fig. 4.1 (a) and (b)) or as a peak spectrally placed between the side and top QWs peaks (Fig. 4.1 (c)). In the case of the 8.8 nm QWR sample, recombination of excitons in the {311} QWs yields an additional peak at $\sim$ 1.73 eV. Finally, the weaker peak around 1.9 eV is due to recombination in the AlGaAs barrier material. We found that the integrated QWR luminescence varies linearly with excitation [1] power density between 1 and 10^3 W/cm^2, which supports the intrinsic and excitonic nature of the recombination process [Fouquet, 1986]. In order
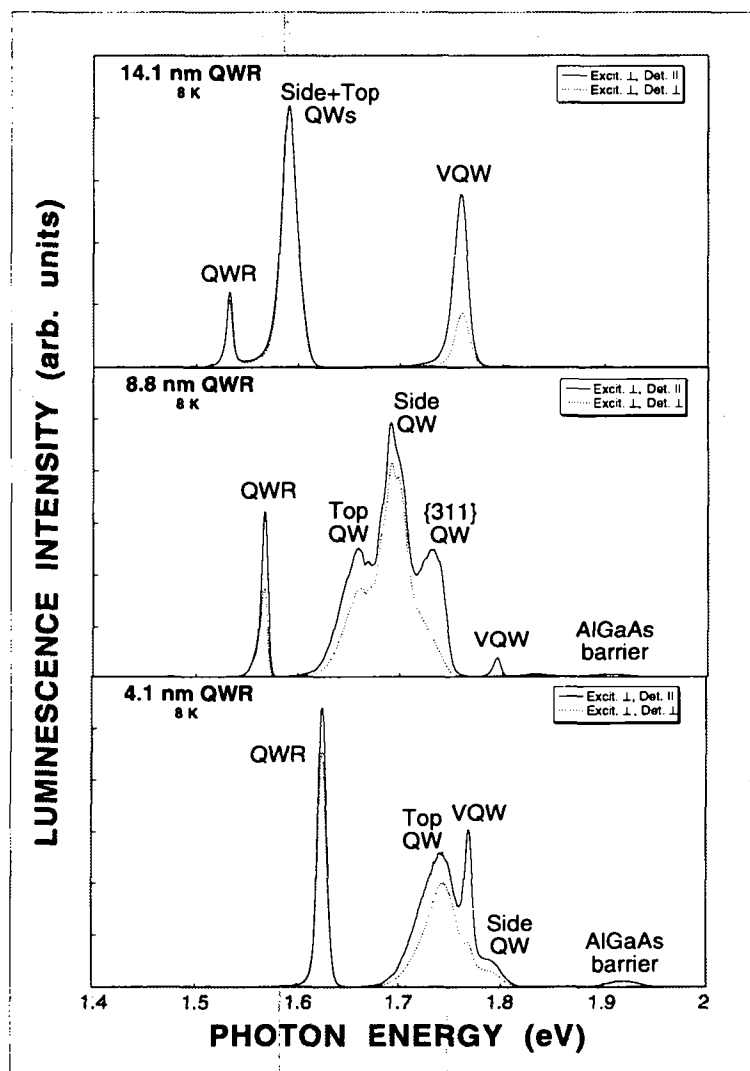
Figure 4.1: PL spectra of QWR samples with a GaAs thickness at the center of the crescent of a) 14.1 nm, b) 8.8 nm, and c) 4.1 nm, excited with the 514.5 nm line of an Ar$^+$-laser ($T = 8$ K). The linear polarization of the luminescence was analyzed parallel (solid line) and perpendicular (dotted line) to the wire axis.

---

[1] Carriers were photoexcited into the wire by using energy-selective excitation
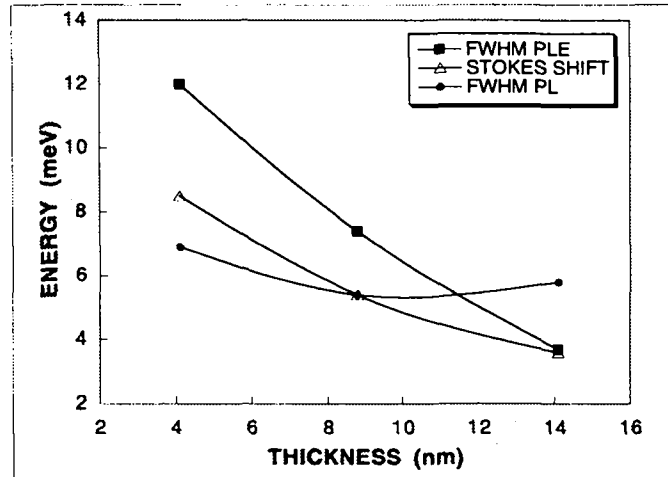
Figure 4.2: FWHM of the PL and of the first PLE peak versus GaAs thickness at the crescent center. The corresponding Stokes shifts are also shown. For PL experiments the exciting photon energy was 1.746 eV.

to identify the origin of these peaks we have combined a polarization analysis of the luminescence of the heterostructure with a calculation of the confinement energies for the side- and top-QWs using a finite potential well model. The widths of the QWs were extracted from the TEM micrograph of the sample. The Al mole fraction at the VQW was determined by cross-sectional atomic force microscopy [Reinhardt et al., 1996] and was found to be 0.09 lower than that of the nominal Al value. The linear polarization of the luminescence was analyzed parallel (solid line in Fig. 4.1) and perpendicular (dashed line in the same figure) to the wire axis. The polarization anisotropy of 2D structures is expected to increase progressively when changing the orientation of the QW from that of the top-QWs to that of the VQWs. Furthermore, we should find a constant luminescence intensity for any polarization of the light in the plane of ideal top-QWs. The discrepancy between this theoretical expectation and the experimental findings likely result from localization effects that introduce an artificial anisotropic structure in the plane of (100)-oriented QWs. Nevertheless, the expected trend for the variation of the polarization anisotropy of the PL emission with the orientation of the wells is clearly observed. In particular, the maximum polarization anisotropy is found for VQWs, in agreement with a recent combined experimental and theoretical study of PL and PLE spectra in such VQWs [Martinet et al., 1997]. These peak assignments are supported by low temperature cross-sectional cathodoluminescence imaging of the emission wavelengths on similar QWR structures [Kapon et al., 1992a].

The PL FWHM of the QWR-peak excited with the Ti:Sa laser ranges from 5.4 to 6.9 meV and the FWHM of the first PLE peak ranges from 3.7 to 12.0 meV for the three samples investigated, as illustrated in Fig. 4.2. The PLE FWHM was determined

by fitting the first three PLE peaks with a superposition of Gaussians. The PLE FWHM is mainly determined by inhomogeneous broadening of an optical transition whereas the PL FWHM strongly depends on relaxation and localization effects. As a consequence, the FWHM of the PLE peaks can be either narrower or broader than that of the corresponding PL peaks [Miller and Bhat, 1988]. The small Stokes shifts (3.6–8.5 meV) and PLE linewidths attest to the high quality of these wires.

4.3.2   Linear polarization analysis of the luminescence

Localization of excitons at interfacial defects can strongly affect the polarization properties of a 2D [Gammon et al., 1996] or a 1D system. PL spectra of QW structures which show a fine structure in micro-PL experiments have been assigned by different groups [Brunner et al., 1994b, Gammon et al., 1995b, Jahn et al., 1996] to recombination of excitons localized at interface defects caused by roughness or composition fluctuations. We find that the polarization anisotropy of PL spectra is dependent both on excitation wavelength and on the spectral position within the emission line thus making any polarization analysis based on extended states insufficient at low temperature. To illustrate these remarks we show in Fig. 4.3 (a) the PL emission of all three QWR samples together with their degree of linear polarization $P = (I_{||} - I_{\perp})/(I_{||} + I_{\perp})$, where $I_{||}$ ($I_{\perp}$) is the PL intensity linearly polarized parallel (perpendicular) to the wires. The excitation wavelength was 514.5 nm for part (a) and 710 nm for part (b) of the figure. It can be seen that the luminescence is mainly linearly polarized in the wire direction and that P strongly depends on the emission wavelength for the 8.8 nm and the 14.1 nm QWRs. In that case, the maximum of P is found at a higher energy than that of the PL peak. When the excitation wavelength is increased to 710 nm (Fig. 4.3 (b)) the maximum of P is also blueshifted from the PL peak. This behavior can be attributed to exciton localization due to disorder along the wire. We first note that localized states dominate at the low-energy tail of an inhomogeneous exciton band [Gurioli et al., 1994]. Because localization is expected to reduce the degree of linear polarization by symmetrizing the exciton wavefunction it leads to the lowest degree of linear polarization on the low energy side of the PL. In this perspective, the quasi-constant and low degree of linear polarization for the 4.1 nm QWR may be explained by a pronounced impact of localization across the whole PL line (effective mobility edge shifted towards the high energy tail of the QWR peak, see Sec. 5.7). Similar results have been found for exciting laser beams polarized perpendicular to the wire axis.
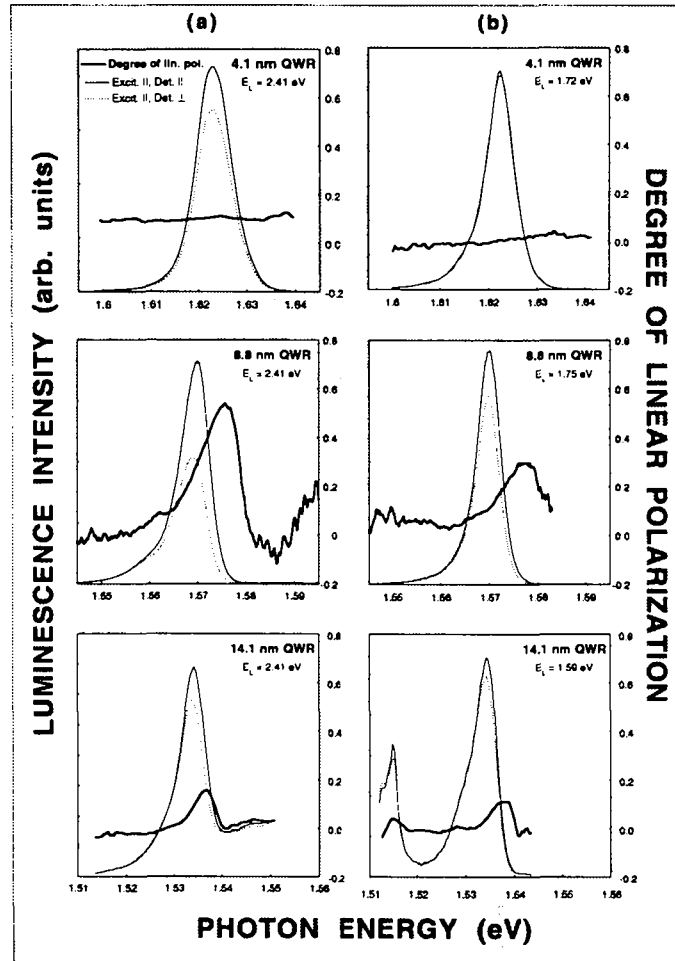
Figure 4.3: PL spectra of the 4.1 nm, 8.8 nm, and 14.1 nm QWRs excited by a a) Ar$^+$-laser (488 nm) and b) Ti:Sa laser (710 nm); in both cases the exciting beams were polarized parallel to the wires. The linear polarization of the luminescence was analyzed parallel ($I_{||}$) and perpendicular ($I_\perp$) to the wire axis. The degree of linear polarization $P = (I_{||} - I_\perp)/(I_{||} + I_\perp)$ is also shown ($T = 8$ K).

4.4 Photoluminescence excitation and its polarization properties

4.4.1 Dependence of photoluminescence excitation on wire thickness

The linearly polarized PLE spectra of the three QWR samples are shown in Fig. 4.4 (a), Fig. 4.4 (b), and Fig. 4.4 (c), respectively. The dependence of the optical spectra on the polarization of the exciting laser reveals a striking polarization anisotropy. The PLE spectra show up to seven peaks corresponding to excitonic transitions of 1D quantum-confined energy levels. A decrease of the wire thickness leads to a blue-shift of the ground state transition, $e_1 - h_1$, that increases from 1.538 eV for the 14.1 nm QWR to
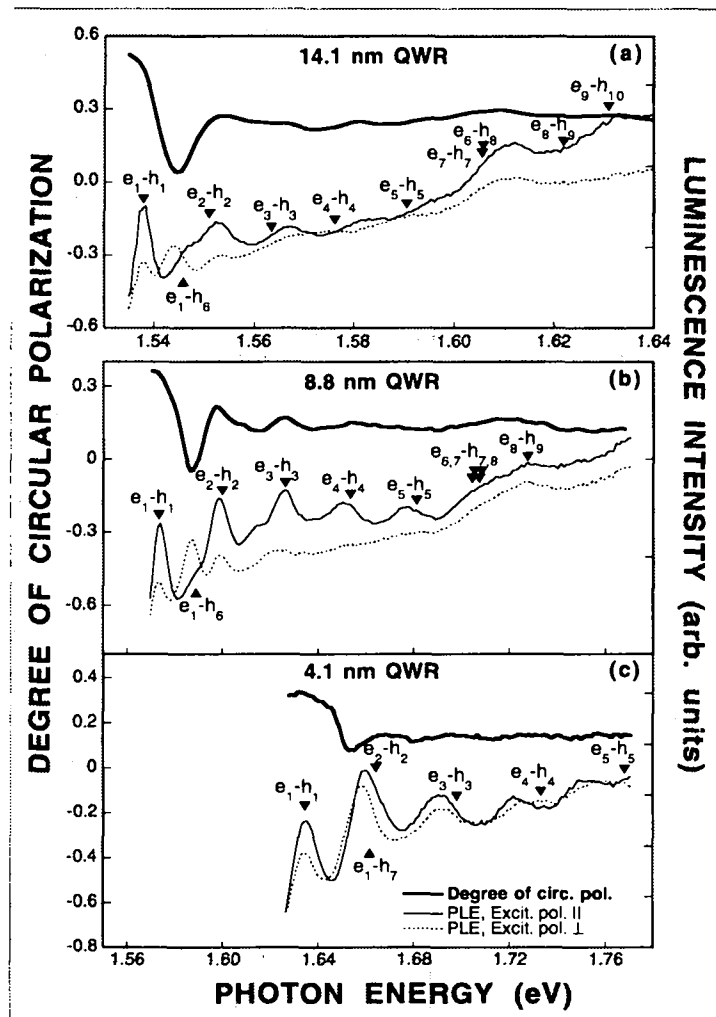
Figure 4.4: Degree of circular polarization (see text for definition) and linearly-polarized PLE spectra for QWR samples with a GaAs thickness at the center of the crescent of a) 14.1 nm, b) 8.8 nm, and c) 4.1 nm. The detection wavelength is set at the maximum of the QWR PL line ($T = 8$ K). Note different energy scale for a).

1.634 eV for the 4.1 nm QWR. An additional effect which arises from the change in the shape of the crescent for thinner wires leads to a modification of the energy separation between the e_n – h_n transitions. As the crescent thickness decreases, the subband separation first increases, due to the lateral tapering. For thin crescents, however, a further thickness reduction results in a more elongated crescent, which prevents further increase in subband separation. This saturation in the subband separation is enhanced by the increased penetration of the wave function into the surrounding barriers. The separations between the e_1 – h_1 and e_2 – h_2 transitions are 15.0, 26.5 and 25.3 meV for the 14.1 nm, 8.8 nm and 4.1 nm QWR, respectively.

4.4.2 Effect of surface corrugations

The presence of corrugations at the surface of a QWR structure causes several electrody-namical effects which may strongly affect the optical properties of the heterostructure. Periodic surface corrugations allow a momentum transfer between photons and the microstructure, giving rise to the so-called grating coupler effect [Kohl et al., 1990]. This leads to a coupling of the photons to nonradiative exciton-polaritons in the structured material, which can become observable as an additional strongly polarized signal in the PL spectrum. This effect has been demonstrated in GaAs/AlGaAs QWs with a modulated cap layer and in etched GaAs/AlGaAs QWRs for wire widths above 150 nm [Kohl et al., 1990, Kohl et al., 1988]. When the wire width is decreased below 150 nm the QW exciton-polaritons localize and a transition to the behaviour of quasi-1D excitons is observed [Kohl et al., 1989]. The polarization dependence of the observed optical transitions is then mainly determined by the intrinsic properties of the 1D system.

Corrugations at the surface of a QWR structure also result in local fields characterized by spatial distributions which are polarization dependent [Bockelmann, 1991]. To identify this electrodynamic polarization effect we measured PLE spectra on two
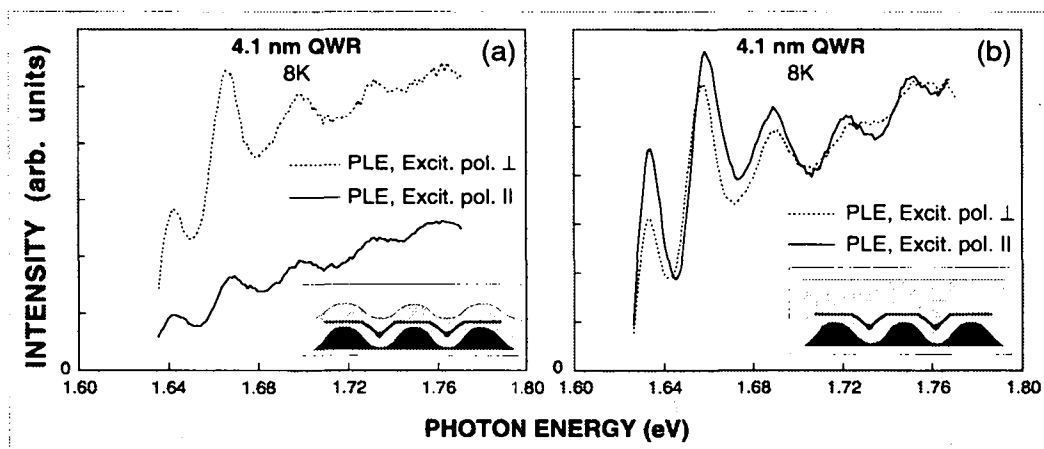
Figure 4.5: PLE spectra of 4.1 nm-QWRs showing the effect of surface corrugation: a) 4.1 nm QWR with deep surface corrugation, and b) 4.1 nm QWR with a planar surface.

different 4.1 nm QWR samples (Fig. 4.5). The first QWR structure was not planarized and exhibited a periodic modulation of its surface with grooves approximately 100 nm deep, whereas the second sample was completely planarized. The vertical shift of the PLE spectrum in Fig. 4.5 (a) for excitation light polarized perpendicular to the wires is well explained by the enhancement of the electric field in the grooves of a surface grating when its polarization is orthogonal to the grooves. This, in turn, increases the relative intensities of the PLE lines associated with the QWR transitions for the perpendicular polarization. The polarization dependence of the exciting light intensity at the position

of the QWRs thus gives rise to an additional polarization anisotropy modifying the intrinsic anisotropy of the 1D system [Bockelmann, 1991].

Fig. 4.5 (b) shows PLE spectra of the planarized 4.1 nm QWR. In this case, essantially the same QWR illumination is achieved for the two polarizations. The difference in the luminescence signal for the two different polarizations of the exciting light reflects then the intrinsic properties of the QWRs. We also checked that the PLE spectra and their optical anisotropy did not depend on the incidence angle α of the exciting laser beam, for $\alpha < 20°$. For angles $\alpha > 20°$ the power reflectance of the incident wave at the surface of the sample critically depends on its polarization state. The PLE spectra presented in Fig. 4.4 were measured at $\alpha = 8.5°$ on planarized structures and are therefore free from surface grating effects.

4.4.3   Influence of localization effects

A PLE spectrum depends both on absorption and emission properties. To investigate the impact of localization effects on the optical anisotropy due to the 1D valence band structure we measured PLE spectra as a function of the detection wavelength across the PL peak. Fig. 4.6 shows the results for all three QWR samples. The spectral positions of the different 1D optical transitions do not change notably when the detection wavelength is moved across the PL line. We note, however, that the relative intensity of the first PLE peak with respect to the other peaks decreases as the detection is moved to lower energies. This may indicate that carriers created at the energy of the first PLE peak relax less efficiently when the final state corresponds to strongly localized excitons. This analysis is corroborated by the temperature dependence of PLE spectra presented in Sec. 5.4. Therefore, in this study of the polarization properties of QWR structures one should keep in mind that PLE experiments do not exactly reproduce absorption measurements.

4.4.4   Relative anisotropy of transition strength for the the two lowest energy transitions

Fig. 4.7 (a) and (b) shows the ratio of the integrated intensity of the $e_1 - h_6$ transition and that of the $e_1 - h_1$ transition as a function of the angle θ between the polarization direction and the wire axis (8.8 nm and 14.1 nm QWRs, respectively). It was determined by fitting the first three PLE peaks with a superposition of three Gaussians. Assuming the squared optical matrix elements $|M|^2_{e_n - h_m}$ to be constant across each peak, this corresponds to $|M|^2_{e_1 - h_6}/|M|^2_{e_1 - h_1}$. The different curves in Fig. 4.7 are for PLE spectra detected at different wavelengths across the PL peak. The variation of these polarization anisotropy curves with detection wavelength results from localization effects described in
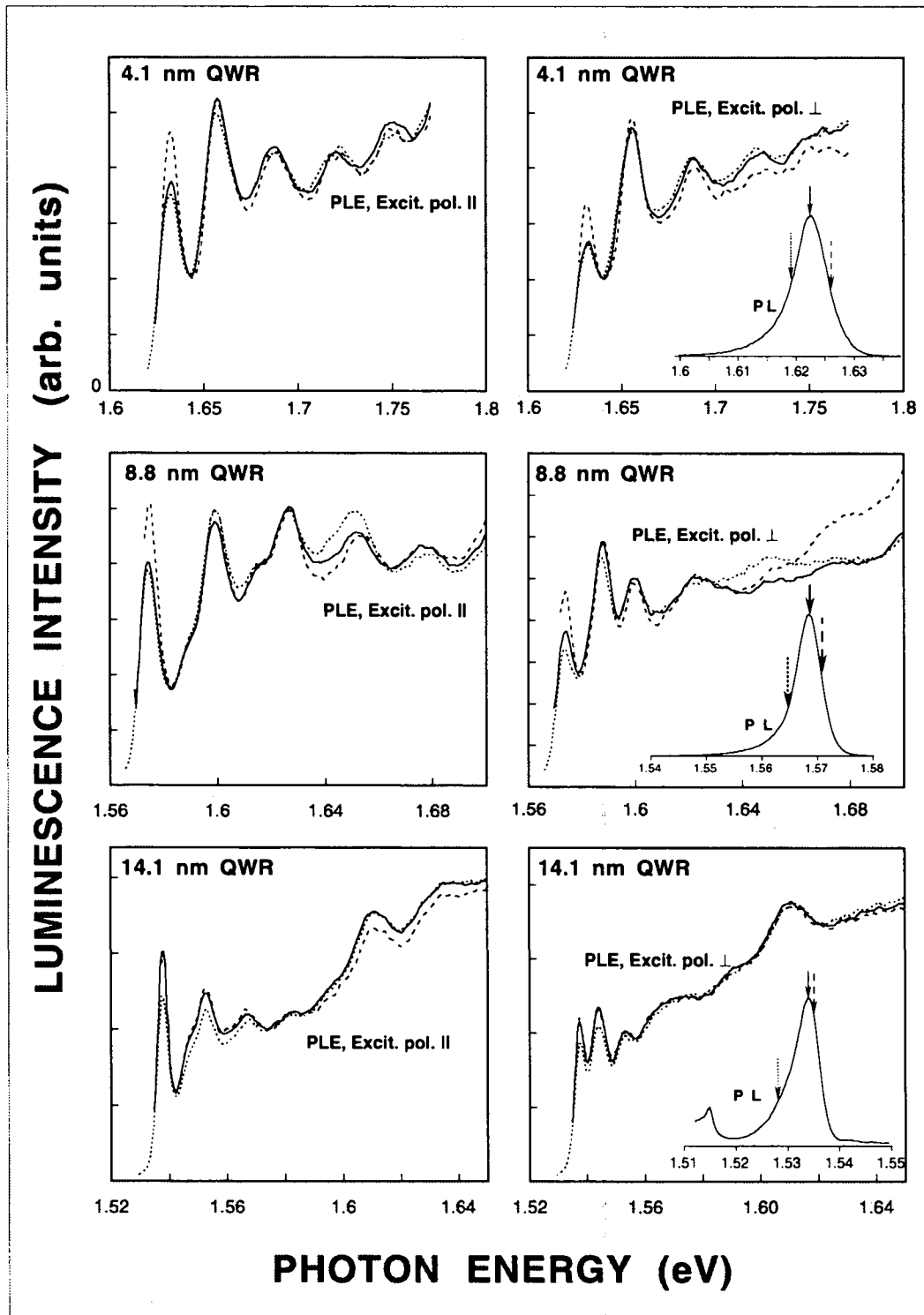
Figure 4.6: PLE spectra of the 4.1 nm QWR measured for different detection wavelengths. The detection positions are indicated by arrows in the insets displaying the QWR PL lines ($T = 8$ K).
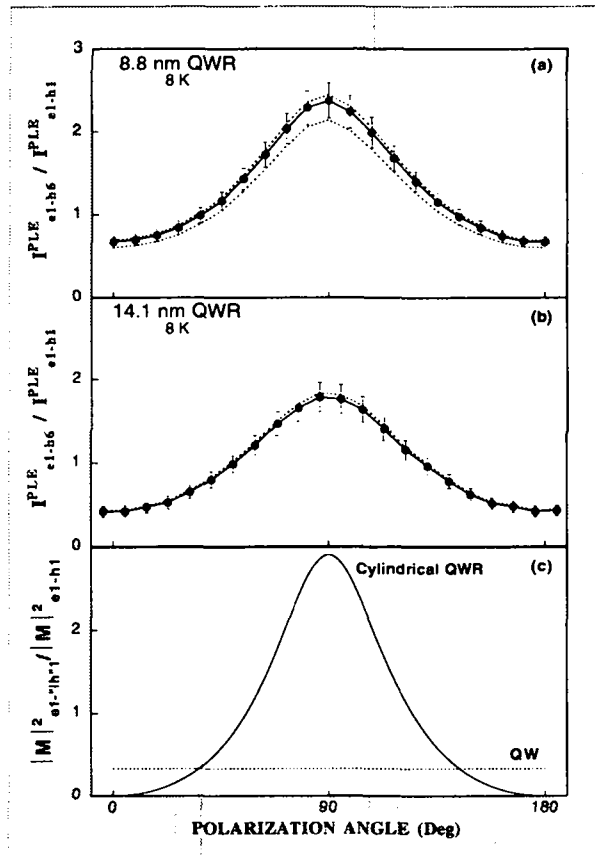
Figure 4.7: Ratio of the integrated intensity of the $e_1 - h_6$ transition and that of the $e_1 - h_1$ transition as a function of the angle θ between the polarization direction and the wire axis (8.8 nm and 14.1 nm QWRs, in part (a) and (b), respectively). It was determined by fitting the first three PLE peaks with a superposition of Gaussians. The error bars result from the uncertainty of the curve fitting process. The solid line is obtained from PLE spectra detected at the maximum of the QWR PL line, while the upper (lower) dashed line corresponds to low (high) detection energy. Part (c) displays theoretical calculations of $|M|^2_{e_1-\text{"lh"}_1}/|M|^2_{e_1-h_1}$ for a cylindrical QWR (10 nm in diameter, GaAs/Al$_{0.3}$Ga$_{0.7}$As) and for a GaAs QW.

the preceding section. Comparison of the data for the 8.8 nm QWR and for the 14.1 nm QWR shows that the maximum ratio (at $\theta = 90°$) increases as the overall size of the wire decreases. Fig. 4.7 (c) displays theoretical calculations of $|M|^2_{e_1-\text{"lh"}_1}/|M|^2_{e_1-h_1}$ for a cylindrical QWR (10 nm in diameter, GaAs/Al$_{0.3}$Ga$_{0.7}$As) [Sercel and Vahala, 1991] and for a GaAs QW. We note that for cylindrical wires a vanishing value for light polarized parallel to the wires (at $\theta = 0°$) is found, unlike our observation of non-vanishing values in crescent-shaped wires.

4.4.5 Circular polarization analysis of photoluminescence excitation spectra

To investigate further the nature of the valence states involved in the observed optical transitions, we use circularly polarized light to excite and analyze the QWR luminescence. In this situation the photon helicity is transferred to the semiconductor through spin orientation of the excited electrons and holes [Lampel, 1968]. If we assume incomplete electron spin relaxation [Twardowski and Hermann, 1987], this leads to circular polarization of the PL, which depends on the initial conduction and valence states. The measurement of the degree of circular polarization of luminescence has been used in QWs to identify the hh and lh transitions [Weisbuch et al., 1981]. In a QWR system light with σ^+ polarization couples hh (lh) component of the wavefunction with $J_z = -\frac{3}{2}(-\frac{1}{2})$ and electron state with spin $s = -\frac{1}{2}(+\frac{1}{2})$, whereas σ^- polarization couples hh (lh) component of the wavefunction with $J_z = +\frac{3}{2}(+\frac{1}{2})$ and electron state with $s = +\frac{1}{2}(-\frac{1}{2})$. The measured degree of circular polarization $\mathcal{P} = (I^+ - I^-)/(I^+ + I^-)$, where $I^+(I^-)$ is the $\sigma^+(\sigma^-)$ circularly polarized luminescence intensity, is also shown in Fig. 4.4 for each QWR structure. The polarization spectra of all three QWRs present strong modulations correlated with the 1D excitonic transitions observed in the linearly polarized PLE spectra. The pronounced dip located at the second lowest energy transition in each polarization spectrum corresponds to the first valence subband with strong lh character.

4.5 Discussion

To analyze the PLE spectral features we implicitly assume a one to one correspondance to absorption peaks as PLE spectra of quantum wells show a close resemblance to calculated absorption spectra [Winkler, 1995]. An exact correspondance holds if the relaxation rate from the excited state towards the emitting state dominates over non-radiative recombination rates. We also note that intersubband coupling modifies the overall shape of a PLE spectrum by transfering the oscillator-strength towards the low-energy region which results in a significant increase of the first exciton peak [Rossi and Molinari, 1996a]. It is well known that excitonic effects play a major role in the optical-absorption spectra of 2D systems [Miller and Kleinman, 1985]. Moreover, the Sommerfeld factor was calculated and found to be much smaller than unity for a direct allowed interband transition in a 1D system [Ogawa and Takagahara, 1991a, Rossi and Molinari, 1996a], in striking contrast to the 3D and 2D cases. This means that electron-hole correlation leads to a strong suppression of the 1D band-edge singularity in the linear-absorption spectra. For these reasons, we believe that our optical

spectra are fully dominated by the excitonic nature of the optical transitions; otherwise, aside from the excitonic peak, a second peak which corresponds to the maximum in the JDOS would have been observed in the PLE spectra at higher energy. This interpretation of PLE spectra as a single series of peaks for each QWR structure is allowed by the small inhomogeneous broadening of the optical transitions combined with large subband separation and by the comparison with theoretical predictions. We note however that band to band transitions may still contribute to the fine structures of the spectra.

In Fig. 4.4, we indicated the positions of the calculated optical interband transitions. In order to compare the observed 1D excitonic transitions with the calculated interband transitions, we introduced a rigid redshift ($\sim$ 10 – 20 meV) of each series of optical transitions $e_n - h_m$. The overall agreement with the theoretical calculations is very good for all three investigated samples. Remaining differences may be attributed to slightly different wire cross section in the sample's piece used for the TEM study, to nonparabolicity of the conduction band and additional excitonic effects, which were not included. The binding energy of excitons is indeed expected to vary with the index of the subband [Rossi and Molinari, 1996b] but the magnitude of this change is small and believed to be comparable to the difference in binding energies of hh and lh excitons in quantum wells of similar thickness (2 to 3 meV) [Bauer and Ando, 1988] for the two lowest optical transitions.

The influence of the lateral confinement in the QWRs on the optical properties manifests itself by a linear-polarization dependence of the PLE spectra. Clear optical anisotropy in absorption is observed for all three samples. The effect is particularly pronounced for the 8.8 nm QWR and for the 14.1 nm QWR where a distinct crossing in the PLE spectra occurs for the second 1D excitonic transition when measured with orthogonal polarizations. This feature is less pronounced in the PLE spectra of the thinnest 4.1 nm QWR. The weakness of the optical anisotropy in the optical spectra of the 4.1 nm QWR is due to the fortuitous superposition of two optical transitions, $e_2 - h_2$ and $e_1 - h_7$. Within the framework of an adiabatic decoupling of the 2D-potential, this occurs when the transverse potential splits the first hh and lh subbands by an amount equal to the energy separating 1D-electron subbands imparted by the lateral potential.

The calculated squared optical matrix elements are displayed in Fig. 4.8 for all three QWR samples. All the main features of the experimental PLE spectra are remarkably reproduced in Fig. 4.8: The dominance of the diagonal optical transitions, $e_n - h_n$, in parallel and perpendicular polarizations is clearly evidenced; in parallel polarization transitions with non-conserving subband indices are strongly suppressed in the low energy part of the spectra whereas in perpendicular polarization the peaks labeled $e_1 - h_6$ in Fig. 4.8 (a) and Fig. 4.8 (b) and $e_1 - h_7$ in Fig. 4.8 (c) carry a significant oscilla-
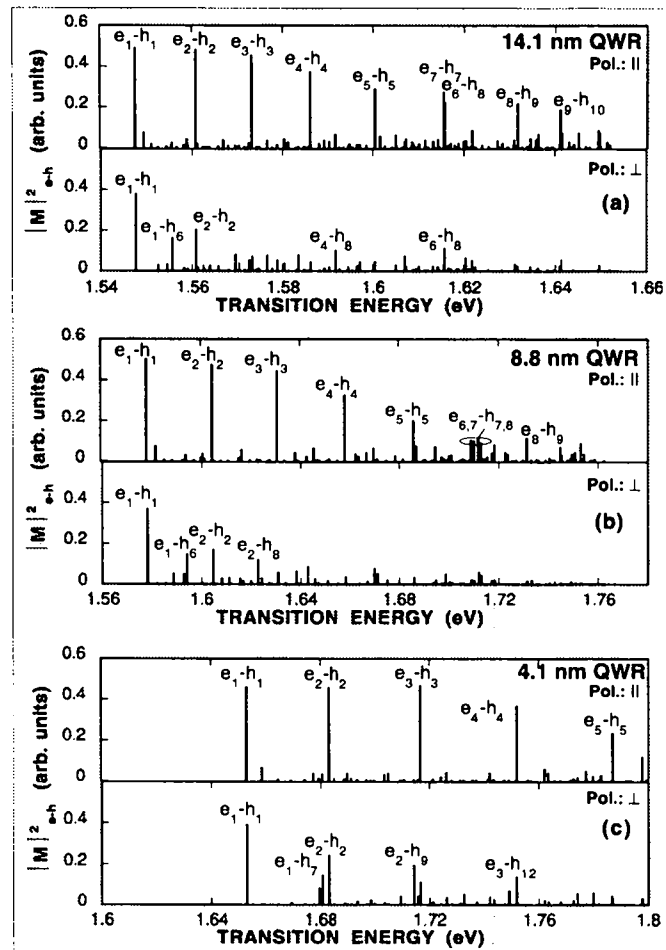
Figure 4.8: Square of the optical matrix elements for interband transitions $e_i - h_j (1 \leq i,j \leq 10)$ calculated at $k = 0$ for QWR samples with a GaAs thickness at the center of the crescent of a) 14.1 nm, b) 8.8 nm, and c) 4.1 nm (no adjustable parameters). Major transitions ($|M|^2_{e-h} > 0.1$) are labeled according to the indices of the participating electron and hole subbands.

tor strength resulting in a notable polarization anisotropy for the two larger QWRs. This latter feature, clearly visible in Fig. 4.4 (a) and Fig. 4.4 (b), originates from the contribution to the valence-subband of Bloch states having a dominant lh character [Bockelmann and Bastard, 1991, Citrin and Chang, 1991]. Indeed we find a value of 70% lh character for the n=6 valence state of the 14.1 nm and 8.8 nm QWR, and 71% lh character for the n=7 valence state of the 4.1 nm QWR (see Table 2.2).

Figure 4.9 shows the envelope functions of the lh-like *ground state* (h_6) in the 8.8 nm QWR. In fact, two maxima can be observed on the plot of the probability density of its lh constituent (h_6:lh in Fig. 4.9) because the mixing with higher order states results in a negative interference at the center. The ground state character is further confirmed by the fact that the two lobes oscillate *in phase* with each other. This state mainly couples to the $n = 1$ conduction subband due to a large overlap as can be seen in Fig. 4.8 (b).
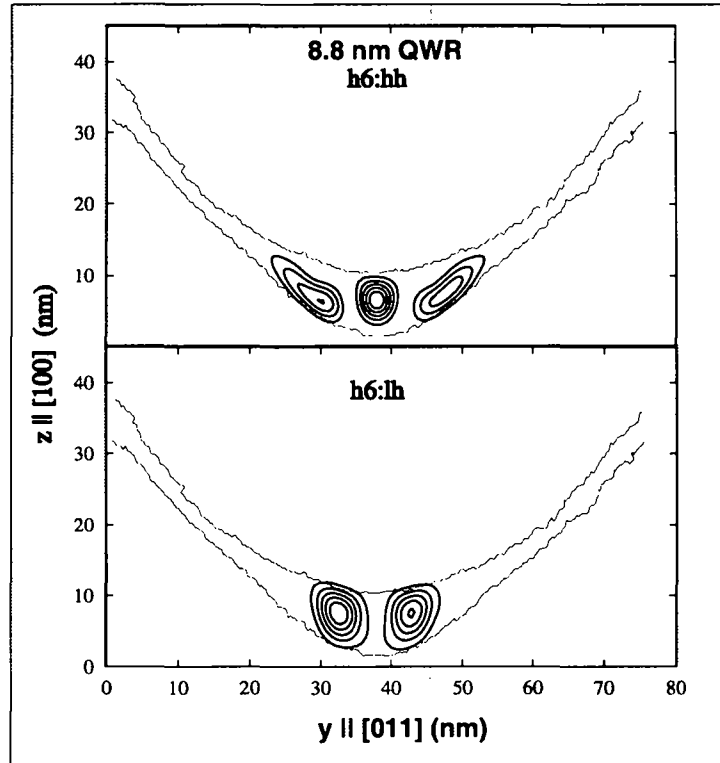
Figure 4.9: Confined zone-center hole states in the 8.8 nm QWR structure. The contours of the probability density are plotted for the h_6 state with its constituents of hh and lh. The wire cross section derived from a TEM micrograph and used in the calculation is also shown.

The wire cross section derived from a TEM micrograph and used in the calculation is also shown in Fig. 4.9. The fluctuations of the boundaries result from the digitalization of the TEM picture; they have no influence on the calculated wave functions. The $e_n - h_m$ transitions with $n > 6$ in Fig. 4.4 (a) and Fig. 4.4 (b) involve transverse electronic states. The corresponding electron wave functions exhibit a node along the growth axis at the centre of the QWR and mainly couple to hole states having similar transverse components. As a consequence, major transitions in this spectral region do not necessarily conserve subband indices.

We explain the circularly polarized PLE spectra of the three QWR samples as follows. In the energy range $E_{exc} < e_1 -$ "lh"$_1$ only electrons from the lowest valence subbands are excited to the conduction subband e_1. Here "lh"$_1$ refers to the first valence subband displaying a dominant lh character. Since the first valence subbands have a dominant hh character (see Table 2.2) the resulting $\mathcal{P}$ is positive, close to 35% at the $e_1 - h_1$ transition in the 4.1 nm and 8.8 nm QWRs and close to 50% in the 14.1 nm QWR. The deviation from a 100% polarization results on one hand from electron and hole spin relaxation and on the other hand from lh admixture in the h_1 wavefunction. For an excitation energy approaching the $e_1 -$ "lh"$_1$ transition, the electrons originating from

the valence subband with strong lh character start to contribute to the luminescence. These electrons are mainly created with $s = +\frac{1}{2}$ and are associated with a negative $\mathcal{P}$ at the $e_1 - h_1$ transition. As the first valence subbands contribute to a positive $\mathcal{P}$, the JDOS for the transition $e_1 - \text{``lh''}_1$ has to be very high to compensate for it giving rise to a decrease in $\mathcal{P}$ [2]. This is further supported by our calculation of the valence band structure: A negative "lh" mass at the center of the Brillouin zone is found in all the QWRs investigated (e.g. see Fig. 2.4 (b)). This effect explains the pronounced dip located at the $e_1 - \text{``lh''}_1$ transition in the polarization spectrum of Fig. 4.4 (b). As the excitation energy increases, the JDOS for the $e_1 - \text{``lh''}_1$ transition falls down and the net polarization increases again. For still higher excitation energies ($E_{exc} > e_1 - \text{``lh''}_1$) electrons from other valence subbands also appear in the conduction subbands. Because the depolarization increases with the kinetic energy of photocreated electrons [Twardowski and Hermann, 1987], these electrons will only weakly contribute to the polarization and, thus, the circular polarization curve features only small amplitude modulations for optical transitions $e_n - h_n$ with $n > 2$.

4.6 Summary

We have studied the optical properties of high quality V-groove $GaAs/Al_{0.3}Ga_{0.7}As$ QWRs with three different thicknesses of the GaAs layer. The systematic investigation of PL and PLE spectra as a function of the wire size combined with model calculations has allowed us to study in detail the effect of two-dimensional quantum confinement on valence band mixing and polarization anisotropy. We have shown that the polarization anisotropy of PL spectra critically depends on localization effects thus making any polarization analysis based on extended states insufficient. The influence of exciton localization and surface corrugation on PLE spectra has also been clarified; the observed large polarization anisotropy has been unambiguously related to the one-dimensional character of our QWRs. Comparison of the experimental results obtained for all three QWR samples with theoretical predictions is clearly compatible with the strong suppression of the 1D band-edge singularity in PLE spectra.

---

[2]Although PLE spectra are dominated by excitonic peaks, band-structure effects are expected to modify the absorption intensity: An exciton formed with a hole subband having an electronlike curvature will correspond to a small exciton Bohr radius, which in turn is related to a high oscillator strength (see also Sec. 3.3.2).

Chapter 5

Temperature dependence of optical properties

5.1 Introduction

The majority of the optical experiments carried out on low-dimensional structures in the past two decades were made at low temperature (T < 30 K). The optical properties at higher temperature, where nonradiative processes usually become significant, are more important from the application point of view; they also reveal phonon coupling effects. Few papers have reported on the temperature dependence of optical processes in QWRs. The temperature dependence of the photoluminescence intensity of strain-confined GaAs/AlGaAs QWRs has been studied up to ~ 80 K [Zhang et al., 1995]; the quantum efficiency has been found to be not only comparable to that of the host QWs at low temperature, but also to persist over the whole temperature range [Zhang et al., 1994]. Photoluminescence spectra of V-groove QWRs have been investigated from 10 K up to room temperature [Wang et al., 1995]; the relatively small linewidth (~ 18 meV for an excitation density ~ 5 W/cm^2) at the highest temperatures was attributed to the specific shape of the 1D density of states. In V-groove QWRs, time-resolved experiments at low temperature have already shown the predominant role of carrier transfer from the VQW into the wire region [Walther et al., 1992]. The impact of the side- and of the vertical-QWs on the temperature dependence of the PL intensity in such QWRs is, however, not clear yet. Another important issue in such structures is the localization of excitons, since interfaces roughness is unavoidable. At low temperatures, localization causes a Stokes shift and affects the free-exciton radiative decay time [Gershoni et al., 1994, Akiyama et al., 1994a, Akiyama et al., 1994b, Zhang et al., 1995]. Moreover, the influence of disorder on the radiative lifetime of excitons in V-groove QWRs has been found to be crucial up to 150 K [Oberli et al., 1998]. The temperature dependence of PLE spectra for various wire sizes has never been stud-

ied, to the best of our knowledge. Furthermore, the role of localization on the shape of PL and PLE spectra at relatively high temperature has not been evaluated yet.

In this chapter,PL and PLE spectra are studied as a function of temperature (up to 300 K for the PL) and wire thickness (4.1 nm, 8.8 nm, and 14.1 nm QWRs). In particular, we investigate the role of disorder on the evolution of the PL *and* PLE line shapes. The interaction of 1D excitons with phonons is also discussed.

5.2   Experimental

The experiments were performed on the 4.1 nm, 8.8 nm, and 14.1 nm QWRs. The optical spectra were obtained in a pseudo-bascattering geometry from the (100) plane using polarized light from an Ar^+ laser (514.5 nm) or from a HeNe laser (632.8 nm) for the PL measurements and from a tunable Ti:Sa laser for PLE experiments. The excitation light was focussed into a spot approximately 35 μm in diameter; typical power densities of 25 W/cm^2 were used. For linear polarization measurements, perpendicular (parallel) refers to the [011] ([01$\bar{1}$]) direction. The spectral resolution was fixed at 4 Å. The samples and the experimental techniques are described in detail in Chap. 3.

5.3   Temperature dependence of photoluminescence

In Fig. 5.1, Fig 5.2, and Fig. 5.3, we display PL spectra of the 4.1 nm, 8.8 nm, and 14.1 nm QWR samples, respectively, as a function of the lattice temperature. Extended PL spectra showing the luminescence of the different parts of the structure are displayed in part (a) of each figure, while PL spectra restricted to the spectral region of the wire luminescence are depicted in part (b). The main spectral features associated with the different parts of the structures are identified (see section 4.3.1 for the assignments). For all three QWR samples, the evolution of PL spectra with increasing temperature clearly shows the progressive extinction of the QWs luminescence, while the PL originating from the wire region persists up to room temperature. At low temperature, the potential barrier V_0 due to the necking between the QWRs and the side-QWs (see TEM pictures in section 3.2.2) prevents efficient carrier transfer from the 2D regions into the wires. The transfer efficiency varies with the wire size, as shown by the different relative intensities of the QWR and QW peaks for each sample. We can distinguish between different transfer processes, as illustrated in Fig. 5.4 [Kapon, 1994]. Carrier transfer from the VQW into the QWR is very efficient as there is no potential barrier between the two regions [Walther et al., 1992, Samuelson et al., 1995, Haacke et al., 1996, Kiener et al., 1996]. Carrier capture may take place directly from the barrier or from the side-QWs if the energy of the carriers is greater than V_0. Tunneling transfer occurs when the exciton
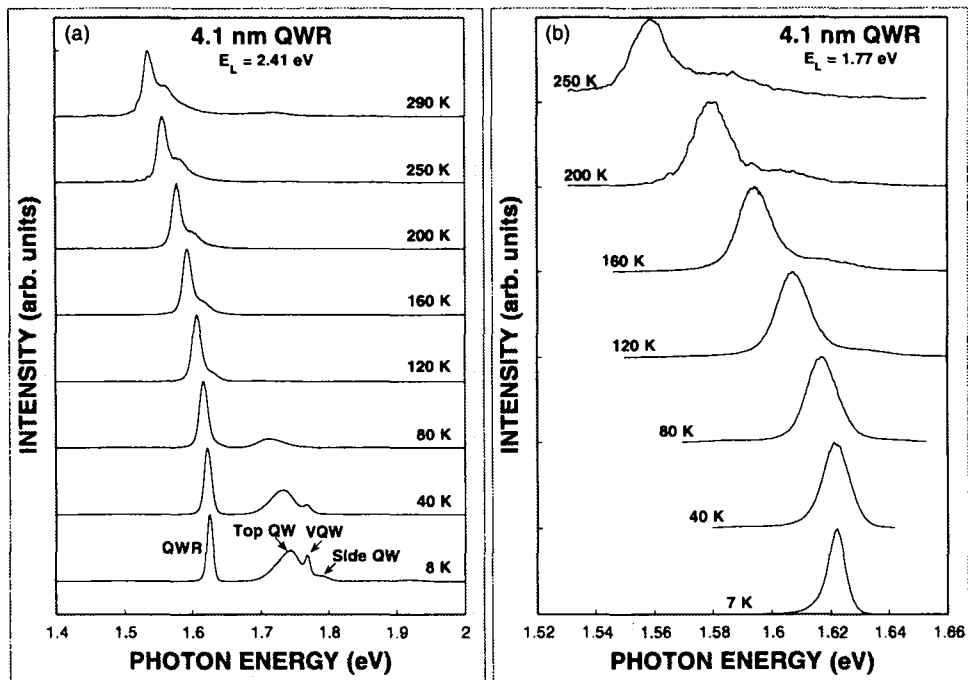
Figure 5.1: Temperature dependence of the PL spectra of the 4.1 nm QWR sample. (a) Excitation in the AlGaAs barrier material, $E_L = 2.41$ eV; (b) excitation below the bandgap of the AlGaAs barrier, $E_L = 1.77$ eV.
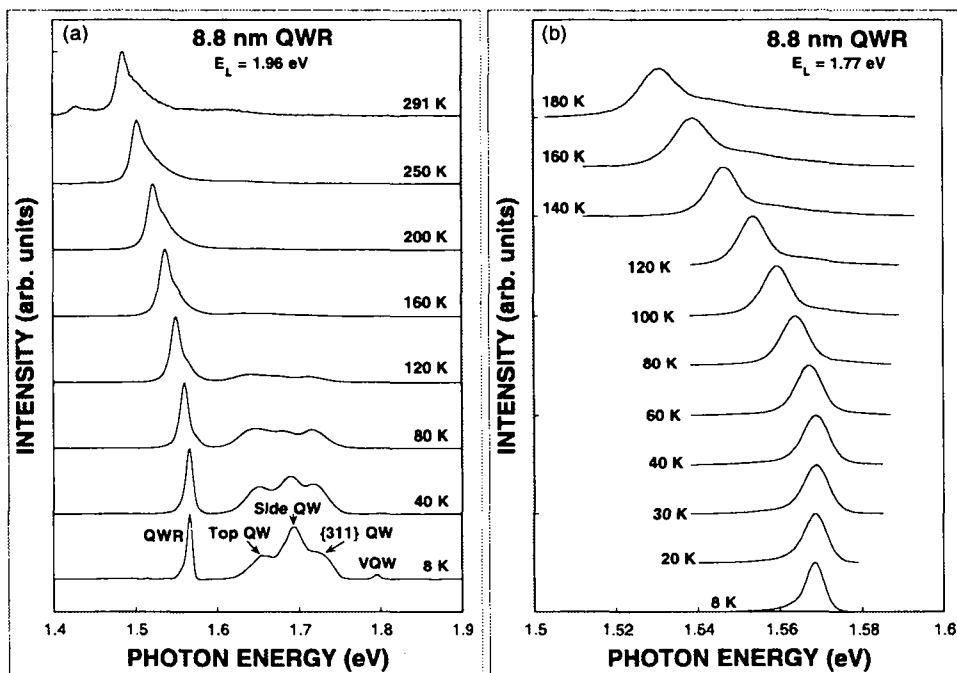
Figure 5.2: Temperature dependence of the PL spectra of the 8.8 nm QWR sample. (a) Excitation in the barrier material, $E_L = 1.96$ eV; (b) excitation below the energy of the barrier, $E_L = 1.77$ eV.
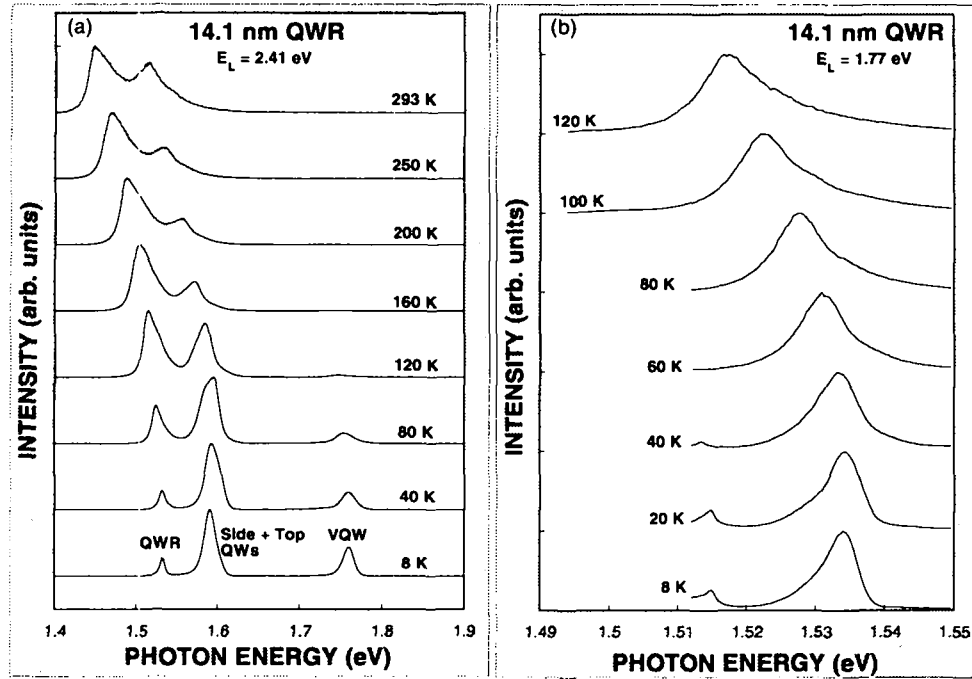
Figure 5.3: Temperature dependence of the PL spectra of the 14.1 nm QWR sample. (a) Excitation in the barrier material, $E_L = 2.41$ eV; (b) excitation below the energy of the barrier, $E_L = 1.77$ eV.
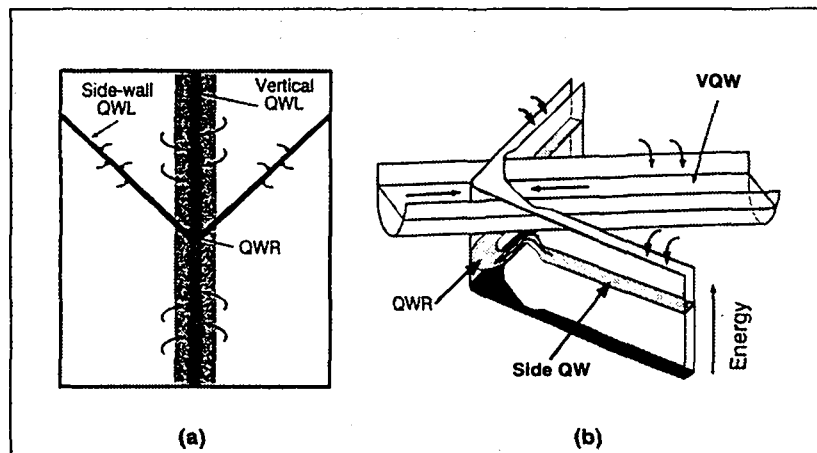
Figure 5.4: QW-assisted carrier capture in our QWR structures: (a) cross section and (b) schematic of the (e.g., conduction) band structure. The outer edges of the structure in (b) represent the band edge of the barrier material, and the arrows indicating the various QW/QWR regions point to the quantum-confined energy levels [Kapon, 1994].

energy is smaller than V_0, and classical activation transfer is due to thermal activation above V_0.

All PL peaks are seen to shift to lower energies with increasing temperature due to the reduction of the GaAs energy gap. Figure 5.5 shows the temperature variation of the integrated luminescence intensities for the three QWR samples. The luminescence
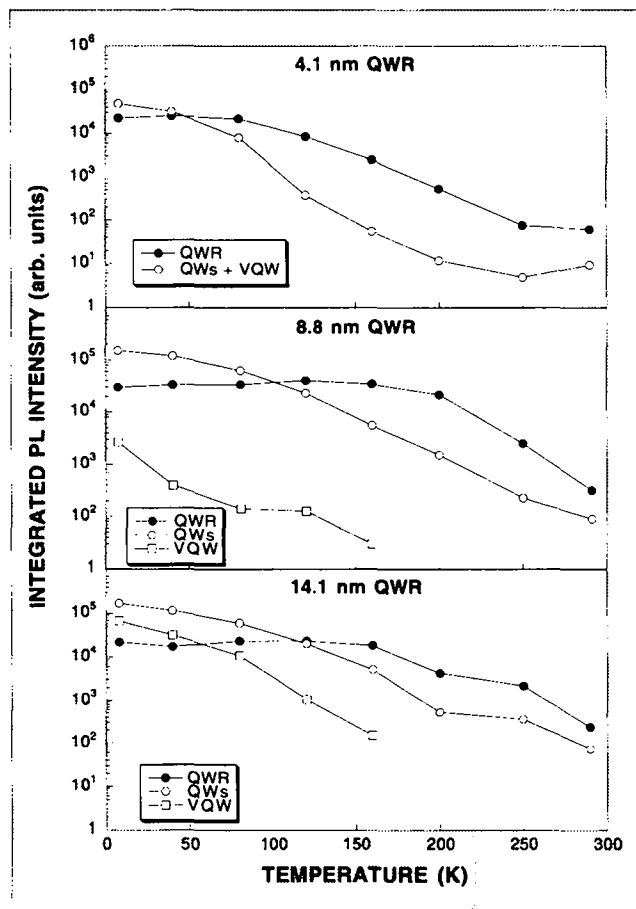
Figure 5.5: Temperature dependence of the integrated QWR and QW PL intensity for the three QWR samples. In the case of the 8.8 nm QWR and of the 14.1 nm QWR structures, "QWs" stands for luminescence spectrally situated between the QWR and the VWQ peaks.

intensity of all QW layers drops with increasing temperature. In contrast, the QWR intensity slowly increases with a maximum around 50 K for the 4.1 nm QWR sample and around 120 K for the 8.8 nm and 14.1 nm QWR samples. The exciton lifetime in QW structures has been found to increase with temperature for $T < 100$ K and well thicknesses in the range $4 - 15$ nm [Hillmer et al., 1989]. Assuming this behavior to be similar for smaller QW thicknesses, the observation of the monotonic decrease of the QW intensity together with the increase of the QWR intensity indicates a more efficient carrier transport from the wells towards the QWR. An asymmetric shape of the
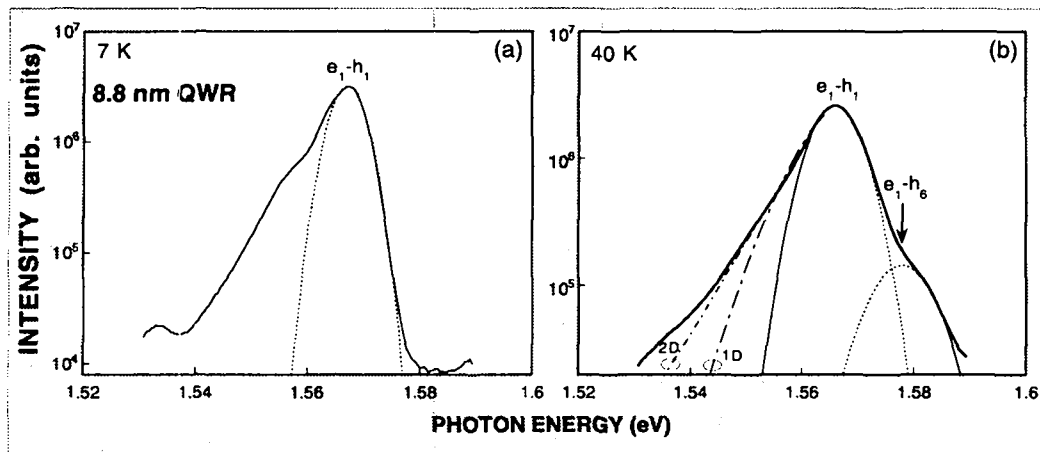
Figure 5.6: Luminescence peak of the 8.8 nm QWR at (a) 7 K, and (b) 40 K. The dotted line represents in (a) a single Gaussian fit, and in (b) a fit with two Gaussians of fixed positions. The superposition of the two Gaussians in (b) yields the solid (thin) line. The dashed line in (b) is a fit following the Urbach rule with $d = 1$, while the dotted-dashed line is obtained with $d = 3/2$.

QWR luminescence peak is clearly observed at all temperatures and for all three wire samples. At low temperatures the low energy tail of the QWR peak distincly departs from a gaussian lineshape while the high energy tail follows a gaussian distribution over two orders of magnitude. Figure 5.6 (a) illustrates this observation for the 8.8 nm QWR at 7 K. These results contrast with line-shape analysis of QW luminescence that showed a high energy Boltzmann tail attributed to partial non-K-conservation [1] [Christen and Bimberg, 1990, Schnabel et al., 1992]. Figure 5.6 (b) shows the luminescence peak at 40 K. Thermally activated population of the lh-like exciton subband is clearly visible and we find that the high energy tail of the PL peak is well fitted by a superposition of Gaussians with fixed positions at the energies of the $e_1 - h_1$ and $e_1 - h_6$ transitions deduced from PLE spectra. Small scale disorder is known to modify the density of states of semiconductors and to introduce an exponential relationship between the low-energy tail of the fundamental exciton absorption line and the photon energy, known as the Urbach tail [Soukoulis et al., 1984]. The energy dependence of this tail is written as:

$$F(E) \propto \exp\left(-\sigma \frac{(E_0 - E)^d}{k_B T}\right),$$

where E_0 is the energy of the exciton transition, $d = 1$ for 3D and 2D systems, and $d = 3/2$ for 1D systems [Schreiber, 1986]. Theoretical fits based on the Urbach rule are depicted on the low energy tail of the peak. Suprisingly, the fit with $d = 3/2$ completely fails whereas fairly good agreement is obtained with $d = 1$.

---

[1] K is the center-of-mass momentum of the 2D excitons.
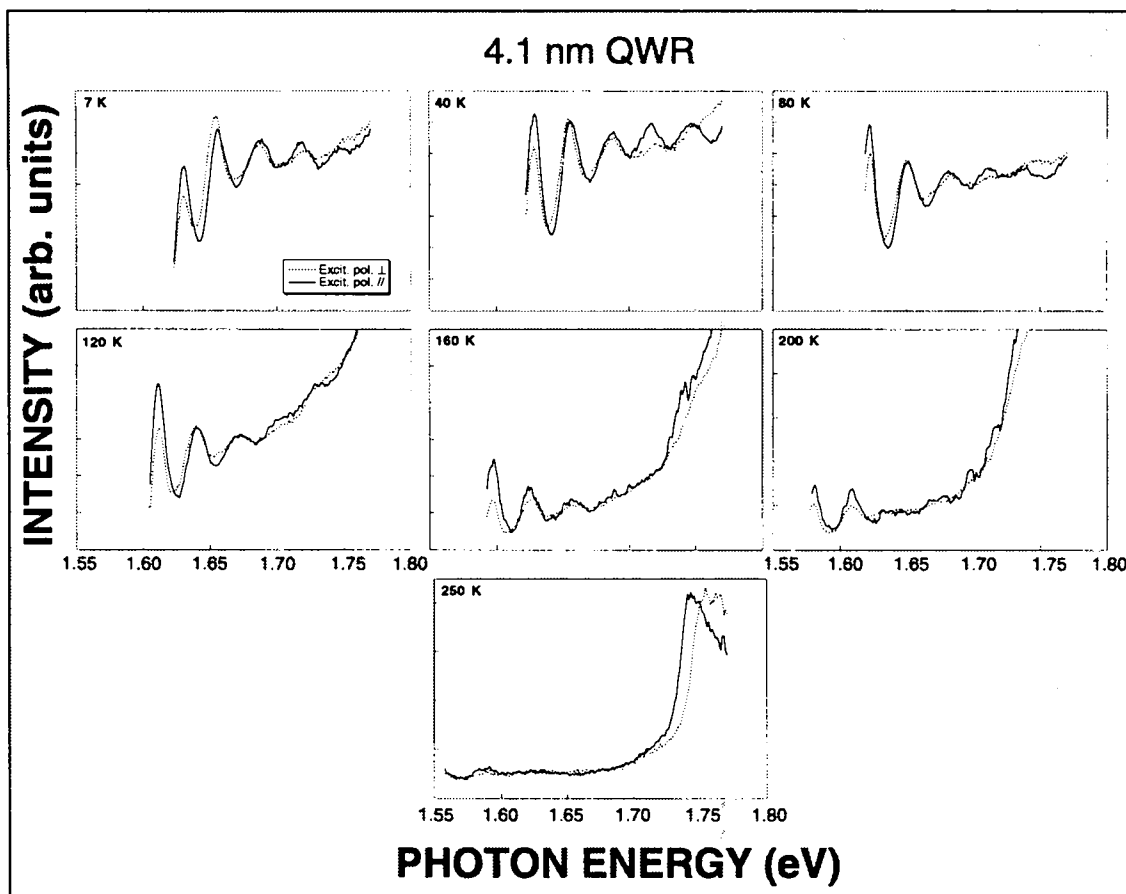
Figure 5.7: Temperature dependence of the PLE spectra of the 4.1 nm QWR.

5.4   Temperature dependence of photoluminescence excitation

The linearly polarized PLE spectra of the 4.1 nm, 8.8 nm, and 14.1 nm QWR samples as a function of the lattice temperature are shown in Fig. 5.7, Fig. 5.8, and Fig. 5.9, respectively. High quantum efficiency, small inhomogeneous broadening, and large subband separation allow us to observe 1D PLE resonances up to 200 K for the 4.1 nm QWR, 180 K for the 8.8 nm QWR, and 100 K for the 14.1 nm QWR. As already observed for PL spectra, all PLE peaks are seen to shift to lower energies with increasing temperature due to the decreasing GaAs band gap. We notice that the relative intensity of the first PLE peak with respect to the other peaks increases with increasing temperature for the 4.1 nm and 8.8 nm QWRs. A similar behavior has been reported in section 4.4.3 when moving the detection wavelength across the PL line at low temperature. This temperature dependence of the PLE line-shape is attributed to the impact of disorder and localization effects. The temperature dependence of PL spectra (see preceding section) has highlighted the thermally enhanced transfer of carriers from the side QWs into the
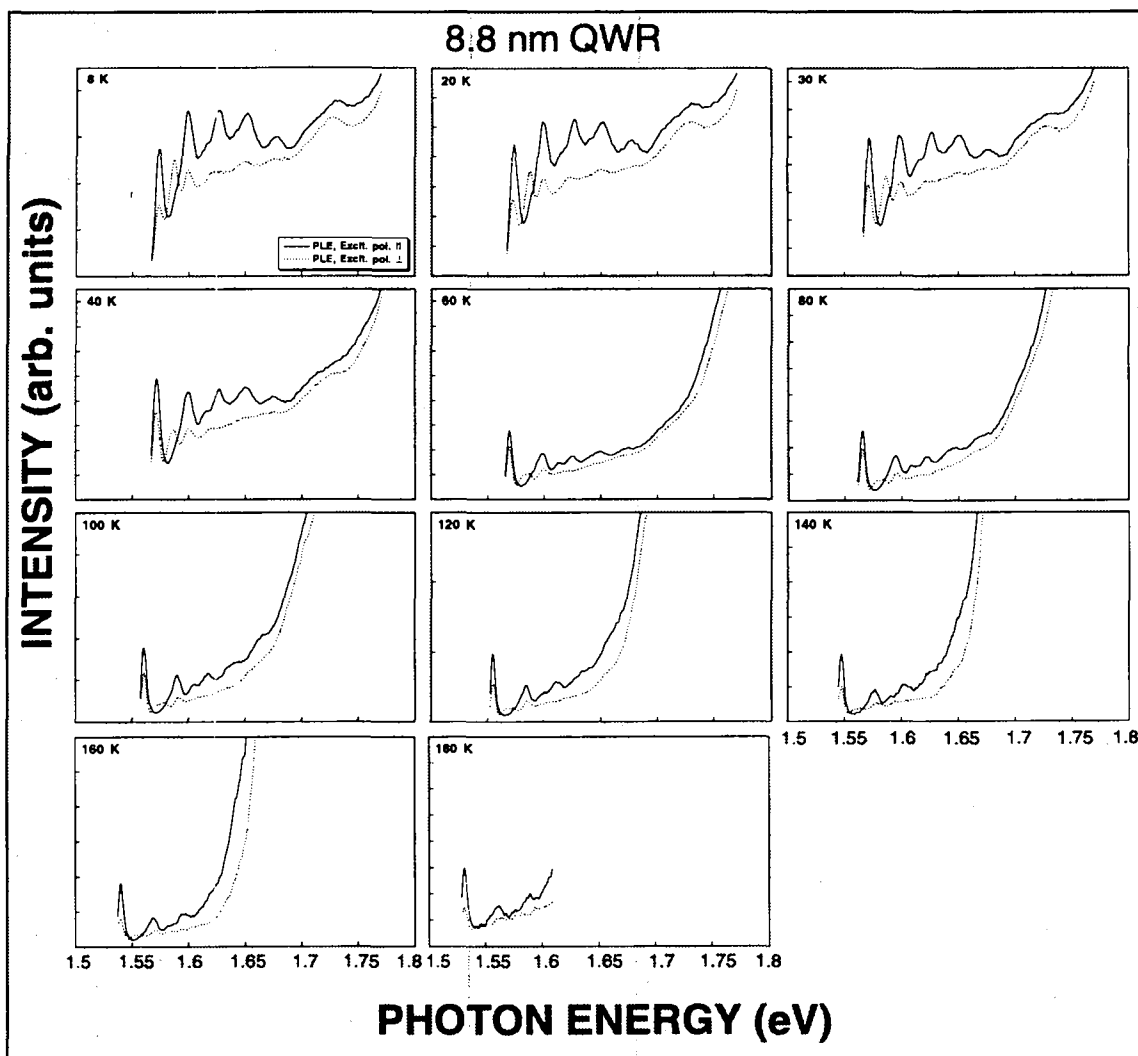
Figure 5.8: Temperature dependence of the PLE spectra of the 8.8 nm QWR.

wire. This effect is also clearly seen on the temperature dependent PLE spectra: An increased absorption is observed for all three wire samples at high photon energies and at sufficiently high temperature. For example, a steep increase of the PLE intensity for the 8.8 nm QWR is found at 100 K for photon energies greater than 1.65 eV; this increase of the absorption gets even more pronounced at higher temperatures.

5.5   Temperature dependence of photoluminescence and photoluminescence excitation linewidths

We show in Fig. 5.10 the FWHM of the first subband contribution to PL and PLE spectra. The PL FWHM was determined by fitting the QWR peak with a superposition of Gaussians, the number of which increases with temperature as a consequence of the thermal population of higher subbands. This situation is illustrated in Fig. 5.6 (b)
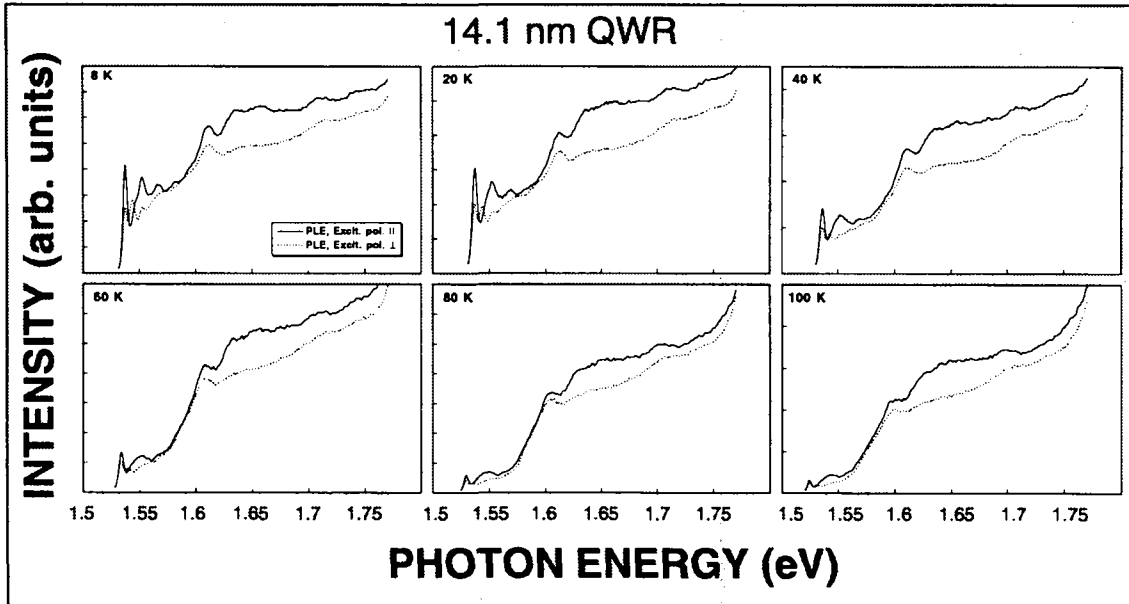
Figure 5.9: Temperature dependence of the PLE spectra of the 14.1 nm QWR.

which shows on the high energy side of the 8.8 nm QWR peak a contribution due to the optical transition $e_1 - h_6$. For all three wire samples, the position of the Gaussians was fixed during the fitting procedure and was determined by the energy separation between the $e_1 - h_1$, $e_1 - h_6$, and $e_2 - h_2$ transitions measured on PLE spectra. Similarly, the PLE FWHM was determined by fitting the first three PLE peaks with a superposition of Gaussians. At high temperatures ($T > 80$ K), an exponential tail corresponding to the contribution of the QW luminescence was removed from the 14.1 nm QWR PL to better determine the FWHM of the 1D transitions. The PL FWHM (Γ^{PL}) for the 4.1 nm and the 8.8 nm QWRs first increases with increasing temperature and then stabilizes around a constant value ($\Gamma^{PL} \sim 15$ meV for the 4.1 nm QWR, $\Gamma^{PL} \sim 12$ meV for the 8.8 nm QWR). The PL linewidth for the 14.1 nm QWR is more difficult to evaluate due to the much smaller subband spacings; therefore, we restricted the fit procedure to a temperature range ($T < 160$ K) where unambiguous values of Γ^{PL} have been obtained. Over this temperature range, Γ^{PL} was found to increase from ~ 6.5 meV up to ~ 12 meV. The PLE FWHM of the two thinnest QWRs first increases with increasing temperature to reach a maximum around 40 K for the 4.1 nm QWR (20 K for the 8.8 nm QWR), then decreases over the range 40 − 80 K (20 − 100 K for the 8.8 nm QWR), and finally increases with a very small slope. For the 14.1 nm QWR, Gaussian fits yielded FWHM in the range 4 − 4.5 meV for all temperatures investigated.
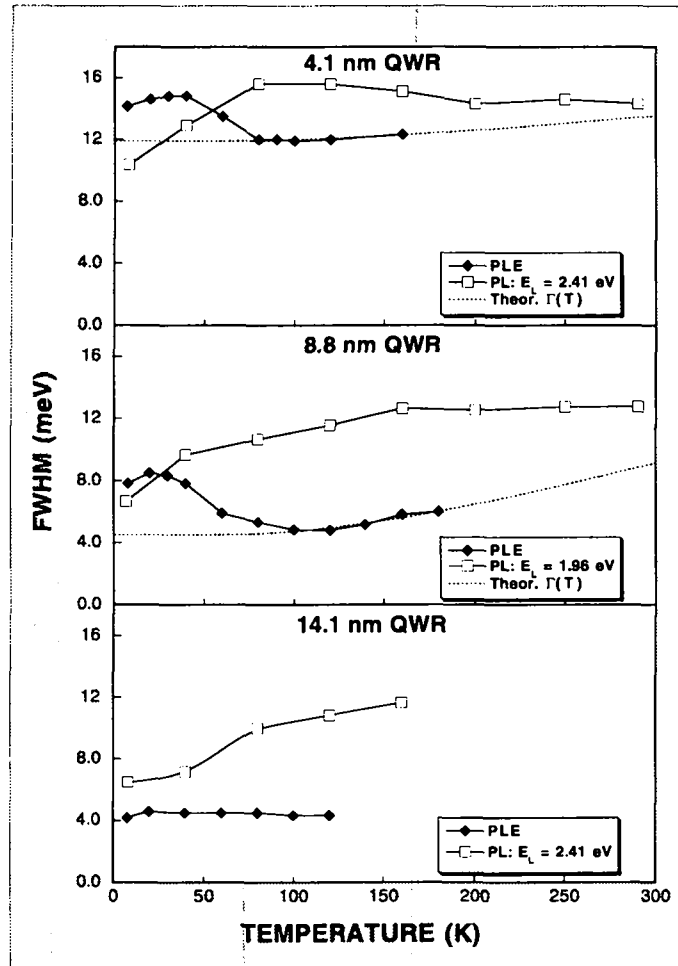
Figure 5.10: Temperature dependence of the full width at half maximum (FWHM) of the first subband contribution to PL and PLE spectra for the 4.1 nm, 8.8 nm, and 14.1 nm QWR structures. The excitation power density is ~ 50 W/cm^2. Dotted lines for the two upper plots represent theoretical fits of $\Gamma(T)$ with a temperature dependence given by Eq. 5.1 and values of γ_{opt} given by Eqs. 5.3 (see discussion in Sec. 5.7).

5.6 Temperature dependence of the energy Stokes shift

Figure 5.11 displays the position of the QWR luminescence peak and that of the lowest-energy PLE peak as a function of temperature. Solid lines on the figure represent the temperature dependence of the energy band gap of GaAs; they are shifted to take into account the confinement energy of the three QWRs and are adjusted to fit the PL peak position at high ($T > 200$ K) temperature. At low temperature, the energy positions of both PL and PLE peaks are seen to lie below the shifted band gap. As the temperature is increased, the Stokes shift progressively decreases and vanishes at a thermal energy which is significantly larger than its magnitude at 8 K. At the same time, the energy
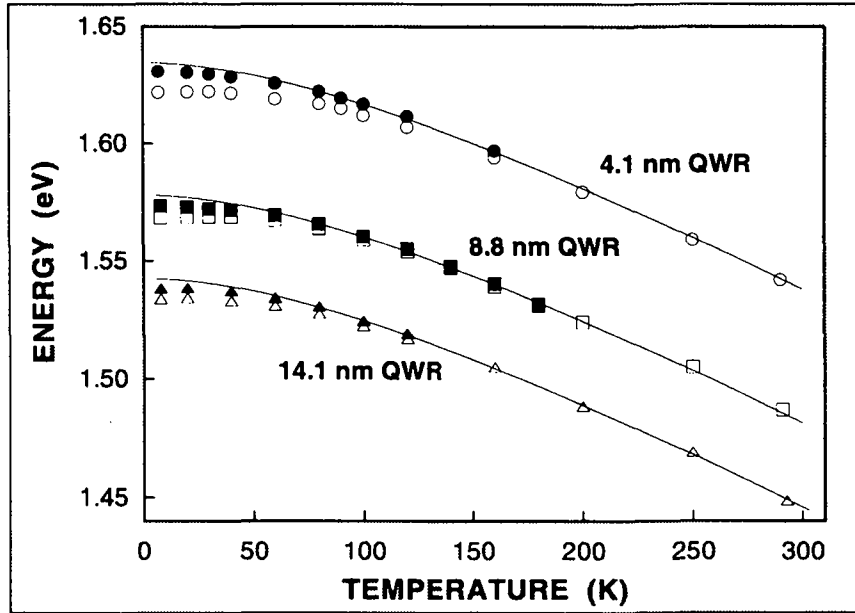
Figure 5.11: Temperature dependence of the PL (open symbols) and PLE (solid symbols) peak position. Solid lines represent the temperature dependence of the energy band gap of GaAs and are shifted to take into account the confinement energy of the three QWRs.

Table 5.1: Stokes shift at 8 K and temperatures T_0 corresponding to a vanishing Stokes shit.

QWR	Stokes shift (8 K)	T_0	$k_B T_0$
4.1 nm	8.5 meV	~ 160 K	~ 14 meV
8.8 nm	5.1 meV	~ 120 K	~ 10 meV
14.1 nm	3.6 meV	~ 120 K	~ 10 meV

position of the PL peak and that of the lowest-energy PLE peak start to follow the temperature dependence of the GaAs band gap. The values of the Stokes shift at 8 K and the approximate values of the temperature T_0 at which it disappears are reported in table 5.1 for all three QWR samples. This vanishing Stokes shift reflects the thermally induced redistribution of excitons from localized states to extended states. Localization of excitons results from fluctuations of the confining potential along the wire axis caused by interface roughness and possibly alloy fluctuations (see chapter 6). Therefore, our results indicate that there is no simple relationship between the value of the Stokes shift at 8 K and the energy related to the localization potential.

5.7 Discussion

Detailed analysis of GaAs QWs have highlighted the influence of exciton localization on recombination line shapes [Colvard et al., 1989, Christen and Bimberg, 1990, Schnabel et al., 1992]. Due to localization the exciton center of mass wave vector K no longer represents a good quantum number, and the $K = 0$ selection rule for optical recombination may be violated. Not only excitons with vanishing wave vector will recombine, but a statistical distribution with a finite width around the $K = 0$ state contributes to the emission spectrum [Schnabel et al., 1992]. Additionally, the potential fluctuations give rise to a broadening in energy. The resulting line shape is asymmetrically shaped, displaying Gaussian and nearly exponential slopes on the low- and high-energy side, respectively. This exponential behavior of the high-energy tail of the PL line has effectively been observed in GaAs/AlGaAs QWs [Colvard et al., 1989, Christen and Bimberg, 1990, Schnabel et al., 1992]. In contrast, the high-energy side of PL spectra for all three QWR structures are very well fitted by single Gaussians at low temperature and by a superposition of Gaussians when excited subbands are thermally populated. This observation may indicate that the effect due to the relaxation of the K selection rule is much smaller than the inhomogeneous broadening in our structures.

Modelling of the low-energy tail of the PL line in low-dimensional semiconductors has received much less attention. However, it has been already shown that localization strongly influences the low-energy side of the PL spectrum in 2D structures [Hegarty et al., 1984]. In bulk material, delocalized and localized states with infinite and finite localization length, respectively, are energetically separated by a sharp boundary, the so-called mobility edge [Abrahams et al., 1979]. The concept of the mobility edge has also been applied to the behavior of 2D excitons [Hegarty et al., 1984, Wang et al., 1990]. From a theoretical point of view, localized states and the position of the mobility edge are found in the low-energy part and near the center of the exciton spectrum, respectively [Kavokin, 1994]. More recent experimental and theoretical considerations have demonstrated that the concept of an effective mobility edge for the exciton motion in 2D systems is applicable [Jahn et al., 1997]. In particular, Jahn et al. (1997) have shown that the effective mobility edge exhibits a shift towards the high-energy side of the exciton spectrum in a strongly disordered system. Similarly, we believe that localized exciton states dominate the low-energy side of our QWR luminescence lines. This expectation is fully corroborated by the observation of low-energy tails that clearly depart from Gaussian distributions. We noted that our spectra do not follow the modified Urbach rule proposed by Schreiber (1986) for 1D systems. However, this modified Urbach rule was only based on calculation of the den-
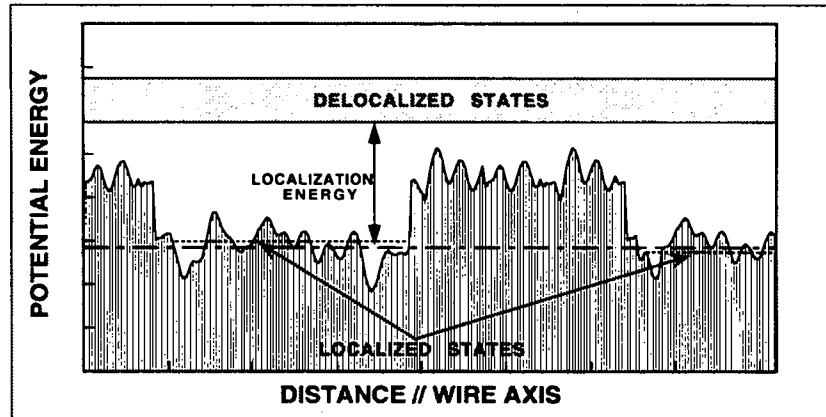
Figure 5.12: Schematic representation of the longitudinal potential. Dotted lines represent ground state energies for different localization sites. The dotted-dashed line represents an average value of these energies. The difference between this average energy and the lowest energy corresponding to a delocalized state defines a mean *localization energy*.

sity of states and was intended to describe absorption tails in disordered 1D structures. Modelling of the luminescence spectrum is much more difficult as both the occupation factor and the probability of transition have to be taken into account for a correct description of the line shape. To the best of our knowledge, none of the present theoretical treatments of low-dimensional structures predicts the exponential low-energy tail that we systematically found for our QWRs.

The considerable impact of disorder on PL spectra is also evidenced by the temperature dependence of the QWR peak position. The position of the PL peak for all three QWR samples lies below the curve representing the shifted GaAs band gap, clearly indicating localization of excitons in local potential minima. The position of the PL peak recover the temperature dependence of the band gap at $\sim$ 160 K for the 4.1 nm QWR, $\sim$ 120 K for the 8.8 nm QWR, and $\sim$ 120 K for the 14.1 nm QWR, when delocalized exciton states start to dominate the PL spectra. Exciton binding energies E_b in our structures are on the order of 15 meV for the 4.1 nm QWR, 12 meV for the 8.8 nm QWR, and 9 meV for the 14.1 nm QWR [Rossi et al., 1997]. We define a localization energy for each structure as the difference between the energy of delocalized states and a mean value of the ground state energy of localized states (see Fig. 5.12). If the shifted GaAs band gap were adjusted at high temperature to band-to-band transitions, the energy difference between this shifted curve and the QWR peak at 8 K should correspond to the sum of the localization energy and of the exciton binding energy. However, this energy difference is smaller than the estimated exciton binding energy for all three QWRs. This observation indicates that the shifted band gap is adjusted to *excitonic recombination up to room temperature*. Furthermore, this

Table 5.2: Localization energy (energy difference between PL peak position and shifted band gap) at 8 K and temperatures T' at which the PL position starts to follow the GaAs band gap.

QWR	Localization energy (8 K)	T'	$k_B T'$
4.1 nm	13 meV	$\sim$ 160 K	$\sim$ 14 meV
8.8 nm	9.5 meV	$\sim$ 120 K	$\sim$ 10 meV
14.1 nm	9 meV	$\sim$ 120 K	$\sim$ 10 meV

result suggests that the energy difference between the PL peak position at 8 K and the shifted band gap represents the localization energy defined above. This interpretation is fully corroborated by the temperature dependence of the PL: The temperature T' at which the PL peak position starts to follow the shifted band gap closely corresponds to the localization energy for all three wire samples, as shown in table 5.2. Obviously, $T' \equiv T_0$, where T_0 has been defined previously as the temperature of a vanishing Stokes shift. Our interpretation of PL spectra in terms of excitonic transitions is supported by experimental studies in GaAs QWs that evidenced the dominance of excitonic recombination up to $\sim$ 300 K [Christen and Bimberg, 1990, Colocci et al., 1990] and by theoretical considerations on the enhancement of electron-hole correlation in QWRs [Rossi and Molinari, 1996a]. Further corroboration is obtained by the analysis of PLE spectra that do not exhibit new transitions on the high-energy side of the excitonic peaks with increasing temperature. Finally, good fits of the PL line shape are obtained with a superposition of finite number of Gaussians up to room temperature, which also indicates the excitonic nature of the luminescence. Indeed, band-to-band recombination would manifest the 1D joint density of states (JDOS) with a $1/\sqrt{E}$ dependence on the high-energy side of the optical transitions. Therefore, we believe that the argument of the JDOS used by Wang et al. (1997) to explain the small FWHM found at room temperature for V-groove QWRs is not appropriate.

The nature of the optical transitions that appear on the high-energy side of the QWR PL peak with increasing temperature is confirmed by a polarization analysis of the luminescence, as illustrated in Fig. 5.13. The pronounced dip in the curve corresponding to the degree of linear polarization corresponds to the first transition involving the valence subband with strong lh character (see section 4.4). A perfect agreement with the energy difference of optical transitions measured on PLE spectra at low temperature is obtained [2].

---

[2] This result is in striking contrast with high densities experiments for which the energy separation between the lowest optical transitions is systematically found to be larger than the energy difference of the optical transitions measured on PLE spectra [Ambigapathy et al., 1997].
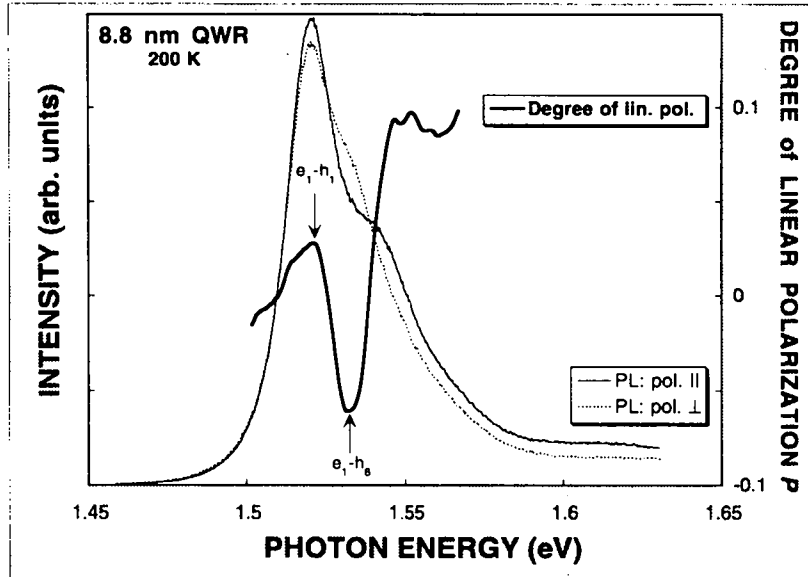
Figure 5.13: PL spectrum of the 8.8 nm QWR at 200 K. The linear polarization of the luminescence was analyzed parallel $(I_{//})$ and perpendicular $(I_\perp)$ to the wire axis. The degree of linear polarization $P = (I_{//} - I_\perp)/(I_{//} + I_\perp)$ is also shown. The optical transitions measured on PLE spectra at low temperature are indicated by arrows; a rigid shift was introduced to adjust the $e_1 - h_1$ transition to the PL maximum.

The impact of disorder on the optical properties of our QWRs is also reflected in the temperature dependence of PLE spectra. Localization effects are evidenced both by the temperature dependence of the lowest-energy PLE peak position and by that of the PLE FWHM. The position of the $e_1 - h_1$ transition is found to lie below the curve representing the shifted GaAs band gap, as for the case of the QWR PL peak, up to about 60 − 80 K. Over the same temperature range, the FWHM of the PLE spectra for the 4.1 nm and 8.8 nm QWRs display an unexpected and non-monotonic behavior. We believe that, at low temperature, localization effects prevent the observation of the actual absorption linewidth as recently reported by Jahn et al. (1997) for the case of GaAs QWs. Actually, they showed that the shape and the width of the hh PLE lines were strongly modified by effects related to disorder. For exciton energies below the effective mobility edge, excitons can not be transferred easily from the excited states in the high-energy regions to the detection states in the low-energy regions of the QW giving rise to a suppression of the hh PLE signal [Jahn et al., 1997]. These effects yield both a weakening and a broadening of the hh PLE line with respect to the lh PLE line [Jahn et al., 1997]. The decrease of the PLE FWHM of our QWR structures with increasing temperature and the enhancement of the lowest-energy PLE peak with respect to the other peaks are consistent with this interpretation. Indeed, acoustic-phonon absorption is expected to increase the migration of excitons among localization
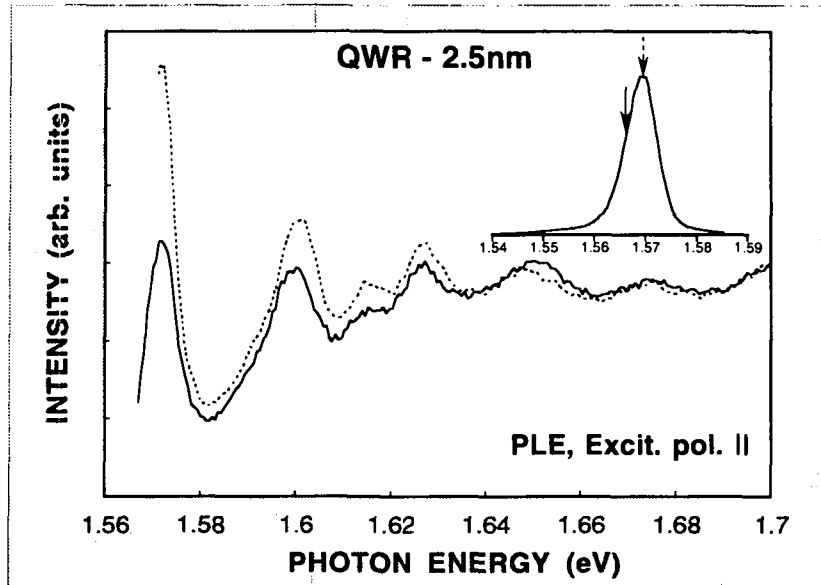
Figure 5.14: PLE spectra of the 8.8 nm QWR at 40 K measured for different detection energies. The polarization of the exciting light is parallel to the wire axis. A clear enhancement of the $e_1 - h_1$ transition is observed for a higher detection energy.

sites for increasing temperatures [Wang et al., 1990]. This process allows the excitons to relax to the detection energy and the PLE spectrum progressively acquires a shape that is not influenced by trapping effects. Therefore, we believe that the linewidth and the magnitude of the PLE peak for the 4.1 nm (8.8 nm) QWR are close to the values expected for a true absorption experiment when the temperature is above ~ 80 K (~ 100 K).

We further demonstrated the impact of disorder on PLE spectra at 40 K by measuring PLE spectra for two different detection positions on the PL line of the 8.8 nm QWR (see Fig. 5.14). A clear enhancement of the $e_1 - h_1$ transition is observed for a higher detection energy, as observed at lower temperatures (see section 4.4.3). We note that the presence of unintentional p-background doping in our structures ($\sim 5 \times 10^{16}$ cm^{-3} in the AlGaAs layer, determined by polaron measurements) may also affect the intensity of the $e_1 - h_1$ transition. In GaAs QWs, a strong suppression of the hh PLE peak at 6 K has already been attributed to hh band filling resulting from carbon contamination; increasing the temperature up to 49 K allowed the formation of some hh excitons due to thermal excitation of the holes out of the bottom of the valence band [Miller and Bhat, 1988].

The enhancement of the PLE intensity at high photon energies and at temperatures typically greater than 40 K may result from two different processes. On one hand, carriers may be absorbed in the QWs adjacent to the QWRs and then diffuse towards the wire with a transfer probability that increases with temperature. Indeed, the PLE
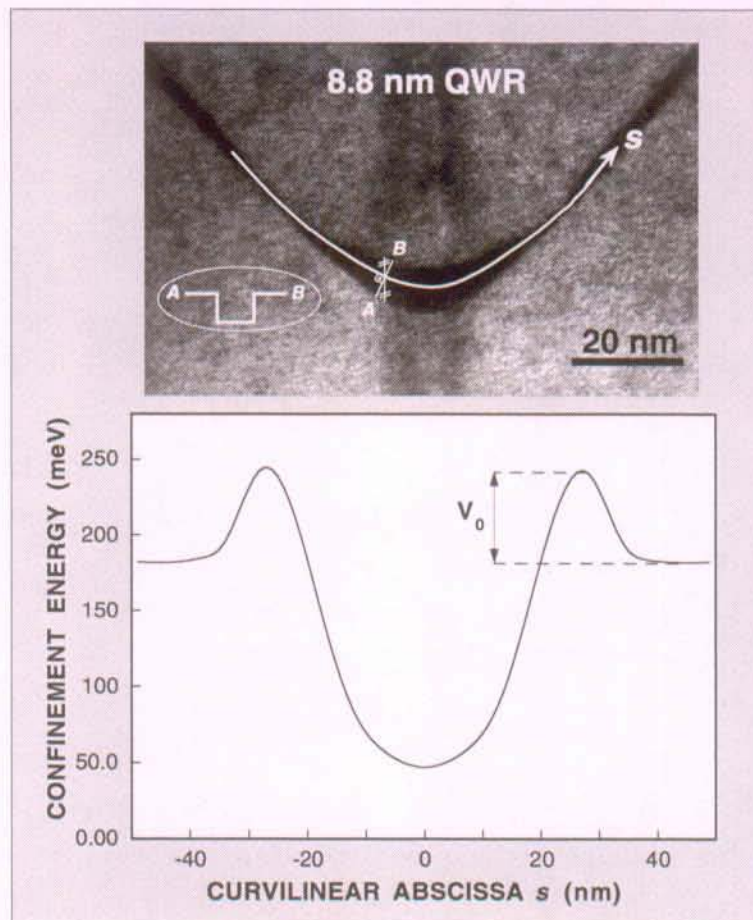
Figure 5.15: (a)TEM cross-sectional picture of the 8.8 nm QWR; a curvilinear axis s is defined at the average height of the upper and lower boundaries of the wire. (b) Lateral confining potential for electrons calculated in an adiabatic decoupling scheme; in this context, it results from the variation of the 1D potential well $A - B$ along the curvilinear axis s. The lateral position is measured along this curve and the width of the well is measured orthogonaly.

intensity of each structure measured at the luminescence wavelength of the QWRs exhibit a dramatic increase in the signal at energies corresponding to absorption in the QWs surrounding the wires (see Fig. 5.1, Fig 5.2, and Fig. 5.3). An estimation of the potential barrier V_0 for electrons due to the necking between the QWR and the side-QWs gives $V_0 \sim 26$ meV, $V_0 \sim 60$ meV, and $V_0 \sim 145$ meV for the 4.1 nm QWR, 8.8 nm QWR, and 14.1 nm QWR, respectively. This potential barrier is illustrated in Fig. 5.15 for the 8.8 nm QWR structure. Part (a) of this figure displays a TEM cross-sectional image of the QWR region. In an adiabatic decoupling scheme [Kapon et al., 1989], the variation of the 1D potential well $A - B$ along the curvilinear axis s yields a lateral confining potential for electrons and holes. The curvilinear abscissa is measured along a curve that lies at the average height of the upper and lower boundaries of the wire. For each discretized position along this line the 1D confinement energy is calculated for a

QW defined perpendicularly to the abscissa curve. The resulting lateral potential well is represented in Fig. 5.15 (b). Obviously, classical activation alone can not account for the strong thermal enhancement of carrier transfer. Two additional effects may contribute to this temperature dependent transfer of carriers: (i) localization of 2D excitons in the side-QWs at low temperature prevents motion of the excitons towards the wire; thermal activation progressively delocalize them, thus enhancing the transfer into the wire; (ii) thermally activated carriers see a lower and thinner barrier thickness with increasing temperature, resulting in an enhanced tunneling transfer. On the other hand, the PLE signal may result from absorption and emission from the QW structures at the spectral position of the QWR luminescence. Although this hypothesis is unrealistic for the 4.1 nm QWR and for the 8.8 nm QWR (see Fig. 5.1 and Fig 5.2), it may be appropriate for the thickest QWR sample (see Fig. 5.3).

In general, the temperature dependence of the linewidth of the lowest-lying $1S$ exciton in semiconductors has the form [Rudin et al., 1990]:

$$\Gamma(T) = \Gamma_0 + \gamma_{ac}T + \gamma_{opt}/\left[\exp(E_{LO}/k_BT) - 1\right],\qquad(5.1)$$

where E_{LO} is the LO phonon energy (36 meV for GaAs). The constant term Γ_0 arises from scattering due to impurities and disorder; the second term on the right-hand side of this equation arises from exciton interactions with acoustic phonons; the last term comes from interactions with LO phonons and is proportional to the Bose function for LO phonon occupation. This third term gives the strongest temperature dependence for $T \geq 80$ K [Rudin et al., 1990]. To date, experimental studies of the exciton linewidths in low dimensional systems have concentrated mainly on the higher-temperature regime (≥ 80 K) in quantum wells [Gammon et al., 1995a, Ruf et al., 1994, Qiang et al., 1992]. Less work has been done on the regime at lower temperatures and/or on systems of lower dimensionality. Mayer et al. (1994) studied exciton-acoustic phonon scattering in 150 nm-wide GaAs/AlGaAs QWRs. They found a stronger interaction with acoustic phonons in QWRs than in QWs, opposite to the trend for 2D systems, in which more confinement leads to a weaker interaction with acoustic phonons. These findings were confirmed by a systematic study of the wire width dependence of the exciton linewidth due to acoustic phonon scattering in the range $5 - 30$ K [Braun et al., 1997]. The temperature dependence ($10 < T < 500$ K) of the coupling to optical phonons has been investigated in bulk GaAs and in 2D structures as a function of the well width; a monotonic decrease of γ_{opt} with reduced dimensionality and size has been found [Qiang et al., 1992].

As already mentioned in section 4.3.1, the PLE FWHM reflects the inhomogeneous broadening of the system whereas the PL FWHM strongly depends on relaxation and localization effects. The distinct increase of the PL linewidth with increasing temper-

ature reflects then a redistribution of the excitons among localization sites and their progressive delocalization to extended states. Therefore, PL linewidths at high temperature are larger than the corresponding PLE FWHM as the latter are determined by the maximum of the density of states only and not by the density of localized states. The investigation of the coupling to acoustic phonons is obviously not possible in our QWR structures as localization effects have been shown to dominate the temperature dependence of the PLE linewidth up to about 80 – 100 K. At higher temperatures, we shall, however, estimate the coupling to optical phonons for the 4.1 nm and 8.8 nm QWRs, using Eq. 5.1 applied to the experimental FWHM of the first PLE peaks (see Fig. 5.10). For the 4.1 nm QWR we restrict the fitting procedure to $T \geq 80$ K while the temperature range is restricted to $T \geq 100$ K for the 8.8 nm QWR. The temperature dynamic range is not sufficient to perform the same estimation for the 14.1 nm QWR. We find:

$$\gamma_{opt}^{4.1nm} = 5 \pm 1 \text{ meV, and} \tag{5.2}$$

$$\gamma_{opt}^{8.8nm} = 14 \pm 2 \text{ meV}. \tag{5.3}$$

In 2D structures, Qiang et al. (1992) estimated γ_{opt} to be of the order of $0.5 - 3$ meV for QW widths between 6 nm and 10 nm. They also found $\gamma_{opt} = 20 \pm 1$ meV for bulk GaAs. Therefore, our results suggest that the thermal broadening due to interactions with optical phonons is increased in QWR structures as compared to 2D systems. Due to the limited temperature range of investigation for the 14.1 nm QWR, we can not establish a systematic wire size dependence of the coupling coefficient γ_{opt}. Moreover, our estimation of γ_{opt} for the 4.1 nm and 8.8 nm QWR is performed on a temperature range of about 100 K which is rather small in view of the slow variation of the third term in Eq. 5.1. In contrast, values of γ_{opt} in QWs have been determined on the basis of photoreflectance experiments realized up to very high temperature ($T \sim 500$ K) [Qiang et al., 1992]. Nevertheless, our result (smaller coupling coefficient for a thinner wire) is in agreement with theoretical calculations of the exciton-optical phonon scattering in model QWRs [Nojima, 1992, Liang et al., 1996]. At this point, it is interesting to note that comparison of experiments with theoretical investigations of the electron scattering by optical phonons (see, e.g., [Bockelmann and Bastard, 1990]) should be done with care, as excitonic effects have been shown to affect such scattering rates in a way similar to the strong Coulomb-reduction of the interband absorption strength [3] [Nojima, 1992]. Finally, we notice that a correct description of the scattering with phonons in our thinnest QWR structure should take into account the coupling to surface-optical phonon modes which can not be neglected for wire sizes below ~ 5 nm

---

[3]Sommerfeld factor much less than unity for 1D systems, see Sec. 2.5.3.

[Stroscio et al., 1990, Rossi et al., 1993].

5.8   Summary

We have presented the temperature dependence of PL and PLE spectra for QWRs of different thicknesses. Photoluminescence could be measured up to room temperature due to high quantum efficiency. Additionally, large subband spacings and small inhomogeneous broadenings allowed us to perform PLE measurements up to 200 K for the 4.1 nm QWR, 180 K for the 8.8 nm QWR, and 100 K for the 14.1 nm QWR. A thermally-enhanced transfer of carriers from the side-QWs into the QWRs has been evidenced and attributed to increasing 2D excitons mobility with increasing temperature and to the combination of classical activation and tunneling through the potential barrier due to the "necking". A strong impact of disorder on the PL (PLE) peak position and on the line shape has been clearly shown. The evolution of the PL and PLE peak positions with increasing temperature, together with a lineshape analysis of PL spectra, indicates the dominance of excitonic correlations over the whole temperature range. The enhancement of the lowest-energy PLE peak with respect to higher-energy transitions with increasing temperature has been explained in terms of an effective mobility edge. Finally, the scattering with optical phonons at high temperature has been discussed.

Chapter 6

Localization and many-body effects

6.1 Introduction

Exciton-exciton interaction has been shown to change considerably due to quantum confinement in semiconductor QWs [Peyghambarian et al., 1984] and QDs [Edamatsu et al., 1995]. In bulk semiconductors a virtually exact cancellation of the red shift due to screening effects and the blue shift related to fermion-exchange interaction takes place, and a constant exciton recombination energy at increasing exciton density is expected [Haug and Schmitt-Rink, 1984]. Quantum confinement is expected to disturb this balance between screening effects and exchange interaction and a blue shift of the exciton resonance has been predicted in two-dimensional [Schmitt-Rink et al., 1985] and zero-dimensional systems [Belleguie and Banyai, 1991, Wojs and Hawrylak, 1996]. Reduced dimensionality also deeply influences the formation and the stability of many-exciton states and their impact on nonlinear optical properties of QDs has been pointed out by Nair and Takagahara [Nair and Takagahara, 1996, Nair and Takagahara, 1997].

A clear observation of such many-body phenomena, in particular a shift of the exciton resonance, is strongly dependent on the quality of the investigated structure. Inhomogeneous broadening of the excitonic lines due to interface disorder or size distribution prevents in part or totally the identification of many-body effects on the photoluminescence (PL) profile. Homogeneously broadened individual exciton lines have already been observed in the optical spectra of QDs naturally formed in QW structures [Brunner et al., 1994b, Gammon et al., 1996] or produced by the cleaved-edge overgrowth technique [Wegscheider et al., 1997]. However, no shifts of these *homogeneous* lines at increasing carrier density have been reported.

In this chapter we report the observation of many-body effects arising from exciton-exciton interaction in QWRs, as inferred from the evolution of the luminescence spectra of localized 1D excitons in GaAs/AlGaAs V-groove wires at increasing carrier densities. In contrast to excitons localized in 2D structures, we find that the self-energy of localized

1D excitons is renormalized at increasing excitation density. Furthermore, additional features in the spectra at high carrier densities are interpreted in terms of multi-exciton states of the QWRs. Parts of theses results have been published in Physica Status Solidi [Vouilloz et al., 1997b] and Physica E [Vouilloz et al., 1998c], and Solid State Communications [Vouilloz et al., 1998b].

6.2 Experimental

The experiments were performed on the 2.5 nm, 6.9 nm, and 8.8 nm QWRs. PL excitation spectra of these QWR structures show clear 1D subbands and polarization anisotropy related to valence band mixing due to 2D confinement. Electron-beam lithography and wet chemical etching were used to open a series of square apertures, $0.2 - 2.0$ μm wide, in an 80 nm thick Al-film deposited on the surface of the sample. The heterostructure was excited at 10 K through a given hole with either an Ar^+ laser (2.41 eV photon energy) or a tunable Ti:Sa laser, and the PL was collected from the same hole and measured using a spectrograph equipped with a nitrogen cooled charge coupled device detector. The spectral resolution was fixed at 80 μeV. The samples and the experimental techniques are described in detail in Chap. 3.

The exciton density in our QWR structure is estimated as $N_X \approx \alpha\beta T N_{phot}\tau_{rad}$. The factor α takes into account the portion of the laser spot profile overlapping the aperture size. The parameter β is the fraction of excitons that recombine in the QWR region only, and is estimated by dividing the integrated intensity of the QWR luminescence by that of the overall spectrum. A transmission factor T of 0.7 at the GaAs surface of the sample is used. N_{phot} is the number of incoming photons per unit time and τ_{rad} the radiative lifetime of excitons which is assumed to have a constant value of 400 ps throughout the heterostructure [Oberli et al., 1997]. To give an order of magnitude, for a 1 μm spot on a 0.2 μm aperture we obtain an exciton density $\sim 6 \times 10^3 cm^{-1}$ for 215 W/cm² excitation power density (photon energy: 2.41 eV).

6.3 Localization of excitons in quantum wires

In Sec. 3.2.3, we investigated structural disorder in QWRs by AFM studies on planar and non-planar AlGaAs and GaAs layers. In particular, fluctuations of the confinement potential have been demonstrated to arise from ML thickness fluctuations at the central (100) facet and step bunching at the inner {311}A facets. This interface disorder has been shown to translate into variations in the confinement energy of the 1D carriers along the wire axis, which can localize them. Localization of excitons in such QWRs has been evidenced by several luminescence features:

(i) The presence of a sizeable Stokes shift between PL and PLE spectra as well as its temperature dependence (Chaps. 4 and 5).

(ii) The nonlinear relationship between the Stokes shift and the inhomogeneous width of PLE excitonic lines [Gurioli et al., 1994].

(iii) The variation of the degree of linear polarization measured across the PL line (see Sec. 4.3.2).

(iv) The influence of the detection wavelength on PLE spectra (see Sec. 4.4.3).

(v) The temperature dependence of the PLE spectra lineshapes (see Sec. 5.4 and 5.5).

(vi) The temperature dependence of the excitonic radiative decay time [Oberli et al., 1998].

By performing PL experiments through small apertures, we are able to directly observe these localization effects in QWRs and investigate interactions between localized excitons.

6.3.1 Influence of the aperture size

Figure 6.1 shows PL spectra of the 2.5 nm QWR measured through holes of different sizes for a constant low power density. A splitting of the inhomogeneously broadened PL line into a series of very sharp lines is observed by decreasing the hole size. The number and the intensity ratio of theses sharp lines depended on the excitation power. Lines with full width at half maximum as small as 140 μeV have been observed. These sharp lines arise from excitons recombining in the local potential minima created by the interface disorder discussed previously. We carefully checked that the position of each peak did not vary in time and was independent of the cooling procedure. We observed typically only 1 to 3 peaks at low excitation density through a given 0.2 μm hole. Excitation of the QWRs with photons having an energy lower than the AlGaAs barrier (excitation wavelength of 690 nm) yielded qualitatively similar results . PL spectra measured for different hole sizes may correspond either to exciton recombination in closely spaced dots located within the aperture or to the ground and excited states transitions of a single dot. Indeed, theoretical calculations have predicted optically active transitions of excited states in analogous 0D semiconductor systems [Benisty et al., 1991, Bockelmann, 1993].

Extended PL spectra from the 2.5 nm QWR sample as measured through a 0.2 μm hole at different excitation power densities are shown in Fig. 6.2. Each part of the heterostructure yields finely-structured PL peaks due to localization of excitons by
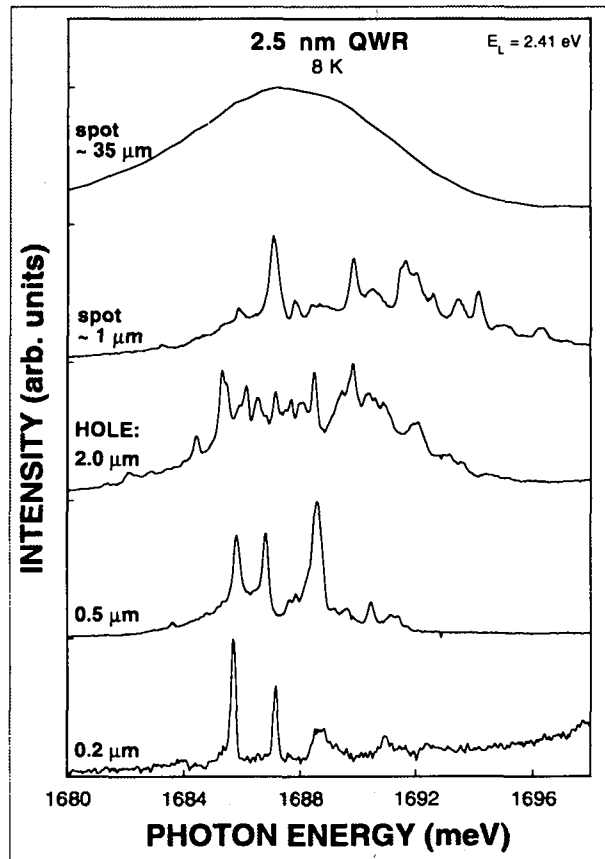
Figure 6.1: PL spectra of the 2.5 nm QWR measured at 8 K through holes of different sizes at a power density $\sim$ 240 W/cm^2. The topmost spectrum is the result of a standard PL experiment with a laser spot $\sim$ 35 μm in diameter. A spectrum obtained by micro-PL from an uncovered part of the sample is shown below it (laser spot $\sim$ 1.5 μm).

fluctuations of the confinement potential. A blow-up of the QWR region is displayed in Fig. 6.3 at different power densities and for an excitation energy above or below the bandgap of the Al$_{0.3}$Ga$_{0.7}$As barrier (parts (a) and (b) of the figure, respectively). With decreasing power density, the broad luminescence peak also splits into a series of very sharp lines. For the lowest excitation power density of 105 W/cm^2, one main peak at 1685.295 meV (peak A) and two weaker transitions at 1686.670 meV (peak B) and 1688.535 meV (peak E) are observed (see Fig. 6.3 (a)). Line A is centered in the middle of the broad PL line measured at higher power density. With increasing power density, new transitions appear on either side of the original line. Similar results were obtained for PL spectra measured through different 0.2 μm holes. We attribute the sharp PL lines detected through a 0.2 μm hole at low power density to recombination of excitons confined in a single QD-like region. Indeed, based on our estimation of GaAs thickness fluctuations at the central (100) facet that determine the distribution of the localization sites along the wire (see Sec. 3.2.3 and Fig. 3.8), we believe that
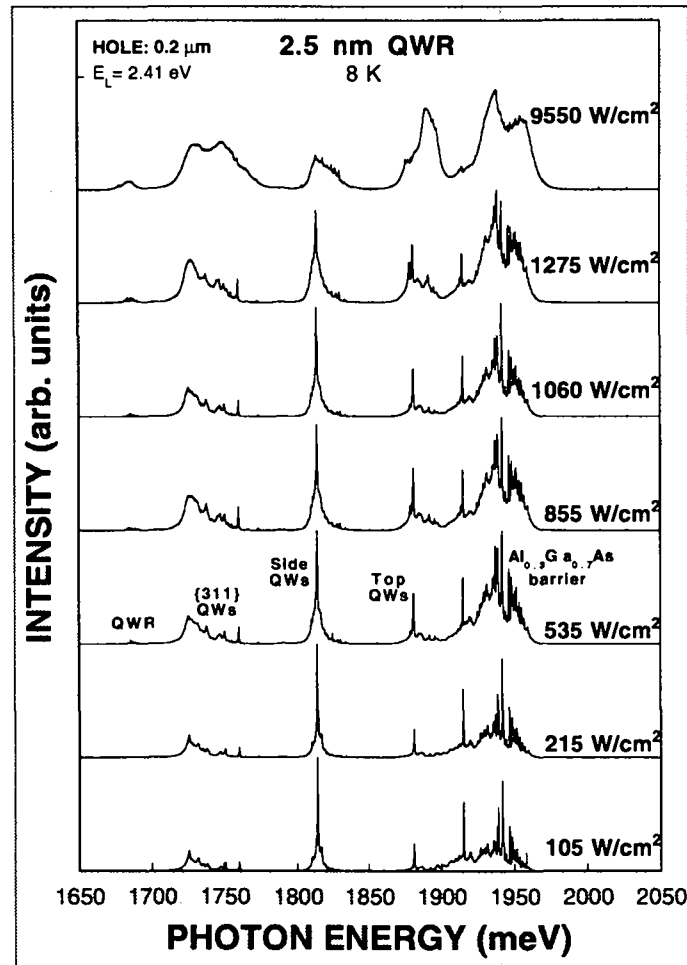
Figure 6.2: PL spectrum of the 2.5 nm QWR measured at 8 K through a 0.2 μm hole. Localization of excitons in the different parts of the heterostructure results in finely-structured PL peaks. The excitation power density is indicated at the right of each spectrum.

the occurence of several closely spaced dot-like regions over a 0.2 μm length is very improbable. Therefore, peak A in Fig. 6.3 is assigned to the exciton ground state of the dot, whereas peaks B and E are assigned to excited single exciton states of the QD. This assignment is consistent with a model describing such a QD as having a few widely separated low energy levels and a dense exciton level spectrum at higher energy (see Fig. 6.4). In this case, exciton relaxation is efficient towards the upper levels (excitons can relax using the closely spaced nonradiative levels) whereas it is less efficient towards lower energies due to the decrease in exciton-phonon scattering rates with increasing energy-level separation [Bockelmann, 1993]. In such a relaxation process, high-energy photo-excited excitons cascade into lower energy states in the wire by emitting acoustic phonons in order to conserve energy. As the exciton localizes, the energy spacing between consecutive drops is predicted to grow rapidly. The momentum of an emitted
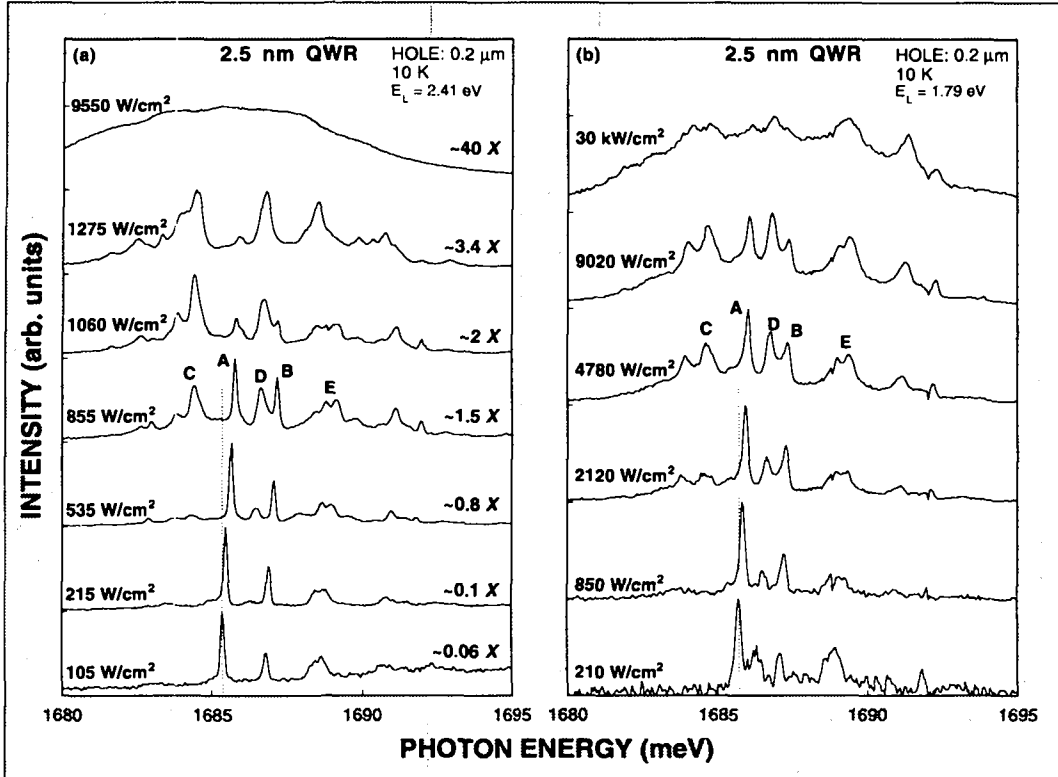
Figure 6.3: PL spectra of the 2.5 nm QWR measured at 10 K through a 0.2 μm hole for different excitation power densities; (a) excitation in the barrier with the Ar^+ laser, and (b) excitation below the bandgap of the $Al_{0.3}Ga_{0.7}As$ barrier. In (a), the estimated number of excitons in the dot-like region is indicated at the right of each spectrum.

phonon is limited by the spatial extent of the localized exciton state. Because the energy of an acoustic phonon is proportional to its momentum, an exciton relaxation bottleneck occurs when the exciton cannot emit a single phonon with enough energy to relax to the next level. Instead, the excitons must relax via higher ordered processes such as a multiphonon emission [Inoshita and Sakaki, 1992]. The relaxation bottleneck has been controversial; however, it has already been clearly evidenced in QDs formed naturally in thin GaAs/AlGaAs QWs [Brunner et al., 1992, Bockelmann et al., 1996] and in T-shape QWRs [Hasen et al., 1997]. In the case of T-shape QWRs, three optical transitions have been observed for a given localization site at ~ 120 W/cm^2 and 4 K ; the corresponding subband separations were 1.5 meV and 2 meV, which are very close to the energy spacings of 1.4 meV and 1.8 meV that we observe between peaks A, B, and E.

6.3.2   Calculation of states localized along the wire axis

From the energy spacing of 1.4 meV between peaks A and B (Δ_{12}), we estimate, based on the potential model presented in Sec. 3.2.3, the longitudinal size L_x of the QD to be
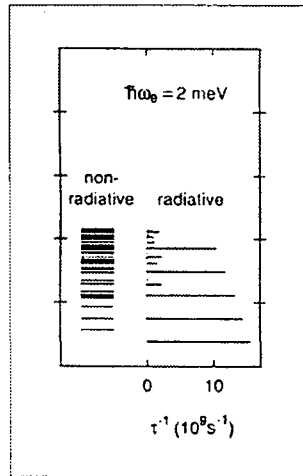
Figure 6.4: Calculated energies and radiative lifetimes of excitons in a GaAs/AlGaAs quantum dot. The parabolic lateral potential is characterized by the separation $\hbar\omega_e = 2$ meV of the single electron states. The inverse recombination time τ^{-1} of the radiative states is given by the length of the horizontal bars, through the bottom scale [Bockelmann et al., 1993].

on the order of 150 nm. This estimation of L_x is consistent with our interpretation of PL spectra detected through 0.2 μm holes as arising from optical transitions of isolated QDs. The probability density associated with the first three electron wave functions along the wire axis is shown in Fig. 6.5 together with the localization potential. We notice that short-range ($\sim$ 10 nm) fluctuations of the $\{311\}$A wire facets result in localization of the electron ground state wave function on a shorter scale than the one (L_x) related to ML thickness fluctuations at the center of the crescent. However, the energy separation of e_{11} and e_{12} will be mainly influenced by L_x as excited states of the localization potential will not, in general, be confined to the same position as the ground state wave function. This remark is illustrated in this figure where e_{11} and e_{12} wave functions are separated by $\sim$ 110 nm. We note that a value of L_x of 100 nm yields $\Delta_{12} \sim 3$ meV and $L_x = 200$ nm yields $\Delta_{12} \sim 1.1$ meV. Obviously, the absolute values of e_{11}, e_{12}, and e_{13} depend on all the details of the potential landscape, which is related both to $\{311\}$A and (100) facets fluctuations. However, it is interesting to notice that the values of the energy separations Δ_{12} or Δ_{23} are much less sensitive to the exact shape of the potential on the short-range scale. In our model, the relative position of ML fluctuations at the central (100) facet is arbitrary choosen with respect to fluctuations at the $\{311\}$A facets. Modifying this position allows us to establish that a fixed value of Δ_{12} yields values of L_x that are precise to about 20 nm. Finally, we note that completely neglecting $\{311\}$A facets fluctuations, namely considering a square well potential model, gives $L_x = 130$ nm. Therefore, we believe the estimated value of L_x to be reliable.
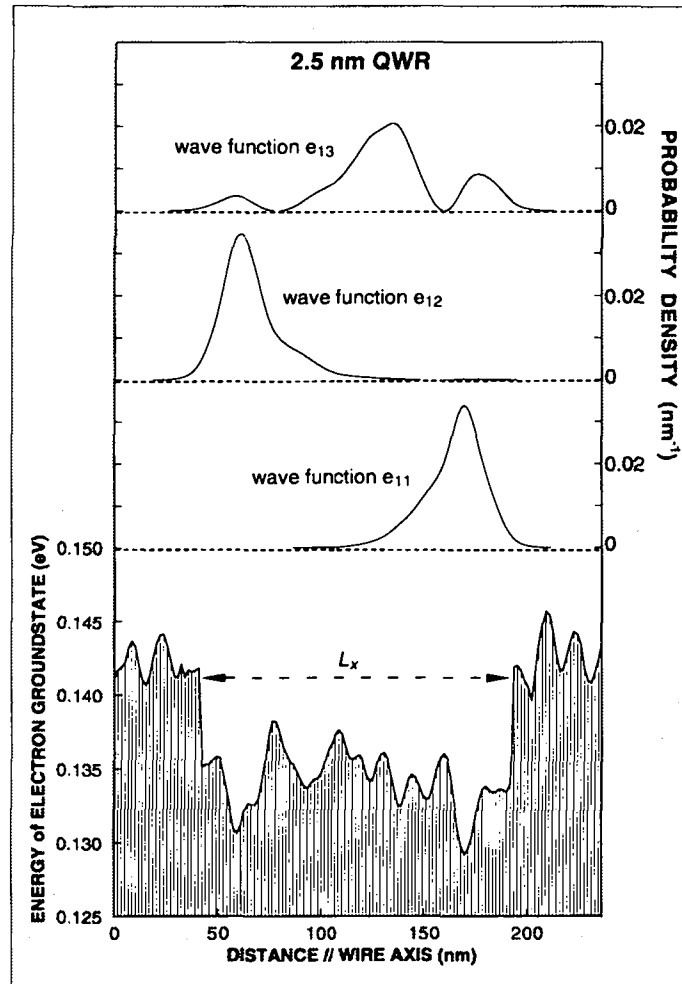
Figure 6.5: Probability density for the first three electron wave functions (labeled e_{11}, e_{12}, and e_{13}, respectively) describing the localization due to fluctuations of the confinement potential. Fluctuations of the electron-ground state energy are displayed at the bottom of the figure.

6.3.3 Dependence on the excitation power density: impact of many-body phenomena

Having identified the nature of the sharp excitonic transitions, we now describe their power dependence. With increasing power density, new transitions appear on either side of the original line. Similar results were obtained for PL spectra measured through different 0.2 μm holes. We attribute the optical transitions occurring below 1685 meV and the transition labeled D in Fig. 6.3 to the formation of exciton complexes in the QD. Moreover, a blue shift of the homogeneously broadened excitonic lines is observed at increasing power. In Fig. 6.6 we display the energy shift of peaks A, B, C, and D in Fig. 6.3 (a) as a function of power density. This blue shift cannot arise from a pump-induced thermal effect that would instead yield a red shift. Rather, the blue shift can be attributed to exciton-exciton interactions leading to a renormalization of the exciton
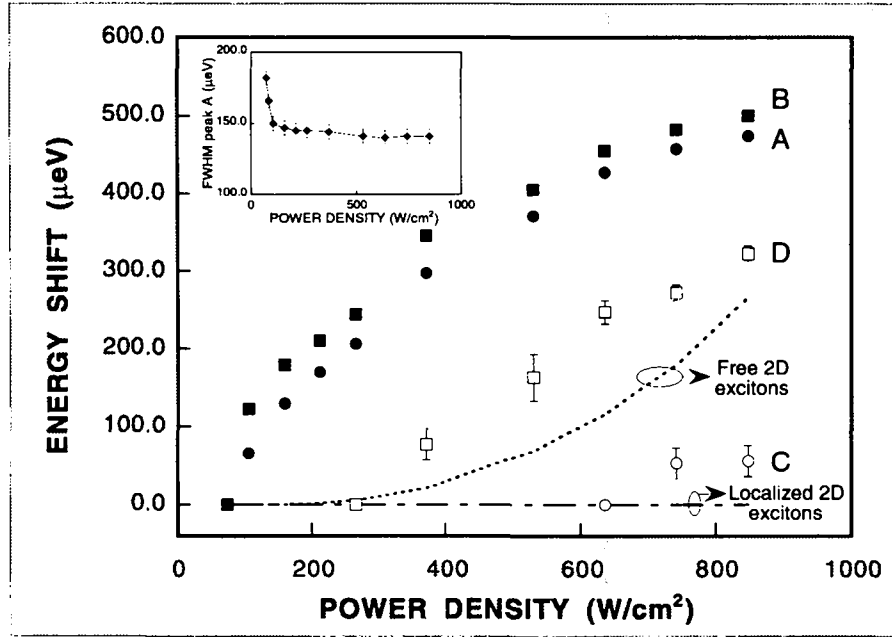
Figure 6.6: Energy shift of peaks A, B, C, and D in PL spectra (see Fig. 6.3 (a)) with power density; the photon energy is 2.41 eV. The dotted line shows the blue shift of a free 2D exciton, according to Eq. 6.1. The dotted-dashed line corresponds to the constant recombination energy of localized 2D excitons. Inset shows the full width at half maximum of peak A as a function of power density.

self-energy, as further discussed below. We have not observed any measurable shift in the exciton energy for similarly sharp spectral features neither in the PL spectra of the QW areas of the nonplanar QWR heterostructure nor in the PL spectra of the AlGaAs barrier material, as illustrated in Fig. 6.7. This demonstrates that the observed blue shift is specific to the wire environment.

6.3.4 Influence of the wire size

The results obtained for the 6.9 nm QWR structure are qualitatively similar to those of the 2.5 nm QWR (see Fig. 6.8). The line splitting is, however, less pronounced in the sense that the different lines are not as well resolved as for the thinnest wire. As can be expected, monolayer fluctuations have a much more pronounced effect on thinner QWRs. Table 6.1 shows the impact of ML fluctuations at the different facets which define the wire morphology on the energy of the electron ground state. These results also highlight the wire size dependence of the impact of {311}A facets fluctuations on the confinement energy. This dependence can be explained by the relative extension of the ground state wave function with respect to the length of the central (100) facet and that of the {311} facets. To illustrate this point, we display in Fig. 6.9 the contours of the electron ground state wave functions in the 2.5 nm and 6.9 nm QWRs. The
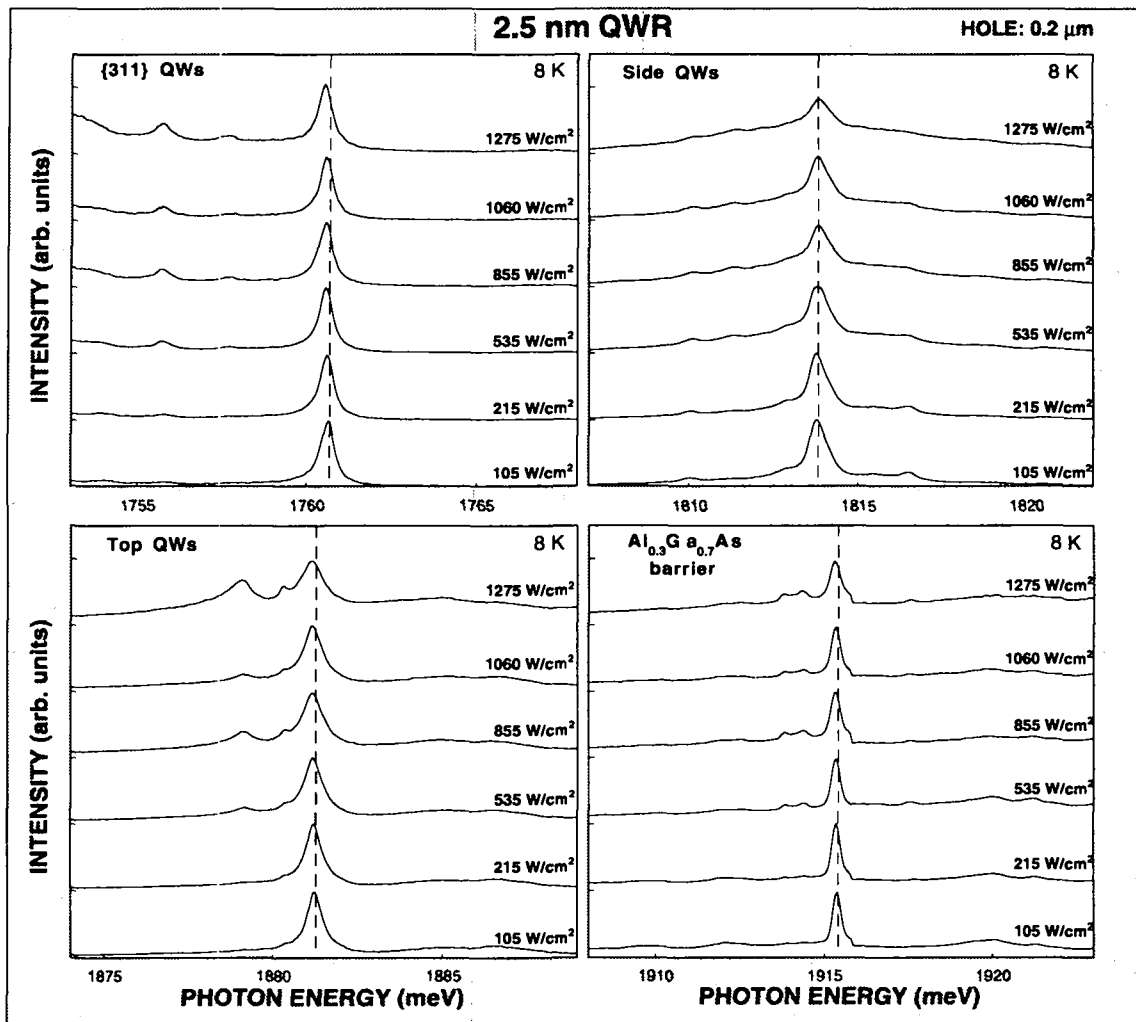
Figure 6.7: PL spectra of the QW parts and of the AlGaAs barrier in the 2.5 nm QWR heterostructure measured through a 0.2 μm hole at different excitation power densities.

extension of the wave function over the {311}A facets is clearly more significant for the thinnest wire, resulting in a more pronounced impact of a ML fluctuation at the {311}A facets on confinement potential fluctuations.

Figure 6.8 shows that the PL line of the thickest QWR sample (8.8 nm QWR) does not exhibit any fine sub-meV structure when decreasing the excitation power or reducing the hole size. In Table 6.1 we compared the impact of a *single* ML fluctuation at the different facets of QWRs which differ by their central thickness. However, we have mentioned in Sec. 3.2.3 that the height and the period of the fluctuations at the {311}A facets increase with increasing GaAs layer thickness. Using a procedure similar to that used for the 2.5 nm QWR structure, we found for the 8.8 nm QWR a period and a height of the {311} step bunching of $\sim$ 25 nm and of 2 − 3 ML, respectively. An increase of 3 MLs at one {311} facet has been calculated to reduce the energy of the electron ground state in this QWR structure by 1.2 meV, which is comparable to the
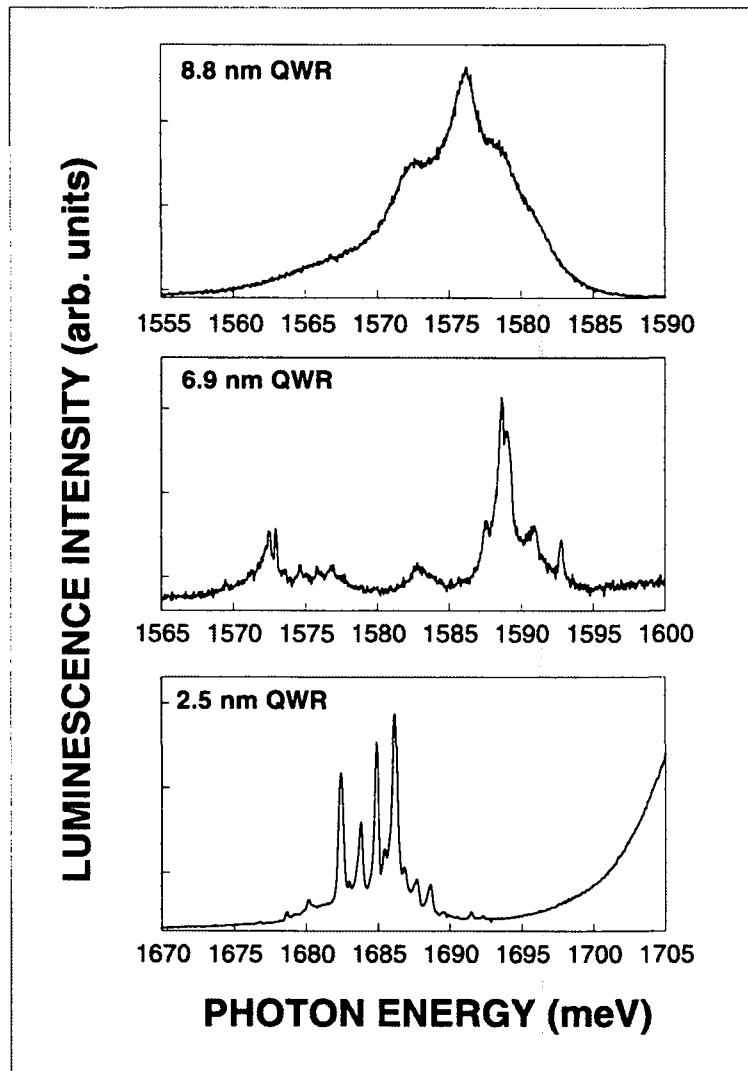
Figure 6.8: PL spectra of the 2.5 nm QWR, 6.9 nm QWR, and 8.8 nm QWR samples measured at 8 K through 0.5 μm holes. The power density is $\sim$ 75 W/cm^2

decrease of 1.6 meV (see Table 6.1) related to a ML increase at the central (100) facet. Therefore, the occurrence of QD-like regions similar to that observed in the 2.5 nm QWR is very improbable. Instead, we believe that the fluctuating potential localizes the excitons all along the QWR; the resulting PL is, thus, a superposition of many sharp lines that merge into an inhomogeneous peaks. Finally, we note that the simultaneous fluctuation of the central (100) facet and of the {311}A facets yields larger potential variation that may explain the structured PL lineshape shown in Fig. 6.8 ("shoulders" at 1572.6 and 1578.1 meV).

Table 6.1: Fluctuations of the electron ground state energy due to interface roughness.

QWR	+1 ML at (100) facet	+1 ML at one {311}A facet	+1 ML at both {311}A facets	+1 ML at (100) facet and {311}A facets
2.5 nm	-7.3 meV	-2.5 meV	-4.7 meV	11.4 meV
6.9 nm	-2.9 meV	-0.5 meV	-1.0 meV	-3.9 meV
8.8 nm	-1.6 meV	-0.4 meV	-0.7 meV	-2.2 meV
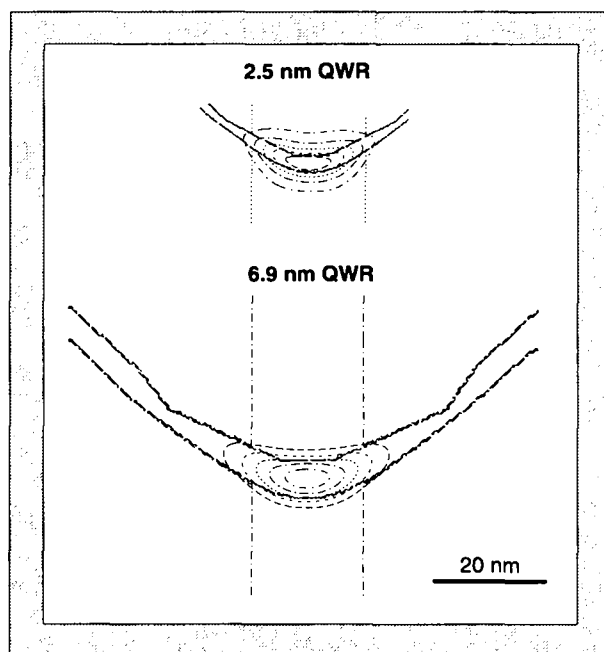
Figure 6.9: Electron ground state in the 2.5 nm and 6.9 nm QWRs. The contours of the probability density are plotted together with the wire cross sections derived from TEM pictures and used in the calculations. The vertical lines represent contour lines of the VQWs.

6.4 Discussion

6.4.1 The inter-excitonic exchange interaction

The renormalization of the exciton self-energy has been investigated in 3D and 2D systems, using the many-exciton Hamiltonian presented in Sec. 2.5.4 (see Eq. 2.38) within the Hartree-Fock approximation [Haug and Schmitt-Rink, 1984, Schmitt-Rink et al., 1985, Fernández-Rossier et al., 1996]. A blue shift of the excitonic resonance found for 2D systems has been explained by the lack of balance between the Hartree-Fock contribution and the negative correlation energy (screening) part in the exciton-exciton interaction in low dimensional systems [Schmitt-Rink et al., 1985]. The

Hartree-Fock contribution is composed of two terms: the first term is a self-energy correction that comprises the electron and hole exchange self-energies, namely the energies that parallel spin particles gain by avoiding each other; the second term corresponds to the weakening of the inter-excitonic e-h attraction due to the Pauli exclusion principle acting on the Fermi particles forming the excitons. Many experiments in bulk semiconductors [Fehrenbach et al., 1982, Majumder et al., 1985, Swoboda et al., 1988] have reported on a constant excitonic recombination energy with increasing excitation density, which can be interpreted in terms of a cancellation between the short-range repulsion due to the Pauli principle and the long-range Van der Waals attraction between excitons [Schmitt-Rink et al., 1985]. Screening effects in QWs are strongly reduced due to the two-dimensional nature of the electron-hole pairs. This explains the blue shift of inhomogeneously broadened excitonic transitions that has been observed in transient pump-and-probe experiments in GaAs/AlGaAs multiple QWs [Peyghambarian et al., 1984]. In QDs, or for localized excitons in our structures, screening is intrinsically absent due to the discrete nature of the energy spectrum. The exciton blue shift is then attributed to the inter-excitonic exchange interaction between fermions of the same type [1].

Up to now, the effects of an interacting gas of excitons on the optical spectra of low-dimensional systems have been calculated for QWs [Schmitt-Rink et al., 1985], microcrystallites [Belleguie and Banyai, 1991], and lens-shaped InGaAs self-assembled QDs [Wojs and Hawrylak, 1996]. Exciton-exciton interactions have also been investigated in QWR structures, but only in the high density regime where screening effects, band renormalization and phase-space filling are predominant [Rossi and Molinari, 1996a]. The limit of a weakly interacting exciton gas has not been studied in 1D systems, to our knowledge. Moreover, the impact of localization on inter-excitonic exchange interaction in 2D and 1D structures has not been studied yet. Comparing the behavior of localized excitons in the QW and QWR parts of our structure and contrasting theoretical predictions for free (delocalized) 2D excitons with experimental results for localized 2D excitons allows us to investigate the influence of dimensionality and to highlight the role of localization effects on exciton-exciton interaction.

The predicted increase of the free exciton energy due to the unscreened exchange interaction in a 2D system obeys the relation [Schmitt-Rink et al., 1985]:

$$\Delta E \simeq 12na_{2D}^2 E_{1s},$$ (6.1)

where n is the exciton density per unit area, $a_{2D} \sim 90$ Å is the two-dimensional exciton

---

[1] The permanent dipole between an electron and a hole in their ground state in our wires, which is caused by the asymmetric confinement potential inherent to these crescent-shaped QWRs and which is oriented along the growth direction, does not change appreciably the exciton-exciton interaction energy. This dipole-dipole interaction energy was calculated to be smaller than 0.03 μeV at the Mott density.

radius, and $E_{1s} \sim 13$ meV is the binding energy of the 2D exciton [Bastard et al., 1982]. For the power range of Fig. 6.3, we calculated that the exciton density varies from $\sim 3 \times 10^3 \text{cm}^{-1}$ up to $\sim 2 \times 10^6 \text{cm}^{-1}$. *Fine-structured* PL spectra in this figure correspond to exciton densities smaller than $2 \times 10^5 \text{cm}^{-1}$, therefore below the expected Mott density [2] of about $8 \times 10^5 \text{cm}^{-1}$ [Rossi and Molinari, 1996a]. The excitation densities for which a clear blue shift is observed correspond to the range $3 \times 10^3 - 8 \times 10^4 \text{cm}^{-1}$. The dotted line in Fig. 6.6 indicates the expected blue shift of free 2D excitons, according to Eq. (1) [3]. The dotted-dashed line in the same figure corresponds to the constant recombination energy of localized excitons in our QW structures. Comparing the results for localized and free 2D excitons suggests the inadequacy of Eq. (1) for describing the exchange interaction of 2D localized excitons. Furthermore, we find a striking difference between localized 2D and localized 1D excitons: a measurable blue shift is observed only for the latter. We suggest therefore that both localization effects and dimensionality influence the interactions between excitons. The different behaviours of localized excitons in 1D and 2D structures may be explained as follows. For excitons localized in QWRs, exciton-exciton interactions may occur within the QD probed through the 0.2 μm aperture or between localized and partially delocalized excitons. We have, then, an interacting gas of excitons linearly aligned along the wire direction, whereas in QWs the interactions take place isotropically in the plane of the well. Finally, our results are supported by a recent experimental and theoretical study on the exciton dephasing dynamics in QWRs that has shown the dominant role and the increase of the inter-excitonic exchange interaction with increasing confinement [Braun et al., 1998].

As shown in the inset of Fig. 6.6, we also observe a surprising and significant narrowing in the excitonic resonance over the same range of power densities. By improving the spectral resolution down to 40 μeV and analyzing the linear polarization of the PL we could not evidence any fine structure splitting, although exchange interaction is expected to lift the angular momentum degeneracy of exciton states in QDs with asymmetric confinement potentials [Gammon et al., 1996]. A dependence of such splitting on exciton density could, however, explain the sharpening of the PL lines. Interaction with excitons outside the dot may also introduce random shifts in the recombination energy of excitons recombining at the dot site, due to fluctuations in the number of interacting excitons. The effect of this interaction would show up as an exciton linewidth broadening, when integrated over the measurement time. At higher exciton densities the effects of exciton number fluctuation would decrease and the linewidth stabilizes at a value determined by dephasing mechanisms.

---

[2]Mott density in the sense of maximum packing density of excitons.

[3]To estimate n in Eq. 6.1 we have used a distance between excitons equal to that deduced from the linear exciton density.

We shall now discuss the impact of unintentional p-background doping of GaAs and $Al_{0.3}Ga_{0.7}As$ layers on the many-body phenomena discussed above. Carbon is known as the dominant background impurity in MOCVD grown GaAs and AlGaAs layers using trimethylgallium and trimethylaluminium as the Ga and Al sources, respectively [Adachi, 1993]. The amount of C incorporation depends on growth temperature, gas phase stoichiometry during growth, operating pressure and substrate orientation. For our growth conditions, the expected acceptor concentration is $\sim 10^{15}$ cm^{-3} for GaAs layers and was determined by polaron measurements to be $\sim 5 \times 10^{16}$ cm^{-3} in the $Al_{0.3}Ga_{0.7}As$ barrier. Assuming that all the acceptors are ionized and that all subsequent holes transfer into the wire, the average separation of two holes in the wires will be ~ 35 nm. An unintentional background acceptor concentration of 5×10^{15} cm^{-3} in the barriers of $GaAs/Al_{0.33}Ga_{0.67}As$ QWs has been demonstrated to produce a significant population of holes in the QWs, resulting in the formation of *positively charged* (X_{2D}^+) *excitons* [Osborne et al., 1996]. The X_{2D}^+ transition was observed as a weak PL peak around $0.97 - 1.35$ meV below the free 2D exciton (X_{2D}, FWHM $= 0.15$ meV). Osborne et al. (1996) studied these charged excitons for different well widths (30, 20, 16.5 and 14 nm), in a variable magnetic field (0.8 T), as a function of temperature ($2-15$ K), and as a function of laser excitation density (0.055 mW/cm^2 – 22 mW/cm^2). In particular they found:

(i) a constant recombination energy for the X_{2D} and X_{2D}^+ transitions at increasing excitation density;

(ii) a strengthening of the X_{2D}^+ peak relative to the X_{2D} peak at increasing power density for a laser energy above the barrier bandgap. This strengthening is explained by the separation of photo-excited electron-hole pairs by the internal electric field, sweeping the holes into the QW and the electrons towards the front surface of the structure;

(iii) a sharp weakening of the X_{2D}^+ transition with increasing temperature. At 15 K, the X_{2D}^+ transition has disappeared, which is interpreted as a dissociation of the 2D exciton from its binding center at temperatures where the thermal energy exceeds its binding energy.

All these results are in striking contrast to our findings. In the perspective of the formation of charged excitons in our dot-like regions, peaks A and B in Fig. 6.3 would be attributed to X_{0D}^+ and X_{0D} transitions, respectively, with a binding energy of the exciton to an excess hole of ~ 1.4 meV. This binding energy would correspond to a dissociation temperature of ~ 16 K. However, we found that both transitions subsist at least up to 35 K, as illustrated in Fig. 6.10.
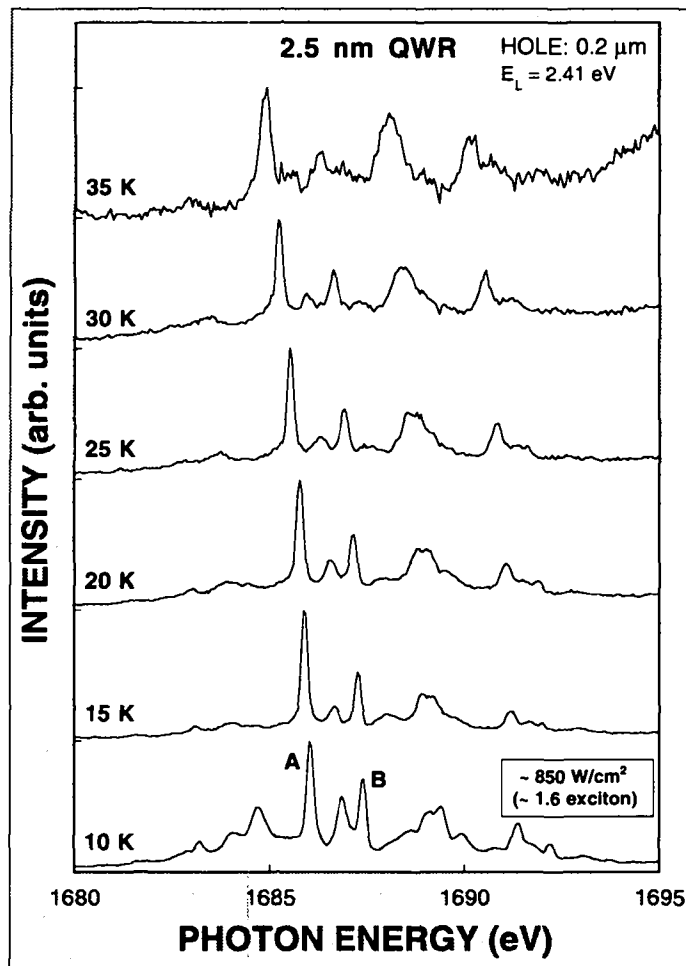
Figure 6.10: Temperature dependence of PL spectra of the 2.5 nm QWR measured through a 0.2 μm hole at $\sim$ 850 W/cm^2. Each spectrum has been normalized to its maximum intensity.

A combined experimental and theoretical study of charged excitons in isolated strained InAs quantum dots has been reported recently [Landin et al., 1998]. Spectra from these QDs consisted of a single line at low excitation power, while additional emission lines appeared at both higher and lower energies at higher excitation density (separation from the main line by about 1 meV). Landin et al. (1998) attributed these lines to neutral and charged excitons and biexcitons, in agreement with perturbative and variational estimates of the binding energies of excitons and charged excitons in similar systems [Lelong and Bastard, 1996a, Lelong and Bastard, 1996b]. However, *they did not observe any shift* of these optical transitions with increasing excitation density.

In summary, we believe that the presence of excess holes in our QWRs may give rise to a fine structure of PL spectra but that it does not yield any convincing explanation of the observed blue shift of individual lines observed at increasing power density. Therefore, the shift of the excitonic transitions very likely results from exciton-exciton

interactions in the dot-like region.

6.4.2 The formation of exciton complexes

Localization of excitons is expected to result in an enhancement of the biexcitonic correlation energy, with respect to free excitons. The measured value of the biexciton binding energy in naturally formed GaAs/AlGaAs QDs is about 4 meV [Brunner et al., 1994a], compared to about 2-3 meV in GaAs/AlGaAs QWs [Bar-Ad and Bar-Joseph, 1992]. Thus, the new transitions in Fig. 6.3 appear in a spectral region expected for excitonic recombination of biexcitonic states. Moreover, the multiplicity of these biexcitonic lines has been predicted by theoretical calculations of quantum many-body states of two electron-hole pairs in a parallelepipedal QD with dimensions comparable to the Bohr radius [Barenco and Dupertuis, 1995]. This interpretation in terms of biexciton states is fully consistent with recent calculations of the two-exciton states in QDs [Nair and Takagahara, 1996]. In this perspective, the multiplet labeled C could be assigned to the biexciton ground state and to excited, but bound, biexciton states, whereas peak D could correspond to a weakly correlated exciton pair. The importance of such a weakly correlated exciton pair has been pointed out by Nair and Takagahara (1996) who found that the wave functions of these states are well approximated by a product of two independent ground states excitons, namely:

$$\Phi_{XX}^{\pm\pm} = \frac{1}{\sqrt{2}}[\phi_X^g(\mathbf{r}_{e_1},\mathbf{r}_{h_1})\phi_X^g(\mathbf{r}_{e_2},\mathbf{r}_{h_2}) \pm \phi_X^g(\mathbf{r}_{e_1},\mathbf{r}_{h_2})\phi_X^g(\mathbf{r}_{e_2},\mathbf{r}_{h_1})], \tag{6.2}$$

where ϕ_X^g is the envelope function of the exciton ground state, $\mathbf{r}_{e_1}$ and $\mathbf{r}_{e_2}$ ($\mathbf{r}_{h_1}$ and $\mathbf{r}_{h_2}$) denote the electron (hole) coordinates, and $\Phi_{XX}^{++(--)}$ is symmetric (antisymmetric) under the interchange of the two electron of the two hole coordinates.

This assignment is further supported by the dependence of the integrated intensity of the different transitions on the excitation density P, as illustrated in Fig. 6.11. The peaks A and B dominate the spectrum at low P and their intensities increase with P. They reach a maximum for $P \sim 750\text{W/cm}^2$ and then saturate at higher values of P. On the other hand, the integrated intensity of the transitions appearing below 1685 meV (labeled C) and the peak D rises more steeply than the intensity of peaks A and B; they dominate the spectrum for $P > 750\text{W/cm}^2$. The steeper increase of the integrated intensity of peaks C and D and the dominance of these peaks at high excitation density strongly support the biexcitonic origin of the additional PL lines [4]. We note that an analogous behavior of 0D-excitons and 0D-biexcitons intensities was observed in QDs

---

[4]The surprisingly superlinear increase of the integrated intensities of peaks A and B with increasing power density may be explained by the non-resonant excitation. This explanation is also consistent with the non-linear increase of the estimated number of excitons in the dot with increasing laser power.
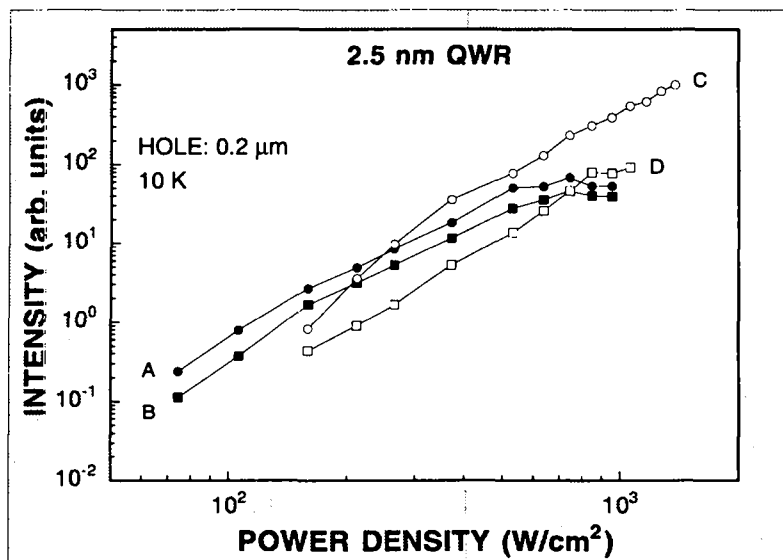
Figure 6.11: Integrated intensities of peaks A, B, C, and D as function of the power density; the photon energy is 2.41 eV. The different density dependence of peaks C, D reflects on the multi-excitonic nature of the states.

naturally formed in GaAs/AlGaAs QWs [Brunner et al., 1994a]. The transitions appearing above 1690 meV in Fig. 6.3 with increasing excitation density may be attributed either to excited excitonic or to multi-excitonic states of the dot. This state filling effect is indicative of Fermi statistics for the exciton gas [Bockelmann et al., 1996]. This corroborates our interpretation of the blue shift based on a dominant repulsive interaction originating from Pauli exclusion principle.

6.5 Summary

We have measured PL spectra of our high-quality QWRs through holes which vary in size from 2.0 μm down to 0.2 μm in width. For sufficiently thin QWRs it was possible to observe directly the localization of 1D excitons in local potential minima. PL spectra detected through the smallest apertures (0.2 μm) were attributed to recombination of excitons in isolated QD-like potential wells. Homogeneously broadened lines could be resolved. The effect of exciton-exciton interactions on the PL properties of localized excitons has been evidenced. A shift to high energy of the exciton resonance at exciton densities much below the Mott density has been attributed to the predominantly repulsive interaction between excitons due to the Pauli exclusion principle. The formation of multi-excitonic states in the dot has also been evidenced by the evolution of the finely structured PL spectrum with increasing excitation density.

Chapter 7

Investigation of the diffusion of 1D excitons

7.1 Introduction

Theoretical studies on transport properties of electrons confined in QWR structures have predicted a drastic suppression of elastic scattering [Sakaki, 1980, Fishman, 1986]. This reduction of particle scattering rates, which results from the reduced phase space in 1D systems, would make these systems useful for ultrafast field effect transistors and new ballistic-electron devices. Sakaki (1980) calculated ionized impurity scattering rates and estimated electron mobilities well beyond 10^6 cm^2/Vs for a properly designed GaAs QWR at zero temperature. For the same ideal 1D system, Fasol predicted very small electron-electron scattering rates resulting in ultra long phase coherence lengths (up to 50 μm around 4 K) [Fasol, 1992]. However, electron mobilities in 1D systems are particularly sensitive to electron correlations and to electron scattering due to disorder [Gold and Ghazali, 1990, Tanatar and Gold, 1995, Thakur and Neilson, 1997]. Disorder has been found to enhance scattering rates and to drive the system toward localization, while electron correlations at low electron densities inhibit the screening which would otherwise suppress localization [Gold and Ghazali, 1990, Tanatar and Gold, 1995, Thakur and Neilson, 1997]. It has also been shown theoretically that in a random potential two repelling or attracting particles can propagate coherently on a distance much larger than the one-particle localization length [Shepelyanski, 1994, Weinmann et al., 1995].

Several experimental methods have been used to measure the transport of excitons in GaAs bulk and QW structures. Hegarty et al. (1984) used a laser-induced transient grating technique to study exciton transport under resonant excitation of the electron-heavy hole transition. Smith et al. (1989) have reported the detailed analysis of the in-plane carrier transport measured by a spatially scanned pumb-probe

technique at relatively high carrier densities and observed the effect of nonequilibrium phonons emitted during the energy relaxation of photogenerated carriers. Another way of studying the motion of carriers is realized by time-of-flight (TOF) arrangements, which require high spatial and temporal resolution. In vertical TOF experiments a high spatial resolution can be obtained by using specific probe layers, e.g., QWs embedded in the sample structure [Hillmer et al., 1986, Hillmer et al., 1991, Deveaud et al., 1987, Deveaud et al., 1988]. The transport distance can be either determined by two different QWs [Hillmer et al., 1986, Hillmer et al., 1991] or by the sample surface and a single QW [Deveaud et al., 1987, Deveaud et al., 1988]. In high resolution lateral TOF studies the flight distance can be defined by opaque masks with transparent windows [Nelson et al., 1982] or apertures [Hillmer et al., 1988, Hillmer et al., 1989, Hillmer et al., 1990] which are placed on the semiconductor surface.

Experimental $e - h$ pair mobilities as a function of temperature in 2D systems have been investigated by Hillmer et al. ($10 < T < 230$ K) [Hillmer et al., 1989, Hillmer et al., 1992], Takahashi et al. ($4 < T < 40$ K) [Takahashi et al., 1993], and Oberhauser et al. ($2 < T < 30$ K) [Oberhauser et al., 1993]. Their results have been explained by the contributions of different scattering mechanisms: Interaction of the excitons with the interface roughness, with barrier-alloy disorder, with acoustic and optical phonons. For all temperatures, an increase of the excitonic diffusivity with increasing well width ($1 < L_z < 20$ nm) has been observed [Hillmer et al., 1992, Hillmer et al., 1993], in agreement with calculations of Basu and Ray (1991). The experimental exciton mobility has also been found to strongly increase with increasing Al content in the barrier [Hillmer et al., 1993]. The investigation of the dependence of the exciton diffusivity on excitation density yielded contradictory results. Takahashi et al. (1993) and Akiyama et al. (1994) reported an increased diffusivity for decreasing excitation density whereas Yoon et al. (1992) found the opposite behavior. We note that Smith et al. (1989) reported a much more complex power dependence of carrier transport in multiple GaAs QWs.

Despite the interest stemming from the theoretical expectations for 1D systems presented in the first paragraph above, the observation of the predicted features has been thwarted by the technological challenge in fabricating QWR structures with small broadening of 1D subbands and with sufficiently large subband spacing. Up to now, the investigation of electron-hole pair transport in 1D systems has been restricted to the determination of ambipolar [Tang et al., 1998] and exciton [Nagamune et al., 1995] diffusion lengths. An anisotropy in the diffusion along and perpendicular to the wire direction has been observed [Tang et al., 1998, Nagamune et al., 1995] and a maximum diffusion length of 4 μm for a 15 nm thick QWR at 15 K and 650 kW/cm^2 exci-

tation power density has been reported [Nagamune et al., 1995]. Excitonic effects are expected [Ogawa and Takagahara, 1991a, Glutsch and Bechstedt, 1993], and have been found experimentally (see Chap. 4), to dominate the optical properties of semiconductor QWRs. Reduced exciton-exciton [Oestreich et al., 1993, Kumar et al., 1998] and exciton-carrier [Kumar et al., 1998] scattering have been inferred from time-resolved optical investigations of etch-patterned QWRs [Oestreich et al., 1993] and lateral super-lattices [Kumar et al., 1998]. Structural disorder in QWR structures has been demonstrated to lead to inhomogeneous broadening of the optical spectra (Chaps. 4,5,6) and to localization of 1D excitons in local potential minima at low temperature (Chap. 6). However, the impact of both the electron-hole Coulomb interaction and disorder related effects on the transport properties of QWR structures has not been evaluated yet.

In this chapter we report the optical investigation of the diffusion of 1D excitons in QWRs. The temperature dependence of the exciton diffusivity for different QWR sizes has been studied. We will show that larger diffusivities for narrower wires at sufficiently high temperature result from the strong suppression of elastic scattering in 1D systems and from the non-negligeable contribution of intersubband scattering. We also examine the dependence of the exciton diffusivity on excitation wavelength and excitation density. Part of these results has been submitted for publication in Physical Review Letters [Vouilloz and Kapon, 1998].

7.2 Experimental

The experiments were performed on the 2.5 nm, 6.9 nm, and 8.8 nm QWRs. An exciton TOF technique has been used in the experiments. Diffusion distances are determined by employing microstructured masks deposited on the surface of the samples. A tunable Ti:Sa laser producing $\sim$ 3 ps pulses at 76 MHz is used for the excitation. The exciting photon energy corresponded to selective excitation of the wires and was 1.76 eV, 1.65 eV, and 1.63 eV for the 2.5 nm, 6.9 nm and 8.8 nm QWR sample, respectively. The emitted light was dispersed by a 46 cm spectrograph and detected with either a cooled CCD for time-integrated PL spectra or a cooled microchannel plate photomultiplier for time-resolved PL. For time-resolved experiments a spectral range corresponding to the QWR PL peak was selected ($\sim$ 6−10 meV). The temporal evolution of the PL was obtained by a time-correlated single photon-counting technique and a typical instrumental response of $\sim$ 60 ps was achieved. For all three investigated structures we estimated an upper value of the photoexcited carriers density in the QWR of about 5×10^5 cm^{-1}. The samples, the method, and the experimental setup are described in detail in Secs. 3.2.2, 3.3.4, and 3.4.5, respectively.

7.3   Photoluminescence decay times

Knowledge of the carrier lifetime and, in particular, its dependence on the wire thickness and the temperature are essential for the evaluations of the diffusivity presented hereafter. Figure 7.1 depicts the lifetime as a function of temperature for the three different wire thiknesses. It corresponds to the PL decay time measured from uncovered parts (no Al mask) of the sample. The lifetimes start at helium temperatures at values
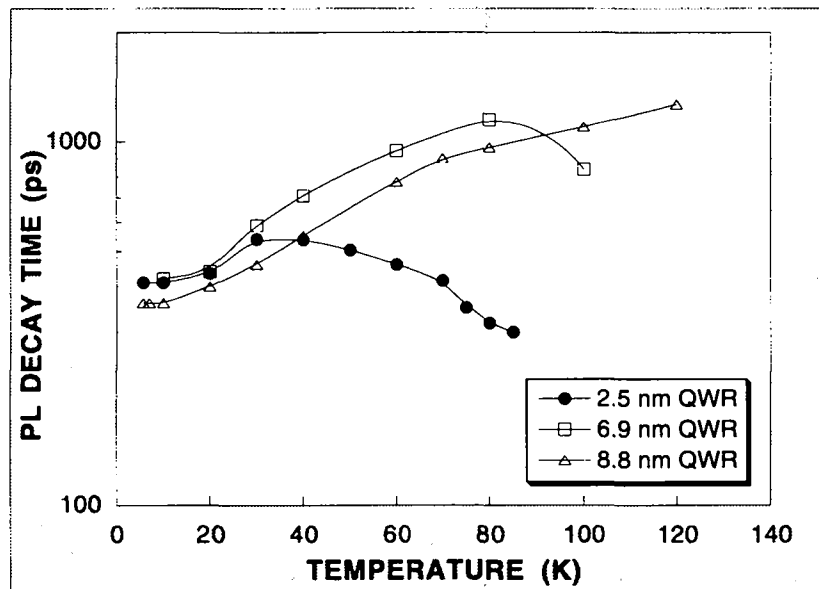
Figure 7.1: QWR lifetimes of the 2.5 nm, 6.9 nm, and 8.8 nm QWRs as a function of temperature. The exciting photon energy corresponds to selective excitation of the wires and is 1.76 eV, 1.65 eV, and 1.63 eV for the 2.5 nm, 6.9 nm and 8.8 nm QWR sample, respectively. The photoexcited carriers density in the QWR is about 5×10^5 cm^{-1} for all three wire samples.

of about 400 ps and increase with rising temperature to values which depend on the wire thickness. At still higher temperatures ($T > 80$ K, e.g., for the 6.9 nm QWR) the lifetime decreases due to dominant role of non-radiative recombination channels. The temperature dependence ($5 < T < 150$ K) of the exciton radiative lifetime has been studied recently [Oberli et al., 1997, Oberli et al., 1998] and found to differ from the $\sqrt{T}$ dependence expected in ideal, perfectly uniform wires, in contrast to previous experimental reports [Gershoni et al., 1994, Akiyama et al., 1994a, Akiyama et al., 1994b]. Instead, an exponential rise of the radiative time is found at temperatures above 50 K; the steepness of this rise is found to be larger for thinner wires. At the lowest temperatures, the similar lifetimes observed for different wire thicknesses are attributed to the effect of localization that enhances more effectively the radiative lifetime of excitons in the presence of stronger disorder thereby balancing the inherently larger oscillator strengths of thinner wires.

7.4 Time-resolved luminescence profiles

Figure 7.2 presents an overview of the time-resolved PL of QWRs with three different thicknesses at various temperatures in the range 5 − 80 K. In this figure, experimental profiles from uncovered parts of the samples (bold solid line) are shown together with profiles measured through a square hole, 2 μm in width (thin solid line). For the unmasked samples, the time evolution is determined by the corresponding lifetime, while the profiles measured through the apertures show the influence of the exciton motion. Excitons moving under the opaque area during their lifetime do not contribute to the detected PL resulting, thus, in a faster PL decay. Figure 7.2 shows that the impact of the exciton motion on the luminescence profiles increases with temperature. The influence of the wire thickness on the diffusion process is more difficult to extract from this figure as PL profiles depend both on the exciton motion and the exciton lifetimes, the latter beeing strongly dependent on the wire structure (see Fig. 7.1). A striking feature is noticed for the 6.9 nm and the 8.8 nm QWR samples: An enhancement of the diffusion is observed with decreasing temperature below 10 K. This behavior has not been observed for the 2.5 nm QWR.

7.5 Evaluation of the diffusivity by line-shape fits

To evaluate the diffusivity for each QWR structure as a function of temperature we compare our experimental results with theoretical calculations based on the 1D diffusion equation (see section 3.3.4). The best fits to the experimental profiles are displayed in Fig. 7.2 by the dashed lines and the corresponding diffusivities are shown in Fig. 7.3 (a). For a nondegenerate distribution, the Einstein relation connects the mobility and diffusivity :

$$\mu = eD/k_BT. \tag{7.1}$$

Even in degenerate distributions, D and μ are linearly related [Yoon et al., 1992]:

$$\mu = C(eD/k_BT), \tag{7.2}$$

where C is a degenerate-dependent constant on the order of 1 − 10. The temperature dependence of the exciton mobility estimated with Eq. 7.1 is displayed in Fig. 7.3 (b).

Overall, we observe a strong dependence of the diffusivities and of the mobilities on temperature: They stay approximately constant and close to zero at low temperature and then increase with temperature with a slope that depends on the wire thickness. The thinner the wire is, the steeper is the variation of D and μ with the temperature. In striking contrast with similar investigations in QWs [Hillmer et al., 1989], we find in
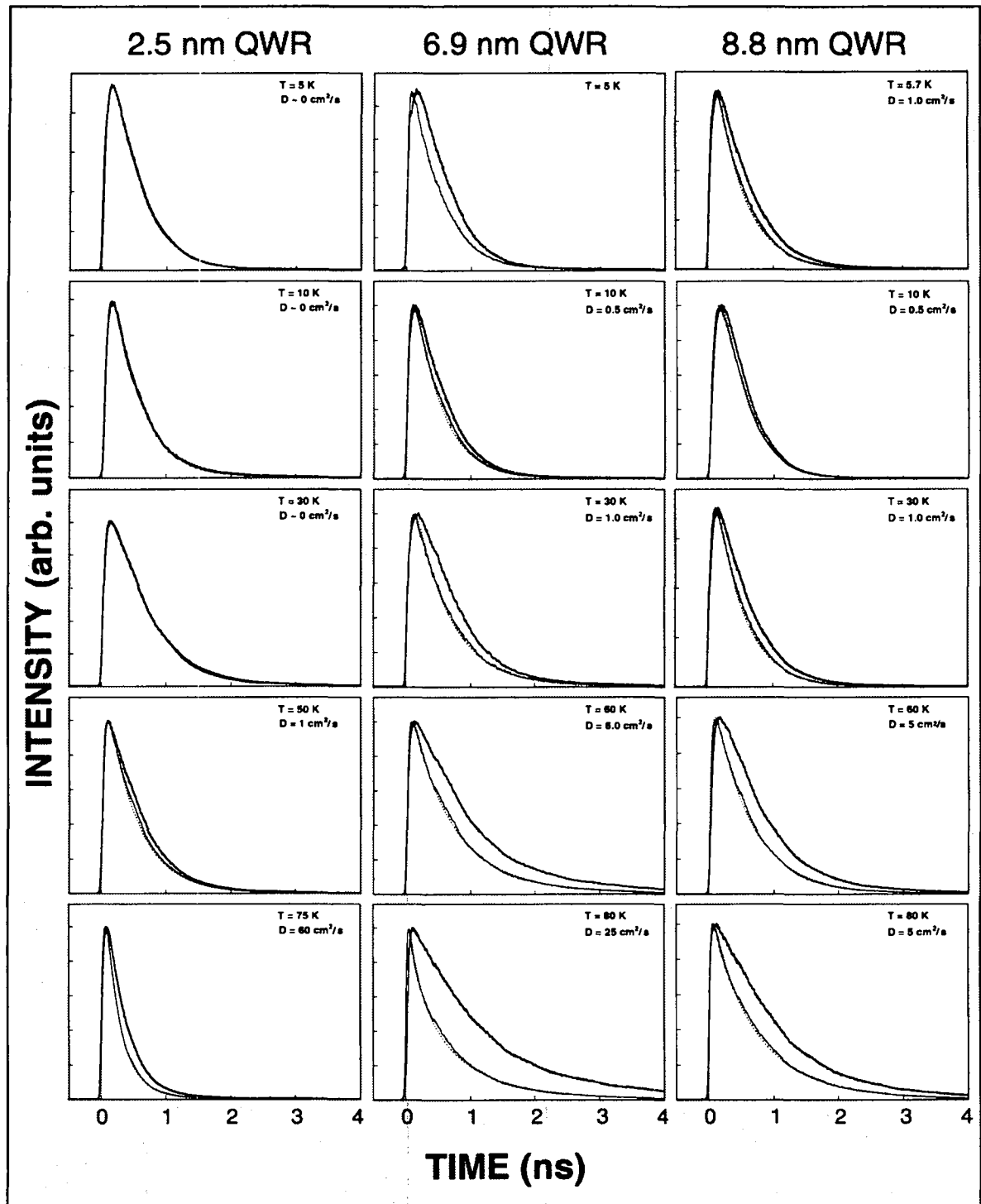
Figure 7.2: Experimental luminescence profiles (thin solid line) measured through a 2 μm hole on three different QWR structures. Corresponding profiles measured from uncovered parts of the samples are given by the bold solid lines. The best theoretical profiles based on the diffusion equation are displayed by dashed lines; the corresponding values of D are given at each temperature. The exciting photon energy corresponds to selective excitation of the wires and is 1.76 eV, 1.65 eV, and 1.63 eV for the 2.5 nm, 6.9 nm and 8.8 nm QWR sample, respectively. The photoexcited carriers density in the QWR is about 5 × 10⁵ cm⁻¹ for all three wire samples.
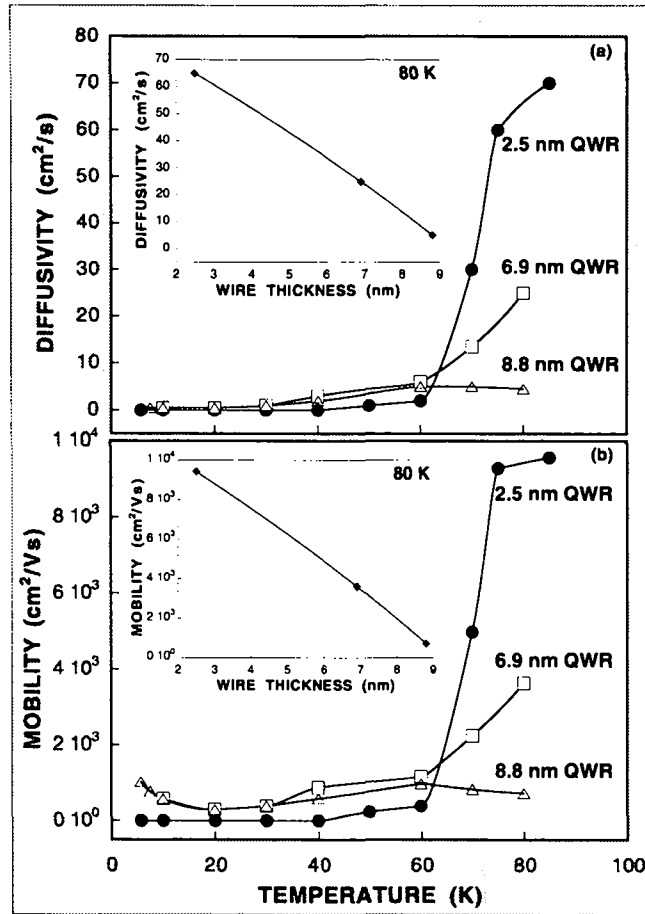
Figure 7.3: (a) Diffusivities and (b) mobilities as a function of temperature for the 2.5 nm, the 6.9 nm, and the 8.8 nm QWRs. The lines are drawn to guide the eye. The exciting photon energy corresponds to selective excitation of the wires and is 1.76 eV, 1.65 eV, and 1.63 eV for the 2.5 nm, 6.9 nm and 8.8 nm QWR sample, respectively. The photoexcited carriers density in the QWR is about 5×10^5 cm^{-1} for all three wire samples. The inset shows the dependence of the diffusivity (a) and of the mobility (b) at 80 K with the wire thickness. Error bars are smaller than the size of the symbols.

this upper part of the temperature range *larger diffusivities and mobilites for thinner wires*. We attribute this peculiar behavior to the effect of lateral confinement on the band structure, as further discussed below. We also note that profiles measured at 5.7 K for the 6.9 nm QWR sample still show an effect of the exciton motion, as displayed in Fig. 7.2. However, our model does not allow us to reproduce the experimental profile as the decay of the luminescence measured from an uncovered part of the sample exhibits two constants of time.

7.5.1 Dependence of the diffusivity on the excitation density

We studied the dependence of D on the excitation power density at low temperature (10 K) corresponding to localized excitons, and at intermediate temperatures (50 K and

60 K for the 2.5 nm and the 8.8 nm QWRs, respectively) for which partial delocalization of excitons by thermal energy is expected to become effective. This dependence is shown in Fig. 7.4. At 10 K, the diffusivity in both QWR structures is found to stay
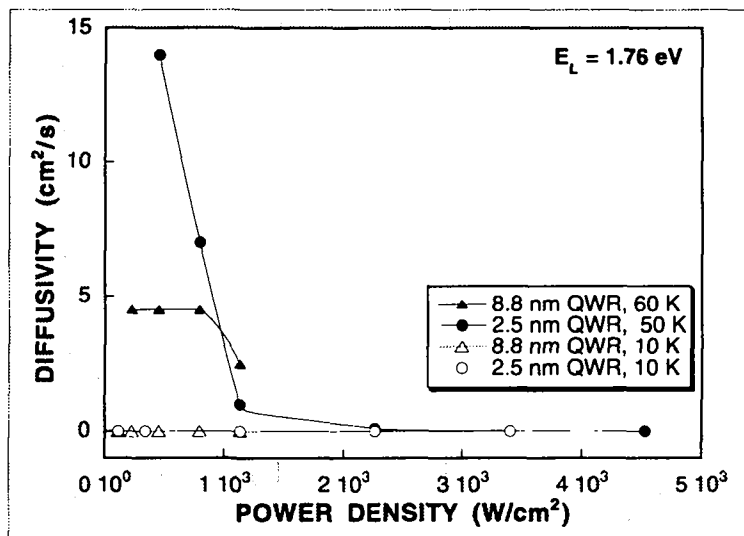
Figure 7.4: Diffusivity as a function of the excitation power density in the 2.5 nm and the 8.8 nm QWRs. The lines are drawn to guide the eye.

constant and close to zero over the investigated power density range. At intermediate temperatures (50 K and 60 K), we observe a slight reduction of D for the 8.8 nm QWR when increasing the power density by a factor of $\sim$ 5, whereas a drastic decrease of D is measured for the 2.5 nm QWR when the power density is increased by a factor of $\sim$ 10. We note that studies as a function of the excitation density are limited at high excitation power by spectral overlapping of PL coming from QW parts of the heterostructure and that related to QWRs.

7.5.2   Dependence of the diffusivity on the exciting-photon energy

Figure 7.5 shows the influence of the exciting-photon energy on the diffusivity of excitons in the 8.8 nm QWR, at 60 K. Photon energies (E_L) in this figure are much below the bandgap of the AlGaAs barrier ($\sim$ 1.9-1.95 eV). The diffusivity rapidly decreases from $D \sim 5$ cm^2/s for $E_L = 1.63$ eV to $D \sim 3.5$ cm^2/s for $E_L = 1.65$ eV and then slowly decreases when further increasing E_L to 1.76 eV.
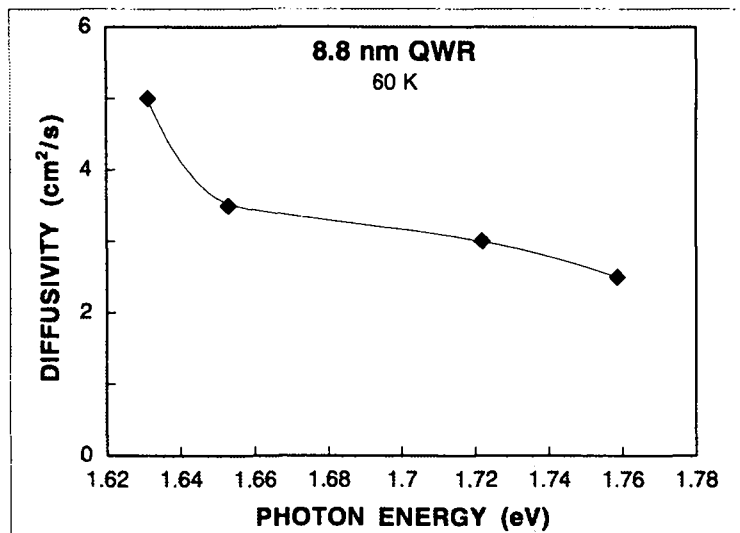
Figure 7.5: Diffusivity as a function of the exciting-photon energy in the 8.8 nm QWR. The line is drawn to guide the eye. The power density is ~ 1 kW/cm^2.

7.6 Evaluation of diffusion lengths

The diffusion lengths for all three QWR structures can be estimated from the values of D (see section 7.5) and the lifetimes (see section 7.3) by the relation:

$$L = \sqrt{D\tau_d}.$$

Figure 7.6 shows the temperature dependence of the diffusion lengths of excitons confined in the 2.5nm, 6.9nm, and 8.8 nm QWRs. We see a global increase of the diffusion lengths with increasing temperature. However, two points should be noted: First, there is a small decrease of the diffusion length in the 8.8 nm QWR when raising the temperature from 5.7 K to 10 K. Second, the diffusion length is close to zero in the 2.5 nm QWR structure for temperatures below 40 K, which results from values of $D \sim 0$ in this temperature range.

7.7 Discussion

We explain the dependence of the diffusivity on temperature and on wire thickness by considering the contributions of different scattering mechanisms: scattering by excess holes, scattering by acoustic and optical phonons, scattering by the interface roughness, and carrier-carrier scattering. In general, two pictures for diffusion should be distinguished:
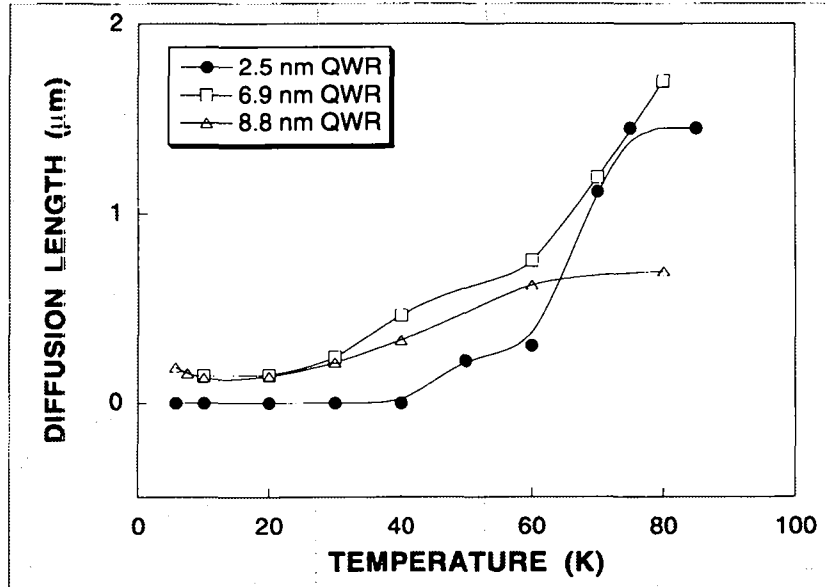
Figure 7.6: Diffusion length as a function of temperature for the 2.5 nm, 6.9 nm, and 8.8 nm QWRs. The lines are drawn to guide the eye. The exciting photon energy corresponds to selective excitation of the wires and is 1.76 eV, 1.65 eV, and 1.63 eV for the 2.5 nm, 6.9 nm and 8.8 nm QWR sample, respectively. The photoexcited carriers density in the QWR is about 5×10^5 cm^{-1} for all three wire samples.

(i) The ambipolar diffusion process; in this case two independent particles (electron and hole) are considered and the ambipolar mobility is given by:

$$\mu_{amb} = \frac{2}{\mu_e^{-1} + \mu_h^{-1}}. \tag{7.3}$$

(ii) The exciton diffusion process; in this case the particle is scattered as a single unit.

Comparison of theoretical calculations with experimental observations of carrier diffusion in GaAs QWs has shown that the experiments can be well described by excitonic diffusion at carrier densities corresponding to our experimental conditions [Hillmer et al., 1989, Akiyama et al., 1994c]. The ambipolar description, on the contrary, leads to much higher diffusivities than those found experimentally. As Coulomb correlations are further enhanced in 1D systems and are found to be relevant at carrier densities up to the optical gain regime (see Sec. 2.5.3 and [Piermarocchi et al., 1998]), we believe the exciton diffusion process to be also dominant in our QWR structures.

The scattering rates corresponding to the different scattering mechanisms can be added using the Mattiessen rule to obtain the total scattering rate:

$$\frac{1}{\langle \tau_X \rangle} = \frac{1}{\langle \tau_h \rangle} + \frac{1}{\langle \tau_{ac} \rangle} + \frac{1}{\langle \tau_{op} \rangle} + \frac{1}{\langle \tau_{rough} \rangle} + \frac{1}{\langle \tau_{X-X} \rangle}, \tag{7.4}$$

where h denotes holes, ac, acoustical phonons, op, optical phonons, $rough$, interface roughness, and $X - X$, exciton-exciton interaction; $\langle \ \rangle$ represents the average over the
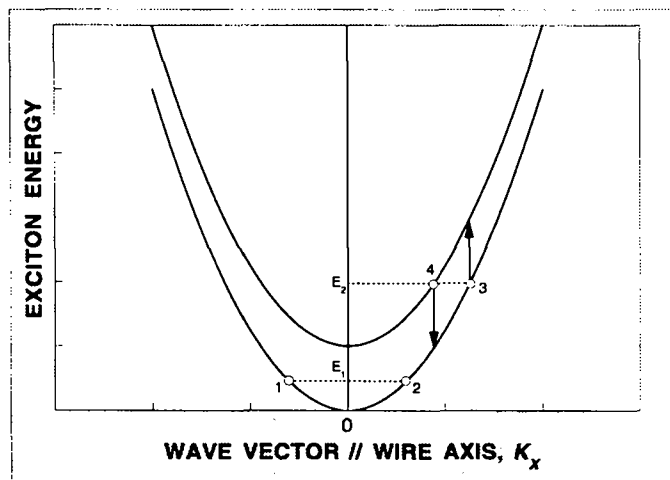
Figure 7.7: Schematic representation of the 1D exciton dispersion along the axis of a perfect QWR. Excitons 1 and 2 in the lowest subband illustrate the drastic reduction of exciton-exciton scattering with strict conservation of energy and wave vector K_X. Intersubband scattering is allowed for higher exciton energies (see excitons 3 and 4 at energy E_2).

distribution function defined in the same way as in the case of electrons [Nag, 1980]. The scattering rate at a given energy E, $\tau_{\nu,i}^{-1}(E)$, is expressed as [Ferry and Goodnick, 1997]:

$$\tau_{\nu,i}^{-1}(E) = \sum_{j,\mathbf{k}'} S_{i,j}(\mathbf{k},\mathbf{k}') \left[1 - \frac{\tau_{\nu,j}(E)}{\tau_{\nu,i}(E)} \cos\theta \right], \tag{7.5}$$

where ν labels a scattering process, $S_{i,j}(\mathbf{k},\mathbf{k}')$ represents the scattering rate from a state in subband i of wave vector $\mathbf{k}$ to a state in subband j with wave vector $\mathbf{k}'$, and θ is the angle between $\mathbf{k}$ and $\mathbf{k}'$. For a 1D system, the only possible choice of scattering is either forwards or backwards, so that $\cos\theta$ is either 1 or -1. Figure 7.7 illustrates this restriction for exciton-exciton scattering with strict conservation of energy and wave vector K_X. The scattering rate $S_{i,j}(\mathbf{k},\mathbf{k}')$ is usually calculated in first-order perturbation theory using the Fermi golden rule:

$$S_{i,j}(\mathbf{k},\mathbf{k}') = \frac{2\pi}{\hbar} |\langle \mathbf{k}',j|V_{\nu}(\mathbf{r})|\mathbf{k},i\rangle|^2 \delta(E_{fin} - E_{in}), \tag{7.6}$$

where $V_{\nu}(\mathbf{r})$ is the potential associated with a particular scattering mechanism, and the delta function applied to the initial (E_{in}) and final (E_{fin}) energies of the system includes the possible contribution of phonon absorption or emission. For a cylindrical QWR with infinite potential barriers at $r = R_0$, the squared matrix element $|M_{\mathbf{k}',\mathbf{k}}|^2 = |\langle \mathbf{k}',1|V_{rough}(\mathbf{r})|\mathbf{k},1\rangle|^2$ for the scattering by interface roughness from state $\mathbf{k}$ to $\mathbf{k}'$ in the first subband can be written as [Gold and Ghazali, 1990, Motohisa and Sakaki, 1992]:

$$|M_{\mathbf{k}',\mathbf{k}}|^2 = \frac{\hbar}{m^2} \frac{\beta_{01}^4}{R_0^6} \sqrt{\pi}\eta \delta^2 e^{-(\mathbf{k}'-\mathbf{k})^2/4}, \tag{7.7}$$

where δ and η are the height and the range parameters of the roughness, respectively. A Gaussian-like decay of the fluctuations has been assumed. β_{nl} is the lth zero of the Bessel function of order n. For intersubband scattering between subband nl and subband mk, β_{01}^4 has to be replaced by $\beta_{nl}^2\beta_{mk}^2$. According to Eq. 7.7, the width dependence of the mobility in the infinite barrier approximation is the same for 1D and 2D systems: $\mu \propto R_0^6$ [Gold and Ghazali, 1990, Basu and Ray, 1991].

In case of a nondegenerate semiconductor, the averaged relaxation time may be written as [Ferry and Goodnick, 1997]:

$$\langle \tau_{\nu,i} \rangle = \frac{\int\limits_0^\infty dE \rho_i(E) E \tau_{\nu,i}(E) e^{-E/k_B T}}{\int\limits_0^\infty dE \rho_i(E) E e^{-E/k_B T}}, \quad \nu \in \{h, ac, op, rough, X - X\}, \tag{7.8}$$

where $\rho_i(E)$ is the density of states per unit energy of subband i. The mobility μ_X of the 1D excitons can be then expressed in terms of τ_X by:

$$\mu_X = (e/M)\langle \tau_X \rangle, \tag{7.9}$$

where M is the effective exciton mass ($M = 0.18\, m_0$ is assumed). Using the Einstein relation between μ_X and D (Eq. 7.1) we get:

$$\langle \tau_X \rangle = (M/k_B T) D. \tag{7.10}$$

For temperatures below 60 K, we found $\langle \tau_X \rangle < 0.12$ ps for all three wire samples [1]. At higher temperatures we found a maximum scattering time of 0.97 ps, 0.37 ps, and 0.1 ps, for the 2.5 nm, 6.9 nm, and 8.8 nm QWRs, respectively. In the following, we will use these scattering times to estimate the significance of different scattering mechanisms.

We have mentioned in Sec. 6.4.1 the possible presence of excess holes in our QWRs due to unintentional p-background doping of the GaAs and AlGaAs layers. Scattering with these holes would give rise to a temperature dependence of the exciton mobility. In 3D semiconductors, scattering of electrons by ionized impurities yields a temperature dependent mobility of the form $\mu_{imp}^{3D} \propto T^{3/2}$, whereas in 2D systems the mobility varies as $\mu_{imp}^{2D} \propto T$ [Ferry and Goodnick, 1997]. Mobility limits for charged-impurity scattering in 1D systems have been calculated by several authors within various approximations [Sakaki, 1980, Fishman, 1986, Lee and Spector, 1983, Gold and Ghazali, 1990, Tanatar and Gold, 1995]; none of these studies, however, reported on the temperature dependence of this scattering process. Although holes are mobile in contrast to ionized impurities, we expect some analogy between the two scattering mechanisms. To the best

---

[1] To estimate mobilities and scattering times we assume equal lattice and carriers temperatures. This assumption is reasonable for lattice temperatures greater than ~ 40 K (see, e.g., [Shah, 1996]), whereas it leads to overestimated values of μ_X and $\langle \tau_X \rangle$ below 40 K.

of our knowledge, calculations or experiments on the scattering of excitons by excess holes in QWR structures have not been performed. Akiyama et al. have studied the 2D exciton mobility at 77 K in GaAs/AlGaAs QWs as a function of p-type doping; they have reported values of the exciton-hole scattering time $\langle \tau_h \rangle$ in the range $0.6 - 1.5$ ps for values of p between 2×10^{10} cm^{-2} and 2×10^{11} cm^{-2} [Akiyama et al., 1994c]. As mentioned in Sec. 6.4.1, the average distance between excess holes in the wire is estimated to be ~ 35 nm, which corresponds to an areal density $\sim 1 \times 10^{11}$ cm^{-2}. Scattering times reported by Akiyama et al. (1994c) are much longer than our values of $\langle \tau_X \rangle$ below 60 K. Therefore, and if we tentatively analyze our measurements by comparison with results obtained for 2D systems, the scattering of 1D excitons by excess holes is expected to be noticeable in a temperature range restricted to $T > 60$ K, for the 2.5 nm and 6.9 nm QWRs. This scattering mechanism may contribute to the increase of the exciton mobility with increasing temperature as excitons with a larger thermal energy are less affected by the coulombic field of the excess holes. The influence of the wire size on this scattering mechanism is not clear yet.

The increase of the exciton diffusivity with temperature for all three wire sizes is attributed, aside from the possible contribution of exciton-holes scattering, to the predominance of the interface-roughness scattering in the investigated temperature range. Interface roughness causes a fluctuation of the confinement energies and acts as a scattering potential for mobile excitons. This process reduces the exciton mobility or even localizes excitons at low temperature. In our experiments, the PL is spectrally integrated over the whole QWR line. Therefore, we can not discriminate between the contribution to PL profiles of localized and delocalized excitons. In the localized regime, the diffusion is determined by phonon-assisted exciton migration among dot-like domains [Takagahara, 1989]. In the delocalized regime, the diffusion of excitons is determined by the inelastic scattering with delocalized phonons and by the elastic scattering with excess charge carriers and interface roughness [Takagahara, 1989]. The increase of the 1D excitons diffusivity with temperature is similar to experimental observations [Hillmer et al., 1989] and theoretical calculations [Basu and Ray, 1991] for 2D excitons in GaAs QWs of various thickness L_z. The mobility of 2D excitons first increases as $T^{3.4}$ due to interface roughness scattering [Basu and Ray, 1991], and exhibits a maximum value around 100 K [Hillmer et al., 1989, Hillmer et al., 1993]. At higher temperature, the mobility decreases due to the dominant contributions of inelastic scattering of delocalized excitons with acoustic and optical phonons [Hillmer et al., 1989, Basu and Ray, 1991]. For $T \leq 60$ K the effect of disorder is strongly pronounced in our 1D structures: Values of D smaller than 6 cm^2/s are found for all three QWR samples and excitons are even

completely localized ($D \sim 0$) in the 2.5 nm QWR at $T < 40$ K. Experimental investigations of the diffusion in 2D systems yielded a $L_z^{2.5}$ dependence of the mobility [Hillmer et al., 1989]. In contrary to these theoretical and experimental results we have observed larger diffusivities for thinner wires above 60 K.

As mentioned above, scattering of localized 1D excitons with acoustic phonons may yield a non-vanishing diffusivity at low temperature. Such a diffusion process is expected to become more efficient with temperature as the occupation number of phonons increases with T. Localization stems from fluctuations of the QWR cross-section and possibly alloy disorder along the wire axis (see Chap. 6). For the three QWRs considered here, we estimated the fluctuation ΔE of the electron ground state energy due to a monolayer increase of the GaAs thickness at the crescent center. We found $\Delta E \approx -7.5$ meV, $\Delta E \approx -3$ meV, and $\Delta E \approx -1.5$ meV, for the 2.5 nm, 6.9 nm, and 8.8 nm QWRs, respectively (see Table 6.1). The depth of these localization potentials is reflected on the temperature dependence of the diffusivity. For the 2.5 nm QWR, the localization potential is deep enough to prevent any hopping of excitons by interaction with acoustic phonons at low temperature, which results in values of D close to zero for $T \leq 40$ K. For $40 < T \leq 60$ K, phonon-assisted migration of excitons becomes effective and the diffusivity slowly increases with T. At still higher temperature, the diffusivity is mainly determined by the contribution of delocalized excitons. Localization potential are shallow in our thickest QWR structures, which shows up as non-vanishing values of D and as a slow increase of the diffusivity with temperature. As for the thinnest QWR, the diffusivity is progressively dominated by the contribution of delocalized excitons with increasing thermal energy.

We attribute our observation of increasing values of the diffusivity for decreasing wire size above 60 K to the strong reduction of the phase space available for any elastic scattering process in the wire, together with the specificity of the band structure associated to each QWR sample. The strong reduction of elastic scattering rates in 1D systems has been predicted by Sakaki who illustrated it by calculations of the mobility limited by electron-ionized impurity scattering [Sakaki, 1980] and of the mobility limited by interface roughness scattering [Motohisa and Sakaki, 1992]. We note that the exact determination of the electron mobility in 1D structures necessitates the inclusion of exchange and correlation effects in the calculations [Gold and Ghazali, 1990, Tanatar and Gold, 1995, Thakur and Neilson, 1997]. Depending on the electron density and on the wire size, these many-body effects may enhance or decrease the electron mobility [Thakur and Neilson, 1997]. For a temperature of 80 K we have found in the 2.5 nm and 6.9 nm QWRs values of the diffusivity larger than the ones measured in QWs of corresponding thicknesses [Hillmer et al., 1989, Hillmer et al., 1993], as displayed in

Table 7.1: Comparison of diffusivities and mobilities of 1D and 2D excitons at 80 K for different wire and well thicknesses. Values of D and μ in QWs are taken from [Hillmer et al., 1993]. Total scattering times $\langle \tau_X \rangle$ are indicated in each case.

	thickness (nm)	D (cm^2/s)	μ (cm^2/Vs)	$\langle \tau_X \rangle$ (ps)
	2.5	65	9430	0.97
QWR	6.9	25	3630	0.37
	8.8	5	730	0.07
	2.5	~ 5	~ 700	~ 0.07
QW	5	~ 17	~ 2500	~ 0.25
	8	~ 21	~ 3000	~ 0.31

Table 7.1; the total scattering times $\langle \tau_X \rangle$ are also indicated in each case. We attribute this result to the 1D nature of the exciton diffusion in our QWRs, although the comparison is done with QW structures grown under different conditions (MBE growth). The wire size dependence of the diffusivity above 60 K is opposite to theoretical calculations in 1D [Gold and Ghazali, 1990, Motohisa and Sakaki, 1992] (see Eq. 7.7) and 2D [Basu and Ray, 1991] systems. These calculations, however, neglect the contribution of intersubband scattering. In QW structures, intersubband scattering is dominated by interface roughness scattering at low temperature and scattering with acoustic and optical phonons at high temperature [Hillmer et al., 1989, Basu and Ray, 1991]. In QWRs and at temperatures where the contribution of delocalized excitons is dominant, elastic scattering is strongly suppressed and intersubband scattering appears to be non-negligeable. Intersubband scattering may stem from exciton-exciton interactions, from the interface roughness (see Eq. 7.7), or from exciton-phonon interaction. Figure 7.8 displays PLE spectra of the 2.5 nm and of the 6.9 nm QWRs; PLE spectra of the 8.8 nm QWR sample have been shown in Fig. 4.4, Sec. 4.4.1. Subband separations between the two lowest excitonic transitions in the 2.5 nm, 6.9 nm, and 8.8 nm QWRs are revealed by these PLE measurements to be 23 meV, 13.4 meV, and 11.9 meV, respectively. Therefore, intersubband scattering may differentiate diffusion processes in QWRs of different sizes, as less final states are available for scattering in thinner wires. Our interpretation is corroborated by Monte-Carlo simulations on the electron velocity at 77 K in a multisubband GaAs/AlGaAs QWR which have evidenced a reduction of intersubband scattering by phonons with increasing confinement [Briggs and Leburton, 1988].

We shall now discuss scattering times associated with exciton-acoustic phonon interaction that is expected to give the most significant contribution of the exciton-phonon scattering at low temperature [Hillmer et al., 1989, Basu and Ray, 1991]. The
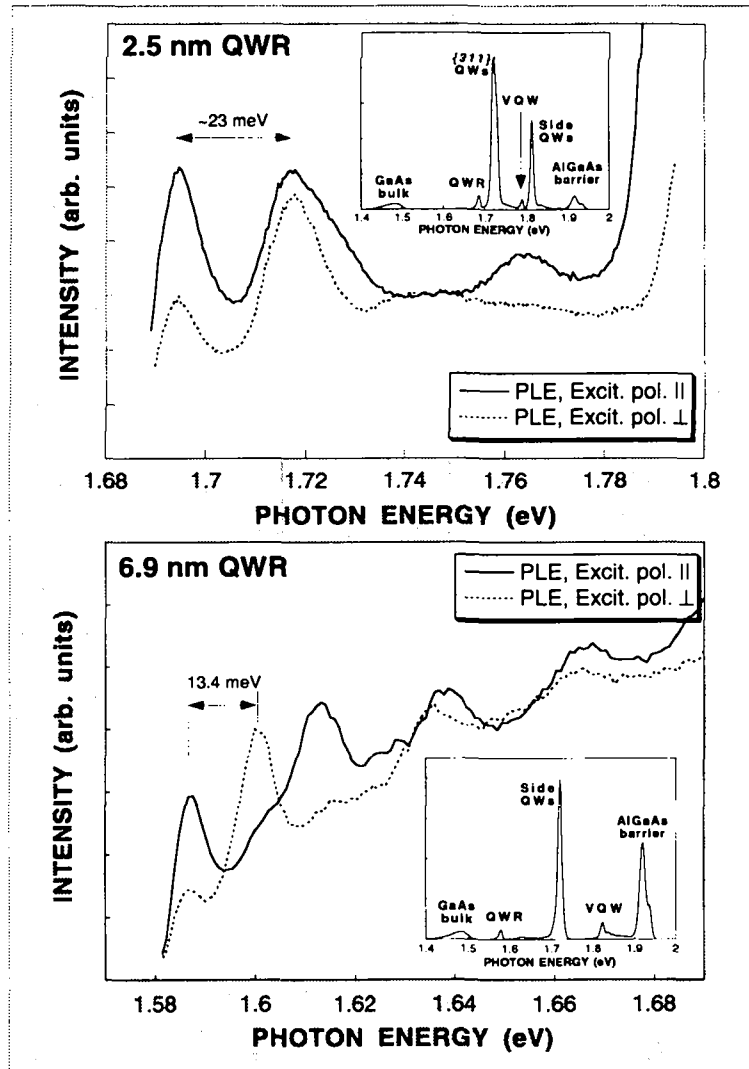
Figure 7.8: Linearly-polarized PLE spectra for (a) the 2.5 nm and (b) 6.9 nm QWR samples. The detection is set at the maximum of the QWR PL line. Insets show extended PL spectra of the heterostructures ($T = 8$ K).

scattering of excitons by acoustical phonons (via the deformation potential) in $GaAs/Al_{0.3}Ga_{0.7}As$ QWRs has been investigated experimentally by four-wave-mixing experiments between 8 K and 40 K [Mayer et al., 1994]. In the case of an inhomogeneously broadened system, the decay of the four-wave-mixing signal T_d is related to the phase relaxation time T_2 by [Mayer et al., 1994, Braun et al., 1997]:

$$T_2 = 4T_d,$$ (7.11)

and the phase relaxation time is connected to the homogeneous linewidth Γ_h by:

$$T_2 = 2\hbar/\Gamma_h.$$ (7.12)

Using values of Γ_h reported by Mayer et al. (1994) we estimated the dephasing time T_2 with Eq. 7.12. We found that T_2 is in the range $2 - 10$ ps for localized and free

excitons and at temperatures between 8 K and 40 K. These values of T_2 are consistent with calculations of the exciton-acoustic phonon scattering in rectangular GaAs QWRs [Jaziri et al., 1995]. At low temperature, the homogeneous linewidth varies linearly with T [Mayer et al., 1994]:

$$\Gamma_h(T) = \Gamma_h(0) + \gamma_{ac}T. \tag{7.13}$$

This relation together with the temperature-dependent values of T_2 reported by Mayer et al. (1994) allowed us to estimate T_2 up to 80 K: We found a minimum dephasing time of $\sim$ 1.6 ps. As this scattering time is much larger than the values of $\langle \tau_X \rangle$ deduced from our measurements for $T < 60$ K, the scattering of excitons by acoustic phonons can be neglected in this temperature range. At higher temperatures, however, this scattering mechanism may contribute to limit the mobility in the two thinnest wires.

Calculations of the relaxation time related to exciton-polar optical phonon scattering (via the Fröhlich interaction) have been reported recently as a function of temperature and wire size for square GaAs/AlGaAs QWRs [Liang et al., 1996]. As expected (due to the phonon occupancy factor), the scattering rate has been found to increase with temperature. For a given temperature, the scattering rate first increases with decreasing wire to attain a maximum (wire size $\sim$ 14 nm), and then decreases as the size decreases further. At 90 K, the scattering time is calculated to be in the range 60−80 ps for a wire size between 2 nm and 10 nm. Obviously, such long scattering times would not limit the mobility observed in our experiments, even at the highest temperature (80 K). However, we note that an exact calculation of the scattering by polar-optical phonon is difficult: similar calculations in QWs have shown that the scattering of 2D excitons by optical phonons completely fails in the description of experimental 2D mobilities, whereas assuming the 3D nature of the excitons (since many subbands are occupied) yields much better agreement with experiments [Hillmer et al., 1989, Basu and Ray, 1991]. Furthermore, calculations of electron-acoustic phonon and electron-polar-optical phonon scattering in a multisubband GaAs QWR have shown that scattering by optical phonons dominates at 77 K [Briggs and Leburton, 1988]. Therefore, we believe that exciton-optical phonon scattering can not be neglected in our experiments at the highest temperatures ($T \sim 70 - 80$ K), although its relative importance with respect to exciton-acoustic phonon scattering is difficult to establish.

We now address the enhancement of the diffusion process (see Fig. 7.2 and Fig. 7.6) when decreasing the temperature below 10 K in the 6.9 nm and the 8.8 nm QWRs. Enhanced diffusivities have already been observed in thin GaAs QWs for decreasing temperatures in the range $10 < T < 40$ K [Hillmer et al., 1992] or below 20 K [Takahashi et al., 1993]. These observations were attributed to thermodiffusion or to the effect of a "phonon wind" [Smith et al., 1989]. Immediately after the excitation

by a laser pulse, optical phonons are generated by the carrier energy relaxation. This provides a nonequilibrium population of optical phonons during a short time interval [Greenstein et al., 1982]. After a short time the optical phonons decay into acoustic phonons [Ulbrich et al., 1981] which are far from equilibrium. If the lattice temperature is high, these nonequilibrium phonons thermalize rapidly through the interaction with ambient thermal phonons. On the other hand, when the temperature is low, since the scattering with ambient phonons is less frequent, nonequilibrium phonons remain for a long time and travel ballistically out of the excitation region in radial directions. These ballistic phonons interact with carriers and act as an expansive force on them. This phonon wind is expected to be greatly reduced when the ambient temperature is raised to the point where the phonon mean free path becomes comparable to the width of the initial carrier distribution [Smith et al., 1989].

At intermediate temperatures (50 − 60 K) the diffusivity is found to be strongly dependent on excitation power density in the 2.5 nm QWR sample whereas this dependence is much less pronounced in the 8.8 nm QWR (see Fig. 7.4). In both structures, D is found to increase with decreasing excitation density, which suggests the contribution from exciton-exciton scattering. This behavior has already been observed in single GaAs QW's at 4 K [Takahashi et al., 1993] and multiple GaAs QWs at 77 K [Akiyama et al., 1994c]. On another hand, an increase of the diffusivity with increasing density has been reported in multiple GaAs QWs at 8.5 K; this increase was attributed to the existence of an electron-hole plasma [Yoon et al., 1992]. Screening of scattering centers and a higher average velocity of carriers in a degenerate distribution are suggested in that latter situation to explain the high values of D. An increase of the diffusion length of excitons with increasing excitation power in the range ($\sim$ 15 − 650) kW/cm^2 has also been observed in a 15 nm GaAs QWR at 15 K [Nagamune et al., 1995]. At such high excitation power density, which corresponds to exciton densities much above the expected Mott density in similar systems, excitons have disappeared [Rossi and Molinari, 1996a]. The diffusion of correlated e-h pairs in this high density regime could not be investigated in our QWR structures as the low energy tail of the adjacent QWs luminescence overlap with the wire PL in this power density range. We note that a diffusion length of 1 μm has been measured by Nagamune et al. (1995) at 15 K with $\sim$ 15 kW/cm^2 excitation density whereas we found $\sim$ 0.2 μm in the 8.8 nm QWR at 20 K with $\sim$ 1 kW/cm^2. Figure 7.4 also highlights the influence of the wire thickness on the power-dependent diffusivity at 50 − 60 K, which may be explained by the increase of the exchange part of the exciton-exciton interaction with increasing confinement [Braun et al., 1998, Wagner et al., 1998]. At low temperature (10 K), the excitons do not move during their lifetime due to localization by interface

roughness and any change in the excitation power density does not modify the values of $D \sim 0$ for both QWR samples. These results legitimate the use of the model of diffusion with a time-independent diffusivity for the 8.8 nm QWR structure. In the case of the thinnest wire, one should keep in mind that the accuracy of the diffusion model will be limited and that the values of D reported in Fig. 7.3 (a) as a function of the lattice temperature correspond to a restricted power range.

Figure 7.5 suggests that the diffusivity depends on the initial kinetic energy of the photoexcited carriers. However, one would expect the opposite behavior due to the more rapid carrier motion at the higher carrier temperatures, as observed in GaAs QWs [Yoon et al., 1992]. Moreover, this variation of D with the exciting-photon energy should take place in a photon energy range determined by the energy of an LO phonon above the wire band gap (~ 1.57 eV for the 8.8 nm QWR). Indeed, the emission of optical phonons is predicted to cause a rapid loss of energy of the photoexcited carriers, whereas the subsequent relaxation by the emission of acoustical phonons is much longer [Piermarocchi et al., 1997]. We believe that the *decrease* of D with increasing excess energy (E_L) is related to the variation of the exciton density in the wire when changing E_L. We discussed in Chap. 5 the efficient transfer of carriers from the top-, side-, and {311}-QWs into the wire region and we showed (see Fig. 5.2) that this transfer was even more pronounced with increasing temperature. In the energy range $E_L < 1.63$ eV, excitons are created selectively in the QWR. As E_L is increased carriers are absorbed in the top-QWs and diffuse towards the QWR, increasing, thus, the 1D exciton density. Increasing further E_L will also slightly increase the number of excitons in the wire due to the absorption of carriers in the side- and {311}-QWs. This interpretation is in agreement with our observations on the power dependence of D (see Fig. 7.4 and discussion in the preceding paragraph). Finally, this analysis in terms of an increasing number of excitons in the wire with increasing E_L is full corroborated by our observation of a simultaneous increase of the integrated QWR PL intensity.

7.8 Summary

We have presented results obtained by a TOF method on the longitudinal motion of excitons in GaAs QWRs. This method combines a high spatial resolution provided by microstructured masks and a high temporal resolution. The diffusion of 1D excitons has been studied as a function of temperature ($5 < T < 80$ K) and wire size (2.5 nm, 6.9 nm, and 8.8 nm QWRs). The longitudinal motion of these 1D excitons can be very well described by isothermal diffusion. A strong dependence of the diffusivity on temperature and wire size was observed. At low temperature, interface roughness has been found to play a predominant role and resulted in complete localization of excitons

in the thinnest QWR below 40 K. Above 60 K, larger diffusivities have been measured for thinner wires. This result, in striking contrast to observations in QW structures, has been explained by the strong suppression of elastic scattering in 1D systems and by the wire size-dependent contribution of intersubband scattering. An enhancement of the diffusivity below 10 K in the 6.9 nm and 8.8 nm QWRs has been discussed in terms of a "phonon wind". Finally, a decrease of the diffusivity with increasing excitation power density has been attributed to exciton-exciton interactions.

Chapter 8

Conclusions and outlook

Two-dimensional patterning of semiconductor heterostructures via epitaxial growth on non-planar substrates offers a number of unique features. All interfaces of the resulting patterned structure are formed in situ, thus having the potential of being free from interfacial defects or contamination, a problem often encountered in other fabrication techniques involving growth interruption. Owing to the high structural and optical quality of our crescent-shaped QWRs, *we could demonstrate unambiguously in this thesis work the 1D nature of this quantum system.* The systematic investigation of PL and PLE spectra as a function of the wire size combined with model calculations has allowed us to study in detail the effect of two-dimensional quantum confinement on valence band mixing and polarization anisotropy. In this context, we have established that the large polarization anisotropy was unequivocally related to the 1D character of our QWRs. Moreover, comparison of the experimental results obtained for different QWR samples with theoretical predictions is clearly compatible with a strong suppression of the 1D band-edge singularity in PLE spectra, which is specific to 1D semiconductor structures. The enhancement of excitonic correlations in 1D systems has also been evidenced by the analysis of PL spectra measured up to room temperature. In addition, the temperature dependence of the exciton diffusivity for different wire thicknesses and, in particular, the dominance of the exciton diffusivity for thinner wires at temperatures above 60 K, has been attributed to the 1D nature of the carriers.

Excitons in model QWR heterostructures are confined in two directions of space and free to propagate along the wire axis. In case of such a perfect QWR, luminescence would be due to recombination of these "free excitons" which are delocalized in the wire direction. However, actual structures are influenced by (weak) disorder related to interface roughness and possibly alloy fluctuations. We have shown that modifications of the wire shape or of the potential barrier result in a fluctuating confinement potential along the wire axis. These localization effects have been demonstrated to influence PL and PLE spectra up to high temperature ($T > 100$ K). An increase of the 1D

excitons mobility with increasing temperature has also been shown to result from the preponderant role of interface disorder. Furthermore, a direct observation of excitons localized along the wire axis in local potential minima has been allowed by micro-PL experiments combined with a metallic mask technique. The pictures of the structural disorder that emerge from temperature dependent PL and PLE measurements and from the optical investigation of the diffusion of excitons are difficult to unify. Each of these investigations is related indirectly to the longitudinal disorder and to the temperature dependent distribution of excitons in the related potential landscape. On one hand, the analysis of PL and PLE spectra, and a fortiori of the Stokes shift, as function of temperature reflects the thermally induced redistribution of excitons among all accessible sites. On the other hand, the increase of the mobility with increasing temperature reflects a thermally activated delocalization of the excitons: As soon as the thermal energy is larger than the shallowest potential minima along the wire, some excitons may be delocalized by thermal activation, therefore resulting in a measurable mobility. As a consequence, qualitative informations about the interface disorder can be deduced from the comparison of temperature dependent experiments for different wire thicknesses, but quantitative data require more direct investigations, such as micro-PL measurements or even scanning near-field optical microscopy [Hasen et al., 1997].

At low temperature, interactions between localized or partially delocalized excitons have been shown to result in a blue shift of the exciton resonance with increasing excitation density, which we attributed to the predominantly repulsive interaction between excitons due to the Pauli exclusion principle. Enhanced exciton-exciton interactions at localization sites along the wire also favoured the formation of multi-excitonic states that have been evidenced by the evolution of the finely structured micro-PL spectra with increasing excitation density.

More work is required to identify unambiguously the origin of the sharp lines observed in micro-PL experiments. Micro-PLE measurements should yield valuable information on the localized states; it necessitates, however, mounting of the CCD detector on the double spectrometer used in standard PL experiments, in order to get both enough laser light rejection and high detection sensitivity. Furthermore, slight modifications in the micro-PL setup would allow polarization dependent measurements that are related to the morphology of the dot-like region, and in particular to its elongation along the wire direction [Gammon et al., 1996, Bellessa, 1998].

High quantum efficiency in our QWR structures should, in principle, allow us to perform PLE measurements up to room temperature. This requires a tunable laser operating in the appropriate wavelength range. Such experiments would complete the picture of phonon coupling effects in 1D systems and give further insight into the impact

of disorder on the optical properties of QWR structures. Moreover, PLE measurements on the 2.5 nm and 6.9 nm QWR samples as a function of temperature should improve our understanding of the impact of the wire morphology on the optical properties.

Preliminary results obtained on the diffusion of 1D excitons should stimulate further work in this direction. At the present time, study of the diffusion process at higher temperature and/or higher excitation densities is limited by the weakness of the QWR luminescence signal detected through small apertures and by spectral overlapping of PL coming from QWs and that coming of QWRs. Using vertically stacked QWRs [Kapon et al., 1996] and selectively etching parts of the QW regions of the heterostructure [Walther et al., 1992] should largely extend the range of investigations. Furthermore, experiments as a function of the exciting photon energy for all QWR samples and over the whole temperature range would be useful to determine the impact of the initial carriers energy on the diffusion process. These investigations would require careful experimental conditions, such as a constant exciton density in the wire region to avoid the influence of varying exciton-exciton scattering rates on the measured diffusivity.

Although disorder related effects have been shown to alter some characteristic features of 1D semiconductor systems, several properties specific to the QWR environment have been clearly observed and pointed out in this thesis work. Besides its contribution to fundamental research in the area of nanostructures, it demonstrate the relevance of crescent-shaped QWRs in the investigation of physical properties peculiar to 1D quantum systems, and it motivates further studies on these low-dimensional semiconductors which represent good candidates for optoelectronic device applications with optimized performance (see, e.g., [Kapon et al., 1992a]).

Nomenclature

Constants

c_0	Speed of light in vacuum	2.99792×10^8 ms^{-1}
e	Elementary charge	1.60218×10^{-19} C
h	Planck constant	6.62617×10^{-34} Js
$\hbar$	Reduced Planck constant	1.05458×10^{-34} Js
k_B	Boltzmann constant	1.38066×10^{-23} JK^{-1}
m_0	Free electron mass	9.1095×10^{-31} Kg
ε_0	Permittivity of vacuum	8.85418×10^{-12} AsV^{-1}m^{-1}

Abbreviations

0D	Zero-dimensional
1D	One-dimensional
2D	Two-dimensional
3D	Three-dimensional
AFM	Atomic Force Microscopy
Ar$^+$	Argon-ion
CCD	Charge Coupled Device
DOS	Density of States
E-beam	Electron-beam
fcc	face-centered cubic
FWHM	Full Width at Half Maximum
hh	heavy-hole
IR	Infra-Red
JDOS	Joint Density of States
lh	light-hole
LO	Longitudinal optical
MBE	Molecular Beam Epitaxy
MCP	Micro-Channel Plate
ML	Monolayer

OMCVD	Organometallic Chemical Vapor Deposition
PL	Photoluminescence
PLE	Photoluminescence Excitation
QD	Quantum Dot
QW	Quantum Well
QWR	Quantum Wire
SEM	Scanning Electron Microscopy
SL	Superlattice
STM	Scanning Tunnelling Microscopy
TEM	Transmission Electron Microscopy
Ti:Sa	Titanium:Sapphire
TOF	Time-of-Flight
UV	Ultra-Violet
VQW	Vertical Quantum Well

Special characters

(100)	Plane, or family of crystallographic planes
{311}	Group of equivalent planes (symmetry)
[100]	Crystallographic direction
a	Lattice parameter
a_B	Exciton Bohr radius
$a_i^\dagger$	Creation operator
a_i	Annihilation operator
a_0	Bohr radius
$C^\dagger$	Creation operator
d	Period of the {311}A step bunching
D	Diffusivity
$\hat{e}$	Polarization vector of light
e_n	n^{th} discrete electron energy level
E	Energy
E_b	Exciton binding energy
E_g	Energy gap
E_i	i^{th} discrete energy level
E_L	Exciting photon energy
E_F	Fermi level
$E_{l.o}$	Energy of longitudinal optical phonons
$f_\nu(\varepsilon)$	Fermi distribution of carriers in subband ν with a quasi-Fermi level at ε_ν

$f^{c,v}(\mathbf{r})$	Carrier envelope wave function
$\lvert f \rangle$	Final state of an optical transition
$F(\mathbf{r})$	Exciton envelope wave function
h	Height of the $\{311\}$A step bunching
h_n	n^{th} discrete hole energy level
hh_n	n^{th} discrete heavy-hole energy level
H	Hamiltonian
$\lvert i \rangle$	Initial state of an optical transition
lh_n	n^{th} discrete light-hole energy level
I^{PL}	Photoluminescence intensity
$I^{+,-}_{//,\perp}$	Photoluminescence intensity
I_{J_z}	Overlap integral of electron and J_z component of hole wave functions
$\mathbf{J}$	Total angular momentum
J_z	z component of the angular momentum $\mathbf{J}$ $(\hbar)$
$k_{x,y,z}$	Carrier wave vector
$\mathbf{K}$	Exciton center-of-mass wave vector
L	Symmetry point of the first Brillouin zone
L_x	Length of the wire
L_z	Well thickness
m^*	Carrier effective mass
m^z_{hh}	Heavy-hole effective mass along z
$m^{\perp}_{hh}$	Heavy-hole effective mass in the well plane
m^z_{lh}	Light-hole effective mass along z
$m^{\perp}_{lh}$	Light-hole effective mass in the well plane
M	Exciton effective mass
M_0	Critical point in the band structure
$\lvert M_{\mathrm{e}_n - \mathrm{h}_m} \rvert^2$	Squared optical matrix element of the $\mathrm{e}_n - \mathrm{h}_m$ transition
$M_{\mathbf{k}',\mathbf{k}}$	Matrix element for scattering from state $\mathbf{k}$ to state $\mathbf{k}'$
n	Carrier density (per unit volume)
	Refractive index
N	Carrier density (per unit length)
N_X	Exciton density (per unit length)
N_{phot}	Number of photons
$\mathbf{p}$	momentum operator
P	Degree of linear polarization
$\mathcal{P}$	Degree of circular polarization
$\mathbf{r}$	Relative coordinate

$\mathbf{R}$	Center-of-mass coordinate
R_0	Radius of a cylindrical wire
R^*	Rydberg constant of the exciton
s_z	Electron spin ($\hbar$)
$S_{i,j}(\mathbf{k}, \mathbf{k}')$	Scattering rate from a state in subband i of wave vector $\mathbf{k}$ to a state in subband j with wave vector $\mathbf{k}'$
t	Time
$t_{x,y,z}$	Well dimension
T	Temperature
T_2	Phase relaxation time
T_d	Decay time of the four-wave-mixing signal
$T_{e,h}$	Kinetic energy operator
$u_{n,\mathbf{k}}$	Periodic Bloch function
$u^c_{s_z}(\mathbf{r})$	Bloch function at the bottom of the Γ_6 bulk band
$u^v_{J_z}(\mathbf{r})$	Bloch function at the top of the Γ_8 bulk bands
V	Sample volume
V_0	Potential barrier
$V(x, y, z)$	Potential distribution
$V_{\nu\nu'}$	Coulomb interaction operator
$V_\nu(\mathbf{r})$	Potential associated with scattering mechanism ν
x	Coordinate along the wire axis
X^+	Positively charged exciton
y	Coordinate in the lateral confinement direction
z	Coordinate along the growth direction

Greek Symbols

$\alpha(\omega)$	Absorption coefficient
β_{nl}	lth zero of the Bessel function of order n
$\chi(x)$	Envelope wave function
δ	Height parameter of the interface roughness
$\delta(x - x_0)$	Dirac delta function
ΔE	Energy spacing
ΔE_c	Conduction band offset
ΔE_v	Valence band offset
ε	Permittivity (dielectric constant)
$\phi^x(y, z)$	Envelope wave function
$\gamma_{1,2,3}$	Luttinger γ parameters

γ_{ac}	Coupling coefficient to acoustic phonons
γ_{opt}	Coupling coefficient to optical phonons
Γ	Symmetry point of the first Brillouin zone
Γ_h	Homogeneous linewidth
$\Gamma^{PL,PLE}$	Inhomogeneous PL/PLE linewidth
η	Range parameter of the interface roughness
λ	Wave length
λ_F	Fermi wave length
μ	Mobility
μ_{red}	Reduced exciton mass
μ_X	Exciton mobility
μ_{amb}	Ambipolar mobility
$\mu_{e,h}$	Electron/hole mobility
$\theta(x)$	Heaviside function
$\rho_{\alpha D}$	Density of states in α-dimensional space
σ	Standard deviation
$\sigma^{+,-}$	Helicity of light
τ_i	Scattering time (ps)
τ_D	Photoluminescence decay time
τ_R	Effective relaxation time
$\tau_{\nu,i}^{-1}(E)$	Scattering rate at energy E in subband i
ω	Circular frequency of light
$\psi(x,y,z)$	Envelope wave function
$\Psi(x,y,z)$	Total wave function

Bibliography

[Abrahams et al., 1979] Abrahams, E., Anderson, P. W., Licciardello, D. C., and Ramakrishnan, T. V. (1979). *Phys. Rev. Lett.*, 42:673.

[Adachi, 1993] Adachi, S. (1993). In *Properties of Aluminium Gallium Arsenide*, London. INSPEC.

[Akiyama et al., 1994a] Akiyama, H., Koshiba, S., Someya, T., Wada, K., Noge, H., Nakamura, Y., Inoshita, T., Shimizu, A., and Sakaki, H. (1994a). *Phys. Rev. Lett.*, 72:924.

[Akiyama et al., 1994b] Akiyama, H., Koshiba, S., Someya, T., Wada, K., Noge, H., Nakamura, Y., Inoshita, T., Shimizu, A., and Sakaki, H. (1994b). *Phys. Rev. Lett.*, Errata, 72:2123.

[Akiyama et al., 1994c] Akiyama, H., Matsusue, T., and Sakaki, H. (1994c). *Phys. Rev. B*, 49:14523.

[Akiyama et al., 1996] Akiyama, H., Someya, T., and Sakaki, H. (1996). *Phys. Rev. B*, 53:R4229.

[Ambigapathy et al., 1997] Ambigapathy, R., Bar-Joseph, I., Oberli, D. Y., Haacke, S., Brasil, M. J., Reinhardt, F., Kapon, E., and Deveaud, B. (1997). *Phys. Rev. Lett.*, 78:3579.

[Arakawa and Sakaki, 1982] Arakawa, Y. and Sakaki, H. (1982). *Appl. Phys. Lett.*, 40:939.

[Arakawa and Yariv, 1986] Arakawa, Y. and Yariv, A. (1986). *IEEE J. Quantum Electron.*, 22:1887.

[Asada et al., 1985] Asada, M., Miyamoto, Y., and Suematsu, Y. (1985). *Jpn. J. Appl. Phys.*, 24:L95.

[Ashcroft and Mermin, 1976] Ashcroft, N. and Mermin, N. (1976). *Solid State Physics.* W.B. Saunders Company, Philadelphia.

[Baldereschi and Lipari, 1971] Baldereschi, A. and Lipari, N. O. (1971). *Phys. Rev. B*, 3:439.

[Bar-Ad and Bar-Joseph, 1992] Bar-Ad, S. and Bar-Joseph, I. (1992). *Phys. Rev. Lett.*, 68:349.

[Barenco and Dupertuis, 1995] Barenco, A. and Dupertuis, M.-A. (1995). *Phys. Rev. B*, 52:2766.

[Bassani, 1975] Bassani, F. (1975). *Electronic States and Optical Transitions in Solids*. Pergamon Press, London.

[Bastard, 1992] Bastard, G. (1992). *Wave Mechanics Applied to Semiconductor Heterostructures*. Les Editions de Physique, Les Ulis.

[Bastard et al., 1984] Bastard, G., Delalande, C., Meynadier, M. H., Frijlink, P. M., and Voos, M. (1984). *Phys. Rev. B*, 29:7042.

[Bastard et al., 1982] Bastard, G., Mendez, E. E., Chang, L. L., and Esaki, L. (1982). *Phys. Rev. B*, 26:1974.

[Basu and Ray, 1991] Basu, P. K. and Ray, P. (1991). *Phys. Rev. B*, 44:1844.

[Bauer and Sakaki, 1991] Bauer, G. and Sakaki, H. (1991). *Phys. Rev. B*, 44:5562.

[Bauer and Sakaki, 1992] Bauer, G. E. and Sakaki, H. (1992). *Surf. Science*, 267:442.

[Bauer and Ando, 1988] Bauer, G. E. W. and Ando, T. (1988). *Phys. Rev. B*, 38:6015.

[Belleguie and Banyai, 1991] Belleguie, L. and Banyai, L. (1991). *Phys. Rev. B*, 44:8785.

[Bellessa, 1998] Bellessa, J. (1998). PhD thesis, Université de Paris VI.

[Benisty et al., 1991] Benisty, H., Sotomayor-Torrès, C., and Weisbuch, C. (1991). *Phys. Rev. B*, 44:10945.

[Biasiol, 1998] Biasiol, G. (1998). PhD thesis, Ecole Polytechnique Fédérale de Lausanne.

[Biasiol et al., 1997] Biasiol, G., Reinhardt, F., Gustafsson, A., and Kapon, E. (1997). *J. Electron. Mat.*, 26:1194.

[Biasiol et al., 1996] Biasiol, G., Reinhardt, F., Gustafsson, A., Martinet, E., and Kapon, E. (1996). *Appl. Phys. Lett.*, 69:2710.

[Birotheau et al., 1992] Birotheau, L., Izrael, A., Marzin, J. Y., Azoulay, R., Thierry-Mieg, V., and Ladan, F. R. (1992). *Appl. Phys. Lett.*, 61:3023.

[Bloch et al., 1994] Bloch, J., Bockelmann, U., and Laruelle, F. (1994). *Europhys. Lett.*, 28:501.

[Bockelmann, 1991] Bockelmann, U. (1991). *Europhys. Lett.*, 16:601.

[Bockelmann, 1993] Bockelmann, U. (1993). *Phys. Rev. B*, 48:17637.

[Bockelmann and Bastard, 1990] Bockelmann, U. and Bastard, G. (1990). *Phys. Rev. B*, 42:8947.

[Bockelmann and Bastard, 1991] Bockelmann, U. and Bastard, G. (1991). *Europhys. Lett.*, 15:215.

[Bockelmann et al., 1996] Bockelmann, U., Roussignol, P., Filoramo, A., Heller, W., Abstreiter, G., Brunner, K., Böhm, G., and Weimann, G. (1996). *Phys. Rev. Lett.*, 76:3622.

[Braun et al., 1998] Braun, W., Bayer, M., Forchel, A., Schmitt, O. M., Banyai, L., Haug, H., and Filin, A. I. (1998). *Phys. Rev. B*, 57:12364.

[Braun et al., 1997] Braun, W., Bayer, M., Forchel, A., Zull, H., Reithmaier, J. P., Filin, A. I., and Reinecke, T. L. (1997). *Phys. Rev. B*, 56:12096.

[Briggs and Leburton, 1988] Briggs, S. and Leburton, J. (1988). *Phys. Rev. B*, 38:8163.

[Brunner et al., 1994a] Brunner, K., Abstreiter, G., Böhm, G., Tränkle, G., and Weimann, G. (1994a). *Phys. Rev. Lett.*, 73:1138.

[Brunner et al., 1994b] Brunner, K., Abstreiter, G., Böhm, G., Tränkle, G., and Weimann, G. (1994b). *Appl. Phys. Lett.*, 64:3320.

[Brunner et al., 1992] Brunner, K., Bockelmann, U., Abstreiter, G., Walther, M., Böhm, G., Tränkle, G., and Weimann, G. (1992). *Phys. Rev. Lett.*, 69:3216.

[Chang et al., 1985] Chang, Y.-C., Chang, L. L., and Esaki, L. (1985). *Appl. Phys. Lett.*, 47:1324.

[Chen et al., 1993] Chen, A. C., Moy, A. M., Pearah, P. J., Hsieh, K. C., and Cheng, K. Y. (1993). *Appl. Phys. Lett.*, 62:1359.

[Cho and Ballamy, 1975] Cho, A. and Ballamy, W. (1975). *J. Appl. Phys.*, 46:783.

[Cho, 1979] Cho, K. (1979). Excitons. In *Topics in Current Physics*, number 14, Berlin Heidelberg. Springer-Verlag.

[Christen and Bimberg, 1990] Christen, J. and Bimberg, D. (1990). *Phys. Rev. B*, 42:7213.

[Christen et al., 1992] Christen, J., Kapon, E., Colas, E., Hwang, D. M., Schiavone, L. M., Grundmann, M., and Bimberg, D. (1992). *Surf. Science*, 267:257.

[Cibert et al., 1986] Cibert, J., Petroff, P., Dolan, G., Pearton, S., Gossard, A., and English, J. (1986). *Appl. Phys. Lett.*, 49:1275.

[Cingolani et al., 1992] Cingolani, R., Lepore, M., Tommasi, T., Catalano, I. M., Lage, H., Heitmann, D., Ploog, K., Shimizu, A., Sakaki, H., and Ogawa, T. (1992). *Phys. Rev. Lett.*, 69:1276.

[Citrin and Chang, 1991] Citrin, D. S. and Chang, Y.-C. (1991). *Phys. Rev. B*, 43:11703.

[Colocci et al., 1990] Colocci, M., Gurioli, M., and Vinattieri, A. (1990). *J. Appl. Phys.*, 68:2809.

[Colvard et al., 1989] Colvard, C., Bimberg, D., Alavi, K., Maierhofer, C., and Nouri, N. (1989). *Phys. Rev. B*, 39:3419.

[Crawford et al., 1991] Crawford, D. L., Nagarajan, R. L., and Bowers, J. E. (1991). *Appl. Phys. Lett.*, 58:1629.

[Deveaud et al., 1988] Deveaud, B., Shah, J., Damen, T. C., Lambert, B., Chomette, A., and Regreny, A. (1988). *IEEE J. Quantum Electron.*, 24:1641.

[Deveaud et al., 1987] Deveaud, B., Shah, J., Damen, T. C., Lambert, B., and Regreny, A. (1987). *Phys. Rev. Lett.*, 58:2582.

[Edamatsu et al., 1995] Edamatsu, K., Iwai, S., Itoh, T., Yano, S., and Goto, T. (1995). *Phys. Rev. B*, 51:11205.

[Elliot, 1957] Elliot, R. J. (1957). *Phys. Rev.*, 108:1384.

[Esaki and Tsu, 1969] Esaki, L. and Tsu, R. (1969). *IBM Research Note*, pages RC-2418.

[Esaki and Tsu, 1970] Esaki, L. and Tsu, R. (1970). *IBM J. Res. Develop.*, 14:61.

[Fasol, 1992] Fasol, G. (1992). *Appl. Phys. Lett.*, 61:831.

[Fehrenbach et al., 1982] Fehrenbach, G. W., Schäfer, W., Treusch, J., and Ulbrich, R. (1982). *Phys. Rev. Lett.*, 49:1281.

[Fernández-Rossier et al., 1996] Fernández-Rossier, J., Tejedor, C., Muñoz, L., and Viña, L. (1996). *Phys. Rev. B*, 54:11582.

[Ferry and Goodnick, 1997] Ferry, D. and Goodnick, S. (1997). *Transport in Nanostructures*. Cambridge University Press, Cambridge.

[Fishman, 1986] Fishman, G. (1986). *Phys. Rev. B*, 34:2394.

[Ford et al., 1988] Ford, C., Thornton, T., Newbury, R., Pepper, M., Ahmed, H., Foxon, C., Harris, J., and Roberts, C. (1988). *J. Phys. C*, 21:L325.

[Fouquet, 1986] Fouquet, J. E. (1986). *IEEE J. Quantum Electronics*, QE-22:1799.

[Frankel, 1931] Frankel, J. (1931). *Phys. Rev.*, 37:1226.

[Gammon et al., 1995a] Gammon, D., Rudin, S., Reinecke, T. L., Katzer, D. S., and Kyono, C. S. (1995a). *Phys. Rev. B*, 51:16785.

[Gammon et al., 1995b] Gammon, D., Snow, E. S., and Katzer, D. S. (1995b). *Appl. Phys. Lett.*, 67:2391.

[Gammon et al., 1996] Gammon, D., Snow, E. S., Shanabrook, B. V., and Katzer, D. S. (1996). *Phys. Rev. Lett.*, 76:3005.

[Gershoni et al., 1994] Gershoni, D., Katz, M., Wegscheider, W., Pfeiffer, L. N., Logan, R. A., and West, D. (1994). *Phys. Rev. B*, 50:8930.

[Gershoni et al., 1990] Gershoni, D., Weiner, J. S., Chu, S. N. B., Baraff, G. A., Vandenberg, J. M., Pfeiffer, L. N., West, K., Logan, R. A., and Tanbun-Ek, T. (1990). *Phys. Rev. Lett.*, 65:1631.

[Gilliland, 1997] Gilliland, G. D. (1997). *Materials Science & Engineering*, R18(3-6).

[Glutsch and Bechstedt, 1993] Glutsch, S. and Bechstedt, F. (1993). *Phys. Rev. B*, 47:4315.

[Gold and Ghazali, 1990] Gold, A. and Ghazali, A. (1990). *Phys. Rev. B*, 41:7626.

[Goldoni et al., 1996] Goldoni, G., Rossi, F., Molinari, E., Fasolino, A., Rinaldi, R., and Cingolani, R. (1996). *Appl. Phys. Lett.*, 69:2965.

[Greene et al., 1984] Greene, R. L., Bajaj, K. K., and Phelps, D. E. (1984). *Phys. Rev. B*, 29:1807.

[Greenstein et al., 1982] Greenstein, M., Tamor, M. A., and Wolfe, J. P. (1982). *Phys. Rev. B*, 26:5604.

[Gurioli et al., 1994] Gurioli, M., Vinattieri, A., Martinez-Pastor, J., and Colocci, M. (1994). *Phys. Rev. B*, 50:11817.

[Gustafsson et al., 1998] Gustafsson, A., Pistol, M.-E., Montelius, L., and Samuelson, L. (1998). *J. Appl. Phys.*, 104:1.

[Gustafsson et al., 1995] Gustafsson, A., Reinhardt, F., Biasiol, G., and Kapon, E. (1995). *Appl. Phys. Lett.*, 67:3673.

[Haacke et al., 1996] Haacke, S., Hartig, M., Oberli, D. Y., Deveaud, B., and Kapon, E. (1996). *Solid-State Electr.*, 40:299.

[Hasen et al., 1997] Hasen, J., Pfeiffer, L. N., Pinczuk, A., He, S., West, K. W., and Dennis, B. S. (1997). *Nature*, 390:54.

[Haug and Schmitt-Rink, 1984] Haug, H. and Schmitt-Rink, S. (1984). *Prog. Quant. Eletr.*, 9:3.

[Hegarty et al., 1984] Hegarty, J., Goldner, L., and Sturge, M. D. (1984). *Phys. Rev. B*, 30:7346.

[Hess et al., 1994] Hess, H. F., Betzig, E., Harris, T. D., Pfeiffer, L. N., and West, K. W. (1994). *Science*, 264:1740.

[Hillmer et al., 1989] Hillmer, H., Forchel, A., Hansmann, S., Morohashi, M., Lopez, E., Meier, H. P., and Ploog, K. (1989). *Phys. Rev. B*, 39:10901.

[Hillmer et al., 1990] Hillmer, H., Forchel, A., Sauer, R., and Tu, C. W. (1990). *Phys. Rev. B*, 42:3220.

[Hillmer et al., 1992] Hillmer, H., Forchel, A., and Tu, C. W. (1992). *Phys. Rev. B*, 45:1240.

[Hillmer et al., 1993] Hillmer, H., Forchel, A., and Tu, C. W. (1993). *J. Phys.: Condens. Matter*, 5:5563.

[Hillmer et al., 1988] Hillmer, H., Hansmann, S., Forchel, A., Morohashi, M., Lopez, E., Meier, H. P., and Ploog, K. (1988). *Appl. Phys. Lett.*, 53:1937.

[Hillmer et al., 1991] Hillmer, H., Mayer, G., Forchel, A., Kuhn, T., Mahler, G., and Meier, H. P. (1991). *Phys. Rev. B*, 43:13992.

[Hillmer et al., 1986] Hillmer, H., Mayer, G., Forchel, A., Löchner, K. S., and Bauser, E. (1986). *Appl. Phys. Lett.*, 49:948.

[Ils et al., 1995] Ils, P., Géus, C., Forchel, A., Kulakovski, V. D., Gippius, N. A., and Tikhodeev, S. G. (1995). *Phys. Rev. B*, 51:4272.

[Inoshita and Sakaki, 1992] Inoshita, T. and Sakaki, H. (1992). *Phys. Rev. B*, 46:7260.

[Jahn et al., 1996] Jahn, U., Kwok, S. H., Ramsteiner, M., Hey, R., Grahn, H. T., and Runge, E. (1996). *Phys. Rev. B*, 54:2733.

[Jahn et al., 1997] Jahn, U., Ramsteiner, M., Hey, R., Grahn, H. T., Runge, E., and Zimmermann, R. (1997). *Phys. Rev. B*, 56:R4387.

[Jaskólski, 1996] Jaskólski, W. (1996). *Physics Reports*, 271:1–66.

[Jaziri et al., 1995] Jaziri, S., Ferreira, R., Bennaceur, R., and Bastard, G. (1995). *Il Nuovo Cimento D*, 17:1513.

[Kajikawa, 1993] Kajikawa, Y. (1993). *Phys. Rev. B*, 47:3649.

[Kapon, 1992] Kapon, E. (1992). *Proc. IEEE*, 80:398.

[Kapon, 1994] Kapon, E. (1994). *Semiconductors and semimetals*, 40:259.

[Kapon et al., 1996] Kapon, E., Biasiol, G., Hwang, D. M., Walther, M., and Colas, E. (1996). *Solid St. Electron.*, 40:815.

[Kapon et al., 1989] Kapon, E., Hwang, D. M., and Bhat, R. (1989). *Phys. Rev. Lett.*, 63:430.

[Kapon et al., 1992a] Kapon, E., Kash, K., E. M. Clausen, J., Hwang, D. M., and Colas, E. (1992a). *Appl. Phys. Lett.*, 60:477.

[Kapon et al., 1988] Kapon, E., Stoffel, N., Dobisz, E., and Bhat, R. (1988). *Appl. Phys. Lett.*, 52:351.

[Kapon et al., 1987] Kapon, E., Tamargo, M., and Hwang, D. (1987). *Appl. Phys. Lett.*, 50:347.

[Kapon et al., 1992b] Kapon, E., Walther, M., Christen, J., Grundmann, M., Caneau, C., Hwang, D. M., Colas, E., Bhat, R., Song, G. H., and Bimberg, D. (1992b). *Superlattices and Microstructures*, 12:491.

[Kash et al., 1989] Kash, K., Bhat, R., Mahoney, D., Lin, P., Scherer, A., Worlock, J., der Gaag, B. V., Koza, M., and Grabbe, P. (1989). *Appl. Phys. Lett.*, 55:681.

[Kash et al., 1986] Kash, K., Scherer, A., Warlock, J., Craighead, H., and Tamargo, M. (1986). *Appl. Phys. Lett.*, 49:1043.

[Kash et al., 1990] Kash, K., Worlock, J. M., Gozdz, A. S., der Gaag, B. P. V.. Harbison, J. P., Lin, P. S. D., and Florez, L. T. (1990). *Surf. Science*, 229:245.

[Kavokin, 1994] Kavokin, A. V. (1994). *Phys. Rev. B*, 50:8000.

[Kiener et al., 1996] Kiener, C., Rota, L., Maciel, A. C., Freyland, J. M., and Ryan, J. F. (1996). *Appl. Phys. Lett.*, 68:2061.

[Knox, 1963] Knox, R. S. (1963). *Theory of Excitons.* Solid State Physics, Supplement 5, Academic Press, New York and London.

[Kodama et al., 1985] Kodama, T., Osaka, Y., and Yamanishi, M. (1985). *Jpn. J. Appl. Phys.*, 24:1370.

[Kohl et al., 1988] Kohl, M., Heitmann, D., Grambow, P., and Ploog, K. (1988). *Phys. Rev. B*, 37:10927.

[Kohl et al., 1989] Kohl, M., Heitmann, D., Grambow, P., and Ploog, K. (1989). *Phys. Rev. Lett.*, 63:2124.

[Kohl et al., 1990] Kohl, M., Heitmann, D., Grambow, P., and Ploog, K. (1990). *Phys. Rev. B*, 42:2941.

[Kumar et al., 1998] Kumar, R., Vengurlekar, A., Gopal, A. V., Mélin, T., Laruelle, F., Etienne, B., and Shah, J. (1998). *Phys. Rev. Lett.*, 81:2578.

[Lage et al., 1991] Lage, H., Heitmann, D., Cingolani, R., Grambow, P., and Ploog, K. (1991). *Phys. Rev. B*, 44:6550.

[Laidig et al., 1981] Laidig, W., Holonyak, N., Camras, M., Hess, K., Coleman, J., Dapkus, D., and Bardeen, J. (1981). *Appl. Phys. Lett.*, 38:776.

[Lampel, 1968] Lampel, G. (1968). *Phys. Rev. Lett.*, 20:491.

[Landin et al., 1998] Landin, L., Miller, M., Pistol, M.-E., Pryor, C., and Samuelson, L. (1998). *Science*, 280:262.

[Lee and Spector, 1983] Lee, J. and Spector, H. (1983). *J. Appl. Phys.*, 54:3921.

[Lelong and Bastard, 1996a] Lelong, P. and Bastard, G. (1996a). *Solid State Commun.*, 98:819.

[Lelong and Bastard, 1996b] Lelong, P. and Bastard, G. (1996b). In Scheffler, M. and Zimmermann, R., editors, *Proc. of the 23rd Int. Conf. on the Physics of Semiconductors*, number 2, pages 1377–1380, Singapore. World Scientific.

[Liang et al., 1996] Liang, S.-D., Chen, C., Jiang, S., and Lin, D. (1996). *Phys. Rev. B*, 53:15459.

[Logothetidis et al., 1991] Logothetidis, S., Cardona, M., and Garriga, M. (1991). *Phys. Rev. B*, 43:11950.

[Loudon, 1959] Loudon, R. (1959). *Am. J. Phys.*, 27:649.

[Luttinger, 1956] Luttinger, J. M. (1956). *Phys. Rev.*, 102:1030.

[Luttinger and Kohn, 1955] Luttinger, J. M. and Kohn, W. (1955). *Phys. Rev.*, 97:869.

[Maialle et al., 1993] Maialle, M., de Andrada e Silva, E., and Sham, L. (1993). *Phys. Rev. B*, 47:15776.

[Majumder et al., 1985] Majumder, F., Swoboda, H.-E., Kempf, K., and Klingshirn, C. (1985). *Phys. Rev. B*, 32:2407.

[Manzke et al., 1998] Manzke, G., Peng, Q., Henneberger, K., Neukirch, U., Hauke, K., Wundke, K., Gutowski, J., and Hommel, D. (1998). *Phys. Rev. Lett.*, 80:4943.

[Martinet et al., 1997] Martinet, E., Gustafsson, A., Biasiol, G., Reinhardt, F., Kapon, E., and Leifer, K. (1997). *Phys. Rev. B*, 56:R7096.

[Marzin et al., 1992] Marzin, J., Izrael, A., Birotheau, L., Sermage, B., Roy, N., Azoulay, R., Robein, D., Benchimol, J.-L., Henry, L., Theirry-Mieg, V., Ladan, F., and Taylor, L. (1992). *Surf. Sci.*, 267:253.

[Marzin et al., 1994] Marzin, J.-Y., Gérard, J.-M., Izraël, A., and Barrier, D. (1994). *Phys. Rev. Lett.*, 73:716.

[Matsubara et al., 1989] Matsubara, K., Ravikumar, K. G., Asada, M., and Suematsu, Y. (1989). *The Transactions of the IEICE E*, 72:1179.

[Mayer et al., 1994] Mayer, E. J., White, J. O., Smith, G. O., Lage, H., Heitmann, D., Ploog, K., and Kuhl, J. (1994). *Phys. Rev. B*, 49:2993.

[Meier et al., 1989] Meier, H., Gieson, E., Ealter, W., and Harder, C. (1989). *Appl. Phys. Lett.*, 54:433.

[Miller et al., 1988] Miller, D. A. B., Chemla, D. S., and Schmitt-Rink, S. (1988). *Appl. Phys. Lett.*, 52:2154.

[Miller and Bhat, 1988] Miller, R. C. and Bhat, R. (1988). *J. Appl. Phys.*, 64:3647.

[Miller and Kleinman, 1985] Miller, R. C. and Kleinman, D. A. (1985). *J. Lumin.*, 30:520.

[Molenkamp et al., 1988] Molenkamp, L. W., Eppenga, R., 't Hooft, G. W., Dawson, P., Foxon, C. T., and Moore, K. J. (1988). *Phys. Rev. B*, 38:4314.

[Motohisa and Sakaki, 1992] Motohisa, J. and Sakaki, H. (1992). *Appl. Phys. Lett.*, 60:1315.

[Mott, 1938] Mott, N. F. (1938). *Trans. Faraday Soc.*, 34:500.

[Nag, 1980] Nag, B. (1980). *Electron Transport in Compound Semiconductors.* Springer, Berlin.

[Nagamune et al., 1992] Nagamune, Y., Arakawa, Y., Tsukamoto, S., Nishioka, M., Sasaki, S., and Miura, N. (1992). *Phys. Rev. Lett.*, 69:2963.

[Nagamune et al., 1995] Nagamune, Y., Watabe, H., Sogawa, F., and Arakawa, Y. (1995). *Appl. Phys. Lett.*, 67:1535.

[Nair and Takagahara, 1996] Nair, S. V. and Takagahara, T. (1996). *Phys. Rev. B*, 53:R10516.

[Nair and Takagahara, 1997] Nair, S. V. and Takagahara, T. (1997). *Phys. Rev. B*, 55:5153.

[Nelson et al., 1982] Nelson, D. F., Cooper, J. A., and Tretola, A. R. (1982). *Appl. Phys. Lett.*, 41:857.

[Nojima, 1992] Nojima, S. (1992). *Phys. Rev. B*, 46:2302.

[Notomi et al., 1998] Notomi, M., Hammersberg, J., Zeman, J., Weman, H., Potemski, M., Sugiura, H., and Tamamura, T. (1998). *Phys. Rev. Lett.*, 80:3125.

[Oberhauser et al., 1993] Oberhauser, D., Pantke, K.-H., Hvam, J. M., Weimann, G., and Klingshirn, C. (1993). *Phys. Rev. B*, 47:6827.

[Oberli et al., 1998] Oberli, D. Y., Dupertuis, M.-A., Reinhardt, F., and Kapon, E. (1998). *submitted to PRB*.

[Oberli et al., 1997] Oberli, D. Y., Vouilloz, F., and Kapon, E. (1997). *Phys. Stat. Sol. (a)*, 164:353.

[Oestreich et al., 1993] Oestreich, M., Rühle, W. W., Lage, H., Heitmann, D., and Ploog, K. (1993). *Phys. Rev. Lett.*, 70:1682.

[Ogawa and Takagahara, 1991a] Ogawa, T. and Takagahara, T. (1991a). *Phys. Rev. B*, 44:8138.

[Ogawa and Takagahara, 1991b] Ogawa, T. and Takagahara, T. (1991b). *Phys. Rev. B*, 43:14325.

[Osborne et al., 1996] Osborne, J., Shields, A., Pepper, M., Bolton, F., and Ritchie, D. A. (1996). *Phys. Rev. B*, 53:13002.

[Othonos, 1998] Othonos, A. (1998). *J. Appl. Phys.*, 83:1789.

[Peierls, 1932] Peierls, R. E. (1932). *Ann. Phys.*, 13:905.

[Petroff et al., 1984] Petroff, P., Gossard, A., and Wiegmann, W. (1984). *Appl. Phys. Lett.*, 45:620.

[Peyghambarian et al., 1984] Peyghambarian, N., Gibbs, H. M., Jewell, J. L., Antonetti, A., Migus, A., Hulin, D., and Mysyrowicz, A. (1984). *Phys. Rev. Lett.*, 53:2433.

[Pfeiffer et al., 1990] Pfeiffer, L., West, K., Stormer, H., Eisenstein, J., Baldwin, K., Gershoni, D., and Spector, J. (1990). *Appl. Phys. Lett.*, 56:1697.

[Piermarocchi et al., 1998] Piermarocchi, C., Savona, V., Quattropani, A., Selbmann, P., Schwendimann, P., and Tassone, F. (1998). *Phys. Stat. Sol. (b)*, 206:455.

[Piermarocchi et al., 1997] Piermarocchi, C., Tassone, F., Savona, V., Quattropani, A., and Schwendimann, P. (1997). *Phys. Rev. B*, 55:1333.

[Qiang et al., 1992] Qiang, H., Pollak, F. H., Sotomayor-Torres, C. M., Leitch, W., Kean, A. H., Stroscio, M. A., Iafrate, G. J., and Kim, K. W. (1992). *Appl. Phys. Lett.*, 61:1411.

[Rashba and Sturge, 1982] Rashba, E. I. and Sturge, M. D. (1982). *Excitons*. North-Holland.

[Reinhardt et al., 1996] Reinhardt, F., Dwir, B., and Kapon, E. (1996). *Appl. Phys. Lett.*, 68:3168.

[Ribeiro et al., 1995] Ribeiro, E., Cerdeira, F., and Cantarero, A. (1995). *Phys. Rev. B*, 51:7890.

[Rinaldi et al., 1994] Rinaldi, R., Ferrara, M., Cingolani, R., Marti, U., Martin, D., Morier-Genoud, F., Ruterana, P., and Reinhart, F. K. (1994). *Phys. Rev. B*, 50:11795.

[Rossi et al., 1997] Rossi, F., Goldoni, G., and Molinari, E. (1997). *Phys. Rev. Lett.*, 78:3527.

[Rossi and Molinari, 1996a] Rossi, F. and Molinari, E. (1996a). *Phys. Rev. Lett.*, 76:3642.

[Rossi and Molinari, 1996b] Rossi, F. and Molinari, E. (1996b). *Phys. Rev. B*, 53:16462.

[Rossi et al., 1993] Rossi, F., Rota, L., Bungaro, C., Lugli, P., and Molinari, E. (1993). *Phys. Rev. B*, 47:1695.

[Rudin et al., 1990] Rudin, S., Reinecke, T. L., and Segall, B. (1990). *Phys. Rev. B*, 42:11218.

[Ruf et al., 1994] Ruf, T., Spitzer, J., Sapega, V. F., Belitzky, V. I., Cardona, M., and Ploog, K. (1994). *Phys. Rev. B*, 50:1792.

[Runge et al., 1995] Runge, E., Schülzgen, A., Henneberger, F., and Zimmermann, R. (1995). *Phys. Stat. Sol. (b)*, 188:547.

[Sakaki, 1980] Sakaki, H. (1980). *Jpn. J. Appl. Phys.*, 19:L735.

[Samuelson et al., 1995] Samuelson, L., Gustafsson, A., Hessman, D., Lindahl, J., Montelius, L., Petersson, A., and Pistol, M.-E. (1995). *Phys. Stat. Sol. (a)*, 152:269.

[Schmitt-Rink et al., 1985] Schmitt-Rink, S., Chemla, D. S., and Miller, D. A. B. (1985). *Phys. Rev. B*, 32:6601.

[Schmitt-Rink et al., 1989] Schmitt-Rink, S., Chemla, D. S., and Miller, D. A. B. (1989). *Adv. Phys.*, 38:89.

[Schnabel et al., 1992] Schnabel, R. F., Zimmermann, R., Bimberg, D., Nickel, H., Lösch, R., and Schlapp, W. (1992). *Phys. Rev. B*, 46:9873.

[Schreiber, 1986] Schreiber, M. (1986). *Phys. Rev. B*, 34:2914.

[Sercel and Vahala, 1991] Sercel, P. C. and Vahala, K. J. (1991). *Phys. Rev. B*, 44:5681.

[Shah, 1996] Shah, J. (1996). *Ultrafast Spectroscopy of Semiconductors and Semiconductor Nanostructures*. Springer, Berlin and New York.

[Shepelyanski, 1994] Shepelyanski, D. (1994). *Phys. Rev. Lett.*, 73:2607.

[Shinada and Sugano, 1966] Shinada, M. and Sugano, S. (1966). *J. Phys. Soc. Jpn.*, 21:1936.

[Smith et al., 1989] Smith, L. M., Preston, J. S., Wolfe, J. P., Wake, D. R., Klem, J., Henderson, T., and Morkoç, H. (1989). *Phys. Rev. B*, 39:1862.

[Someya et al., 1995] Someya, T., Akiyama, H., and Sakaki, H. (1995). *Phys. Rev. Lett.*, 74:3664.

[Someya et al., 1996] Someya, T., Akiyama, H., and Sakaki, H. (1996). *Phys. Rev. Lett.*, 76:2965.

[Soukoulis et al., 1984] Soukoulis, C. M., Cohen, M. H., and Economou, E. N. (1984). *Phys. Rev. Lett.*, 53:616.

[Stroscio et al., 1990] Stroscio, M. A., Kim, K. W., Littlejohn, M. A., and Chuang, H. (1990). *Phys. Rev. B*, 42:1488.

[Swoboda et al., 1988] Swoboda, H.-E., Majumder, F., Lyssenko, V., Klingshirn, C., and Banyai, L. (1988). *Z. Phys.*, 70:341.

[Takagahara, 1989] Takagahara, T. (1989). *J. Lumin.*, 44:347.

[Takahashi et al., 1993] Takahashi, Y., Muraki, K., Fukatsu, S., Kano, S. S., Shiraki, Y., and Ito, R. (1993). *Jpn. J. Appl. Phys.*, 32:5586.

[Tanatar and Gold, 1995] Tanatar, B. and Gold, A. (1995). *Phys. Rev. B*, 52:1996.

[Tang et al., 1998] Tang, Y., Rich, D., Moy, A., and Cheng, K. (1998). *Appl. Phys. Lett.*, 72:55.

[Thakur and Neilson, 1997] Thakur, J. and Neilson, D. (1997). *Phys. Rev. B*, 56:7485.

[Tsang and Cho, 1977] Tsang, W. and Cho, A. (1977). *Appl. Phys. Lett.*, 30:293.

[Twardowski and Hermann, 1987] Twardowski, A. and Hermann, C. (1987). *Phys. Rev. B*, 35:8144.

[Ulbrich et al., 1981] Ulbrich, R. G., Naranyanamurti, V., and Chin, M. A. (1981). *J. Phys. (Paris)*, 42:C6-222.

[Vouilloz and Kapon, 1998] Vouilloz, F. and Kapon, E. (1998). *Phys. Rev. Lett.*, submitted.

[Vouilloz et al., 1997a] Vouilloz, F., Oberli, D. Y., Dupertuis, M.-A., Gustafsson, A., Reinhardt, F., and Kapon, E. (1997a). *Phys. Rev. Lett.*, 78:1580.

[Vouilloz et al., 1998a] Vouilloz, F., Oberli, D. Y., Dupertuis, M.-A., Gustafsson, A., Reinhardt, F., and Kapon, E. (1998a). *Phys. Rev. B*, 57:12378.

[Vouilloz et al., 1998b] Vouilloz, F., Oberli, D. Y., Lelarge, F., Dwir, B., and Kapon, E. (1998b). *Solid State Commun.*, in press.

[Vouilloz et al., 1997b] Vouilloz, F., Oberli, D. Y., Wiesendanger, S., Dwir, B., Reinhardt, F., and Kapon, E. (1997b). *Phys. Stat. Sol. (a)*, 164:259.

[Vouilloz et al., 1998c] Vouilloz, F., Wiesendanger, S., Oberli, D. Y., Dwir, B., Reinhardt, F., and Kapon, E. (1998c). *Physica E*, 2:862.

[Wagner et al., 1998] Wagner, H., Langbein, W., Hvam, J., Bacher, G., Kümmel, T., and Forchel, A. (1998). *Phys. Rev. B*, 57:1797.

[Walther et al., 1992] Walther, M., Kapon, E., Christen, J., Hwang, D., and Bhat, R. (1992). *Appl. Phys. Lett.*, 60:521.

[Wang et al., 1990] Wang, H., Jiang, M., and Steel, D. G. (1990). *Phys. Rev. Lett.*, 65:1255.

[Wang et al., 1995] Wang, X.-L., Ogura, M., and Matsuhata, H. (1995). *Appl. Phys. Lett.*, 67:3629.

[Wannier, 1937] Wannier, G. H. (1937). *Phys. Rev.*, 52:191.

[Wegscheider et al., 1993] Wegscheider, W., Pfeiffer, L. N., Dignam, M. M., Pinczuk, A., West, K. W., McCall, S. L., and Hull, R. (1993). *Phys. Rev. Lett.*, 71:4071.

[Wegscheider et al., 1997] Wegscheider, W., Schedelbeck, G., Abstreiter, G., Rother, M., and Bichler, M. (1997). *Phys. Rev. Lett.*, 79:1917.

[Weinmann et al., 1995] Weinmann, D., Müller-Groeling, A., Pichard, J.-L., and Frahm, K. (1995). *Phys. Rev. Lett.*, 75:1598.

[Weisbuch et al., 1981] Weisbuch, C., Miller, R. C., Dingle, R., Gossard, A. C., and Wiegmann, W. (1981). *Solid State Commun.*, 37:219.

[Weisbuch and Vinter, 1991] Weisbuch, C. and Vinter, B. (1991). *Quantum Semiconductor Structures*. Academic Press, New York.

[Weman et al., 1996] Weman, H., Potemski, M., Lazzouni, M. E., Miller, M. S., and Merz, J. L. (1996). *Phys. Rev. B*, 53:6959.

[Winkler, 1995] Winkler, R. (1995). *Phys. Rev. B*, 51:14395.

[Wojs and Hawrylak, 1996] Wojs, A. and Hawrylak, P. (1996). *Solid State Commun.*, 100:487.

[Yariv, 1988] Yariv, A. (1988). *Appl. Phys. Lett.*, 53:1033.

[Yoon et al., 1992] Yoon, H. W., Wake, D. R., Wolfe, J. P., and Morkoç, H. (1992). *Phys. Rev. B*, 46:13461.

[Yu and Cardona, 1996] Yu, P. Y. and Cardona, M. (1996). *Fundamentals of semiconductors*. Springer-Verlag, Berlin Heidelberg.

[Zhang et al., 1995] Zhang, Y., Sturge, M. D., Kash, K., der Gaag, B. P. V., Gozdz, A. S., Florez, L. T., and Harbison, J. P. (1995). *Phys. Rev. B*, 51:13303.

[Zhang et al., 1994] Zhang, Y., Sturge, M. D., Kash, K., der Gaag, B. P. V., Gozdz, A. S., Florez, L. T., and Harbison, J. P. (1994). *J. Lumin.*, 60/61:400.

[Zimmermann, 1992] Zimmermann, R. (1992). *Phys. Stat. Sol. (b)*, 173:129.

[Zrenner et al., 1994] Zrenner, A., Butov, L. V., Hagn, M., Abstreiter, G., Böhm, G., and Weimann, G. (1994). *Phys. Rev. Lett.*, 72:3382.

Curriculum vitae

VOUILLOZ Fabrice

Nationality	Swiss and French
Date of birth	June 29, 1970
Place of origin	1920 Martigny, Switzerland
Civil status	Married

EDUCATION

1984-1986	Collège des Creusets, Valais (High scool)
1986-1989	Collège St-Michel, Fribourg (High scool)
(June 89)	- Maturité Fédérale C (Scientific high scool diploma)
1989-1994	Study at the Physics Department,
	Ecole Polytechnique Fédérale de Lausanne
	1015 Lausanne, Switzerland
(1993-1994)	- Diploma in Physics under the direction of Prof. C. Flytzanis,
	Ecole Polytechnique (Palaiseau, France)
	Diploma thesis: "Spectres de rotation Faraday dans les semiconducteurs semimagnétiques de $Cd_{1-x}Mn_xTe$"
1994-1998	- Doctoral thesis work and teaching assistant at the Physics Department, Ecole Polytechnique Fédérale de Lausanne, under the direction of Prof. E. Kapon.

PUBLICATIONS

1998

- F. Vouilloz and E. Kapon "Observation of strongly reduced phase space for elastic scattering in quantum wires", submitted to Physical Review Letters.
- F. Vouilloz, D.Y. Oberli, F. Lelarge, B. Dwir, and E. Kapon, "Observation of many-body effects in the excitonic spectra of semiconductor quantum wires", *Solid State Commun.*, in press.
- F. Vouilloz, S. Wiesendanger, D.Y. Oberli, B. Dwir, F. Reinhardt, and E. Kapon, "Direct observation of localized excitons in quantum wires by spatially resolved photoluminescence", *Physica E*, **2**:862.
- F. Vouilloz, D.Y. Oberli, M.-A. Dupertuis, A. Gustafsson, F. Reinhardt, and E. Kapon, "Effect of lateral confinement on valence-band mixing and polarization anisotropy in quantum wires", *Phys. Rev. B*, **57**:12378.
- M.-A. Dupertuis, F. Vouilloz, D.Y. Oberli, H. Weman, and E. Kapon, "Band-mixing and coupling in single and double quantum wire structures", *Physica E*, **2**:940.

1997

- F. Vouilloz, D.Y. Oberli, M.-A. Dupertuis, A. Gustafsson, F. Reinhardt, and E. Kapon, "Polarization anisotropy and valence-band mixing in semiconductor quantum wires", *Phys. Rev. Lett.*, **78**:1580.
- F. Vouilloz, D.Y. Oberli, S. Wiesendanger, B. Dwir, F. Reinhardt, and E. Kapon, "Density dependence of localized excitonic recombination in quantum wires", *Phys. Stat. Sol. (a)*, **164**:259.
- D.Y. Oberli, F. Vouilloz, and E. Kapon, "Temperature dependence of exciton lifetimes in quantum wires", *Phys. Stat. Sol. (a)*, **164**:353.

1996

- F. Vouilloz, D.Y. Oberli, and E. Kapon, "Polarization anisotropy in V-groove quantum wires", *Proc. of the 23rd Int. Conf. on the Physics of Semiconductors*, Vol. **2**:1189.

1995

- D.Y. Oberli, F. Vouilloz, M.-A. Dupertuis, A. Gustafsson, F. Reinhardt, and E. Kapon, "Optical spectroscopy of semiconductor quantum wires", *Nuovo Cimento D*, **17**:1641.

1994

- S. Hugonnard-Bruyère, C. Buss, F. Vouilloz, R. Frey, and C. Flytzanis, "Faraday-rotation spectra of semimagnetic semiconductors", *Phys. Rev. B*, **50**:2200.

CONFERENCES

1997

• F. Vouilloz, S. Wiesendanger, D.Y. Oberli, B. Dwir, F. Reinhardt, and E. Kapon "Direct observation of localized excitons in quantum wires by spatially resolved photoluminescence", 8th *International Conference on Modulated Semiconductor Structures*, Santa Barbara (USA), July 14-18. Oral presentation.

• F. Vouilloz, D.Y. Oberli, S. Wiesendanger, B. Dwir, F. Reinhardt, and E. Kapon "Exciton blue-shift in one dimensional quantum wires", 5th *International Meeting on Optics of Excitons in Confined Systems*, Göttingen (Germany), August 11-14. Oral presentation by D.Y. Oberli.

1996

• F. Vouilloz, D.Y. Oberli, and E. Kapon, "Polarization anisotropy in V-groove quantum wires", 23rd *International Conference on the Physics of Semiconductors*, Berlin (Germany), July 21-26. Poster presentation.

• F. Vouilloz, D.Y. Oberli, and E. Kapon, "Polarization anisotropy in V-groove quantum wires", *NATO Advanced Study Institute, Optical Spectroscopy of Low Dimensional Semiconductors*, Ankara (Turkey), September 9-20. Poster presentation.

1995

• F. Vouilloz, D.Y. Oberli, E. Kapon, and E. Colas, "Localization and optical spectroscopy of quantum wires grown by OMCVD", 4th *International Meeting on Optics of Excitons in Confined Systems*, Cortona (Italy), August 28-31. Oral presentation by D.Y. Oberli.